IMPERIAL COLLEGE LONDON

DEPARTMENT OF EARTH SCIENCE AND ENGINEERING

APPLIED 3D FULL-WAVEFORM INVERSION:
INCREASING THE RESOLUTION AND DEPTH PENETRATION

Akela Tian Theresa Silverton

October 2015

Supervisors: Professor Mike Warner and Professor Joanna Morgan

SUBMITTED IN FULFILMENT OF THE REQUIREMENTS FOR THE DEGREE OF DOCTOR OF PHILOSOPHY AND THE DIPLOMA OF IMPERIAL COLLEGE LONDON

Disclaimer and Declaration

Legal Disclaimer

I declare this thesis is entirely my own work and that where any material could be construed as the work of others, this had been fully cited and referenced, and/or with appropriate acknowledgements given.

Signature: _____

Name of Student: Akela Tian Theresa Silverton

Copyright Declaration

The copyright of this thesis rests with the author and is made available under a Creative Commons Attribution Non-Commercial No Derivatives licence. Researchers are free to copy, distribute or transmit the thesis on the condition that they attribute it, that they do not use it for commercial purposes and that they do not alter, transform or build upon it. For any reuse or redistribution, researchers must make clear to others the licence terms of this work.

“Patience attains all that it strives for”

(Saint Teresa of Avila)

Abstract

High-resolution velocity models, at near surface and deeper reservoir depths are produced with three-dimensional, acoustic, anisotropic, full-waveform inversion. Industry experts show eager interest in the development of this technology with a drive to push its application to reflection-dominated streamer datasets as well as ocean-bottom-node datasets in geologically complex environments. Here, a robust methodology employing the use of key strategies to address the inversion of such datasets, attaining increased resolution and depth penetration, is explored.

Synthetic tests were undertaken to exploit the use of reflected energy. Key strategies: muting of direct arrivals, time windowing, and layer-stripping, all produced highly resolved, full-waveform inversion models. These strategies have been incorporated into inversion schemes focusing solely on reflection targets. Strategies to further improve model resolution for field datasets were then investigated. Close examination of a full-waveform inversion model for a shallow-water ocean-bottom-node dataset, revealed a systematic mismatch between the observed and predicted data. After conducting a series of tests, it was illustrated that systematic errors in the starting model, source wavelet, incomplete convergence, or an inadequate finite-difference mesh did not cause the mismatch. Instead, inadequacies in the physics used during inversion are believed to be the cause. The introduction of an offset-variable density scheme during inversion, compensated efficiently and heuristically for these inaccuracies, removing the mismatch and increasing the model resolution.

The sensitivity of full-waveform inversion to local minima, where the computed model is stuck away from the real global-minimum solution and further iterations of the optimisation bring no reward, was kept in mind during the inversion of two deep-water ocean-bottom-node datasets. Thus, full-waveform inversion was undertaken using conditioned data obtained through adaptive matching, incorporating higher frequencies and a greater weight on reflected energy, valuably pushing the limits of resolution and depth penetration of the update. The use of all these robust methodologies improved the travel-time match; better flattened common-image gathers giving a closer fit to well logs and an improvement in the pre-stack depth-migrated image. Effectively, the reflectivity was non-linearly migrated into the velocity model via the inversion acting on raw unprocessed waveforms. Thus, full-waveform inversion can eventually replace conventional processing and migration – all that is needed, is a full-bandwidth velocity model.

Acknowledgements

I will like to thank my supervisors, Professor Mike Warner and Professor Joanna Morgan for their continual support and motivation over the years. Thank you very much.

I will like to thank the sponsors of the Fullwave consortium, for funding my PhD studies.

I will like to thank the postdocs, particularly, Adrian Umpleby, Lluis Guasch, Tenice Nangoo, Gang Yao and Nuno Vieira Da Silva. Thank you for all your support.

I will like to thank all the PhD students of my research group: Henry, Tim, Jack, Oscar and many others, particularly Kenneth Irabor, for the fun times and valuable discussions.

I will like to thank the Earth Science Support staff, all of which have always been helpful.

I will like to thank Chevron for the internship opportunity and the permission to include this work in my thesis. Specific mention to Nikhil Shah (then Chevron now Sub Salt), Uwe Albertin, Zhemin Tan and many others for meaningful discussions.

I will like to thank CGG and Chevron for providing the RTM images when requested.

I will like to thank my friends, both at Imperial and all over the world, for their continued support and encouragement and for all the good times as an international student.

I will like to thank all my friends of the Soulfood Catholic Charismatic prayer group in London. Being part of this Soulfood family has been a true blessing.

I will like to thank my country, Trinidad and Tobago, for the opportunities I have been afforded, and the members of my village in Trinidad, Morne Diable, for the support.

I will like to thank my family: my parents Richard and Tusca, my siblings: Akeem and Anisa, my aunt, uncle and cousin here in London: Pat, Fonda, Kannee, my grandfather: Oliver and many many many others, all over the world, I love you all.

I will like to thank my husband, for his continued encouragement, confidence, love and support for me. Love you Ifeanyi.

Lastly and most importantly, I will like to thank God for the countless blessings He has bestowed and continue to bestow upon me during the course of my studies here in London and always.

Dedication

I dedicate this thesis to my husband Ifeanyi, my daughter Chidera and my family.

TABLE OF CONTENTS

DISCLAIMER AND DECLARATION ..... **I**

ABSTRACT ..... **III**

ACKNOWLEDGEMENTS ..... **IV**

DEDICATION ..... **V**

LIST OF FIGURES ..... **IX**

LIST OF TABLES ..... **XIX**

NOMENCLATURE ..... **XX**

CHAPTER 1 : INTRODUCTION **1**

OVERVIEW 1

FULL WAVEFORM INVERSION (FWI) 1

EVOLUTION OF FWI 2

DEFINITION OF RESEARCH PROBLEM 9

THESIS STRUCTURE 10

CONTRIBUTIONS 10

CHAPTER 2 : BACKGROUND **12**

MATHEMATICAL THEORY 12

STABILITY CONDITIONS 20

DOMAIN OF APPLICATION 20

APPLICATION OF FULL WAVEFORM INVERSION 21

Key Parameterisation *21*

Data Requirements *24*

The Starting Model *27*

The Source Signature *28*

Model QC techniques *29*

ADVANTAGES AND LIMITATIONS 30

FWI: Transmission verses reflection data *30*

SUMMARY 31

CHAPTER 3 : REFLECTION FWI STRATEGIES **32**

OVERVIEW 32
INTRODUCTION 33
STRATEGIES FOR REFLECTION FWI 35
Gaussian Windowing *36*
Muting of Direct Arrival *37*
Multi-scale approach *38*
RESULTS AND DISCUSSIONS 42
Choosing the starting frequency *43*
Sensitivity to acoustic impedance contrast *45*
Transmission verses reflection target *47*
Choosing the parameterisation *49*
KEY FINDINGS 57
SUMMARY AND FURTHER WORK 58
CHAPTER 4 : OFFSET-VARIABLE DENSITY FULL-WAVEFORM INVERSION ..59
INTRODUCTION 59
PREVIOUS RESEARCH 62
MISMATCH 67
Time-domain traces *67*
Phase Residuals *68*
TESTS TO IMPROVE MISMATCH 69
Varying the source wavelet *69*
Increasing the number of iterations *72*
Perturbing the velocity model *72*
Changing the finite difference grid spacing *73*
Test deductions *74*
Possible physical effects *75*
USE OF NON-PHYSICAL WATER DENSITY 77
Implementation *80*
RESULTS 81
Well Ties *82*
Forward Synthetics *84*
Depth Migration *85*
SUMMARY 88

CHAPTER 5 : 3D TIME DOMAIN FWI – NON-LINEARLY MIGRATING REFLECTIVITY INTO THE VELOCITY MODEL 89
OVERVIEW 89
INTRODUCTION 91
FWI SETUP AND A NEW WORKFLOW 96
Data Match *96*
OPTIMIZING THE FIT OF THE WATER-BOTTOM MULTIPLE 97
TEST ONE SHOT GRADIENT DIRECTION 101
DESIRED VERSES UNDESIRED CONVERGENCE 103
RESULTS AND CONSEQUENCES OF RESULTS 106
Field A Results *108*
Field B Results *131*
Reflectivity sections from FWI models *135*
SUMMARY 138
CHAPTER 6 : CONCLUSIONS 141
REFERENCES 143
APPENDICES 150
APPENDIX I –ELASTIC 150

List of Figures

FIGURE 1-1: SCHEMATIC ILLUSTRATING DIFFERENT ARRIVALS THAT LEAD TO THE GENERATION OF THE FULL SEISMIC RECORD AT THE RECEIVER LOCATION. A REPRESENTATION OF A SINGLE TRACE AT THE RECEIVER LOCATION IS SHOWN IN A) THE FULL SEISMIC RECORD B) THE PRIMARY REFLECTIONS OBTAINED AFTER PRE-PROCESSING. THE FULL SEISMIC RECORDS ARE USED IN FWI WHILE THE PRIMARY REFLECTIONS ONLY ARE USED IN MIGRATION 3

FIGURE 1-2: SCHEMATIC OF KEY ARRIVALS EVIDENT IN A SHOT RECORD AS OBTAINED FROM SEVERAL RECEIVER LOCATIONS AS IN FIGURE 1-1. HERE THE REFRACTED ARRIVALS ARE ABSENT DUE TO THE INSUFFICIENTLY LONG OFFSETS AS SETUP BY THE ACQUISITION DESIGN FOR THIS SHOT RECORD. 4

FIGURE 1-3: PRE-STACK DEPTH MIGRATED IMAGE OF A CHANNEL AND UNDERLYING REFLECTOR. USING A FWI VELOCITY MODEL (RIGHT) VERSES A CONVENTIONAL VELOCITY MODEL, SPURIOUS STRUCTURE ON THE UNDERLYING REFLECTOR (BOTTOM ARROW) HAS DISAPPEARED AND GEOLOGICAL STRUCTURE WITHIN THE CHANNEL (TOP ARROW) IS MORE REASONABLE (WARNER *ET AL*. 2008). 6

FIGURE 1-4: FWI APPLICATION TO THE VALHALL FIELD. A) VERTICAL SLICE THROUGH THE REFLECTION TOMOGRAPHY VELOCITY MODEL AND B) CORRESPONDING REFLECTION TOMOGRAPHY MIGRATED IMAGE; C) VERTICAL SLICE THROUGH THE FWI VELOCITY MODEL WITH D) CORRESPONDING FWI MIGRATED IMAGE. HORIZONTAL SLICE AT 1050M SHOWING ITS EVOLUTION OVER THE COURSE OF FWI: (E) THE 2007 STARTING MODEL; (F) AFTER USING ONLY THE LOWEST FREQUENCY OF 3.5 HZ; AND (G) AFTER SIX FREQUENCIES FROM 3.5 TO 7.0 HZ WERE USED (SIRGUE *ET AL*. 2009). 7

FIGURE 2-1: SYNTHETIC ILLUSTRATION OF THE FORWARD AND INVERSE PROBLEM USING MODELLING CODES USED HERE AND A 3D SYNTHETIC MARMOUSI MODEL.....14

FIGURE 2-2: FLOWCHART SUMMARISING THE THEORY OF FWI.....19

FIGURE 2-3: SCHEMATIC ILLUSTRATING THE RELATIONSHIP BETWEEN THE DIFFERENT ARRIVALS AND THE DEPTH OF INVESTIGATION.....25

FIGURE 2-4: SCHEMATIC ILLUSTRATING THE BENEFITS OF OBTAINING GLOBAL CONVERGENCE USING LOW FREQUENCY AS OPPOSE TO HIGH FREQUENCY. THE STARTING MODEL NEEDS TO BE CLOSE TO THE TRUE MODEL WHEN STARTING INVERSIONS FROM HIGHER FREQUENCIES (DRAWN). 26

FIGURE 2-5: SYNTHETIC ILLUSTRATING SHOWING THE EFFECT OF THE STARTING MODEL AND USING HIGH VERSES LOW FREQUENCIES FOR A DATASET OF FREQUENCY RANGE 0 – 6 HZ.28
FIGURE 2-6: ILLUSTRATION OF THE SOURCE GHOST AND THE FIRST AND SECOND ORDER MULTIPLES, WHICH ARE INITIALLY REMOVED AND REMODELLED DURING THE MODELLING PROCESS.....29
FIGURE 3-1: CONCEPTUAL DIAGRAM ILLUSTRATING THE THEORETICAL RELATIONSHIP BETWEEN REFLECTION AND TRANSMITTED AMPLITUDES AT A REFLECTOR BOUNDARY OF AMPLITUDE R. CROSS-CORRELATION OF THE FORWARD SOURCE WAVEFIELD OF AMPLITUDE 1 (SOLID RED) WITH THE REFLECTED RECEIVER WAVEFIELD OF AMPLITUDE R^2 (DASHED BLUE) ALONG WITH THE CROSS CORRELATION OF THE BACK-PROPAGATED RECEIVER WAVEFIELD OF AMPLITUDE R (SOLID BLUE) WITH THE REFLECTED SOURCE WAVEFIELD OF AMPLITUDE R (DASHED RED) FORMS THE MACRO-MODEL UPDATE OF AMPLITUDE R^2. THE AMPLITUDE AT REFLECTION POINT REMAINS R. GIVEN THAT R IS LESS THAN 1; THE REFLECTIVITY UPDATE IS STRONGER THAN THE MACRO-MODEL UPDATE. 34
FIGURE 3-2: TRUE MODEL USED IN THE GENERATION OF A REFLECTION-DOMINATED SYNTHETIC DATA USED IN THE TESTING OF REFLECTION STRATEGIES. THE DIMENSIONS OF THE MODEL ARE SUCH THAT REFLECTIONS ARE THE KEY ARRIVALS EVIDENT. 36
FIGURE 3-3: TRAVEL-TIME PLOT SHOWING A COMPARISON OF THE SYNTHETIC AND OBSERVED DATASET INDICATING THE KEY ARRIVALS. THE DIRECT ARRIVAL IS ACCURATE IN TIMING BUT SLIGHTLY DIFFERENT IN AMPLITUDE DUE TO THE APPLICATION OF TRACE NORMALISATION. 38
FIGURE 3-4: A SHOT RECORD ILLUSTRATING THE OFFSET CONTINUATION AND TIME LIMITING APPROACH.....39
FIGURE 3-5: COMPARISON BETWEEN A) PREDICTED DATA FOR THE HOMOGENOUS STARTING MODEL AND B) OBSERVED DATA. ENLARGEMENT OF THESE DATA AT: NEAR, MID AND FAR OFFSETS IN FIGURE 3-6 SHOW CLEARER THAT THE DIRECT ARRIVAL IS WELL-MATCHED IN PHASE AND AMPLITUDE AT NEAR OFFSETS AND IN PHASE AT THE FURTHER OFFSETS INDICATING THE DATA IS NOT CYCLE-SKIPPED. 40
FIGURE 3-6: ENLARGED VIEW AT A) NEAR B) MID C) FAR OFFSETS FOR THE PREDICTED DATA (LEFT) AND OBSERVED DATA (RIGHT). 41
FIGURE 3-7: 9HZ FWI RECOVERED MODELS OBTAINED USING A) STARTING FREQUENCY OF 2.5HZ B) STARTING FREQUENCY OF 1 HZ AND C) TRUE MODEL. THE WHITE DASHED LINE INDICATES THE CENTRAL 1D PROFILE EXTRACTED BELOW. 44

FIGURE 3-8: COMPARISON OF THE VELOCITY-DEPTH PROFILE THROUGH THE CENTRE OF THE TRUE AND 9HZ FWI RECOVERED MODELS AT DIFFERENT STARTING FREQUENCIES OF A) 2.5HZ B) 1HZ 45

FIGURE 3-9: COMPARISON BETWEEN THE FWI RECOVERED MODELS (LEFT) AND THE TRUE MODEL (CENTRE) WITH A VELOCITY-DEPTH PROFILE (RIGHT) FOR DIFFERENT ACOUSTIC IMPEDANCE CONTRASTS. THE CHANGE IN THE VELOCITY ACROSS THE REFLECTOR INTERFACE IS A) 150MS^{-1} B) 300MS^{-1} C) 600MS^{-1}. THE BACKGROUND VELOCITY IS FIXED AT 2000MS^{-1}. FOR ALL THE CASES ABOVE THE TOP INTERFACE IS FAIRLY WELL RECOVERED, WITH THE RECOVERED VELOCITIES NEAR THE LOWER REFLECTOR INTERFACE BEING 50% ACCURATE, THAT IS, 50% OF THE TRUE. 46

FIGURE 3-10: A) STARTING MODELS B) FWI RECOVERED MODELS C) TRUE MODEL 48

FIGURE 3-11: FULL-FOLD REGION OF THE VELOCITY MODEL FOR A) STANDARD FWI, B) FWI WITHOUT GAUSSIAN WINDOWING C) FWI WITH MUTED DIRECT ARRIVAL MUTED D) FWI COMBINING ALL KEY PARAMETERISATIONS ABOVE. 50

FIGURE 3-12: 1D VELOCITY DEPTH PLOT OF THE TRUE AND 9HZ FWI RECOVERED MODELS CORRESPONDING TO THE MODELS DISPLAYED IN FIGURE 3-11. 51

FIGURE 3-13: 9HZ FWI RECOVERED MODELS USING A) COMBINED PARAMETERISATION B) TIME-OFFSET LIMITING STRATEGY TOGETHER WITH COMBINED PARAMETERISATION C) TRUE MODEL. THE WHITE DASHED LINE INDICATES THE CENTRAL 1D PROFILE EXTRACTED FOR MORE DETAILED ANALYSIS 53

FIGURE 3-14: COMPARISON BETWEEN THE VELOCITY-DEPTH PROFILES EXTRACTED FROM THE CENTRE OF THE TRUE AND FWI RECOVERED MODELS OBTAINED USING THE DIFFERENT PARAMETERISATION: A) COMBINED PARAMETERISATION B) TIME-OFFSET LIMITING STRATEGY TOGETHER WITH COMBINED PARAMETERISATION. THE TIME-OFFSET STRATEGY RECOVERS THE HIGH VELOCITY LAYER WELL WITH AN OVER-ESTIMATE AT THE INTERFACES. THE BACKGROUND VELOCITIES ARE ALSO OVERESTIMATED ABOVE AND BELOW THE HIGH VELOCITY LAYER 54

FIGURE 3-15: FWI RECOVERED MODELS SHOWING THE INVERSION RESULTS AFTER THE A) INITIAL B) THE INTERMEDIATE AND C) THE FINAL ITERATIONS. AFTER 20 ITERATIONS, THE TOP AND BASE REFLECTOR POSITIONS ARE ALREADY CORRECTLY POSITIONED. THE INTERMEDIATE ITERATIONS SERVE TO INCREASE THE VELOCITIES WITHIN THE HIGH VELOCITY LAYER AS WELL AS CORRECT FOR SHALLOW INACCURACIES. THE FINAL

ITERATIONS SERVE CONTINUE TO IMPROVE THE VELOCITIES WITHIN THE HIGH VELOCITY LAYER. THESE MODELS WERE GENERATED USING THE COMBINED PARAMETERISATION....55

FIGURE 3-16: PREDICTED DATA OBTAINED FROM A) THE STARTING MODEL, THE FWI RECOVERED MODELS AT B) 1 ITERATION C) 20 ITERATION (1HZ) D) 60 ITERATIONS (2HZ) E) 100 ITERATIONS (3HZ) F) 120 ITERATIONS (5HZ) G) 140 ITERATIONS (7HZ) H) 160 ITERATIONS (9HZ) AND THE I) OBSERVED DATA. AT THE EARLY ITERATIONS, THE TOP AND BASE REFLECTORS REPRESENTING THE VELOCITY CONTRAST AT THE HIGH VELOCITY LAYER ARE INSERTED WITH MINOR REFLECTORS ADDED AS WELL. WITH INCREASING FREQUENCY AND NUMBER OF ITERATIONS, MINOR REFLECTORS ADDED AT THE EARLY ITERATIONS WITH THE IMPROVEMENTS IN THE HIGH VELOCITY CONTRAST LAYER, ARE EVENTUALLY REMOVED FROM THE DATA.....56

FIGURE 4-1: (A) COMPARISON BETWEEN FIELD AND PREDICTED DATA FOR THE FWI-RECOVERED MODEL, FOR WHICH THE WAVEFIELD PASSES THROUGH THE GAS CLOUD. THE AMPLITUDES, AND INDIVIDUAL PEAKS AND TROUGHS, WITHIN THE FIELD AND SYNTHETIC DATA MATCH EACH OTHER WELL. ENLARGEMENT OF THESE DATA AT: NEAR, MID AND FAR OFFSETS SHOW CLEARER THE SYSTEMATIC MISMATCH IN FIGURE 4-6.....60

FIGURE 4-2: (A) RAW SHOT RECORD, TRACE EQUALIZED WITH NO GAIN RECOVERY (B) THE SAME RECORD PREPROCESSED IMMEDIATELY PRIOR TO FWI – DATA WAS LOW-PASS FILTERED DECIMATED AND MUTED AS DESCRIBED ABOVE. (SOURCE: WARNER *ET AL.* 2013). 63

FIGURE 4-3: OBSERVED DATA PHASE FOR A COMMON RECEIVER GATHER (LOCATION INDICATED BY BLACK ARROW) AT A) 2HZ AND B) 3HZ. A GAUSSIAN TIME WINDOW HAS BEEN APPLIED TO THE DATA WHEN EXTRACTING THE PHASE THEREBY FOCUSING ON THE EARLY ARRIVALS FOR THIS PHASE ANALYSIS. IT WAS DERIVED THAT THE 3 HZ PHASE IS FAR MORE SPATIALLY COHERENT THAN THE 2 HZ PHASE AND WAS HENCEFORTH CHOSEN AS THE LOWEST USEABLE FREQUENCY FOR FWI (MODIFIED FROM SHAH *ET AL.* 2014) 64

FIGURE 4-4: VERTICAL SLICES THROUGH THE STARTING VELOCITY MODEL: (A) THROUGH THE PERIPHERY OF THE GAS CLOUD, AND (B) THROUGH THE CENTRAL PORTION OF THE GAS CLOUD (SOURCE: WARNER *ET AL.* 2013). 65

FIGURE 4-5: PLOT OF THE ONE-DIMENSIONAL ANISOTROPY MODELS OF DELTA AND EPSILON USED IN ALL OUR FWI RUNS, WITH A VERTICAL AXIS OF SYMMETRY. THESE ARE KEPT FIXED AND WERE ORIGINALLY GENERATED FOR PSDM BY CGG - THE PROCESSING CONTRACTOR. 66

FIGURE 4-6: ENLARGED VIEW OF FIGURE 4-1 AT: A) NEAR, B) MID AND C) FAR OFFSET LOCATIONS COMPARING THE FIELD AND PREDICTED DATA TIME DOMAIN TRACES ILLUSTRATING THE SYSTEMATIC MISMATCH. 68

FIGURE 4-7: PHASE RESIDUAL PLOTS FOR A) THE STARTING MODEL AND B) THE ORIGINAL FWI RECOVERED MODEL. 69

FIGURE 4-8: SOURCE SIGNATURES (A) FULL-BANDWIDTH WAVEFORMS. (B) LOW-PASS FILTERED WAVEFORMS AT DIFFERENT SCALE (SOURCE: WARNER *ET AL*. 2013) 70

FIGURE 4-9: COMPARISON BETWEEN (I) FIELD DATA, (II) PREDICTED DATA OBTAINED FOR THE FWI-RECOVERED MODEL OBTAINED WHEN USING THE ORIGINAL SOURCE WAVELET, AND (III) PREDICTED DATA OBTAINED FROM FWI WHEN USING A WAVELET THAT HAS BEEN ADVANCED IN TIME. (A) NEAR, (B) MID, AND (C) FAR OFFSETS ARE SHOWN. THE DELAY LARGELY REMAINS, DEMONSTRATING THAT INCORRECT SOURCE TIMING DOES NOT CAUSE THE MISMATCH. 71

FIGURE 4-10: COMPARISON BETWEEN (I) FIELD DATA, PREDICTED DATA OBTAINED FROM THE RECOVERED FWI MODEL (II) AFTER 108 ITERATIONS, (III) AFTER 216 ITERATIONS, AND (IV) AFTER 108 ITERATIONS, PERTURBATION BY +1% FOLLOWED BY A FURTHER 108 ITERATIONS. (A) NEAR, (B) MID, AND (C) FAR OFFSETS ARE SHOWN. IT WAS DISCERNED THAT THE DELAY REMAINS IN EACH CASE ILLUSTRATING THAT THE MISMATCH IS NOT CAUSED BY INCOMPLETE CONVERGENCE, OR BY A SYSTEMATIC BIAS IN THE STARTING MODEL AS CONVERGENCE HAS PERHAPS REACHED A PLATEAU. 73

FIGURE 4-11: COMPARISON BETWEEN (I) OBSERVED AND (II) PREDICTED DATA FOR DIFFERENT FINITE DIFFERENCE MESHES OF A) 50 M, AND B) 20 M, AT C) NEAR, D) MID, AND E) FAR OFFSET. IT WAS DISCERNED THAT THE DELAY REMAINS IN EACH CASE ILLUSTRATING THAT THE MISMATCH IS NOT CAUSED BY IMPROPER REPRESENTATION OF KEY REFLECTIVE/ELASTIC HORIZONS E.G. SEABED BOUNDARY, ON THE FINITE DIFFERENCE MESH. 76

FIGURE 4-12: COMPARISON BETWEEN (I) FIELD DATA, (II) PREDICTED DATA OBTAINED USING THE ORIGINAL RECOVERED FWI MODEL WATER DENSITIES OF 250 KG M^{-3}, (III) 500 KG M^{-3}, (IV) 750 KG M^{-3}, (V) 1000 KG M^{-3}, (VI) 1250 KG M^{-3}, AND (VII) 1500 KG M^{-3}. (A) NEAR, (B) MID, AND (C) FAR OFFSETS ARE SHOWN. THESE NON-PHYSICAL WATER DENSITIES CHANGE THE REFLECTIVITY OF THE SEABED AND THE AMPLITUDE OF WATER-BOTTOM MULTIPLES, THEREBY CHANGING THE INTERFERENCE PATTERN OF DIFFERENT ARRIVALS RESULTING IN

an apparent change in travel time. A better match is obtained with a density of 500 kg m^{-3} at near offset and 250 kg m^{-3} at far offsets.....77
Figure 4-13: Normalized cross-correlation between the observed and predicted data and the corresponding maximum correlation time lag for different water densities at (a), (b) near and (c), (d) far offsets. Time lags range between 5 and 12ms with zero lag corresponding to a good data match. A linearly decreasing water density from b) near to d) far offset results in a time lag close to zero, implying a good match between field and predicted data.....79
Figure 4-14: Horizontal slices at 1200 m depth through: a) the starting velocity model b) original FWI recovered model and c) FWI recovered model using an offset-variable water density. The model shown in (c) suggests improved definition of the gas-cloud and of gas-charged faults within the offset-variable model. 81
Figure 4-15: Vertical depth slices through: a) Starting model b) Conventional FWI model c) Offset-variable water-density FWI model.....82
Figure 4-16: Well log comparison to vertical pseudo profiles from the starting model, original FWI recovered model and the offset-variable density FWI model 83
Figure 4-17: Data at (a) near, (b) mid, and (c) far offsets, for: (i) field data, (ii) synthetics generated from the conventional FWI model, (iii) synthetics generated from offset-variable density FWI model. The offset-variable density FWI model better fits the field data. 84
Figure 4-18: Vertical depth slices, inline on the left and crossline on the right, through the RTM images generated by CGG obtained using (a) the starting model, (b) the original FWI model, and (c) the offset-variable density FWI model. There is continuous improvement in the imaging from (a) to (b) to (c). 86
Figure 4-19: Horizontal depth Slices through the RTM images produced by CGG, illustrating an improvement with increased simplification in the structure moving from (a) starting model to (b) original FWI model to (c) offset-variable density FWI Model. 87
Figure 5-1: Comparison between the tomographic velocity model and the high bandwidth FWI velocity model obtained via processes described in this

chapter. The independent migrated vendor volume based on the tomographic velocities is also illustrated. 90
Figure 5-2: Illustration of the use of time-domain FWI to recover a high-resolution, heterogeneous velocity model (right) using raw shot gathers (left). This example is of the best result on the synthetic Chevron benchmark test (Warner, 2014). 92
Figure 5-3: Comparison between the low (red) and the high (green) bandwidth observed data used for FWI, to the raw observed data (black) at full bandwidth. 92
Figure 5-4: Comparison of the observed (a & b) and modelled (c & d) data at near (top), and far (bottom) offset locations for the 0 -6 Hz low frequency bandwidth 93
Figure 5-5: Comparison of the observed (a & b) and modelled (c & d) data at near (top), and far (bottom) offset locations for the 0 -15 Hz high frequency bandwidth 94
Figure 5-6: Illustration of the a) starting models obtained from Chevron b) 3-6Hz FWI recovered models c) indication of climbing to higher frequencies and d) seismic image; for Field A and Field B 95
Figure 5-7: A closer look at the data, illustrating the key arrivals in the observed, and the starting model predicted data. The source signature extracted from the observed data and a schematic of these arrivals is also indicated. 97
Figure 5-8: Forward model tests revealed the correct reflectivity parameterization necessary to correct time shifts of the multiple events between the predicted and observed data. A water velocity of $1490 ms^{-1}$ and minimum rock velocity of $1515 ms^{-1}$ was sufficient to correct apparent travel-time shift. 98
Figure 5-9: Comparison between the observed data (left), predicted data obtained by inserting seabed reflectivity into the starting model resulting in the generation of the sea-bottom multiple (middle), and predicted data obtained by both inserting the seabed reflectivity in the model as well as conditioning the data through an adaptive matching technique (right). These are shown at the near, mid and far offset locations. 100

FIGURE 5-10: HORIZONTAL AND VERTICAL SLICES THROUGH THE GRADIENT SHOWING THE EFFECT OF THE NEW WORKFLOW ON A ONE-SHOT GRADIENT DIRECTION TEST 102
FIGURE 5-11: COMPARISON BETWEEN THE OBSERVED DATA OBTAINED FROM CHEVRON AND THE RECOVERED MODEL SYNTHETICS GENERATED WITH (DESIRED-MINIMUM CASE) AND WITHOUT (LOCAL-MINIMUM CASE) THE APPLICATION OF THE NEW WORKFLOW BEFORE FWI 104
FIGURE 5-12: COMPARISON BETWEEN A) STARTING MODEL SLICES OBTAINED FROM CHEVRON B) FWI MODEL SLICES WITHOUT THE USE OF THE WORKFLOW – LOCAL MINIMUM CASE C) FWI MODEL SLICES WITH THE USE OF THE WORKFLOW – DESIRED MINIMUM CASE; AT THE SHALLOWER DEPTH 1 AND DEEPER DEPTH 2 LEVELS. 105
FIGURE 5-13: SHALLOWER DEPTH SLICE SHOWING TAKEN THROUGH THE STARTING MODEL (TOP) AND 6 HZ RECOVERED MODEL (BOTTOM). LOW VELOCITY SHALLOW GAS POCKETS OF VARYING DIMENSIONS EVIDENT IN THE RED DASHED RECTANGLE. THESE WILL BE CLOSER EXAMINED IN FIGURE 5-14.....109
FIGURE 5-14: ZOOMED VERSION OF THE SHALLOW GAS POCKETS AT THE SHALLOWER DEPTH (TOP), THE CORRESPONDING SEISMIC IMAGE (MIDDLE) AND VELOCITY-SEISMIC OVERLAY (BOTTOM) SHOWING EXACT CONFORMANCE OF THE LOW VELOCITY POCKETS OF VARYING DIMENSIONS WITH THE INDEPENDENT SEISMIC IMAGE.....110
FIGURE 5-15: DEPTH SLICE (250 M BELOW THE SHALLOWER DEPTH) THROUGH THE STARTING MODEL (TOP), RECOVERED MODEL (MIDDLE) AND CORRESPONDING INDEPENDENT SEISMIC IMAGE (BOTTOM) SHOWING VARYING EXTENTS OF LOW VELOCITY ANOMALIES 111
FIGURE 5-16: RECOVERED MODEL OVERLAY (TOP), UPDATE MODEL OVERLAY (MIDDLE) AND THE CORRESPONDING INDEPENDENT SEISMIC IMAGE (BOTTOM) AT DEPTH SLICE (250 M BELOW THE INITIAL). THE WHITE CIRCLE INDICATES AREA OF KNOWN GAS ANOMALY NOT EVIDENT IN INDEPENDENT IMAGE; THE ARROW INDICATES REGIONS WITH SHARP VARIATIONS IN VELOCITY. 112
FIGURE 5-17: SHOWCASE OF FWI CAPABILITY FOR THE BEKAPAI FIELD INDONESIA BY BEELE *ET AL*. (2014). THE INDEPENDENT SEISMIC IMAGE IS ILLUSTRATED ON THE LEFT AND THE FWI MODEL IS ILLUSTRATED ON THE RIGHT. 114
FIGURE 5-18: CAPABILITY AT 6HZ SHOWING THE RECOVERY OF FAULTS FOR FIELD A. THE INDEPENDENT SEISMIC IMAGE IS ILLUSTRATED ON THE LEFT AND THE 6HZ FWI MODEL IS ILLUSTRATED ON THE RIGHT. 115

FIGURE 5-19: CAPABILITY AT 15HZ SHOWING THE INTERPRETABILITY OF THE FAULTS AND INDIVIDUAL BEDDING PLANES WITH SATURATED SANDS NEAR THE FAULTS. THIS ADDED CAPABILITY INVOLVES THE USE OF THE NEW WORKFLOW. THE INDEPENDENT SEISMIC IMAGE IS ILLUSTRATED ON THE LEFT AND THE 15HZ FWI MODEL IS ILLUSTRATED ON THE RIGHT. 116

FIGURE 5-20: VERTICAL INLINE THROUGH STARTING (TOP) AND 6HZ FWI RECOVERED MODEL (BOTTOM). SHALLOW GAS POCKETS ARE CLEARLY VISIBLE AND EMERGENCE OF SATURATED SANDS BOUNDED BY A NORMAL FAULT IS EVIDENT. 117

FIGURE 5-21: VERTICAL INLINE THROUGH THE STARTING (TOP) AND 15HZ FWI RECOVERED MODEL (BOTTOM) OVERLAY. CLEAR DEFINITION OF GAS POCKETS, SATURATED SANDS, FAULTS AND SHALLOW DIAPER STRUCTURE ARE SHOWN. THE WHITE BOX INDICATES THE ENLARGED REGION THAT FOLLOWS IN FIGURE 5-22. 118

FIGURE 5-22: ZOOMED IN SEGMENT OF THE ANTICLINAL STRUCTURE OF FIGURE 5-21 THROUGH THE A) RECOVERED MODEL, B) MODEL-SEISMIC OVERLAY, C) INDEPENDENT SEISMIC IMAGE. 119

FIGURE 5-23: VERTICAL SLICE THROUGH A) THE STARTING MODEL OVERLAY AND B) 15HZ FWI MODEL OVERLAY. A SERIES OF NORMAL FAULTS ARE CLEARLY DISCERNABLE AT THE CREST OF THE ANTICLINE. THE WHITE BOX HIGHLIGHTS THE ZOOMED REGION THAT FOLLOWS IN FIGURE 5-24 120

FIGURE 5-24: ZOOMED IN SEGMENT ACROSS THE CREST OF THE ANTICLINE SHOWING THE SERIES OF NORMAL FAULTS IN THE FWI MODEL, THE MODEL-SEISMIC OVERLAY AND THE INDEPENDENT SEISMIC IMAGE. 121

FIGURE 5-25: RAW MIGRATION GATHERS GENERATED BY THE CHEVRON MIGRATION TEAM FOR A) INITIAL MODEL AND B) FWI MODEL PRODUCED FROM THIS RESEARCH. INCREASED FLATNESS OF THE GATHERS ATTRIBUTABLE TO A BETTER VELOCITY MODEL GENERATED BY FWI. 122

FIGURE 5-26: STACKED MIGRATION IMAGE GENERATED BY THE CHEVRON MIGRATION TEAM GENERATED USING A) THE STARTING MODEL AND B) FWI MODEL PRODUCED BY THIS RESEARCH. BETTER DEFINITION OF FAULTS AND GEOLOGICAL INTERFACES. 123

FIGURE 5-27: REPRESENTATION OF OBJECTIVE FUNCTION SURFACE IN TERMS OF HORIZONTAL AND VERTICAL VELOCITIES 126

FIGURE 5-28: THE A) TRUE EPSILON MODEL; B) TRUE VELOCITY MODEL AND THE C) CORRESPONDING OBSERVED DATASET 127

FIGURE 5-29: THE INVERSION FOR ANISOTROPY USING A) START EPSILON OF ZERO AND THE FWI RECOVERED EPSILON MODELS AFTER B) 2 SUB-ITERATIONS C) 8 SUB-ITERATIONS D) 32 SUB-ITERATIONS AND THE CORRESPONDING E) TRUE EPSILON MODEL. THE UPDATE IS FOCUSED IN THE CENTRAL PORTION OF THE MODEL. 128
FIGURE 5-30: THE LONG OFFSET ARRIVALS FOR DIFFERENT MODELS: A) STARTING MODEL B) SUB-ITERATION 2 FWI MODEL C) SUB-ITERATION 4 FWI MODEL D) SUB-ITERATION 32 FWI MODEL AND THE CORRESPONDING E) OBSERVED DATASET EXTRACTED FROM THE SHOT GATHER AS SHOWN IN F). 129
FIGURE 5-31: 2050M DEPTH SLICES SHOWING THE RECOVERY OF SPECIFIC STRUCTURES IN THE EPSILON MODEL 130
FIGURE 5-32: STARTING MODEL PRODUCED BY CHEVRON (TOP) AND HIGH RESOLUTION FWI MODEL - GROWTH FAULT, RESERVOIRS ARCHITECTURE, EXTENT OF RESERVOIR, SHALLOW GAS POCKETS ARE ALL IDENTIFIED 132
FIGURE 5-33: DEPTH SLICE THROUGH GAS POCKETS AT SHALLOW DEPTH SHOWING ITS GEOMETRY AND EXTENT 133
FIGURE 5-34: DEPTH SLICE SHOWING THE RESERVOIR FORMATION IN THE UPTHROWN BLOCK WITH FAULT & DIP CLOSURE 134
FIGURE 5-35: SCHEMATIC OF THE MEANING OF AN IMPEDANCE INCREASE AND DECREASE.....135
FIGURE 5-36: REFLECTIVITY SECTIONS OBTAINED DIRECTLY FROM THE FWI VELOCITY MODELS AT A) 3-10HZ BAND B) 3-15HZ BAND C) 3-20HZ BAND WITH THE CORRESPONDING FWI RECOVERED VELOCITY MODELS IN THE INSETS 136
FIGURE 5-37: SCHEMATIC SHOWING THE 2 FIELDS EXTRACTED FROM FWI – THE MACRO-VELOCITY AND THE FWI REFLECTIVITY. THE GRADIENT REPRESENTATION ON THE LEFT IS THE CURRENT PRACTICE AND THE DECOMPOSED GRADIENT REPRESENTATION ON THE RIGHT IS THE NEXT LOGICAL STEP TO CLOSE THE LOOP 137
FIGURE 5-38: ILLUSTRATION OF THE A) STARTING MODELS B) 3-6HZ FWI RECOVERED MODELS C) 3-15HZ FWI MODELS AND D) INDEPENDENT SEISMIC IMAGE; FOR FIELD A AND B. .140

List of Tables

TABLE 2-1: COMPARISON OF THE DIFFERENT KERNELS 22
TABLE 2-2: SUMMARY OF FORMULAE USED IN THE PARAMETERISATION OF 'AMPLITUDE' AND 'NORMALISE' 23
TABLE 3-1: SUMMARY OF PARAMETERS KEPT CONSTANT FOR THE INVERSIONS 42
TABLE 5-1: SUMMARY OF INVERSION PARAMETERS FOR THE DIFFERENT INVERSIONS, WHERE (L) REPRESENTS LOW BANDWIDTH AND (H) REPRESENTS HIGH BANDWIDTH. PARAMETER SETS ARE DEFINED IN CHAPTER 2. 106
TABLE 5-2: SOURCE AND RECEIVER GEOMETRY FOR THE DIFFERENT DATASETS 107

Nomenclature

General Notations

a scalar constant, variable or function

a column vector

A matrix

$\mathbf{A}^{\boldsymbol{T}}$ transpose of A

$\mathbf{A}^{-1}$ inverse of A

Specific Notations

p acoustic pressure (or ϕ or u)

s driving source

V_p acoustic velocity (or v or c)

ρ density

t time

A operator resulting from the numerical discretisation of the wave equation (or B or G)

p pressure wavefield at every point and time in a discretised model (or ϕ or u)

s driving source at every point and time in a discretised model

m discretised model parameters

G function that generates a wavefield from the model parameters

d a seismic dataset – typically this will be a subset of a wavefield p

D diagonal matrix that selects a subset of a wavefield such that d = Dp

$\mathbf{d}_{\boldsymbol{obs}}$ observed seismic dataset

$\mathbf{d}_{\boldsymbol{calc}}$ calculated seismic dataset

$\delta\mathbf{d}$ residual dataset, $\delta\mathbf{d} = \mathbf{d}_{calc} - \mathbf{d}_{obs}$ (or $\Delta\mathbf{d}$ or $\mathbf{r}$)

$\mathbf{m_0}$ starting model parameters

$\delta\mathbf{m}$ perturbation to model parameters (or $\Delta\mathbf{m}$)

f the objective (or cost or misfit) function

$\mathbf{H}$ Hessian matrix

α step length

$\delta\mathbf{p}$ wavefield generated by back propagating the residuals (or p$back$ or v)

$\mathbf{q}$ change in data residuals, i.e. $\mathbf{q} = \delta\mathbf{d_0} - \delta\mathbf{d_1}$ for a change of model from $\mathbf{m}_0$ to $\mathbf{m}_1$

$\nabla\mathbf{m}$ gradient with respect to m

These notations were adopted from Warner (2012).

Chapter 1 : Introduction

Overview

Seismic imaging is an important tool, which aims to produce high resolution, accurate subsurface images of the Earth, thereby facilitating structural interpretations, rock volume estimations, optimal well locations/trajectories, and reservoir characterisation. This quality/potential of seismic images need to be maximized as exploration for new hydrocarbon resources continues in increasingly complex domains worldwide. Additionally the increased necessity for improved production from existing fields accentuates this need.

With increased computational capabilities and algorithmic advancements, rapid and continuous developments in the field of seismic imaging, have led to better seismic images over the past two decades (Virieux and Operto, 2009). As well as extraction of quantitative information from the seismic data, there is a continued commercial drive for further improvements, desiring even greater resolution and image fidelity. Over the years, a natural progression from ray-tracing methods, to one-way wave equation methods, to two-way wave equation methods, has allowed for further improvements in imaging. Full-waveform inversion, commonly referred to as FWI, is an advanced velocity determination tool that exploits the two-way wave equation (Pratt *et al*. 1998).

Applied 3D FWI aims to enhance the extraction of subsurface information: p-wave velocity, Vp, shear-wave velocity, Vs, and measurements of anisotropic parameters, from seismic data at all length scales. However, challenges are evident, in particular a good starting model, low frequencies and long offsets have always been key to obtaining a high-resolution model from FWI. This thesis will explore different strategies by which even higher resolution models can be obtained with FWI. But, firstly in this chapter, the historical evolution of FWI will be outlined.

Full waveform Inversion (FWI)

FWI is a non-linear inverse problem, which follows a local iterative optimisation scheme whereby information in the recorded seismic wavefield is used to invert model parameters. It

begins from a starting model that is assumed to be sufficiently close to the true model, and seeks to make a series of step-wise improvements to this model, which successively reduces the objective function (the L2 Norm residuals between the observed and calculated data) towards zero (Warner, 2011). Over the last decade, technological advances have allowed for the application of 3D FWI to 3D seismic datasets with impressive recovery of complex models beneath heterogeneous overburden (Sirgue *et al*. 2010, Ratcliffe *et al*. 2011).

Evolution of FWI

Tarantola (1984), together with Lailly (1983), Gauthier *et al*. (1986) and Mora (1988), played a fundamental role in establishing the interest and knowledge of FWI in the academic world. Tarantola (1984) first illustrated that an inverse problem can be solved using an iterative algorithm where each step essentially consists of a forward propagation of the actual sources in the current model and a backward propagation of the data residuals. This is the essence of FWI. It differs to migration as it utilises the full, raw, recorded seismic wavefield as opposed to just the primary reflections. This is illustrated in the schematic shown in Figure 1-1, comparing different arrivals forming the full seismic record verses the primary reflections only. A schematic of a shot record generated at receiver locations with these key arrivals is illustrated in Figure 1-2. A key finding in the early stages of the development of FWI was that it is very sensitive to the accuracy of the initial model (Gauthier *et al*. 1986).

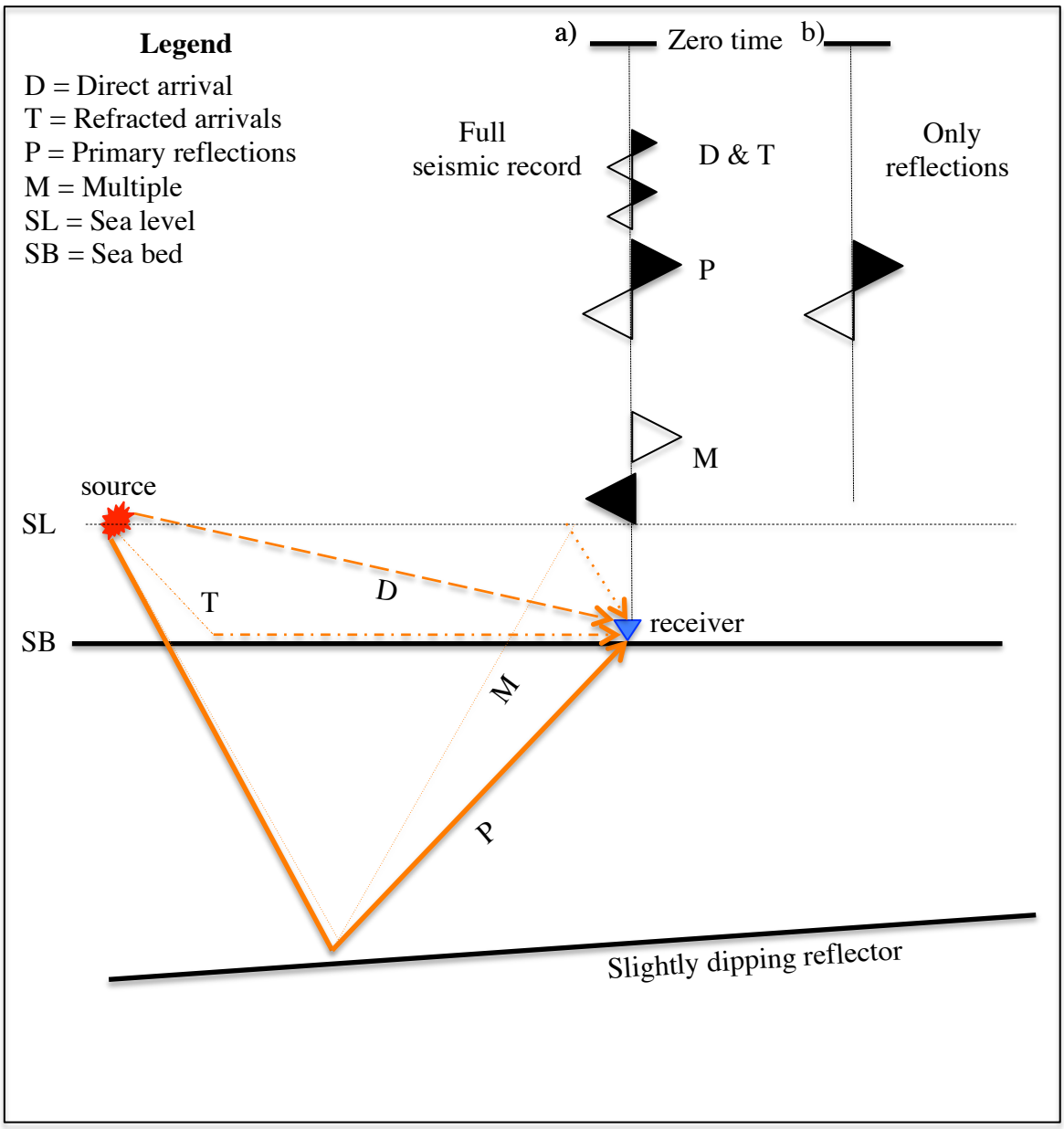


Figure 1-1: Schematic illustrating different arrivals that lead to the generation of the full seismic record at the receiver location. A representation of a single trace at the receiver location is shown in a) the full seismic record b) the primary reflections obtained after pre-processing. The full seismic records are used in FWI while the primary reflections only are used in migration

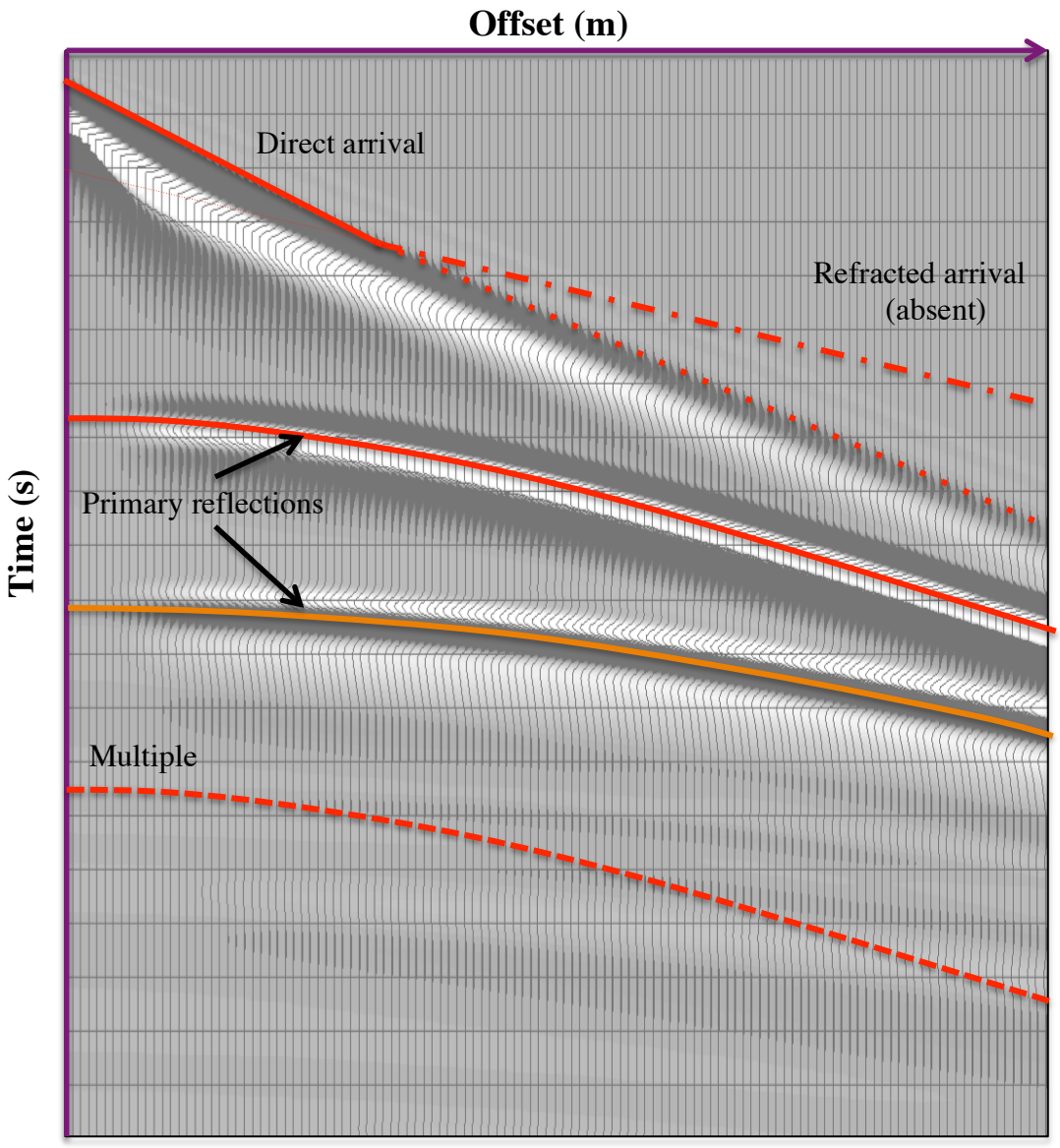
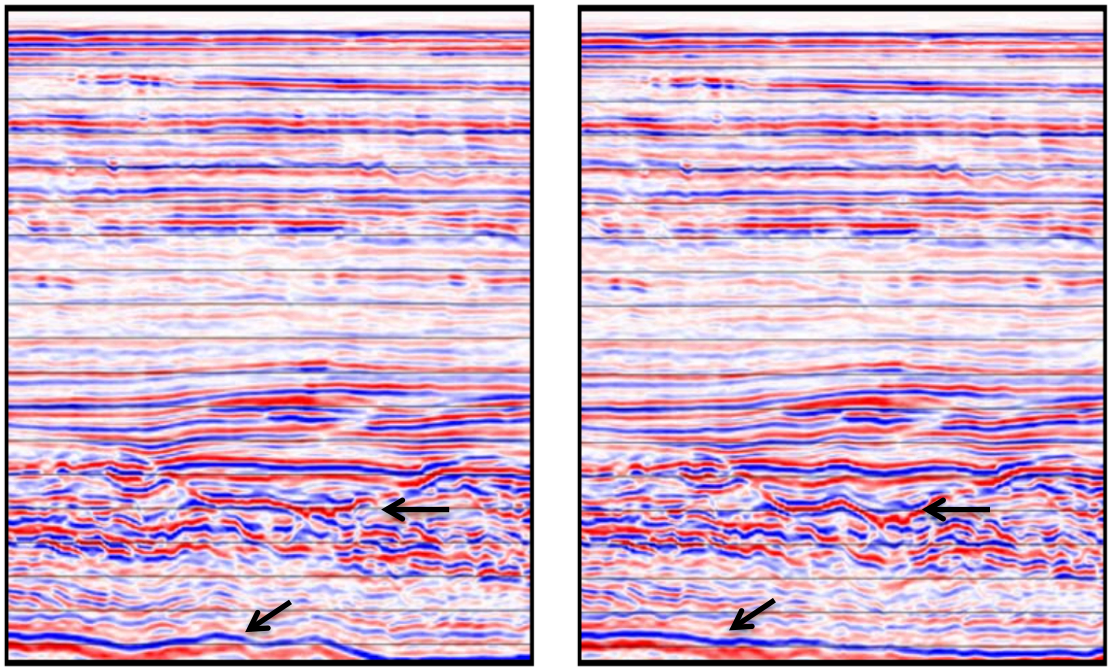


Figure 1-2: Schematic of key arrivals evident in a shot record as obtained from several receiver locations as in Figure 1-1. Here the refracted arrivals are absent due to the insufficiently long offsets as setup by the acquisition design for this shot record.

FWI can be carried out in the time domain (Lailly, 1983; Tarantola, 1984, 1986) or frequency domain (Pratt *et al*. 1998). Pratt and Worthington (1990) and Song *et al*. (1995) developed the first 2D frequency domain direct solvers for the acoustic wave equation, then applied 2D frequency domain FWI to cross-hole data and recovered geologically complex structures. Further examples of successful 2D FWI applications include the work by Bunks *et al*. (1995) where the advantage of using a multi-scale seismic waveform inversion strategy with applications to the synthetic Marmousi model, is demonstrated. This approach initially inverts for the macro-structures at low frequencies, that is, the long-wavelength features; followed by the recovery of the microstructures at the higher frequencies, that is, the short-wavelength features, resulting in improved resolution. This strategy improves the chance of recovery towards a global minimum. In the academic world, FWI became well established in 2D with further applications by Shipp and Singh (2002), Wang and Rao (2006). However, the Earth is three-dimensional (3D) and advances in computer technology fuelled further developments for the petroleum industry.

Warner *et al*. (2007) realised the practical benefits of FWI was possible in 3D, leading to the development of the first 3D frequency domain FWI algorithm. Several successful applications to 3D synthetic datasets followed. These applications were not without their limitations. Low starting frequencies and relatively long-offset data were deemed necessary for successful FWI applications (Warner *et al*. 2008, Sirgue *et al*. 2009).

The first 3D FWI field application was undertaken by Warner *et al*. (2008), on a 3D streamer dataset, leading to imaging improvement of shallow high-velocity channels and significant uplifts in the migrated images at deeper depths (Figure 1-3). One year later, Sirgue *et al*. (2009) demonstrated spectacular results, for a 3D FWI application to a wide-angle ocean-bottom-cable (OBC) dataset from the Valhall field in the North Sea (Figure 1-4). These results were later used by BP to successfully plan and drill three wells avoiding problems due to shallow gas hazards previously encountered during drilling prior to FWI (Sirgue *et al*. 2010). Subsequent successful applications to field data include work carried out by Plessix and Perkins (2010), Vigh *et al*. (2010), Ratcliffe *et al*. (2011) and Nangoo *et al*. (2012).



Migrated image: conventional Vp model Migrated image: FWI model

Figure 1-3: Pre-stack depth migrated image of a channel and underlying reflector. Using a FWI velocity model (right) verses a conventional velocity model, spurious structure on the underlying reflector (bottom arrow) has disappeared and geological structure within the channel (top arrow) is more reasonable (Warner *et al.* 2008).

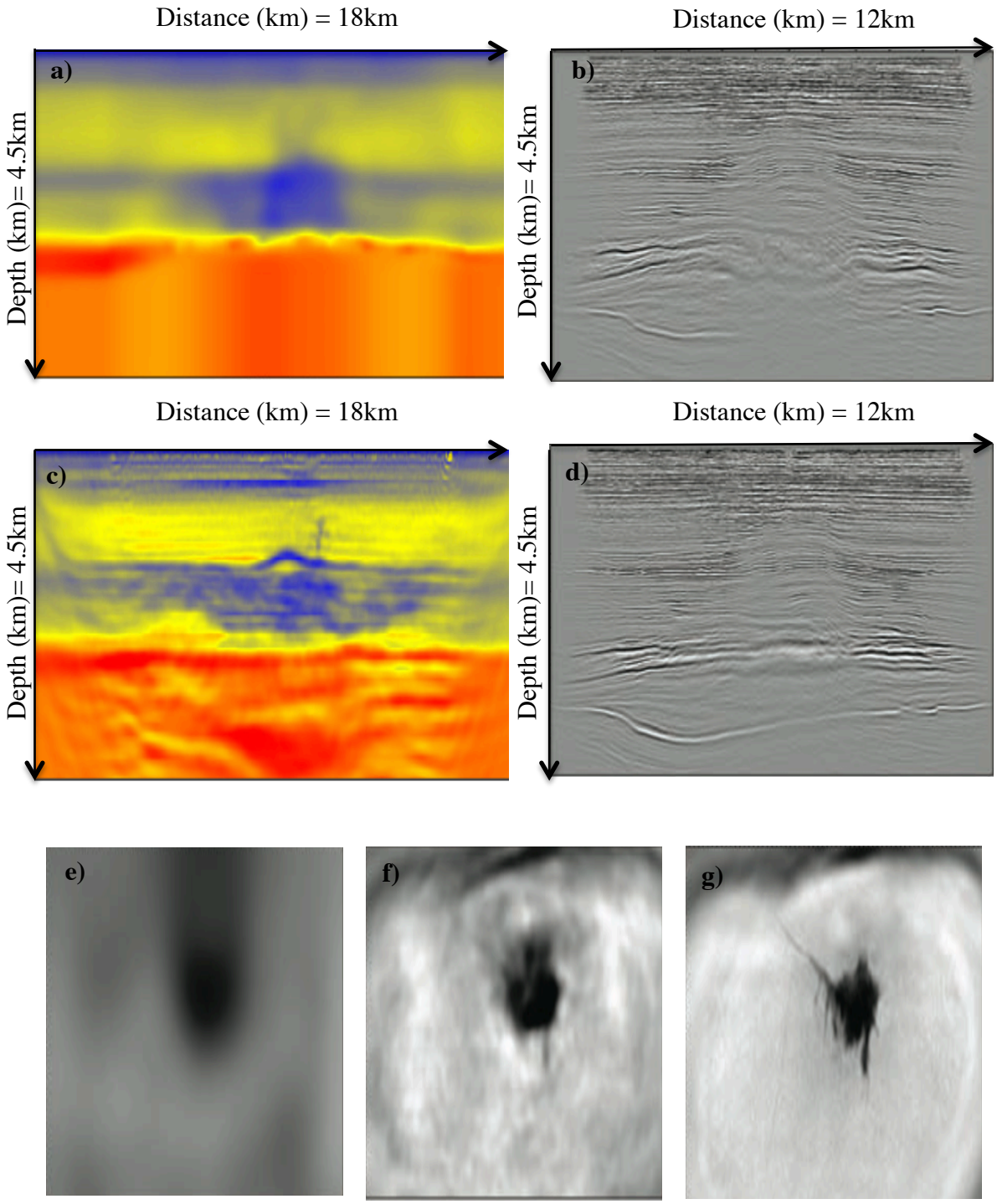


Figure 1-4: FWI application to the Valhall field. a) Vertical slice through the reflection tomography velocity model and b) corresponding reflection tomography migrated image; c) Vertical slice through the FWI velocity model with d) corresponding FWI migrated image. Horizontal slice at 1050m showing its evolution over the course of FWI: (e) the 2007 starting model; (f) after using only the lowest frequency of 3.5 Hz; and (g) after six frequencies from 3.5 to 7.0 Hz were used (Sirgue *et al.* 2009).

A key indicator to a successful FWI application is whether the recovered velocity model is capable of matching individual seismic waveforms of a raw field dataset. In current commercial practice, an acoustic approximation to the wave equation is almost always used, the kinematic effects of anisotropy are properly included, but an independent density model is not used, and the full dynamic effects of elasticity, attenuation and fine-scale variations in anisotropy are not accounted for (Plessix and Perkins, 2010; Sirgue *et al*. 2010; Vigh, Kapoor and Li, 2011; Kapoor *et al*. 2013; Morgan *et al*. 2013; Warner *et al*. 2013). Several key strategies are normally adopted to mitigate for the elastic effects of the Earth, which allow an acoustic approximation to be used.

Current 3D acoustic FWI practice shows that anisotropic acoustic wave equation is sufficient for 3D FWI to generate a p-wave velocity model for depth migration, provided that there is: suppression of surface waves with the most significant being scholte waves, shear waves, and reflections in the observed dataset; trace-to-trace amplitude normalisation in both time and offset for the predicted and observed datasets, incorporation of Thomsen anisotropic parameters in the forward modelling propagator to fit the kinematics, a good starting model, a long-offset observed dataset with wide-azimuthal coverage and low frequencies (Sirgue *et al*. 2006, Warner *et al*. 2012, and Warner, *et al*. 2013). This approach leads to a good match to the kinematics of the field data, and a reasonable match of the amplitudes in each individual trace, and it produces a significant and verifiable improvement in the resultant velocity model. These improved models give a closer fit to well logs, better flattening of common-image gathers and an improvement in the pre-stack depth-migrated image with improved reflector continuity. To match amplitude variations accurately however requires accurate knowledge of short-wavelength density and anisotropy variations, and of attenuation and shear-wave properties (Warner *et al*. 2012).

Wang and Rao (2009) demonstrated that, for offset-limited reflection seismic data, it is difficult for FWI to recover long-wavelength velocity variations, especially those occurring at deeper subsurface depths, that is, deeper parts of the model. FWI of reflection dominated, short-offset datasets is required to take the technology forward. Many authors including: Xu *et al*. (2012); Yao *et al*. (2014); have undertaken recent studies on reflection FWI. Yao *et al*. (2014) proposed that interleaving least squares RTM with a version of FWI, such that the background macro-model is separated from the reflectivity gradient during forward modelling, allows for FWI of reflection energies. Even further developments in the area of

multi-parameter inversion have seen the technique of FWI continually advancing (Alkhalifah and Plessix 2014).

To include s-wave velocity as a model parameter requires using an elastic wave equation and this is an order of magnitude more computational expensive (a synthetic demonstration of elastic modelling is shown in the Appendices). Elastic FWI has been applied to 3D field data (Guasch *et al*. 2012; Vigh, Jiao, and Watts, 2012; Lu *et al*. 2013), but problems with cross-talk between the solution spaces, uncertainties about density, attenuation and elastic anisotropy, together with the increased computational cost, means that elastic FWI is not yet widely used in a commercial setting.

Definition of research problem

FWI is a relatively immature technology and the aim of this research is to make improvements that will either increase the fidelity of the recovered images, ensuring that its application is more reliable and robust and/or extend its use to deeper in the subsurface through including reflections in the inversions. Such improvements are important and likely to lead to the more widespread use of FWI within the petroleum sector. To achieve this, a suite of different strategies has been investigated with synthetic tests, and successful ones applied to field datasets.

Different strategies to successfully use reflection energy for FWI on deeper reflected energy targets will be examined through synthetic tests. FWI on a shallow-water OBC dataset will follow, whereby an offset-variable density scheme will be developed to further improve the resolution of FWI in the shallow section, with resultant enhancement of the seismic image at deeper depths. Lastly, FWI will be undertaken on two deep-water OBC datasets. A scheme whereby the data are conditioned using an adaptive matching technique, to avoid local convergence, will be described. Using all the data in the inversion, FWI will be performed at the low frequencies initially. The presence of the long-offset transmitted arrivals in the data will lead to a good macro-model update, after which the reflected energy and all other arrivals will allow for deeper updates. This novel contribution is as a result of the successful demonstration of the extension of the bandwidth for FWI to higher frequencies, which, along with the combined use of refraction and reflection energy leads to a high-resolution image of velocity structure that has a comparable resolution to a depth migration. FWI can eventually

replace conventional processing and migration – all that is needed, is a full-bandwidth velocity model.

Thesis structure

This thesis is organised in six chapters. The current chapter, Chapter 1, gives an overview of the evolution and current state of the topic of full-waveform inversion (FWI). The research problem is then defined. Chapter 2 discusses the mathematical formulations of FWI with a comprehensive outlook of the technique. Chapter 3 examines the application of FWI to reflection-dominated datasets in different geological environments, through synthetic tests. Chapter 4 develops an application of an offset-density FWI scheme to a field dataset. A comprehensive discussion of all possible tests to investigate a mismatch between observed and predicted data ruled out many possible causes. The offset-density scheme, however, resulted in better convergence and completely removed the mismatch. Chapter 5 applies our new developments of FWI to deep-water datasets, whereby the bandwidth is extended to higher frequencies, exploiting the reflection energy, which further increases the resolution of FWI and generating directly interpretable velocity models of the Earth. Finally, Chapter 6 summarises the outcomes of this research and states the conclusions drawn.

Contributions

Outlined below, is contribution list for the development of the FWI technique, facilitated by this study. These are,

1. To push FWI to work better with pure reflection data. Various strategies, including a combination of time windowing; offset limiting; strategic muting and alternating inversion schemes that flip-flop between migration-like (reflector building) and tomography-like (background velocity) processes, are examined.
2. To develop a strategy to improve the match between the predicted data after FWI and field data for a shallow-water OBC dataset. An offset-variable density scheme is developed, further improving the resolution of FWI in the shallow section, with resultant enhancement of the seismic image at deeper depths.

3. To extend the bandwidth of FWI, further exploit the reflection energy and increase the model resolution, all without being stuck in a local minimum thereby facilitating further uplift in the velocity model than that at a conventional low bandwidth for two deep-water OBC datasets.

Chapter 2 : Background

Mathematical Theory

Two-way wave propagation refers to the change in direction of wave paths either on their way from the shot down (down-going direction) to the reflector or coming back up (up-going direction) from the reflector to the receiver. The wave equation relates the local density of the medium, the local elasticity of the medium and how the wave evolves in space (the derivative of particle displacement with depth), as time unfolds (the derivative of particle displacement with time). FWI uses the two-way wave equation to produce high-resolution velocity models. For an acoustic, isotropic, inhomogeneous, non-attenuating medium, it can be represented as:

$$\frac{1}{{V_p}^2}\frac{\partial^2 p}{\partial t^2} - \rho\nabla.\left(\frac{1}{\rho}\nabla p\right) = \mathrm{s}\,,$$

(2-1)

where the acoustic pressure wavefield, p and driving source, s, vary in both space and time, and the acoustic propagation velocity, $V_{P,}$ and density, ρ, vary in space. The wave equation represents a linear relationship between the wavefield, p, and the source s that generates the wavefield. Discretisation of the wave equation using finite differences, writing equation 2-1 in matrix form gives:

$$\mathbf{Ap} = \mathbf{s}\,,$$

(2-2)

where the matrix **A** depends upon both the model properties and represents the discrete numerical implementation of the forward modelling operator,

$$\frac{1}{{V_p}^2}\frac{\partial^2 p}{\partial t^2} - \rho\nabla.\left(\frac{1}{\rho}\nabla\right).$$

(2-3)

Additionally, the wave equation can also be represented as a non-linear relationship between the model vector **m,** and the predicted wavefield, **p**:

$$\mathbf{G}(\mathbf{m}) = \mathbf{p}\,,$$

(2-4)

where **G** is the forward modelling operator, a non-linear function that describes how to calculate a wavefield **p** given a model **m**, which depends upon the source. The model vector, **m,** contains the model parameters at every point in the model, usually velocity (V_p) or slowness ($1/V_p$) values. The matrix operator, **A**, differs from the non-linear function, **G**, which is not a matrix. The matrix **A** depends upon both the model properties and the details of the numerical implementation, while the function **G** depends upon the source. As the forward problem is well-posed (Jones, 2010), a unique solution exists that depends continuously on the model.

In contrast, inversion aims to derive from field data a model to describe the subsurface consistent with the data. The inverse problem extracts a model, **m**, from a dataset, **d**, using a mapping operator **G**, and minimising artifacts. This is defined as:

$$\mathbf{m} = \mathbf{G^{-1}d}\,.$$

(2-5)

However, the inverses mapping operator may not exists, and the available field data might be noisy and insufficient to uniquely determine the actual Earth velocity distribution. The inverse problem is then ill-posed and in most cases would require additional information/constraints for an unambiguous solution.

Figure 2-1 shows a synthetic example of the forward problem, whereby a defined source and an estimated model representation of the Earth is used to predict data. The inverse problem, whereby the accurate model representation of the Earth, is obtained from the data are also illustrated.

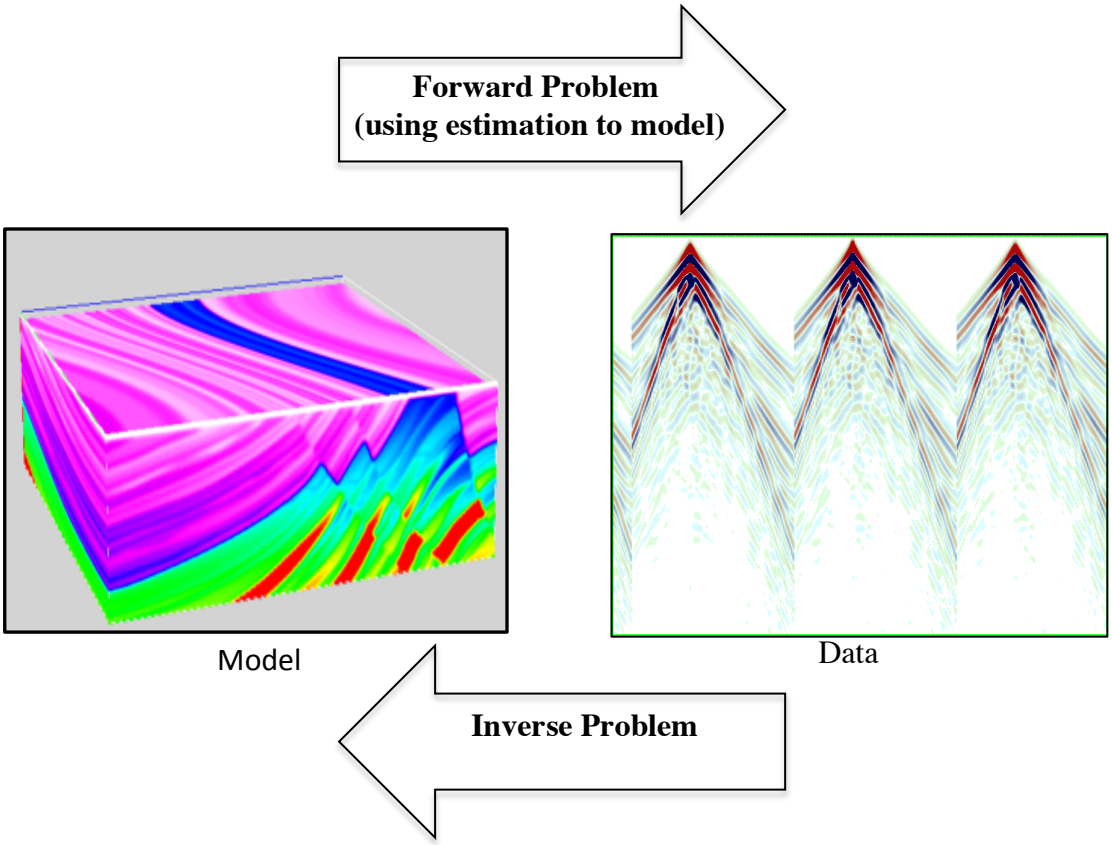


Figure 2-1: Synthetic illustration of the Forward and Inverse Problem using modelling codes used here and a 3D synthetic Marmousi model

FWI is an inverse problem. Its central purpose is to find a model of the subsurface that minimises the difference between an observed seismic dataset, $\mathbf{d}_{\text{obs}}$, and the predicted dataset, $\mathbf{d}_{\text{calc}}$, from the model. The L2-norm, the sum of the squares of the differences between the two datasets over all sources and receivers, and over all times, serves as a means to measure this difference. The L2-norm of the data residuals is known as the misfit or objective function,

$$f(\mathbf{m}) = \frac{1}{2} \left|\left| \mathbf{d}_{\text{obs}} - \mathbf{d}_{\text{calc}}(\mathbf{m}) \right|\right|^2. \tag{2-6}$$

Several other misfits/objective functions may be used, such as the L1-norm, the phase residual, and the cross-correlation misfit (Warner *et al*. 2012, Brossier *et al*. 2015). These all

have their advantages (particularly in reference to accuracy) and disadvantages (particularly in reference to computational efficiency). However, the computationally efficient, well-investigated difference misfit function has proven effective for conventional FWI.

FWI is a local iterative scheme. It starts with some estimate of the model $\mathbf{m_o}$ and iteratively reduces the objective function, *f*, towards zero. Thus, the objective function, $f(\mathbf{m_o})$ for the starting model and the new model $f(\mathbf{m_o} + \delta\mathbf{m})$ need to be considered. To minimise the objective function with respect to the model parameters **m,** it is necessary to differentiate $f(\mathbf{m})$ with respect to **m**, set the differentials to zero, and solve for the model update $\delta\mathbf{m}$, and subsequently **m**. The model updates is thus given by:

$$\delta\mathbf{m} \approx -\left(\frac{\partial^2 f}{\partial \mathbf{m}^2}\right)^{-1} \frac{\partial f}{\partial \mathbf{m}} = -\mathbf{H}^{-1}\nabla_{\mathbf{m}} f \,, \tag{2-7}$$

where **H** is the Hessian matrix of the second differentials, which gives an indication of the curvature, and $\nabla_{\mathbf{m}} f$ is the gradient of the objective function. This method is referred to as the Newton method. Calculating the Hessian for a realistic 3D problem is expensive (long computation times and large storage requirements), and inverting it is not normally computationally feasible. Newton methods are usually constrained to sparse 2D problems and Gauss-Newton or quasi-Newton methods use an approximation to the Hessian matrix, avoiding its explicit calculation. The inversion algorithm used throughout this thesis, is based upon adjoint-state method. The adjoint-state method computes efficiently the gradient of the objective function, $\nabla_{\mathbf{m}} f$, without explicit building the Frechet derivative matrix (Plessix, 2006).

The gradient, $\nabla_{\mathbf{m}} f$, (from equation 2-7), tells us in what direction to change the model. To find the gradient, it is necessary to calculate the forward wavefield **p**, and differentiate the numerical operator **A** with respect to the model parameters. This can be expressed as:

$$\nabla_{\mathbf{m}} f = -\mathbf{p}^{\mathrm{T}} \left(\frac{\partial \mathbf{A}}{\partial \mathbf{m}}\right)^{\mathrm{T}} (\mathbf{A}^{-1})^{\mathrm{T}} \, \delta\mathbf{d}. \tag{2-8}$$

The final term, $(\mathbf{A^{-1}})^T\ \delta\mathbf{d}$ (equation 2-8) computed over all sources at each point in the model, represents the back-propagation of the residual wavefield from the receiver location where:

$$(\mathbf{A}^{-1})^{\mathrm{T}}\,\delta\mathbf{d}\ =\ \delta\mathrm{p}\,,$$

(2-9)

which when re-arranged gives:

$$\mathbf{A}^T\delta\mathbf{p}\ =\ \delta\mathbf{d},$$

(2-10)

where a wavefield $\delta\mathbf{p}$ generated by a (virtual) source $\delta\mathbf{d}$, and propagated by the operator $\mathbf{A}^T$ the adjoint of the operator in the original wave equation. As such, in computing the gradient, essentially the solution of a modified wave equation, with the data residuals used as a source, is computed. The expression for the gradient can be simplified as:

$$\nabla_{\mathbf{m}} f\ =\ -\mathbf{p}^{\mathrm{T}}\left(\frac{\partial\mathbf{A}}{\partial\mathbf{m}}\right)^{\mathrm{T}}\delta\mathbf{p}.$$

(2-11)

Simply, the gradient essentially represents the zero lag of the temporal cross correlation of the forward wavefield, $\mathbf{p}$, for a particular source with the back-propagated residual wavefield, $\delta\mathbf{p}$, for all the receivers for the same source, weighted by the differential of the numerical operator $\mathbf{A}$ which can be obtained analytically.

Using the steepest decent local optimisation scheme, the inverse of the Hessian (equation 2-7) is replaced by a simple scalar, α, called the step length. The step length, α, tells us how much to change the model by. The step length is normally carried out by perturbing the model by a small amount in the opposite direction to the gradient, which gives a direction of steepest-ascent. The forward wavefield for this new model, $\mathbf{m}_\alpha$, and the corresponding new set of data residuals, $\delta\mathbf{d}_{1,}$ is then computed and this is used to optimise the step length by assuming a linear relationship (Born approximation) between changes in the residuals and changes in the model:

$$\delta\mathbf{d}_{\boldsymbol{\alpha}} = \delta\mathbf{d}_0 + \alpha(\mathbf{d}_1 - \mathbf{d}_0) = \delta\mathbf{d}_0 + \alpha(\delta\mathbf{d}_1 - \delta\mathbf{d}_0).$$

(2-12)

To find this new model $\mathbf{m}_{\boldsymbol{\alpha}} = \mathbf{m}_0 + \alpha\,\delta\,\mathbf{m}$, that generates residuals $\delta\mathbf{d}_{\boldsymbol{\alpha}}$, where α minimizes, the L2-norm is computed:

$$\frac{1}{2}||\delta\mathbf{d}_\alpha||^2 = \frac{1}{2}(\delta\mathbf{d}_\alpha - \alpha\mathbf{q})^{\mathrm{T}}(\delta\mathbf{d}_0 - \alpha\mathbf{q}),$$

(2-13)

where:

$$\mathbf{q} = \delta\mathbf{d}_0 - \delta\mathbf{d}_1 .$$

(2-14)

Differentiating with respect to α, setting the differential to zero, and solving for α (the step length) gives:

$$\alpha = \frac{\delta\mathbf{d}_0{}^{\mathrm{T}}\mathbf{q}}{\mathbf{q}^{\mathrm{T}}\mathbf{q}}.$$

(2-15)

Calculation of the step length α, thus involves a forward calculation with a perturbed model, and the combination of the residuals from both the original and the perturbed models, thereby providing the optimum scaling/step length calculation that minimises the objective function. The model update can now be summarized as,

$$\delta\mathbf{m} = -\alpha\frac{\partial f}{\partial\mathbf{m}} \approx -\alpha\mathbf{S}\nabla_{\mathbf{m}}f,$$

(2-16)

where the final parameter, **S**, is a spatial preconditioned matrix with weighted diagonals. Spatial preconditioning, a gross approximation to the diagonal of the inverse Hessian, is applied to the model update as a pre-conditioner. This preconditioning is achieved by normalisation, using a quantity that depends upon the total energy of the incident wavefield. In other words, every point of the diagonal, if the inverse Hessian approximated to 1, is

divided by the square of the incidence wavefield. The preconditioning is stabilised to avoid normalisation by unduly small values that may be dominated by noise. This stabilization factor is a fraction of the maximum wavefield everywhere. The preconditioner is applied to the gradient in two steps. Part of the normalisation is performed locally, source-by-source, and part is performed globally. Once the model update is computed, the original starting model m_0 is replaced by the new model, $\mathbf{m_\alpha = m_0 + \alpha \delta m}$, and the process is repeated by continual iterations. Iterating, generally improves on these approximations repeatedly, and thus solves a non-linear problem using a sequence of linearised step. **Error! Reference source not found.** is a flowchart summarizing the theory of FWI.

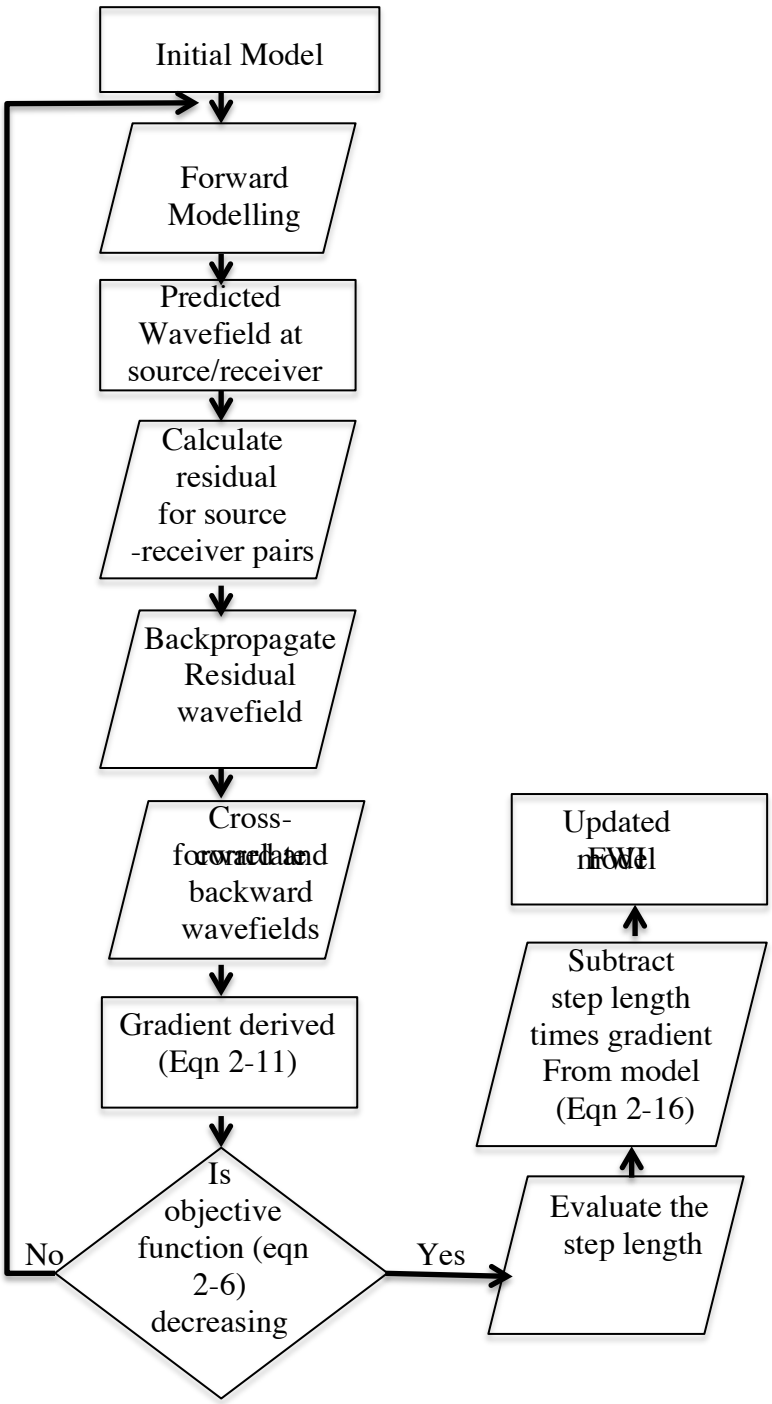


Figure 2-2: Flowchart summarising the theory of FWI

For the acoustic approximation, described above, only compressional waves are taken into consideration. However, a more complete description takes into account the fact that the Earth is a solid body and hence it includes elastic phenomena. A single data type (pressure) and model parameter (P-wave velocity, Vp) are involved in acoustic FWI. In the elastic case, more than one data types are involved and two model parameters (P- and S-wave velocities).

Stability Conditions

Conventional finite-difference methods used for solving the acoustic wave equation suffer from numerical dispersion when too few samples per wavelength are used (Fei and Larner, 1995). The shortest wavelengths in the velocity model need to be sampled at a minimum of five (5) grid points per wavelength to avoid numerical dispersion (Levander, 1988). In most situations the shortest wavelength appears in the shortest S-wave region of the model, and therefore V_{min} always correspond to shear wave velocity model thereby limiting the grid spacing, δx,

$$\delta x = \frac{V_{min}}{5 * f_{max}} . \tag{2-17}$$

On the other hand, the time-step interval, δt, should obey the stability criterion such that the distance travelled by the wavefield per time step is less than half a cell for the highest velocity (i.e. the pressure wave velocity) grid cells (Graves, 1996),

$$\delta t \leq \frac{\delta x}{2 * V_{max}}. \tag{2-18}$$

The lowest velocity in the model details the maximum grid spacing, whereas the highest velocity controls the maximum time-step. There is thus a compromise between selecting the appropriate grid spacing, δx, the maximum frequency, f_{max}, allowed by the inversion and the computational cost associated with dense time sampling, δt.

Domain of Application

Two-dimensions (2D) frequency domain FWI has advantages of computational efficiency and data selection flexibility over its time-domain counterpart (Song *et al*. 1995; Aifei and Wenhui, 2011). For two-dimensions (2D) cases frequency-domain methods are much faster than the time-domain explicit solutions, due to direct factorisation of the matrix equations.

However, the computational resources required for practical wavefield tomography in three-dimensions (3D) can be rather similar in both time and frequency domains (Umpleby *et al*. 2010). Working with geologically complex datasets, this study was undertaken using the time-domain algorithm. Time-domain modelling and inversion allows for muting/windowing, or time-weighting, of field data, unlike the case in the frequency domain (Umpleby *et al*. 2010).

The time-domain algorithm for standard FWI uses explicit, second-order, time stepping and fourth-order spatial discretisation (a 37-point stencil with an optimal combination of rotated and non-rotated fourth-order finite-difference operators). The forward wavefield for cross-correlation during the back propagation is not stored making the algorithm efficient (Umpleby *et al*. 2010).

Application of Full Waveform Inversion

Key Parameterisation

Kernel

Full-waveform inversion at low frequencies followed by reverse-time migration (RTM) is a current common practice in seismic imaging. For these low-frequency inversions, a low-order kernel that is 4^{th} order in space and 2^{nd} order in time is used. Using this low order kernel, a minimum of 4-5 grid points per wavelength is required for stability of the finite difference grid thereby preventing dispersion (equation 2-17). The time step must be set so that less than 50% of any cell is crossed in one time step (equation 2-18). As such, higher frequency inversions using the low-order kernel require a finer mesh, which increases the computational costs and leads to inefficiency. Thus, for higher frequency inversions a more sophisticated high-order kernel is used.

The high-order kernel, a recent addition to the current fullwave3D code initiated by a consortium sponsor, is 10^{th} order in space and either 2^{nd} or 4^{th} order in time. For the 2^{nd} order stencil in time, it is accurate down to about 3.6 grid points per wavelength and is stable when the time step is set so that less than 38% of any cell is crossed in one time step. The 4^{th} order stencil in time is generated essentially by the double application of 2^{nd} order stencil. It is accurate down to 2.61 grid points per wavelength, and is stable when crossing less than 66% of any cell in one time step. For forward modelling the 4^{th} order stencil is automatically

selected for better accuracy. For inversion, the code uses the minimum velocity in the model together with the frequency for the current iteration block to determine whether the accuracy and stability criteria are met for the 2nd and 4th order stencils. If both criteria are met, then the 2nd order is used. If only the criteria for 4th order stencil are met, then that stencil is used. If neither is met, then the code will terminate. Table 2-1 summarises the comparison between the different kernels. The low-order kernel works for 2D/3D, acoustic/elastic and isotropic/anisotropic (VTI/TTI) problem types. The high-order kernel is currently only implemented and woks for acoustic, anisotropic, 3D problem types.

Kernel	**Min Grid Points / λ**	**Max Crossing Factor**
Low-Order: 4th order in space, 2nd in time	4-5	50%
High-Order: 10th order in space, 2nd in time	3.6	38%
High-Order: 10th order in space, 4th in time	2.6	66%

Table 2-1: Comparison of the different kernels

Amplitude Normalisation

Two parameters control the trace-by-trace amplitude normalisation – amplitude and normalise (Table 2-2). These two-parameter sets form part of the fullwave3D FWI code of the Imperial College FWI consortium. Amplitude looks at the RMS trace-by-trace amplitude differences between the two datasets and Normalise makes the RMS value of each trace identical. The table below shows the effect of different combinations of Amplitude and Normalise parameterisation. If Amplitude is 'yes' and Normalise is 'no' minimal scaling is applied to either observed or predicted datasets. If both Amplitude and Normalise are 'yes' the same scaling factor is applied to both observed and predicted datasets. With both Amplitude and Normalise being 'no' a scaling is undertaken such that the two-norm of the predicted data matches the observed data. Lastly, if Amplitude is 'no' and Normalise 'yes', the predicted and observed data are more or less the data difference with both being scaled. Based on previous field data applications, the latter parameterisation is effective and so it was

used in all the inversions undertaken in this study. Table 2-2 summarises the formulae used in the parameterisation of 'Amplitude' and 'Normalise.'

AMPLITUDE	NORMALISE	Observed Data	Predicted Data
yes	no	$\mathbf{d}_{obs}$	$\mathbf{d}_{calc}$
yes	yes	$\mathbf{d}_{obs}$ / | $\mathbf{d}_{obs}$ |	$\mathbf{d}_{calc}$ / | $\mathbf{d}_{obs}$ |
no	no	$\mathbf{d}_{obs}$	($\mathbf{d}_{calc}$ / | $\mathbf{d}_{calc}$ |) (| $\mathbf{d}_{obs}$ |)
no	yes	$\mathbf{d}_{obs}$ / | $\mathbf{d}_{obs}$ |	$\mathbf{d}_{calc}$ / | $\mathbf{d}_{calc}$ |

Table 2-2: Summary of formulae used in the parameterisation of 'Amplitude' and 'Normalise'

The scaling applied through the use of the parameter Amplitude and Normalise does not include the application of a fitting factor to both observed and modelled data. The fitting factor is applied to all traces, at all times, at once and can be computed as in Equation 2-19 where $\mathbf{d}_{calc}$ is the predicted data, and $\mathbf{d}_{obs,}$ the observed data with fixed scalars. The fitting factor serves as a means of stabilisation thereby reducing the effect of noise. Additionally, this fitting factor does not allow for any negative fitting factors due to possible negative correlations and so the minimum factor is hard-wired at $0.2\sqrt{\frac{\mathbf{d}_{obs}^T\mathbf{d}_{obs}}{\mathbf{d}_{calc}^T\mathbf{d}_{calc}}}$. Thus,

$$\text{Fitting factor} = \max\left(0.9\frac{\mathbf{d}_{calc}^T\mathbf{d}_{obs}}{\mathbf{d}_{calc}^T\mathbf{d}_{calc}},\ 0.1\sqrt{\frac{\mathbf{d}_{obs}^T\mathbf{d}_{obs}}{\mathbf{d}_{calc}^T\mathbf{d}_{calc}}}\right) + 0.1\sqrt{\frac{\mathbf{d}_{obs}^T\mathbf{d}_{obs}}{\mathbf{d}_{calc}^T\mathbf{d}_{calc}}} \tag{2-19}$$

Spatial

The parameter set, Spatial - part of the fullwave3D FWI code of the Imperial College FWI consortium, was used in all the inversions being set as 'yes'. As such, for all the inversions a spatial pre-conditioning parameterisation was used. This preconditioning represents a gross

approximation to the diagonal of the inverse Hessian, which is applied to model update. Let $\mathbf{H}_D$ be a matrix representative of the Hessian hat only contains the diagonal elements of $\mathbf{H}_a$:

$$\boldsymbol{H}_D = \begin{bmatrix} H_D^{1,1} & 0 & 0 & 0 \\ 0 & H_D^{2,2} & \ddots & 0 \\ 0 & \ddots & \ddots & 0 \\ 0 & 0 & 0 & H_D^{n,n} \end{bmatrix}.$$

(2-20)

The inverse is simply,

$$\boldsymbol{H}_D = \begin{bmatrix} \frac{1}{H_D^{1,1}} & 0 & 0 & 0 \\ 0 & \frac{1}{H_D^{2,2}} & \ddots & 0 \\ 0 & \ddots & \ddots & 0 \\ 0 & 0 & 0 & \frac{1}{H_D^{n,n}} \end{bmatrix}.$$

(2-21)

Its purpose is to balance updates across the model; without it only the uppermost part of the model (the region of maximum data coverage) would be updated.

Data Requirements

Long Offsets

Conventional FWI of field datasets is usually accomplished using diving waves with their long travel paths that sample subsurface velocity. To illustrate this, a schematic demonstrating the relationship between long-offsets and the depth of investigation is shown in Figure 2-3. The length of streamers used in marine seismic acquisition directly affects the depth of investigation of the diving waves. For such datasets, the reliance on the use of diving waves for conventional FWI limits subsurface sampling to the shallow section. Ocean-bottom-cable (OBC) datasets are generally attractive for FWI since they generally contain low frequencies, and long offsets with good azimuthal coverage (Plessix and Perkins, 2010); however, the problem of shallow depth penetration still exists. To benefit more from the

structural, high-resolution detail that FWI adds, there is a need to go beyond diving waves, to that of short-offset reflection waves.

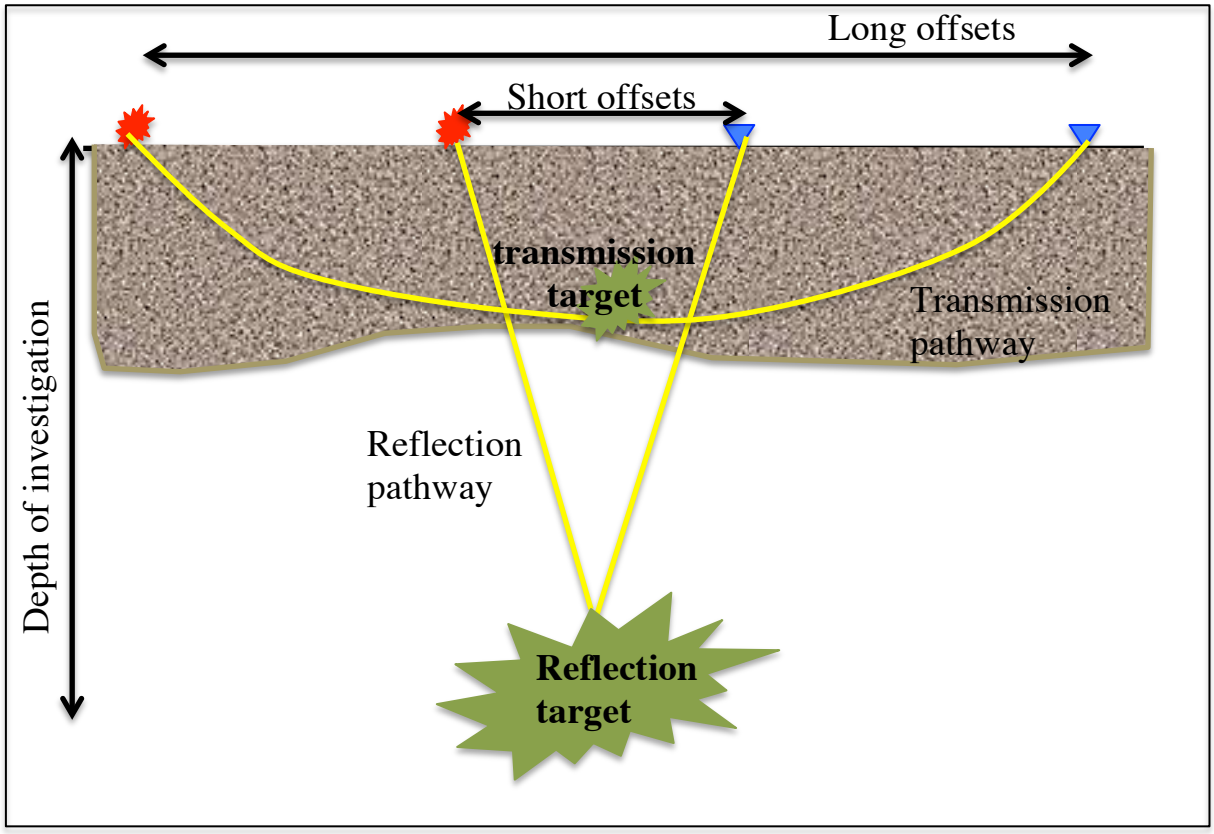


Figure 2-3: Schematic illustrating the relationship between the different arrivals and the depth of investigation

Low frequencies

The probability of achieving an accurate FWI solution is dependant on the complete, global minimization of the objective function. For this, low frequencies are desirable. The topography of the objective function at low frequency has a broader global minimum, making it highly desirable to start an inversion at as low frequency as permitted by the seismic acquistion limitations (Pratt and Worthington, 1990; Song *et al*. 1995, Sirgue, 2006; Plessix *et al*. 2010 and Baeten *et al*. 2013). Figure 2-4 illustrates this. Seismic inversion generally suffers from the lack of low frequency content of the seismic data. However, over the past few years, improvements in seismic acquisition techniques, has allowed an extension to the

bandwidth of seismic data at the low end of the frequency spectrum. With lower frequencies, there is an increased confidence that FWI updates will move towards a global minimum.

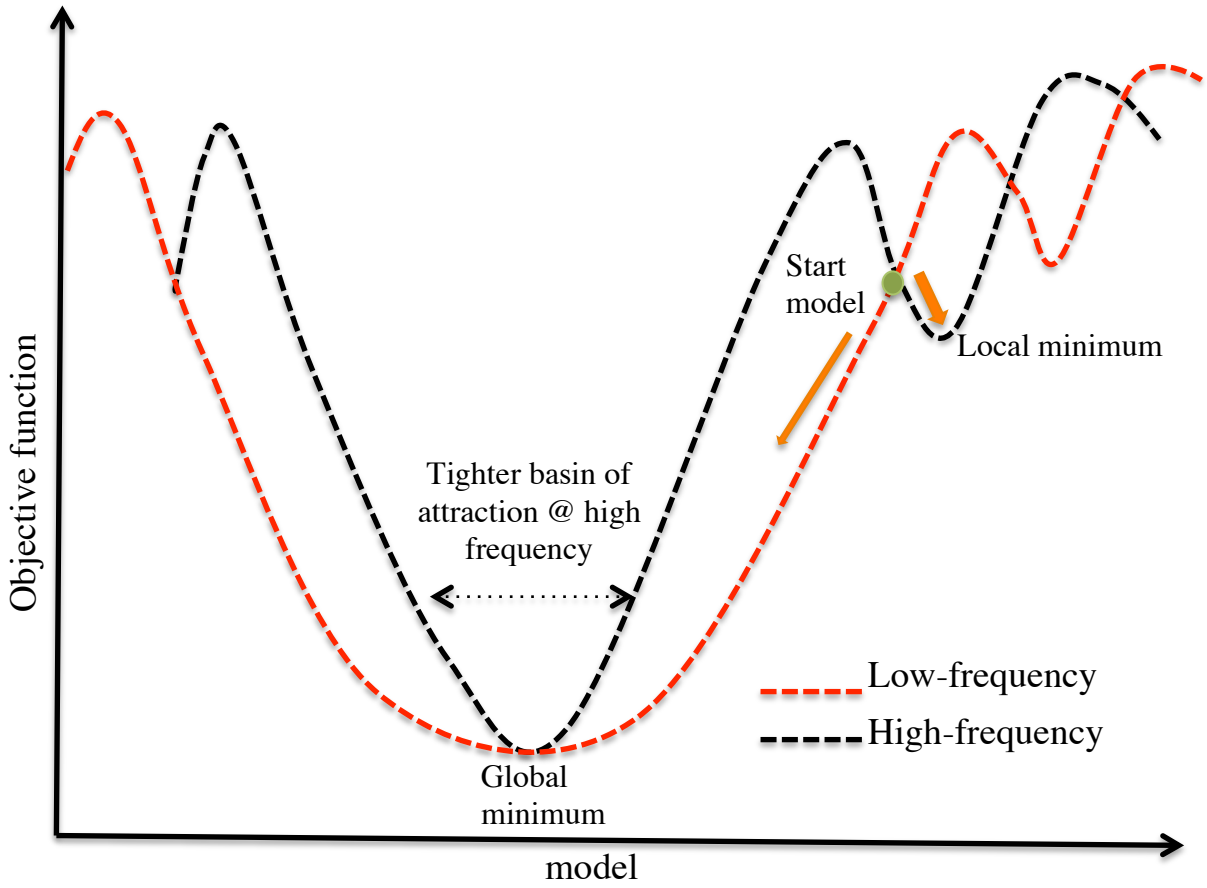


Figure 2-4: Schematic illustrating the benefits of obtaining global convergence using low frequency as oppose to high frequency. The starting model needs to be close to the true model when starting inversions from higher frequencies (Drawn).

Minimal FWI pre-processing

Usually, for FWI, the data is filtered to the frequency required for the inversion. The rectangular mesh of sources and receivers are rotated such that the orthogonal axis is shifted to N-S and E-W direction respectively. In the case of OBC datasets, source-receiver reciprocity is applied, labeling sources as receivers and receivers as sources, due to the large number of shots verses receivers. This is to reduce the total number of effective sources that is modelled. All the data can be used in the inversion, without the application of offset-dependant, manually picked mutes which exclude those parts of the traces that contain noise and reflected energy.

The Starting Model

The initial model highly impacts whether convergence occurs to the undesired local or an improved, desired minimum during the local optimisation FWI scheme. When there is a mismatch of travel-time greater than half a period between the calculated and observed data, the data at the frequency inverted are 'cycle skipped'. These kinematic errors between the modelled and observed data that result in cycle skipping, increase the likelihood of convergence to a local minimum. Additionally, a multimodal correlation function also increases the probability of an undesired convergence to a local minimum (Bunks *et al*. 1995). To tackle this problem, extensive time and effort is placed on building the starting model. Usual approaches adopted when building the starting model for a standard FWI include: phase unwrapping (Shah *et al*. 2012); wave equation tomography (Wang *et al*. 2012), Migration Velocity Analysis (MVA), Reverse Time Migration (RTM), Laplace-Fourier Domain Inversion (Shin, 2009) among others. In addition the schematic in Figure 2-4, a synthetic test was undertaken to demonstrate the need for low frequency and a good starting model (Figure 2-5). This synthetic demonstration, generated using the Marmousi model, shows the effect of using high verses low frequencies for a dataset of frequency range 0 – 6 Hz.

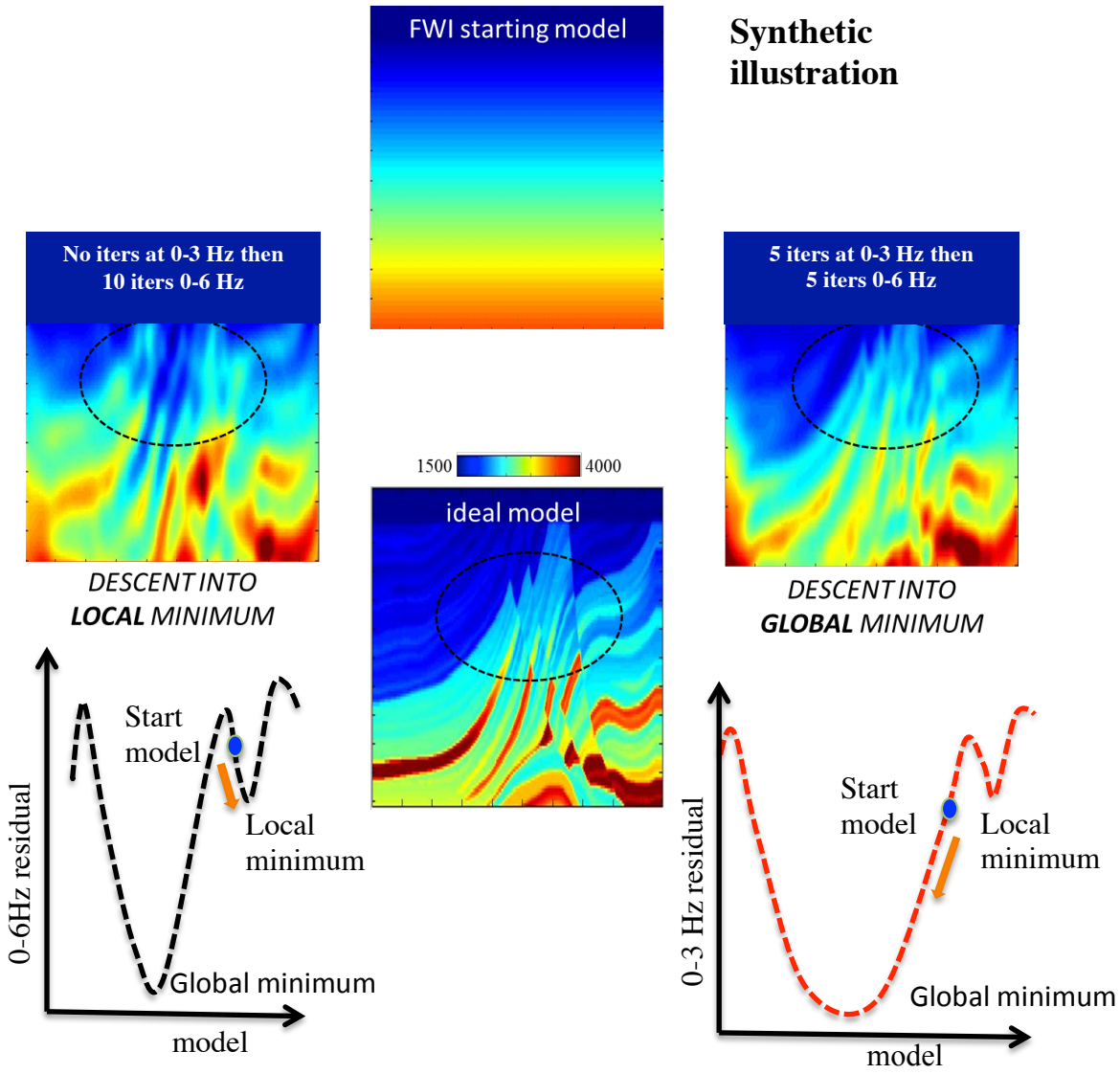
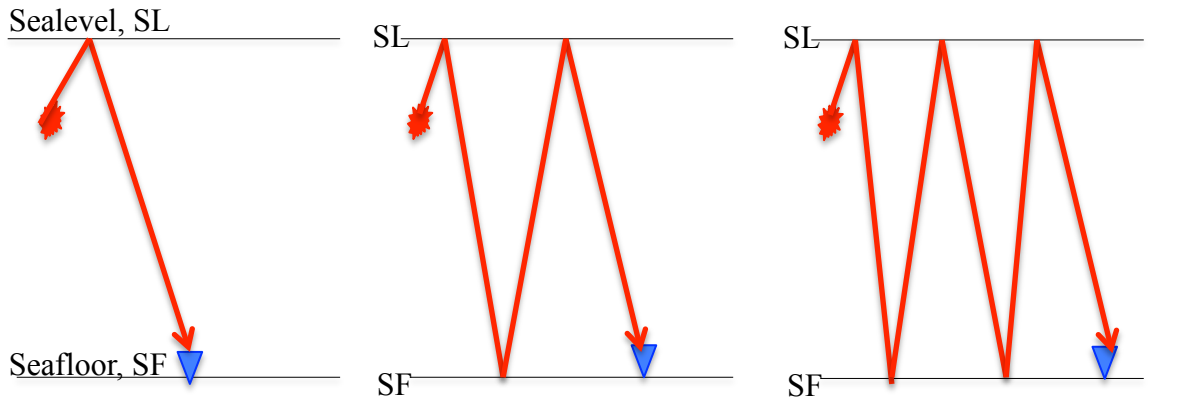


Figure 2-5: Synthetic illustrating showing the effect of the starting model and using high verses low frequencies for a dataset of frequency range 0 – 6 Hz

The Source Signature

The accuracy of the source wavelet is important for FWI particularly at the lowest frequencies (Lua *et al*. 2007; Warner *et al*. 2012). Previous inversion tests using the contractor wavelet lead to a poor match between the observed and predicted first arrivals at short offsets for the low frequencies (Warner *et al*. 2013). The contractor wavelet was originally designed to produce a good match at high frequencies rather than at the lower frequencies required for FWI. As such, the strategy of Warner *et al*. (2013) is adopted whereby the source wavefield is extracted from the data as opposed to using the contractor wavelet. This usually involves obtaining the source from the direct arrivals recorded on short-

offset ocean bottom nodes, with the source ghost and the first and second seafloor multiples removed (Figure 2-6). The ghost and sea-bottom multiples are modelled during the forward modelling of the wavefield for FWI through the use of a free surface boundary condition. The extracted source is quality controlled ensuring that the source zero time and that of the observed data are identical.



a) Source ghost

b) Source ghost and first seafloor multiple

c) Source ghost and second seafloor multiple

Figure 2-6: Illustration of the source ghost and the first and second order multiples, which are initially removed and remodelled during the modelling process.

Model QC techniques

A suite of different measures help us quality control (QC) velocity models obtained from FWI. If the FWI model is more accurate than the starting velocity model, the following is expected:

- Common midpoint (CMP) gathers will be flatter after pre-stack depth migration using the recovered FWI model, and individual stacked events will be stronger.
- Major reflectors will be more continuous, especially those beneath heterogeneous overburden such as gas or salt.
- Synthetic data, generated using the FWI model, will be a better match to the observed data than data generated from the starting model (judged by misfit).
- FWI velocities will match velocities obtained in well logs.

Advantages and Limitations

FWI has major advantages. It yields high-resolution (superior) velocity models, which can be directly interpretable or used to improve seismic images through subsequent migration and geological interpretation. FWI models can thus, be treated as an attribute, providing absolute layer properties of the Earth that complement reflection amplitude information. However, FWI is not without its limitations. The inverse problem is ill-posed and non-unique, and so obtaining an accurate solution is challenging. Practical issues to be addressed include non-linearities, and sensitivity to the initial model. Cycle-skipping makes the associated objected function highly non-linear. Additionally, the sinusoidal nature of the wavefield as well as the complex nature of the Earth's reflectivity introduces further non-linearities (Bunks *et al*. 1995). Existing solutions to mitigate the effect of these non-linearities include: a classical multiscale approach, which inverts the low frequency data first (Bunks *et al*. 1995, Sirgue and Pratt, 2004) since the modelling operator is more linear at low frequencies and more non-linear at higher frequencies (Symes, 2012) and phase unwrapping of the data which identifies the exact starting frequency of the data for FWI without the possible occurrence of cycle skipping (Shah *et al*. 2012).

In view of these deficiencies, this study therefore focuses on further advancing the FWI technology, particularly to increasing resolution and the depth of penetration. To achieve this, the need for the use of FWI of reflection data as against to just transmission data in FWI is more apparent. This has proven to be a challenge for reasons outlined below.

FWI: Transmission verses reflection data

Conventional FWI predominantly uses transmission data - mainly refracted arrivals and turning rays. All other arrival information, particularly reflections, is muted before FWI. The reasons are as follows:

- Transmission data are sensitive to mainly velocity changes whereas reflection data are strongly dependant on both velocity and density. Thus, it is more difficult to independently estimate velocity values from reflections than it is from transmitted data. As such, recovering long wavelength information features if only short-offset information is available presents a challenge since short-offset reflection waveforms

are highly sensitive to contrasts in impedance (product of velocity and density) and less sensitive to long-offset, refraction velocity variations (Mora, 1988, 1989).

- For reflection data, information about the amplitude of a propagating wave is predominant since acoustic impedance contrasts are frequent. Additionally, details about the phase can be derived - a negative reflection coefficient means that the reflected wave receives a 180° (π) phase shift. For transmission data, travel-time relationships can be developed from the phase of the data. Once the phase (timing) is correct, cycle skipping can be avoided and so the recovery of macrostructures is made much easier.

- The non-linearity of reflections (hyperbolic approximation) compared to the refractions (generally linear) further complicates the FWI problem. Increased non-linearity of the inverse problem occurs when reflections are introduced especially since the FWI process involves a linear approximation (Born approximation during the step length calculation).

- Changes in the elastic properties of the Earth at the different boundaries from which reflections are generated make reflections elastic. Also, reflections are much more elastic than refractions. There is a numerical cost associated with accounting for the elasticity of the reflections and so acoustic approximations result. However, elastic codes are being developed so this problem of accounting for the increased elasticity of reflections can be mitigated.

Summary

Extensive parameterisation and testing during the application of FWI to both transmission and reflection dominated datasets are required to improve the robustness. As a result the aim is to investigate: strategies for reflections FWI; strategies to enhance the resolution of FWI models with little to no additional costs; extending the bandwidth of FWI thereby increasing the model-resolution and image fidelity and also increasing the depth of penetration through the use of reflection events.

Chapter 3 : Reflection FWI Strategies

Overview

Three-dimensional full-waveform inversion (FWI) has been successfully applied to field datasets to update the macro-velocity model, thereby improving PSDM images. However, sufficiently long-offsets that allow turning wave energy to reach the velocity target, a good starting model and frequencies as low as 2 to 4Hz, are often critical for a successful conventional FWI approach. These conditions have, in practice, limited most of the productive FWI applications to OBC type data dominated by refracted waves. FWI of reflection-dominated datasets, for example moderate-offset towed-streamer surveys targeting deeper reservoirs and sub-salt reservoir targets, have proven to be more difficult. The deep-water environment holds great opportunities for exploration geoscientists and it would thus be advantageous to advance FWI technology to incorporate reflection energy.

FWI of reflection energy introduces added non-linearity into the inverse problem resulting in two major added challenges. An extremely accurate starting model to mitigate errors due to incorrect migration of reflectors in depth is required and the favoured gradient update of conventional FWI, which is biased towards updating reflector amplitudes more than background velocities, must be adjusted.

To solve this problem, and to push FWI to work better with pure reflection data, various strategies are explored here. A combination of time windowing; offset limiting; strategic muting and alternating inversion schemes that flip-flop between migration-like (reflector building) and tomography-like (background velocity) processes, will be examined. A key additional ingredient is to formulate the FWI methodology so that it does not require an unduly accurate starting model, and to modify the raw gradient so that it favours macro-velocity updates (Yao *et al*. 2014).

Introduction

Long-offset turning rays, of low-frequency content, are associated with long-wavelength macro-structures whereas short-wavelength microstructures are associated with high-frequency reflection events. FWI, at present, uses the long-offset refracted waves to improve the macro-model whereas migration uses the reflection data to improve the finer detail. The aim is to improve the macro-model using pure reflection data through an effective combination of tomography and migration thereby overcoming the challenges associated with FWI of reflection-dominated datasets.

Conventional FWI, beginning from a starting model sufficiently close to the true model, seeks to make a series of step-wise improvements by minimising the objective function of the L2-norm of the data residual, that is, the difference between the predicted and observed data. This iterative inversion scheme updates the model guided by the direction of the local gradient of the objective function. With increasing number of iterations, conventional FWI focuses its gradient updates on matching the amplitude of the reflectors rather than the background velocities. Figure 3-1 demonstrates the theoretical relationship between reflection and transmitted amplitudes at a reflector boundary. The forward propagation through the smooth initial model consists only of transmitted arrivals (source amplitude = 1), and the residual wavefield consists of only the back-propagated reflection-dominated observed data (reflection amplitude = R) for the first iteration. Cross-correlation of these wavefields will build a reflector into the model with reflectivity of order R. With continued iteration the reflector update is of the order R, but the macro-model update is of the order R^2. The cross-correlation of the forward source wavefield of amplitude 1 with the reflected receiver wavefield of amplitude R^2 as well as the cross correlation of the back-propagated receiver wavefield of amplitude R with the reflected source wavefield of amplitude R forms the macro-model update of amplitude R^2. Since, $|R| << 1$, the update of the reflectivity will be much stronger than the update of the background velocity (Yao *et al*. 2014).

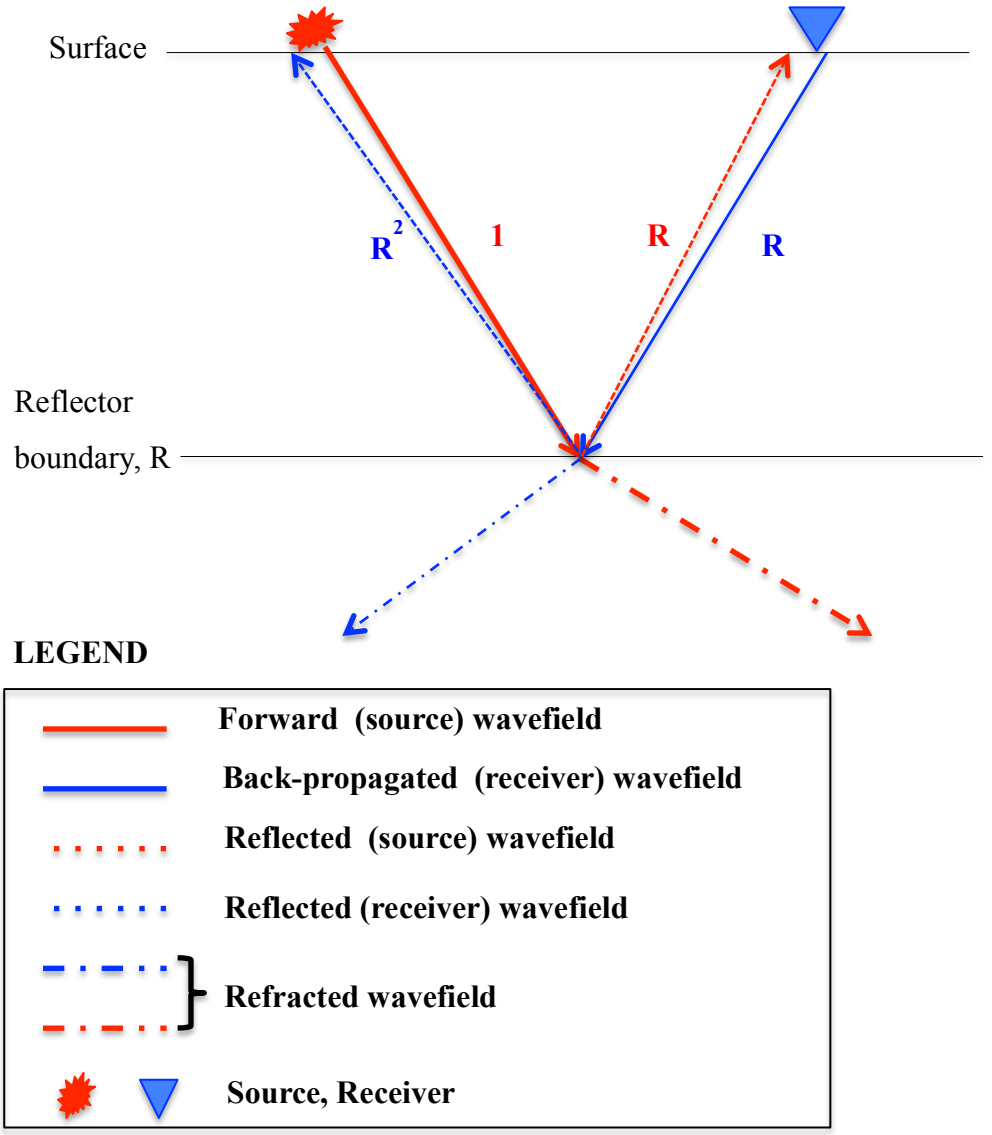


Figure 3-1: Conceptual diagram illustrating the theoretical relationship between reflection and transmitted amplitudes at a reflector boundary of amplitude R. Cross-correlation of the forward source wavefield of amplitude 1 (solid red) with the reflected receiver wavefield of amplitude R^2 (dashed blue) along with the cross correlation of the back-propagated receiver wavefield of amplitude R (solid blue) with the reflected source wavefield of amplitude R (dashed red) forms the macro-model update of amplitude R^2. The amplitude at reflection point remains R. Given that R is less than 1; the reflectivity update is stronger than the macro-model update.

Conventional FWI of reflection-dominated datasets thus significantly adjusts the reflectivity and minimally adjusts the macro-model as attempts to match the observed data are made. Reflection FWI has thus proven to be challenging mainly because:

- The first few iterations of the inversion is immediate with the building of the reflectors whereas the macro-model update is gradual.
- Velocity verses depth trade-off (depth of reflector changes with minor velocity changes).
- Bandwidth of FWI gradient (e.g. 2 – 7Hz) different form bandwidth of the subsurface.
- Misfit surface appears to be very flat for reflection FWI, so many iterations are required.

In order to successfully apply FWI to sub-critical reflection data only, an update to the velocity at all length scales is required. Use of reflection data allows velocity updates equivalent to that obtained by transmitted data, allowing deeper penetration. Conventional FWI effectively migrates reflectors into the correct position. However, a shift in focus from updating short-wavelength to updating long-wavelength structures, and the subsequent correct positioning of the updated reflectors are essential for the application of FWI to reflection-dominated datasets.

To facilitate this, it is necessary to enhance the tomographic aspects of reflection-dominated FWI and rebuild the reflectivity as the macro-model evolves and improves. Use of a simple 1D model, time and offset windowing, muting of direct arrival, and low frequencies were investigated to determine which parameters are key to the successful inversion of reflection-dominated data. In addition, with the use of a fairly good starting model, an alternating inversion scheme between updating the reflectors and then the macro-model, for each iteration, was investigated. With successful preconditioning of the starting model using the above schemes for reflection FWI, conventional FWI can then proceed towards an accurate final model.

Strategies for reflection FWI

Here a laterally continuous velocity layer, 2600 ms^{-1}, embedded within a homogeneous background, 2000 ms^{-1}, is inverted (Figure 3-2). With the layer to be recovered being fast, the homogenous background model of 2000 ms^{-1} is used as the starting model. Sources and receivers are located at the same positions, in a regular pattern, along the top of the 2D model

at a depth of 12.5m. They are spaced 25m apart, with 96 sources and receivers in total. The model dimensions, 3000m wide by 3025m deep, and acquisition layout is designed so that the experiment is reflection dominated with two reflections and a direct wave. The absence of turning rays means that conventional FWI is unlikely to be successful if applied to these data. Different strategies were examined in an attempt to solve this problem. The parameters investigated include the effect of Gaussian windowing, muting of the direct arrival and the use of a multi-scale approach.

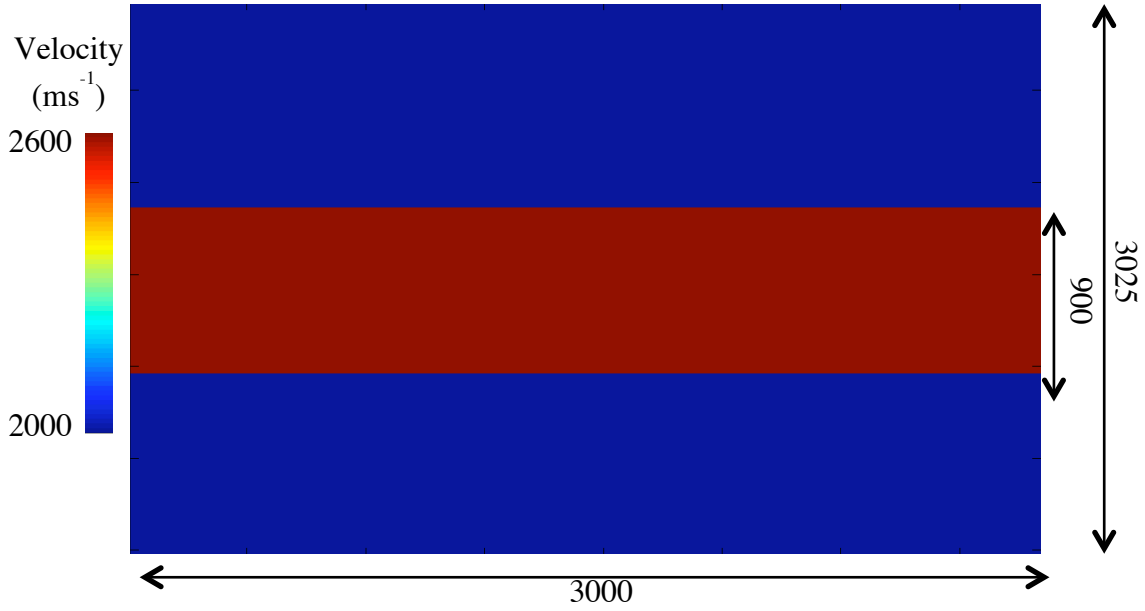


Figure 3-2: True model used in the generation of a reflection-dominated synthetic data used in the testing of reflection strategies. The dimensions of the model are such that reflections are the key arrivals evident.

Gaussian Windowing

The sliding Gaussian window is used to weight the data in time during inversion. This allows for emphasis on specified arrival information, early or late arrivals, at any one time, thereby controlling the data used in the inversion for individual iterations. A multiplier representative of the width of this sliding Gaussian window is specified. A value of zero disables the Gaussian data windowing. For some datasets, the use of a Gaussian window, whose width is specified as a non-zero value, can help to accelerate convergence and reduce the time

required for individual iterations. However, this can have undesirable consequences if an incorrect weighting is applied to the data. For reflection-dominated datasets, the effect of this parameterization is tested.

Muting of Direct Arrival

Unlike conventional reflection imaging whereby different stages of pre-processing is required before a reflection image can be produced, a conventional FWI workflow involves minimal pre-processing. The minimal pre-processing applied is data-dependent. Near-offset reflections, shear waves and surface waves, when present, are muted in some instances whereas all the arrivals may generally be used in other instances. For this synthetic reflection dominated dataset, the starting background velocity model is correct and so, the first break (direct arrival) times are matched between its predicted data and the synthetic observed data (Figure 3-3). As the amplitudes of the first arrivals are quite large, removing the direct wave will focus the inversion on the later events – the two reflections. As such, the effect of removing the direct arrival is tested.

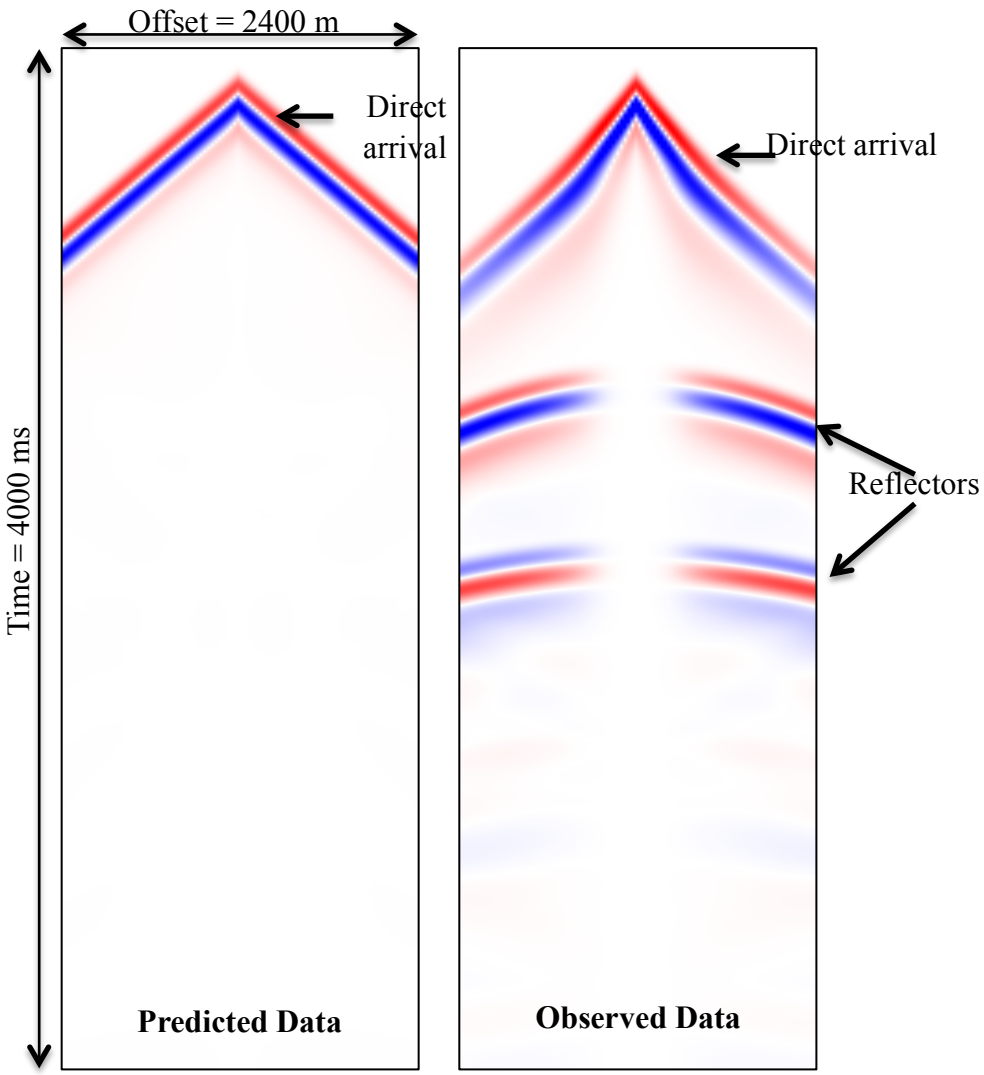


Figure 3-3: Travel-time plot showing a comparison of the synthetic and observed dataset indicating the key arrivals. The direct arrival is accurate in timing but slightly different in amplitude due to the application of trace normalisation.

Multi-scale approach

FWI workflows can include layer stripping (Aifei and Wenhui, 2011), offset weighting (Shipp and Singh, 2002), time windowing (Kolb *et al*. 1986; Yoon *et al*. 2012), and in some cases a depth-controlled update (Wang and Rao, 2009) or damping (Aifei and Wenhui, 2011). Here, both offsets and time-windows are used to steer FWI to be performed on early-arriving, short-offset data initially and subsequently on the later-arriving, long-offset data (Figure 3-4).

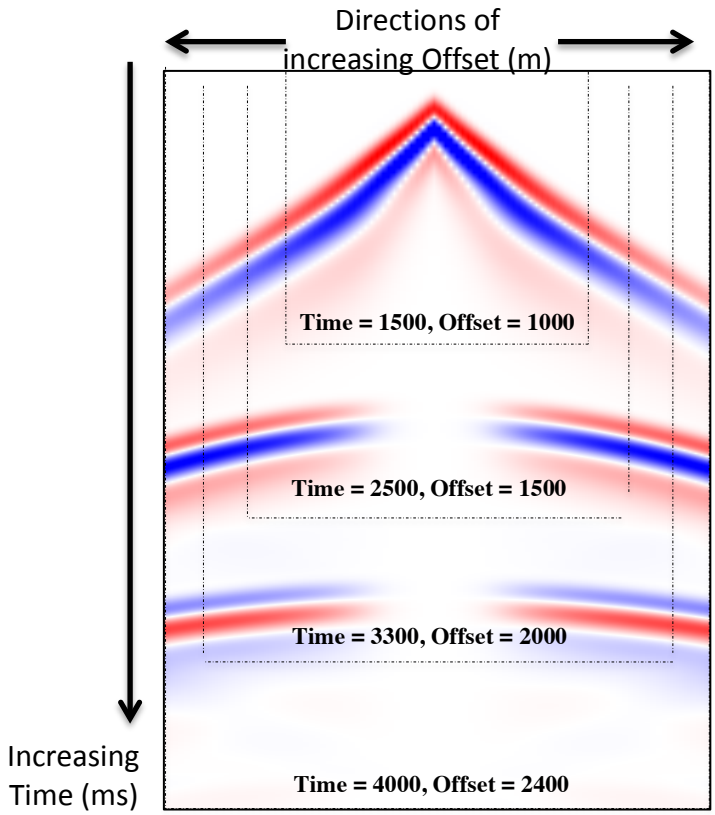


Figure 3-4: A shot record illustrating the offset continuation and time limiting approach

In this model, the predicted data are not cycle skipped at the shortest offsets. Figure 3-5 shows a comparison between the observed data and the predicted data from the homogenous starting model. Enlargement of these data at: near, mid and far offsets in Figure 3-6 clearly shows that there is a good match at the near-offsets, in both phase and amplitude, between the observed and predicted data from the homogenous starting model. At the far-offset locations the predicted data is well within half-a-cycle of the observed data, confirming the data is not cycle-skipped. Hence the input data can be limited to include only these shortest offsets and early times. As the inversion proceeds, the offset and time-windows are successively opened, in order to limit the data at each stage to that portion that is not cycle skipped.

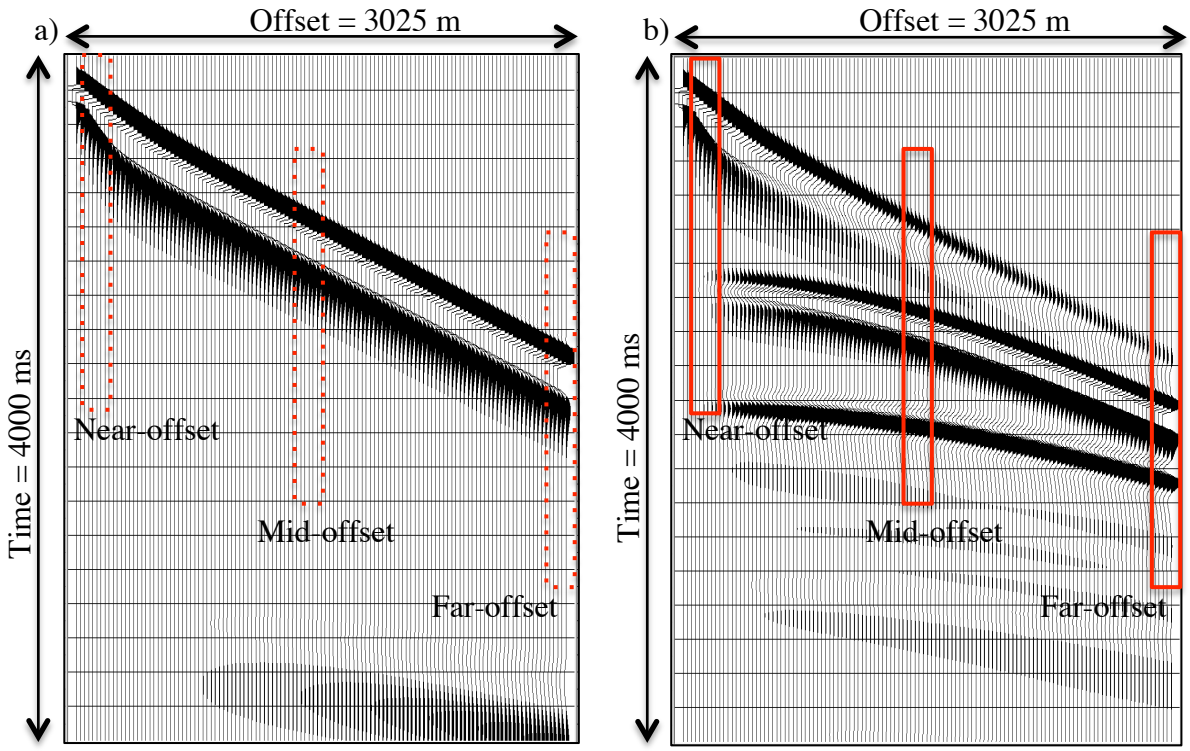


Figure 3-5: Comparison between a) predicted data for the homogenous starting model and b) observed data. Enlargement of these data at: near, mid and far offsets in Figure 3-6 show clearer that the direct arrival is well-matched in phase and amplitude at near offsets and in phase at the further offsets indicating the data is not cycle-skipped.

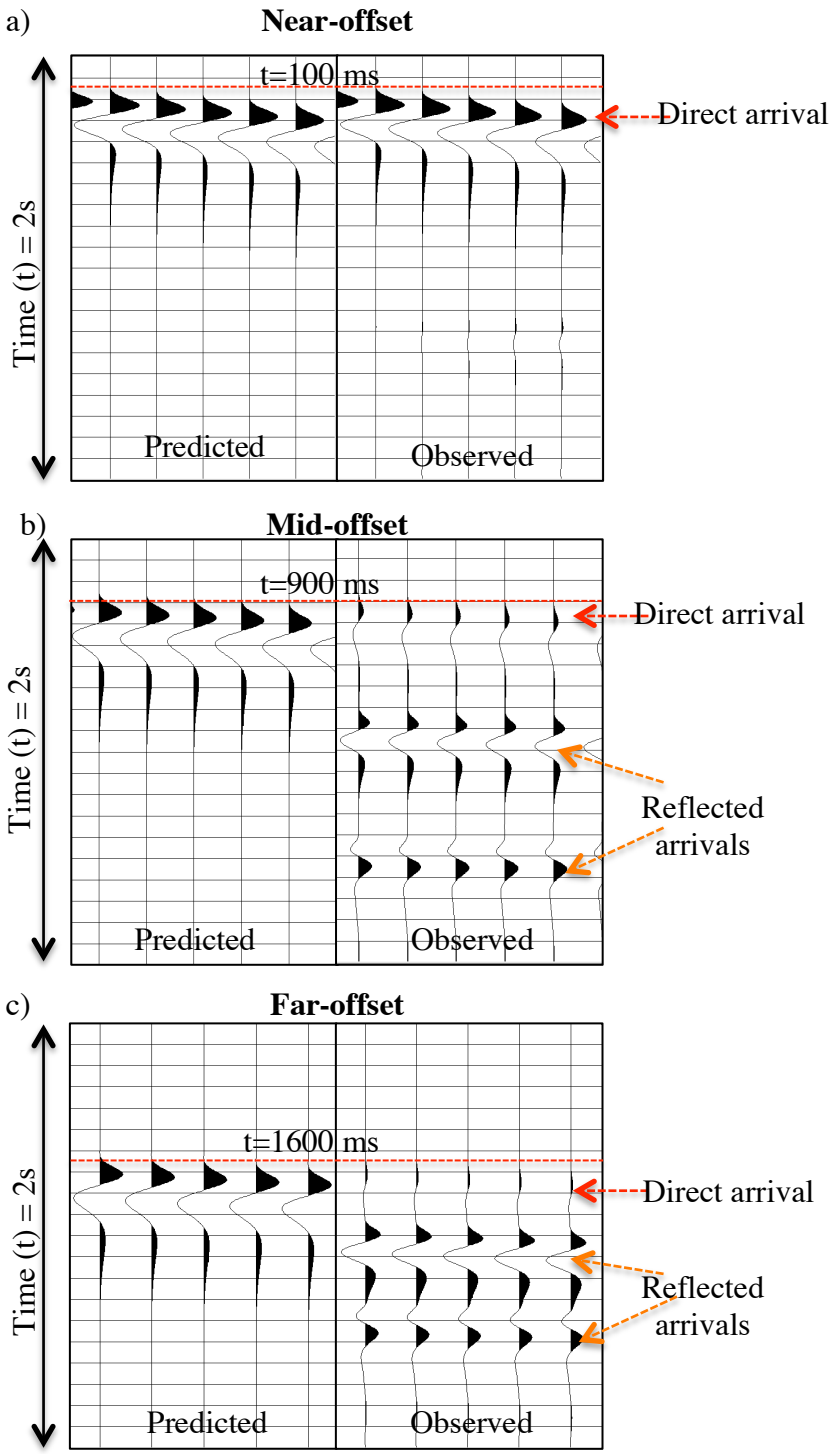


Figure 3-6: Enlarged view at a) near b) mid c) far offsets for the predicted data (left) and observed data (right).

All strategies above were tested individually initially, and then in combination. All modelling and inversion runs were performed with a free-surface layer thereby allowing for the presence of free-surface multiples. Using the best results from these inversions, the effect of the 1D layer thicknesses and the acoustic impedance contrast were then investigated.

Results and Discussions

2D acoustic, time-domain FWI was carried out. Table 3-1 shows the inversion parameters kept constant during the inversions. Trace normalisation, spatial pre-conditioning and slowness parameterisation with minor emphasis on the amplitude was deemed suitable based on inversion experience with transmission-dominated datasets. All the inversion tests were run using a multi-scale approach with frequencies increasing from 1 to 9 Hz (1, 1.5, 2, 2.5, 3, 5, 7 and 9 Hz). At 9 Hz, a grid spacing of 50 m provides more than 4.2 grid points per wavelength as is required by the finite-difference algorithm. In addition, all the inversions were run using a multiple generating free surface at the top of the model, thereby allowing for the presence of multiples, which give an additional view of the subsurface, during the inversion.

Minimum velocity (m/s)	1900
Minimum frequency (Hz)	1
Grid spacing (m)	25
Maximum frequency (Hz)	9
Maximum velocity (m/s)	2700
Time step (ms)	4
Number of frequencies	8
Number of iterations/frequency	20
Free Surface	Yes
Slowness	Yes
Normalise	Yes
Amplitude	No
Spatial Preconditioning	Yes

Table 3-1: Summary of parameters kept constant for the inversions

Choosing the starting frequency

Choosing a suitable starting frequency is essential for FWI. For this synthetic dataset, noise like sea swell and ground roll present in real datasets, is absent. Also, low frequencies are present, tapering down to 0Hz. Without the added need to eliminate noise and account for the low-frequencies, or lack thereof, that comes with FWI of real field datasets, the choice of the ideal starting frequencies for these synthetic tests was chosen by trial and error. With the added non-linearity that comes with reflection FWI, the lower the starting frequency, the better the likelihood for convergence to a global minimum. Figure 3-7 shows the full-fold region of FWI recovered models using a starting frequency of a) 2.5 Hz and b) 1 Hz. The key difference between using the 2.5Hz starting frequency verses 1Hz is illustrated in the analysis of the central trace (Figure 3-8). The high velocity anomaly is significantly underestimated with the use of the higher starting frequency. As a result, all further tests were performed using a starting frequency of 1Hz for this synthetic test.

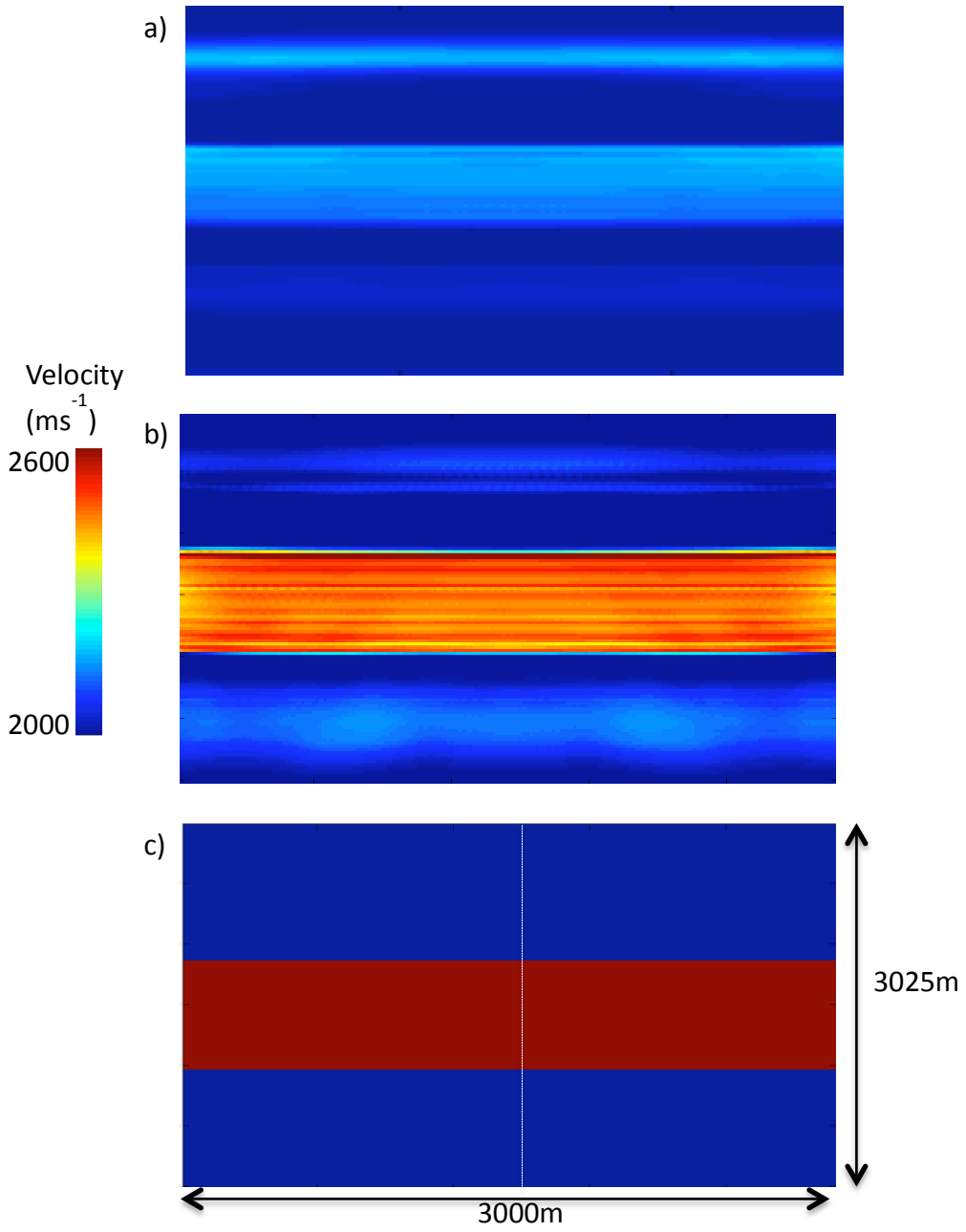


Figure 3-7: 9Hz FWI recovered models obtained using a) starting frequency of 2.5Hz b) starting frequency of 1 Hz and c) True model. The white dashed line indicates the central 1D profile extracted below.

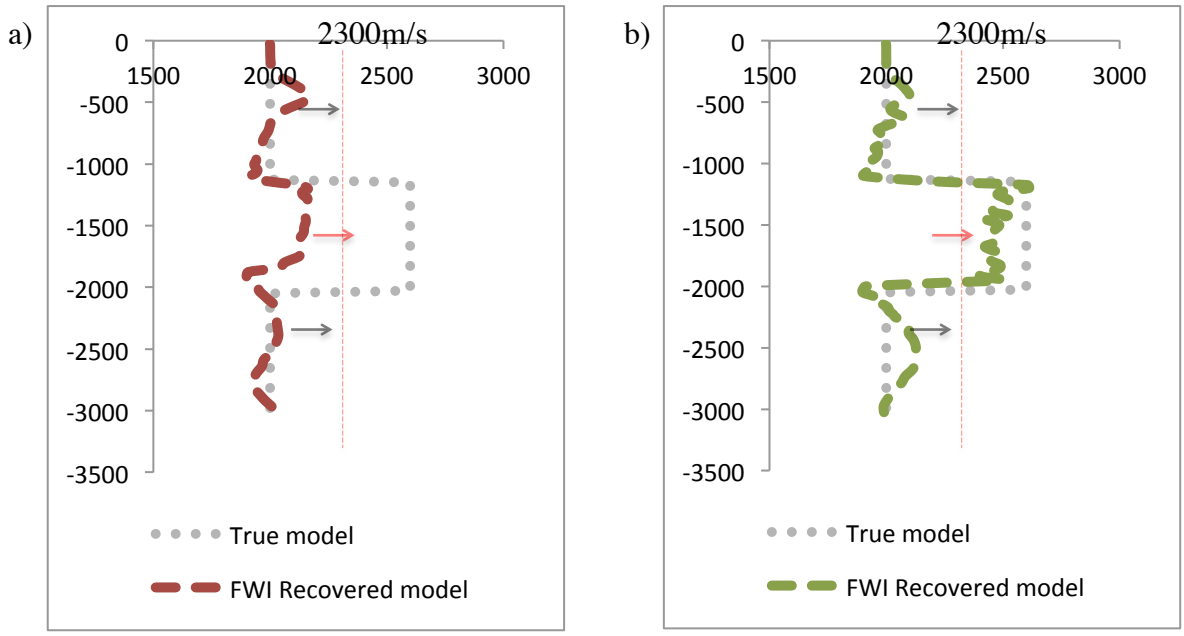


Figure 3-8: Comparison of the velocity-depth profile through the centre of the true and 9Hz FWI recovered models at different starting frequencies of a) 2.5Hz b) 1Hz

Sensitivity to acoustic impedance contrast

The impact of the acoustic impedance contrast at the reflector interfaces was tested. Figure 3-9 illustrates that the same effect of a fairly accurate velocity at the top interface and a bottom interface that is 50% accurate, is common for all tests regardless of the change in velocities across the interfaces. If the perturbation at the top reflector interfaces is meant to be +100 m/s, FWI recovers models that are -50 m/s outside the layer and +50 m/s inside the layer, the net absolute perturbation being correct at 100 m/s. As such, regardless of the acoustic impedance contrast, the perturbation inside the high velocity layer is on average 50% of its true value. The FWI model reproduces the reflection amplitudes correctly, but the moveout is slightly wrong. Given that the difference in the acoustic impedance contrast across the reflector interface did not affect the overall result, the exact model with the largest contrast was chosen for subsequent tests (Figure 3-9c).

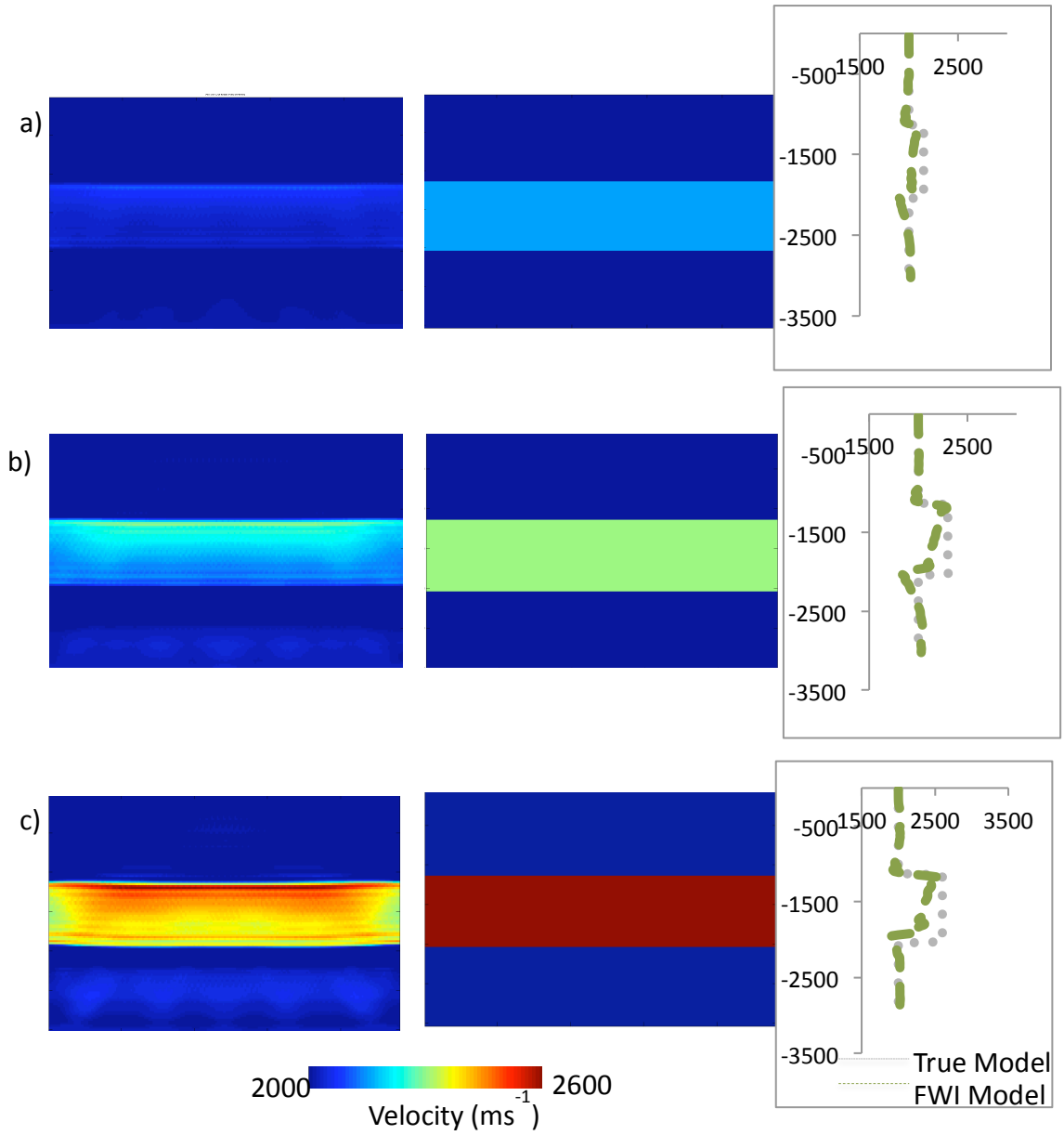


Figure 3-9: Comparison between the FWI recovered models (left) and the True model (centre) with a velocity-depth profile (right) for different acoustic impedance contrasts. The change in the velocity across the reflector interface is a) 150ms^{-1} b) 300ms^{-1} c) 600ms^{-1}. The background velocity is fixed at 2000ms^{-1}. For all the cases above the top interface is fairly well recovered, with the recovered velocities near the lower reflector interface being 50% accurate, that is, 50% of the true.

Transmission verses reflection target

Figure 3-10 shows a synthetic test whereby the true model contains both a transmission target – a low-velocity anomaly, and a reflection target. Using a 1D constant starting velocity of 2000ms^{-1}, FWI successfully recovers the low-velocity 'blob', but overestimates the surrounding background velocities, and velocities at the top reflector interface, whilst underestimating the velocities at depth (Figure 3-10b). However, when the starting velocity model has the reflector position in the correct place, FWI recovers the low-velocity 'blob', and performs slightly better overall. This indicates that the transmission target is easier resolved compared to the reflection target and suggests that the having the deeper reflections accurate, help in better recovering the structure above. The next tests were designed to determine how to optimise FWI to recover the reflection target.

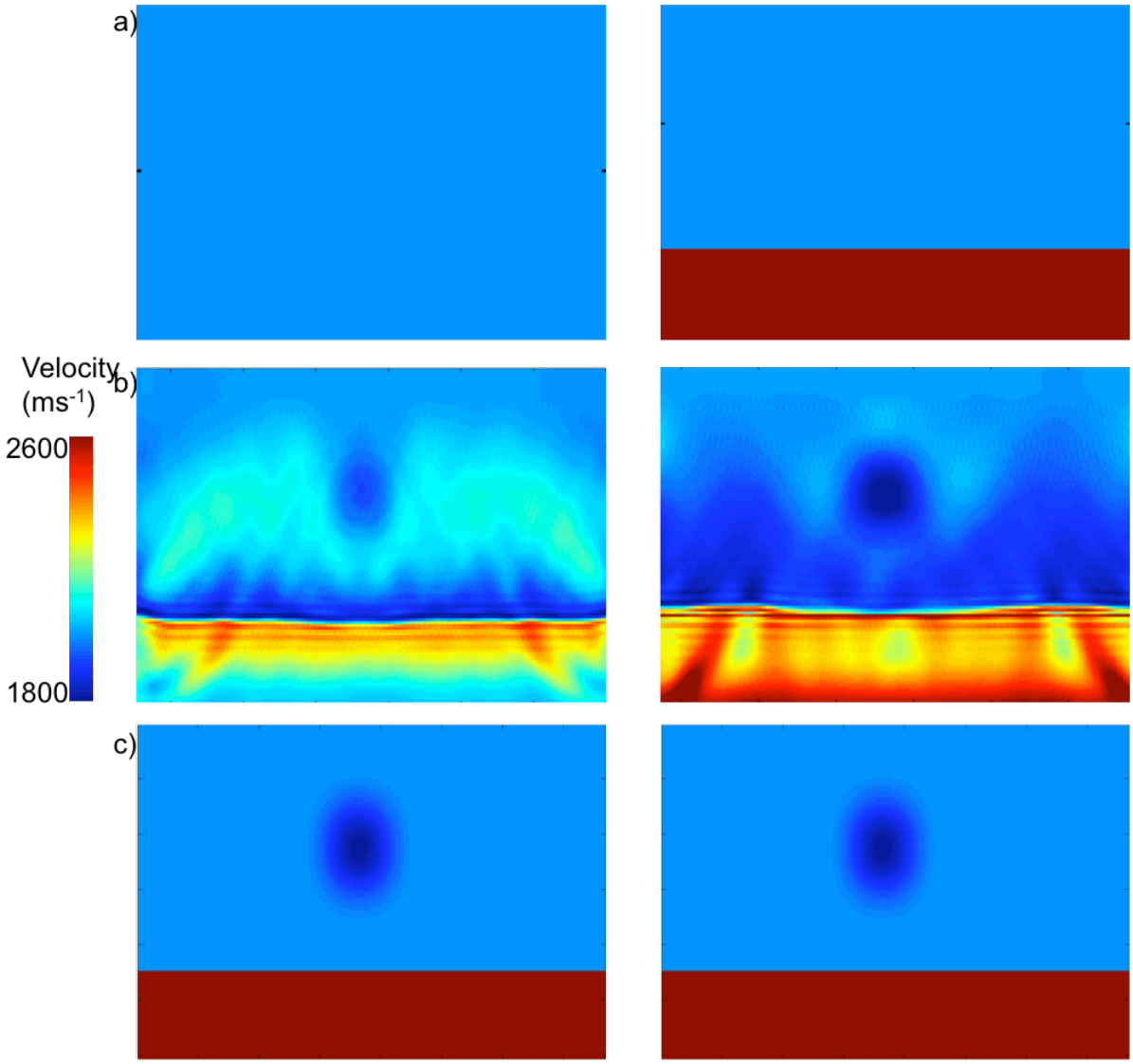


Figure 3-10: a) starting models b) FWI recovered models c) True model

Choosing the parameterisation

Figure 3-11 summarises the full-fold region of the FWI recovered models derived as a result of using: the standard FWI approach, FWI without the use of Gaussian windowing, omission/muting of the first arrivals, and finally – a combined approach using the key parameterisation from all three methods. Thorough analysis of the velocity-depth profile at the centre of the model, Figure 3-12, and gives a clear visualisation of the velocity changes throughout the model. FWI builds the velocity perturbation symmetrically about the starting model. The top interface of the high velocity layer is recovered well for all the inversions. However the 900 m high velocity anomaly is not well recovered. Adopting the different strategies individually in the FWI scheme yields varying results in the recovery of this high velocity perturbation.

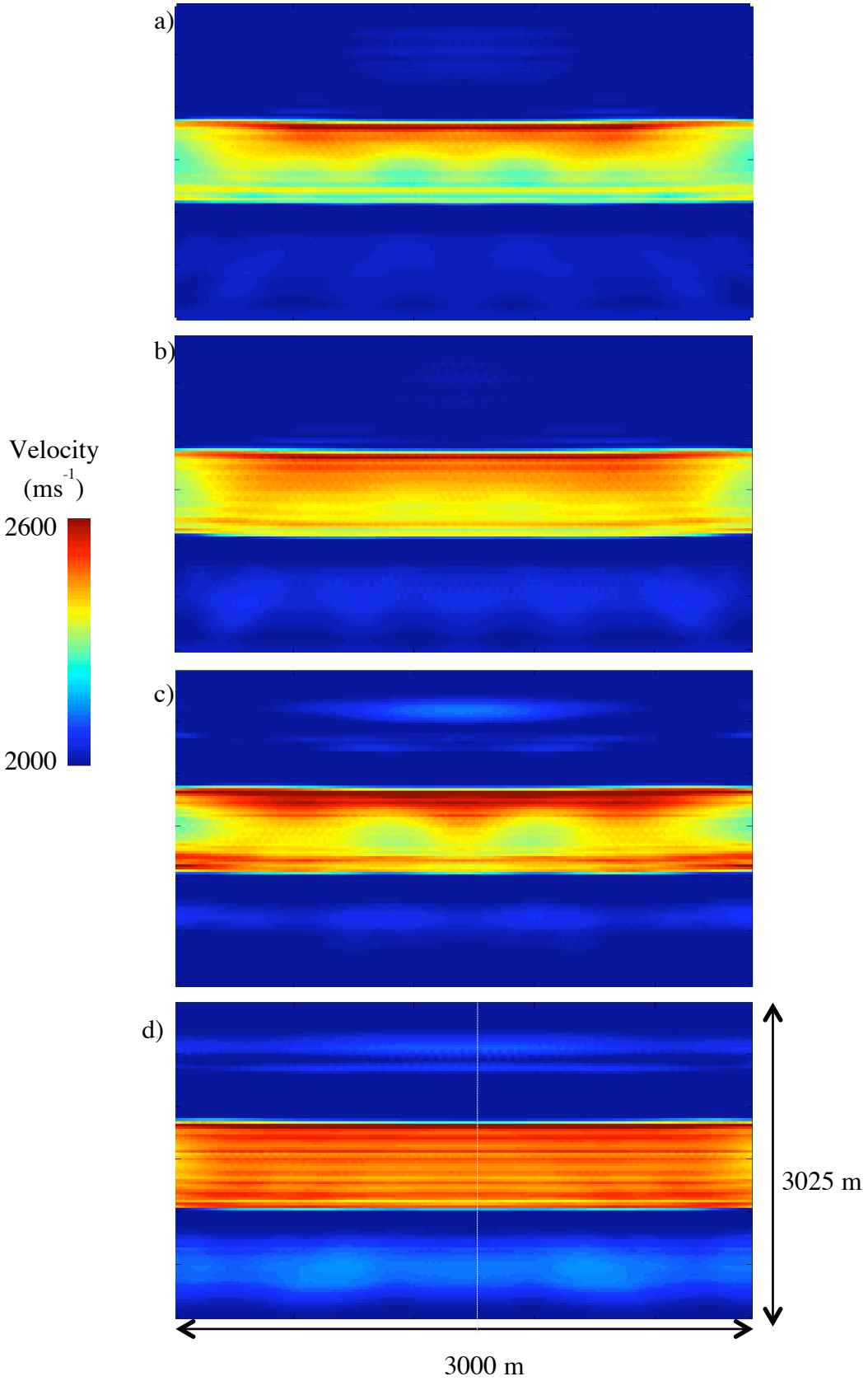


Figure 3-11: Full-fold region of the velocity model for a) standard FWI, b) FWI without Gaussian windowing c) FWI with muted direct arrival muted d) FWI combining all key parameterisations above.

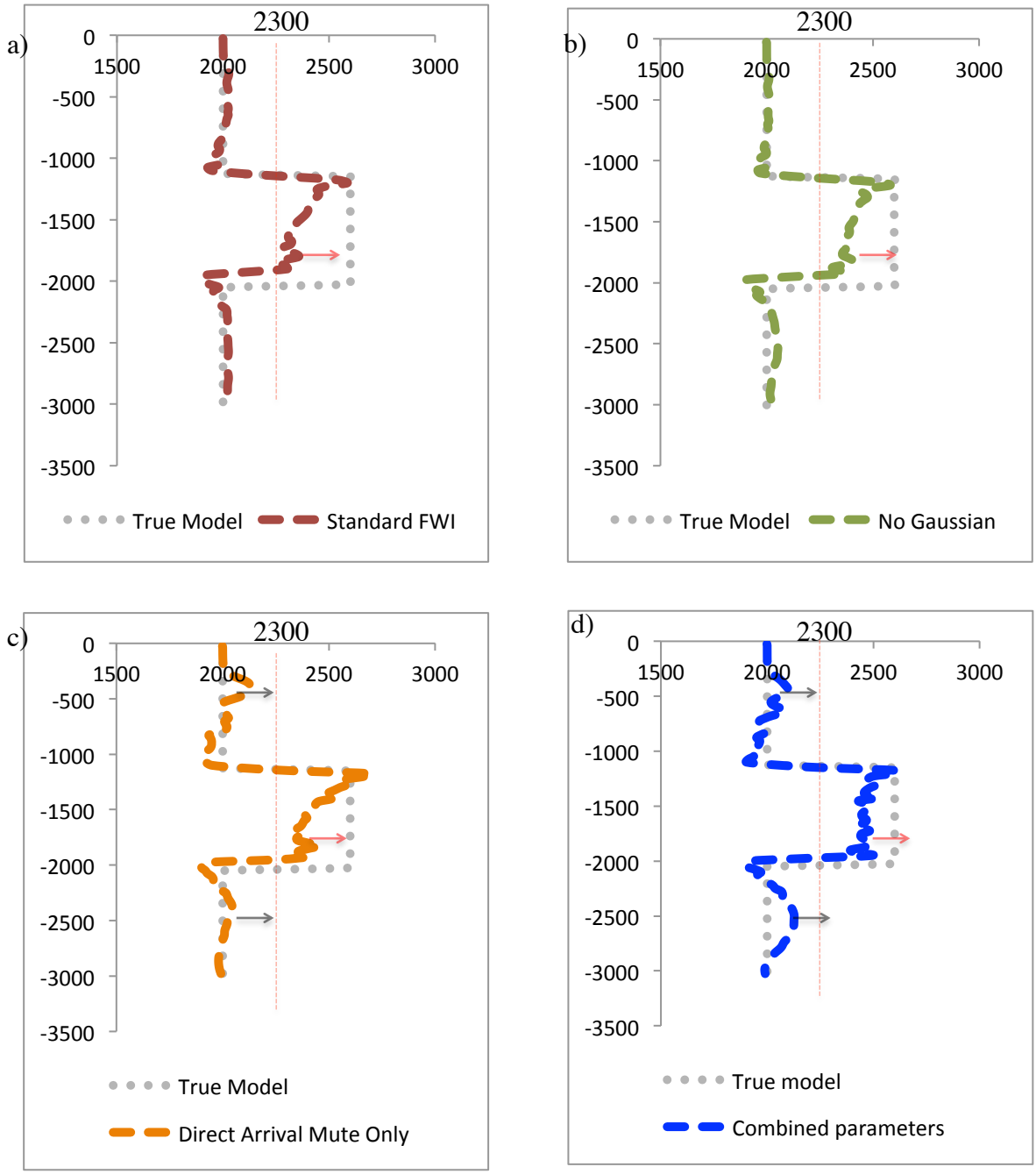


Figure 3-12: 1D velocity depth plot of the true and 9Hz FWI recovered models corresponding to the models displayed in Figure 3-11.

Using the correct background velocity of 2000 ms^{-1}, the standard approach FWI inversion recovers only about half the total velocity perturbation within the layer [Figure 3-11(a) and Figure 3-12(a)]. The background velocity, above and below the 900m high-velocity layer, was unperturbed, remaining close to 2000 ms^{-1}. Omitting the use of the Gaussian window to weight the data in time improved the recovery of the high-velocity layer, with the velocities near the base of the layer being close to the true value [Figure 3-11(b) and Figure 3-12(b)]. Muting the direct arrival steers the inversion towards improving the later reflection events. As such, the 900 m high-velocity layer is much better resolved, with the velocities being even closer to the true value, near the base of the interface (Figure 3-12). A negative effect of removing the direct arrival is the overestimation of velocities above and below the high velocity layer. Nonetheless, combining all the key strategies above, significantly recovers both the anomaly interfaces as well as the entire width of the high velocity layer (Figure 3-12). In addition, when the multi-scale strategy was also included, the recovered models further improved (Figure 3-13).

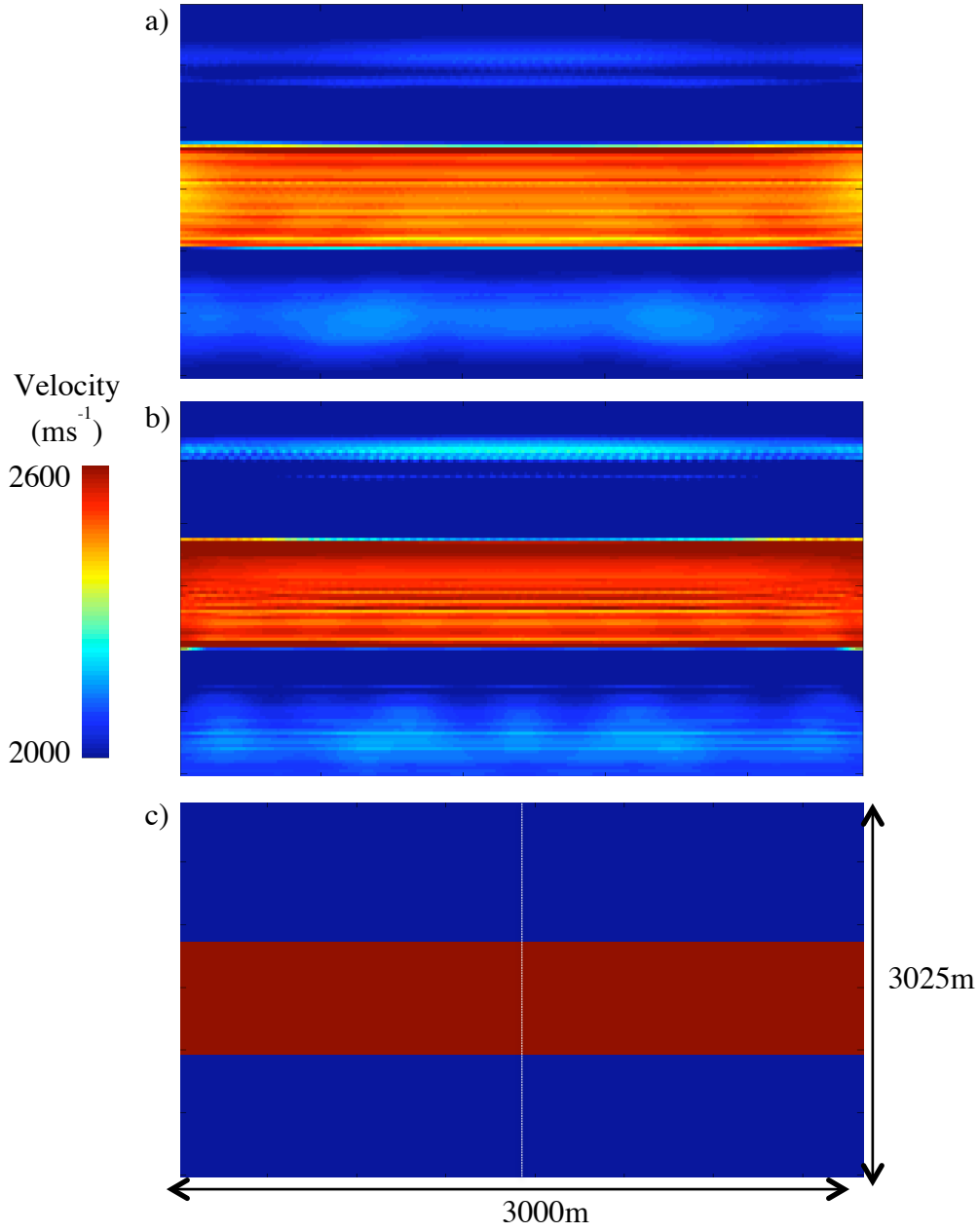


Figure 3-13: 9Hz FWI recovered models using a) combined parameterisation b) time-offset limiting strategy together with combined parameterisation c) true model. The white dashed line indicates the central 1D profile extracted for more detailed analysis

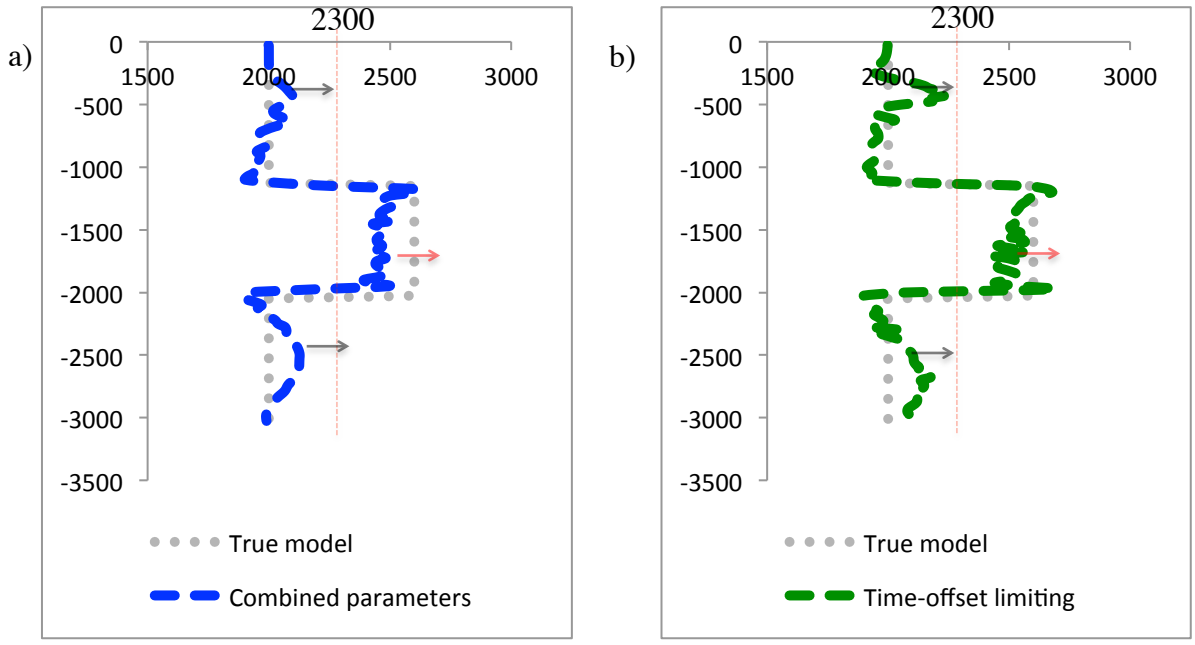


Figure 3-14: Comparison between the velocity-depth profiles extracted from the centre of the true and FWI recovered models obtained using the different parameterisation: a) combined parameterisation b) time-offset limiting strategy together with combined parameterisation. The time-offset strategy recovers the high velocity layer well with an over-estimate at the interfaces. The background velocities are also overestimated above and below the high velocity layer.

Figure 3-14 illustrates that the combined parameterisation together with the time-offset limiting strategy results in the accurate recovery of the high velocity layer. However, the top and base reflector interfaces are overestimated as well as the velocities above and below the high velocity layer. The tests performed show that the accuracy of the reflections in terms of kinematics and amplitude is affected by the parameterisation chosen. With the early iterations of FWI, the top and bottom reflectors are recovered in the correct location after only 20 iterations at the starting frequency (Figure 3-15a). The intermediate iterations completed at every 0.5Hz served to correct for shallow inaccuracies and increase the velocities within the high velocity layer (Figure 3-15b). The final set iterations continue to fine-tune the model, particularly the velocities within the high velocity layer (Figure 3-15c). Also, the FWI model predicted data illustrates the added minor reflective interfaces introduced in the data at the early and intermediate stages and finally removed at the higher frequencies with increased number of iterations where the match is very close to that of the observed data (Figure 3-16).

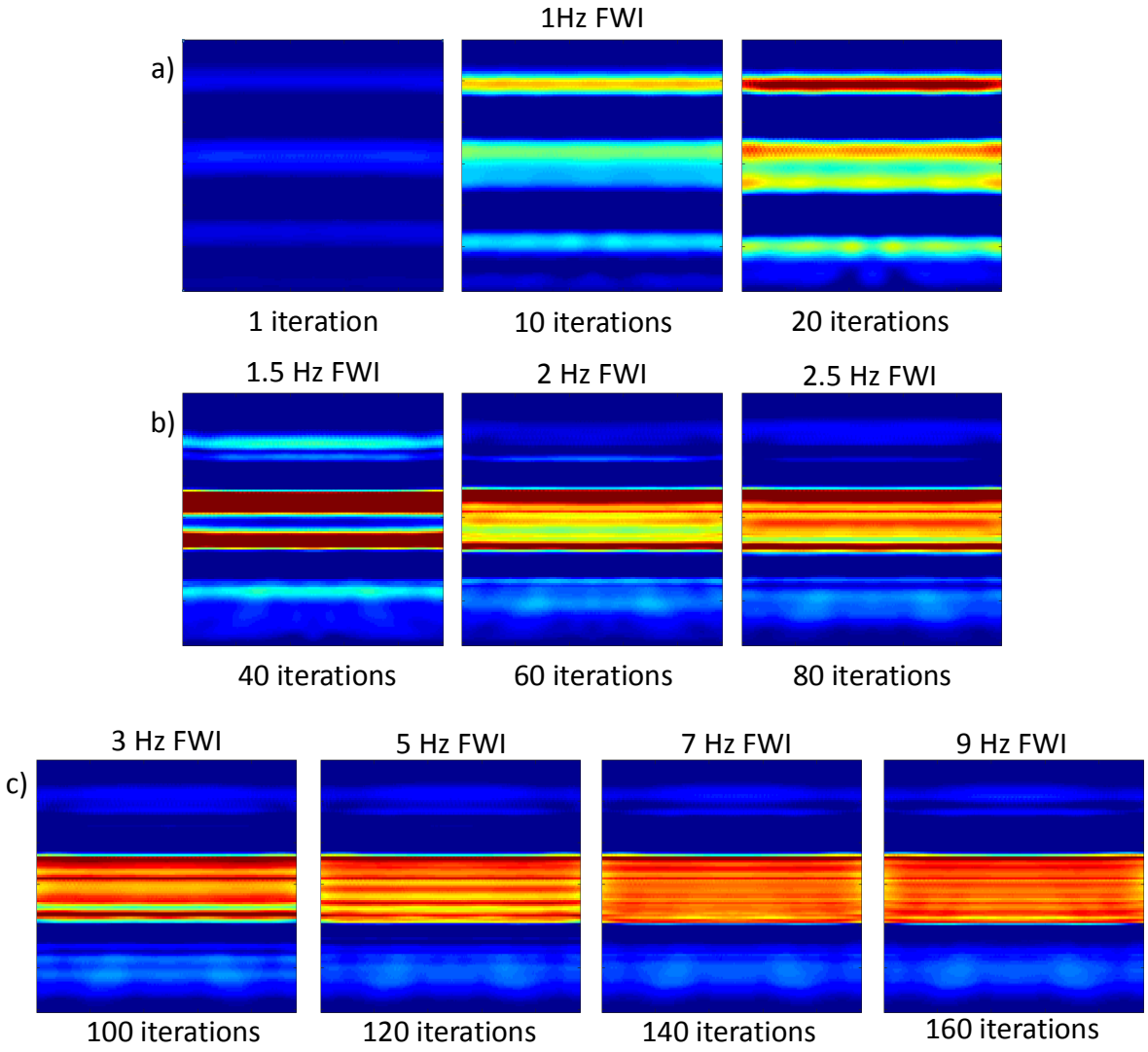


Figure 3-15: FWI Recovered models showing the inversion results after the a) initial b) the intermediate and c) the final iterations. After 20 iterations, the top and base reflector positions are already correctly positioned. The intermediate iterations serve to increase the velocities within the high velocity layer as well as correct for shallow inaccuracies. The final iterations serve continue to improve the velocities within the high velocity layer. These models were generated using the combined parameterisation.

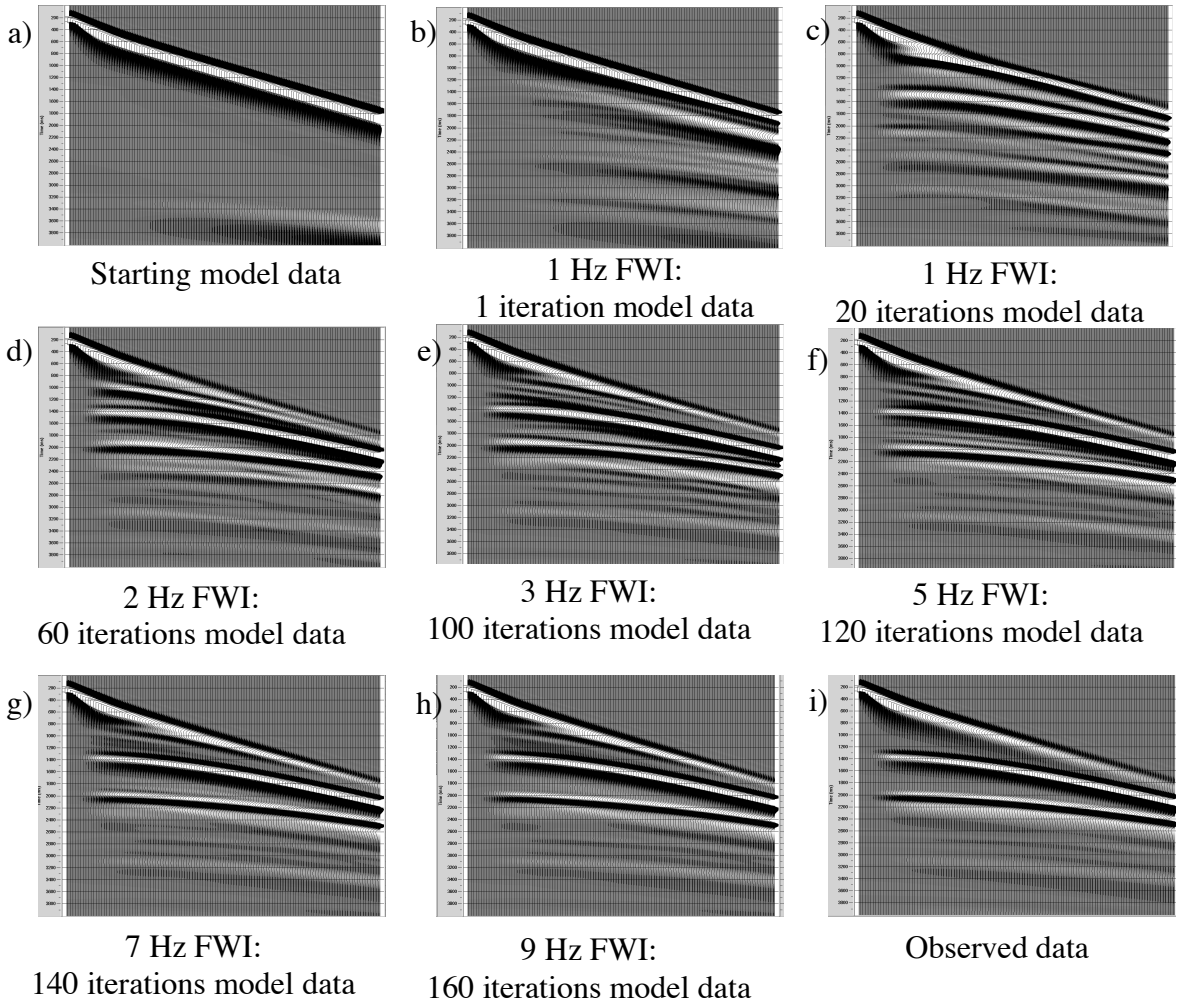


Figure 3-16: Predicted data obtained from a) the starting model, the FWI recovered models at b) 1 iteration c) 20 iteration (1Hz) d) 60 iterations (2Hz) e) 100 iterations (3Hz) f) 120 iterations (5Hz) g) 140 iterations (7Hz) h) 160 iterations (9Hz) and the i) observed data. At the early iterations, the top and base reflectors representing the velocity contrast at the high velocity layer are inserted with minor reflectors added as well. With increasing frequency and number of iterations, minor reflectors added at the early iterations with the improvements in the high velocity contrast layer, are eventually removed from the data.

Comparisons of the predicted data generated from these models, show that the zero-offset data is well matched but the moveout is incorrect. Subsequently, the inversion leads to an increase in the velocity within the layer in order to match the moveout. This causes the reflection amplitudes to become too large, which outweighs the effect of marginally changing the moveout. Instead, FWI slowly changes the velocity way above the layer, making this on average a little faster, to match the normal moveout. In addition, during this process, the reflections are positioned a little deeper with FWI. This will eventually fix the moveout on the top reflector more or less exactly. The position of the top reflector is correct, as the average velocity is fairly correct above the reflector. It cannot fix the moveout on the bottom reflector much, because anything that it tries to do will be outweighed by its effect on the reflection amplitudes, so it is stuck in a local minimum - not due to cycle skipping though. However, the reflection amplitude depends upon the contrast across the reflector's interface, and not upon the absolute values of velocity. This explains the correct amplitude contrast at both the top and bottom reflectors giving the correct reflectivity.

The anisotropic acoustic FWI algorithm essentially normalises amplitudes so that the inversion fits amplitude only locally. However, an overall fit of both the amplitude and moveout is desirable. Decoupling the reflection amplitudes and velocity perturbations may serve to downplay the importance of the moveout; parameterisation independent of all other parameters (velocity, density, amplitude) may be required.

Key Findings

- Most of the velocity updates occurred during the early iterations, at the starting frequency.
- A very low starting frequency of 1Hz yields a better FWI result.
- The increased resolution with higher frequencies is minimal.
- Convergence is very slow - this implies that (very) many iterations are required for the inversions.
- Local minima is not the dominant problem (this means cycle skipping is not much of a problem).

Summary and Further Work

Some useful strategies for improving FWI of reflection targets have been demonstrated. These strategies have been incorporated into other schemes being developed on FWI of reflection targets by other Imperial college researchers, (Yao, *et al*. 2014, Yao, *et al*. 2015). The ray paths for reflection data are around vertical; thereby reflection data could not constrain the velocity model along the horizontal direction as well as in the case of transmission targets. Consequently, for the inversion of pure reflection datasets, Yao *et al*. (2014) proposed interleaving least-squares RTM with a version of FWI. This combined procedure effectively separates the tomographic gradient which updates the background macro-model from the reflectivity gradient obtained using the Born approximation during forward modelling, thereby providing a good update to the macro-model for pure reflection datasets. When followed by conventional FWI, a high-fidelity, high-resolution FWI result can be obtained using only reflection data. Additionally, continued developments by other research groups are ongoing with the aim of on day successfully performing FWI on short-offset, reflection-dominated field data (Guasch and Warner, 2014; van Leeuwen *et al*. 2014; Brossier, *et al*. 2015).

Chapter 4 : Offset-Variable Density Full-waveform inversion

Introduction

Acoustic, anisotropic FWI has been successfully applied to a 3D full azimuth ocean-bottom-cable (OBC) dataset in the North Sea (Ratcliffe *et al*. 2011; Nangoo *et al*. 2012; Warner *et al*. 2013). FWI produced measurable improvements in the resolution of the velocity model and fidelity of the pre-stack depth-migrated (PSDM) image, as well as a better match to the sonic logs and a reduction in misfit between the predicted and field data. Surprisingly, however, individual peaks and troughs in the predicted data generated by the final FWI model arrive consistently late by up to 12 ms (Figure 4-1). Although this mismatch is small, it should be easily resolved and removed by FWI. Such mismatches are not encountered during the inversion of synthetic test examples. There are many potential effects in FWI that can produce systematic errors in the resultant velocity model, but there are rather few that can produce a systematic mismatch in arrival times, since FWI is specifically designed to vary the model in order to remove such a data mismatch.

A range of possible reasons why such a mismatch might occur was considered and a comprehensive suite of tests to investigate the importance of each of these was undertaken. The inaccuracies in the timing and shape of the source wavelet, incomplete convergence resulting from too few iterations, systematic bias in the starting velocity model, and the effect of inaccurate wavefield simulation through the use of an insufficiently fine finite-difference grid for forward modelling, were all explored. However, in all cases, an explanation for the mismatch or its complete removal using such mechanism was unattainable. For example, biasing the starting velocity model to either high or low velocity leads always to a final model with late arrival times. Shifting the source timing or changing the assumed source wavelet to remove the apparent timing mismatch, then rerunning the inversion, always restored the original mismatch. Changing the mesh size and the corresponding time-step for the inversion does not change the mismatch. Inverting synthetic data generated on one mesh with data inverted on another does not reproduce the effect seen in the field data. The robustness of this result, leads to the conclusion that the problem is most likely caused by the

approximations inherent in the acoustic forward modelling, especially when it is applied at and close to the seabed.

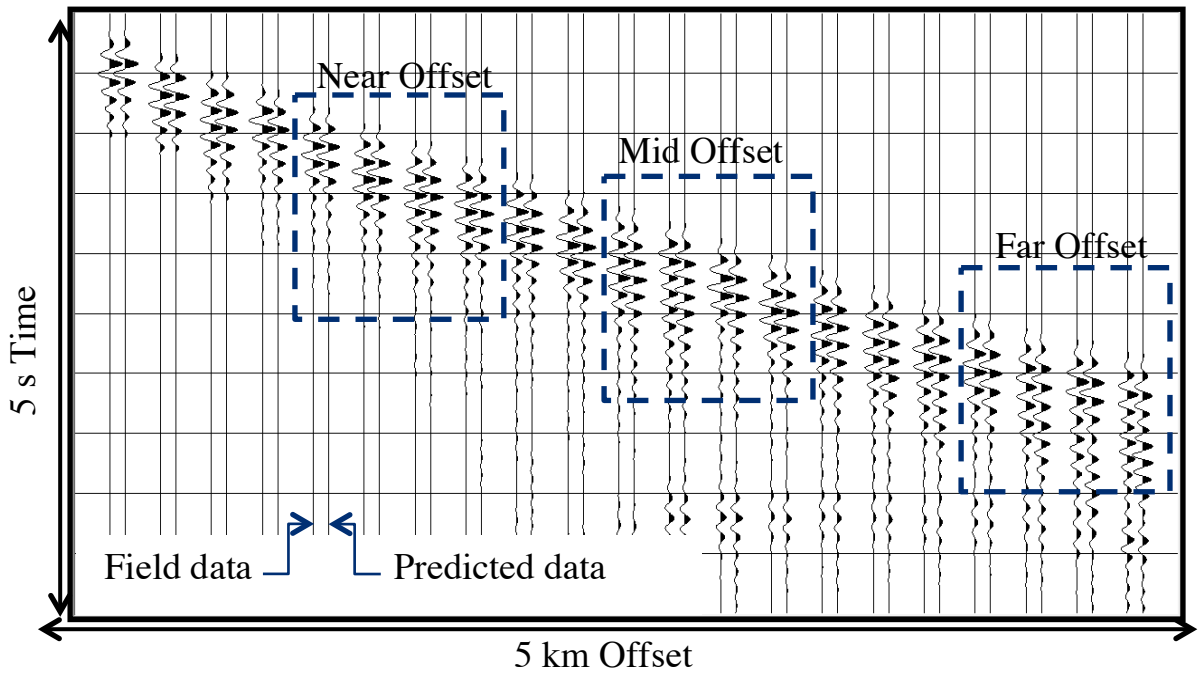


Figure 4-1: (a) Comparison between field and predicted data for the FWI-recovered model, for which the wavefield passes through the gas cloud. The amplitudes, and individual peaks and troughs, within the field and synthetic data match each other well. Enlargement of these data at: near, mid and far offsets show clearer the systematic mismatch in Figure 4-6.

In an acoustic code, several effects are unaccounted for, including anelastic attenuation and elasticity. Attenuation in the shallow part of the model may be significant, for example, in changing the phase spectrum of the wavelet and creating apparent delays to the data. The implicit representation of the seabed at 75m in a velocity model that is computed on a 50m mesh can also introduce inaccuracies into the modelled wavefield. In addition, the use of Gardner relationship for density, (Gardner *et al*. 1974), is unlikely to be correct in detail, especially in the shallowest portion of the model. Together these effects will all tend to lead to an incorrect impedance contrast at the seabed, and to incorrect variations of amplitudes with reflection angle. This in turn changes the strength of the sea-bottom multiples and strongly affects the character and coda of the wavefield (Silverton *et al*. 2014). This means that the approximate representation of the sea-bottom in the velocity model can produce

physical effects that can cause an apparent travel-time mismatch. Here, an inexpensive and efficient way of dealing with such a travel-time mismatch heuristically through the use of an offset-variable density of seawater is explored.

The density of seawater can be considered as a free parameter if FWI is used to match the kinematics of seismic data. In the approach adopted here, and in Warner *et al*. (2013), the inversion is steered principally to match the phase spectrum of each trace, and secondarily the amplitude variation along the trace. The trace-to-trace amplitude variation, however, is not modelled. This means that non-physical changes to the water density can be made, as this will affect only amplitudes and will not directly alter travel-times. Changing water density as a function of source-receiver offset can also be used to influence how the amplitudes of sea-bottom multiples vary with offset. While changes in density do not directly influence the kinematics of the data, changes in sea-bottom density contrast do nonetheless affect apparent arrival times of low-frequency events in the wavefield which result from the interference pattern between the refractions and sea-bottom multiples. That is, density changes can and do effect the positions in time of the individual troughs and peaks in the composite waveforms which act to drive FWI.

Here, an investigation into the effects of changing seawater density to test whether the sea-bottom reflectivity can be better reproduced thereby removing the apparent travel-time mismatch without introducing other undesirable consequences, is conducted. Mulder and Plessix (2008) used a similar approach when inverting a synthetic elastic dataset with an acoustic FWI code to obtain models of velocity and density. With the use of a variable density, Mulder and Plessix (2008) found that it helped address the differences in amplitude and phase between elastic and acoustic data, and led to an improvement in the recovery of velocity at the expense of density. Here, the adopted approach has been to generate a suite of synthetics using different densities for seawater, and then establish which best matches the shallow marine field data at different source-receiver offsets. The use of an offset-variable density in the water layer has led to an improved match between the field and predicted data. Using this scheme, an even-higher-resolution FWI velocity model is recovered, and this model leads to an improvement in the migrated seismic image.

Previous Research

The field dataset used for our study is from a field in the Norwegian North Sea, where there are two fractured, hydrocarbon-charged reservoirs at about 3 km depth within a broad anticline of the Cretaceous chalk. The presence of gas at depths of approximately 1-2 km in the overlying clastic section inhibits p-wave reflection imaging and results in a seismically obscured reservoir section (Granli *et al*. 1999). A high-density, full-azimuth, 3D, 4-component, ocean-bottom-cable survey was acquired to help improve the images of the reservoir beneath the gas cloud. The dataset comprises three swaths of eight parallel cables, each 6 km in length, with 96,000 sources and 5760 receivers (Warner *et al*. 2013). The receiver cable separation was 300 m and receivers were spaced every 25 m along the cable in the inline direction. Air gun sources were fired using a flip-flop shooting pattern that was orthogonal to the cables, with a 75-m cross line and 25-m inline separation. These hydrophone data have good azimuthal coverage for offsets of up to 7 km, and reduced coverage to a maximum offset of 11 km. The early arriving data at each receiver are dominated by wide-angle turning rays and sea-bottom multiples (due to the shallow water depth of 75 m), and post-critical reflections and their multiples at larger offsets. The presence of strong refractions, as well as the large offsets and good azimuthal coverage, make this dataset particularly favorable for FWI.

Data pre-processing included a top mute ahead of the first arrivals, deletion of bad traces, low-pass filtering of the data to the required frequency range for FWI, a bottom mute that was designed primarily to remove Scholte waves, and decimation of the dataset such that three in four receivers have been removed (Warner *et al*. 2013). With every third source and fourth receiver, the data subset contained a total of 1440 receivers with a spacing of 100 m in the inline direction and 300 m in the crossline direction; and approximately 30,000 shots (about 10,000 per receiver) with a spacing of 75 m in both directions. Additionally, the time sampling was reduced to 4 ms, and only 8.4 s of data was used. The sources and receivers were not spatially aliased at the frequency range for FWI, with the Nyquist frequencies being 7.5 and 10 Hz, computed using the water velocity and the shot and receiver spacing in the inline directions. The data were trace-equalised so that the inversion fits relative amplitudes within a single trace, rather than between traces. Bad (noisy) shots and receivers were removed, and the principle of reciprocity was applied to swap sources and receivers thereby reducing the total number of effective sources modelled, as the inversion algorithm is more

computationally-efficient, working best with a small number of sources and large number of receivers. Figure 4-2 summarises the pre-processing steps applied to the dataset.

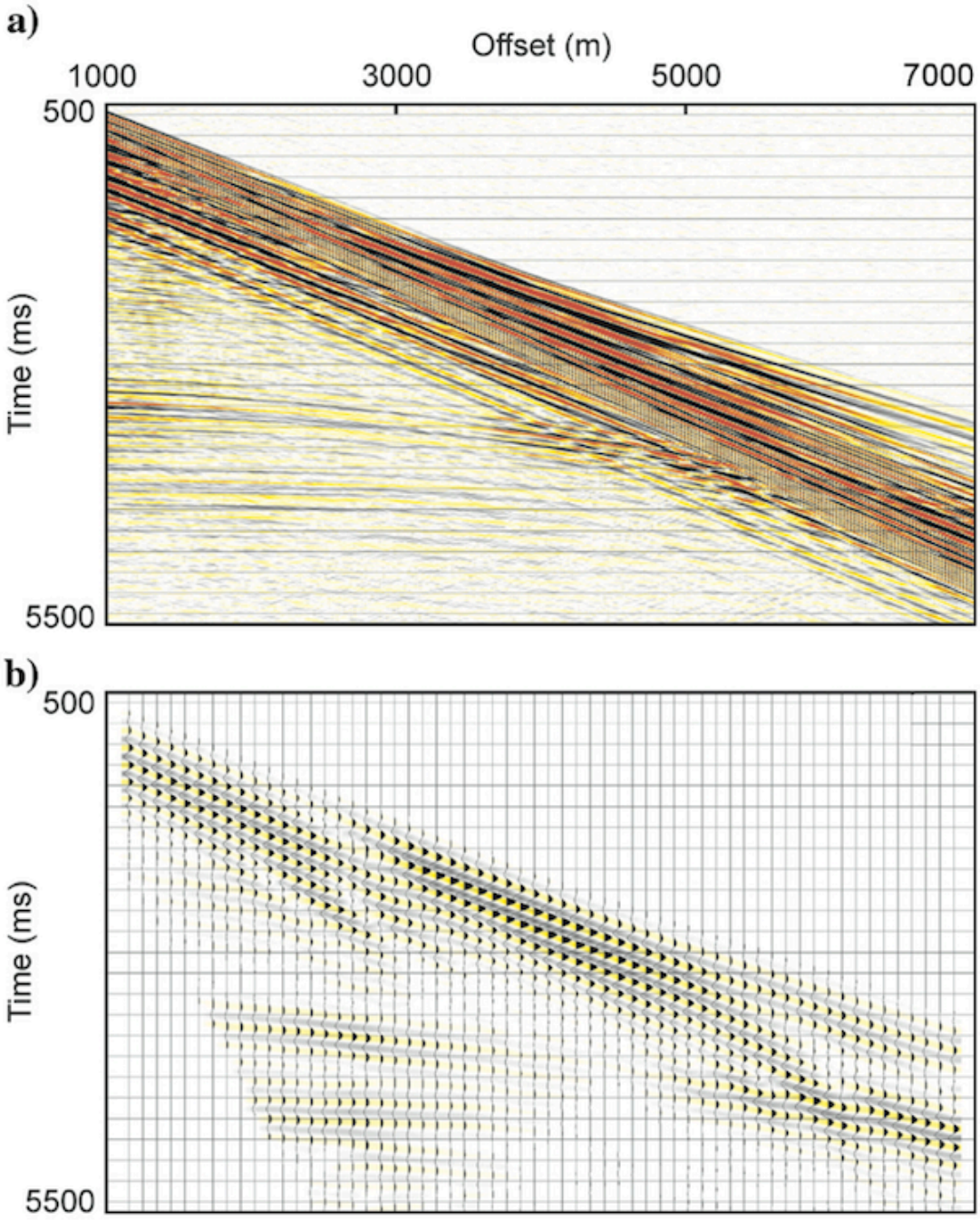


Figure 4-2: (a) Raw shot record, trace equalized with no gain recovery (b) The same record preprocessed immediately prior to FWI – data was low-pass filtered decimated and muted as described above. (Source: Warner *et al.* 2013).

The lowest useable starting frequency for FWI of 3Hz, was strategically selected through the identification of coherent signal on a common receiver gather phase plot (Figure 4-3) (Shah *et al*. 2014). The signal-to-noise ratio, rather than the amplitude at the lowest inversion frequency, is an important element of our FWI scheme (Warner *et al*. 2013). With the velocity in the water being 1480 m/s and the velocity in the gas sediments as indicated by well data being ~1500 m/s, the maximum useable frequency is ~ 5.9 - 7.4 Hz with the selected 50m grid spacing. FWI was thus performed for a frequency range with the maximum frequency being lower than 7.4Hz.

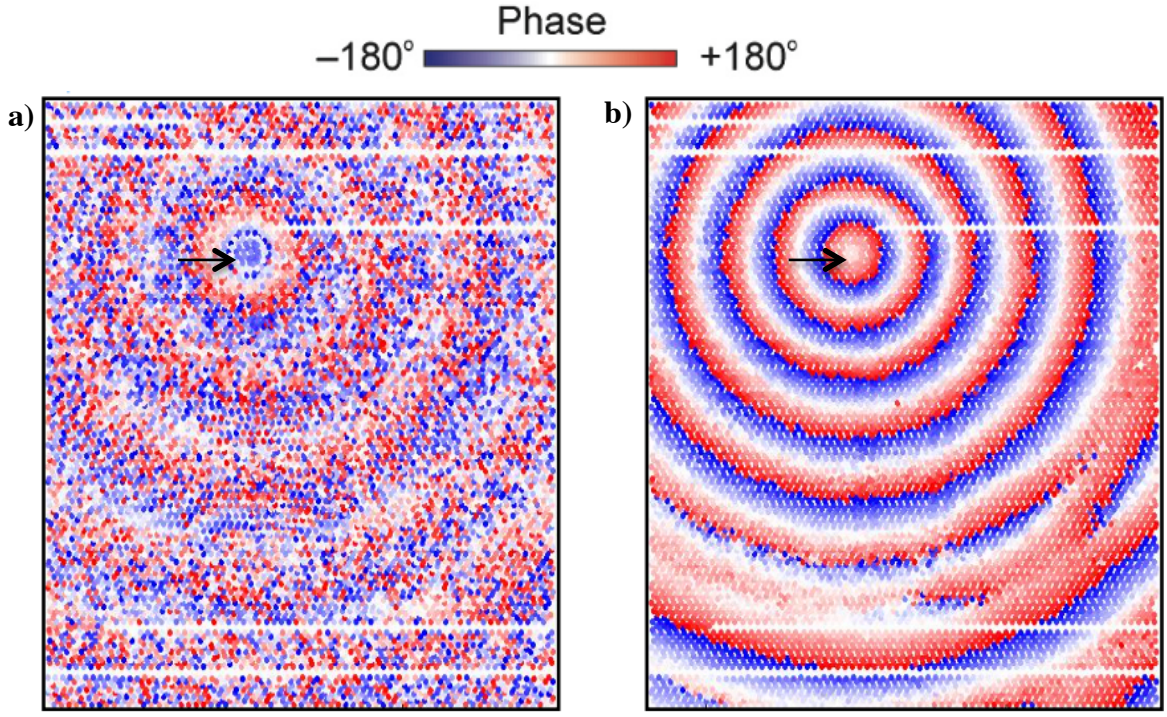


Figure 4-3: Observed data phase for a common receiver gather (location indicated by black arrow) at a) 2Hz and b) 3Hz. A Gaussian time window has been applied to the data when extracting the phase thereby focusing on the early arrivals for this phase analysis. It was derived that the 3 Hz phase is far more spatially coherent than the 2 Hz phase and was henceforth chosen as the lowest useable frequency for FWI (modified from Shah *et al*. 2014)

3D anisotropic FWI was undertaken with the aim of improving the imaging beneath the seismically obscured region, thereby allowing for better interpretation of the underlying chalk reservoirs (Ratcliffe *et al*. 2011; Nangoo *et al*. 2012; Warner *et al*. 2013). An anisotropic starting model that was originally generated for PSDM by the original processing contractor, using a combination of techniques: migration, well velocities and travel-time tomography.

The low wavenumber initial velocity model was sufficiently accurate, such that it predicts the travel time to within half a period of the dominant wavelength at the lowest inversion frequency, avoiding cycle-skipping and assuring convergence to the global minimum (Figure 4-4).

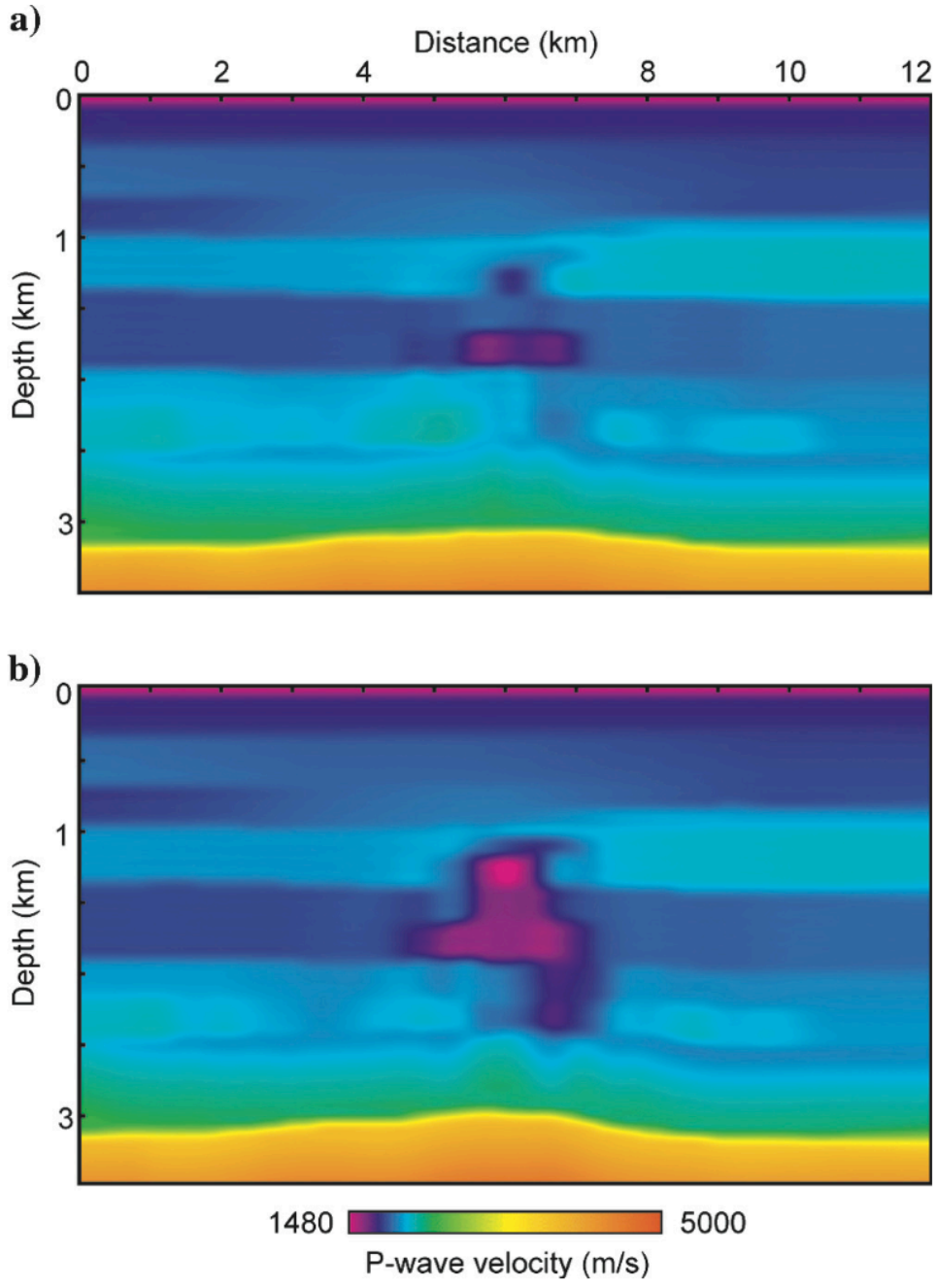


Figure 4-4: Vertical slices through the starting velocity model: (a) through the periphery of the gas cloud, and (b) through the central portion of the gas cloud (source: Warner *et al.* 2013).

A vertical transverse isotropic (VTI) model, whereby the intrinsically different horizontal and vertical velocities are related by Thomsen's anisotropic parameters delta (δ) and epsilon (ε), was used (Warner *et al* 2013). Due to limited lateral variations in these models, a one-dimensional profile was used for the inversions (Figure 4-5).

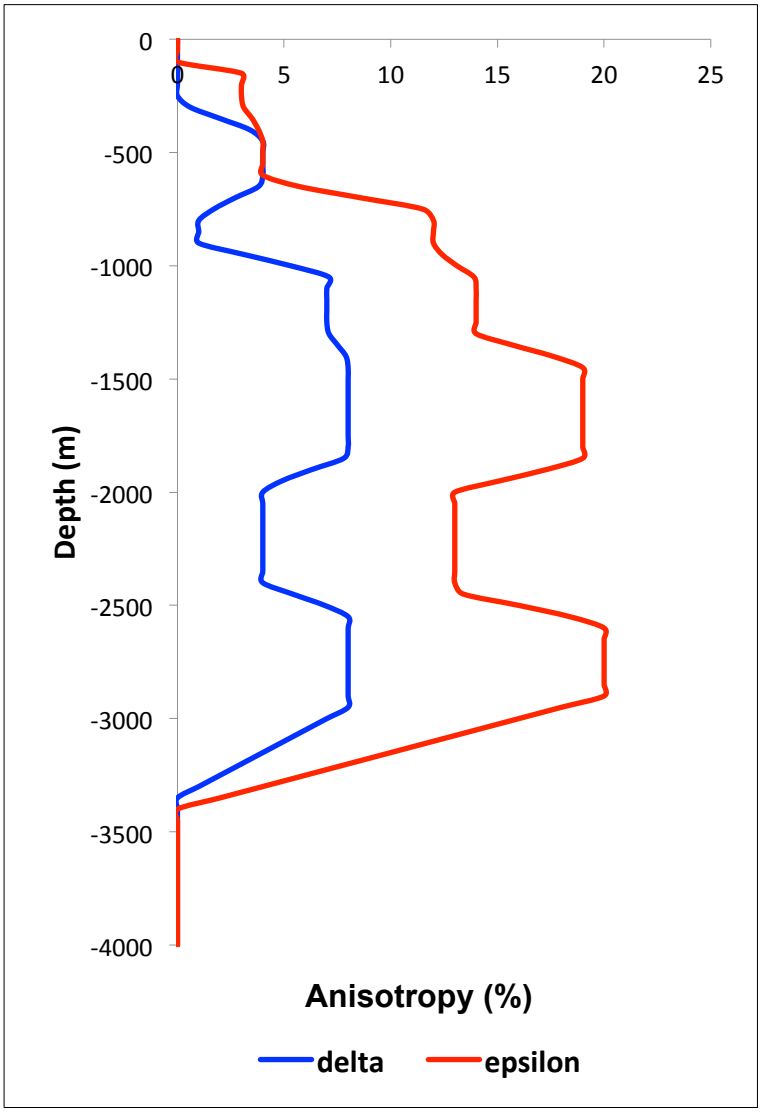


Figure 4-5: Plot of the one-dimensional anisotropy models of delta and epsilon used in all our FWI runs, with a vertical axis of symmetry. These are kept fixed and were originally generated for PSDM by CGG - the processing contractor.

Delta values ranged from 2 to 8%, and epsilon values ranged from 10%, to 20% with a total depth of 4km. Although the inversion only updates the velocity keeping the anisotropy fixed,

the latter is accounted for during the modelling steps. Like anisotropy, the inversion does not invert for density. A deterministic relationship between velocity and density was used.

The gas cloud region lies close to the center of the survey; there are four wells within the survey area that either penetrate the gas cloud or are located on its periphery. 3D acoustic, anisotropic FWI was thus performed using a multiscale approach, for a frequency range of 3.0-6.5 Hz incrementing linearly for six frequency bands to recover a high-resolution velocity model. The acoustic finite-difference algorithm that honours TTI, does not account for attenuation and elastic effects but have been proven to be sufficient in recovering high-resolution FWI velocity models (Warner *et al*. 2013).

With FWI, the recovered velocity model better matches the well logs, improves the flattening of common image gathers, and improves the PSDM image. Thus, acoustic 3D FWI improved the velocity characterisation of the thin, shallow gas-charged layers as well as the imaging beneath the seismic obscured area. However, the systematic mismatch between the observed and modelled data remains.

Mismatch

Time-domain traces

While there are many effects that can lead to a systematic mismatch in time between an observed and a modelled dataset, the vast majority of these are not able to explain such a mismatch when it arises as the final result of full-waveform inversion. This is because FWI is designed specifically to alter the Earth model in order to minimize such a data mismatch, and in almost all reasonable circumstances, it does indeed achieve that. FWI will deal with any systematic mismatch in time, whatever its cause, by simply changing the velocity model to improve the data fit. Consequently, it is difficult for any such simple mechanism to explain the effects that are seen in this study. Although small, the modelled data remains systematically late by 12 ms relative to the observed data after FWI. The comparison of the observed and modelled time-domain traces illustrated in Figure 4-6 clearly shows this mismatch.

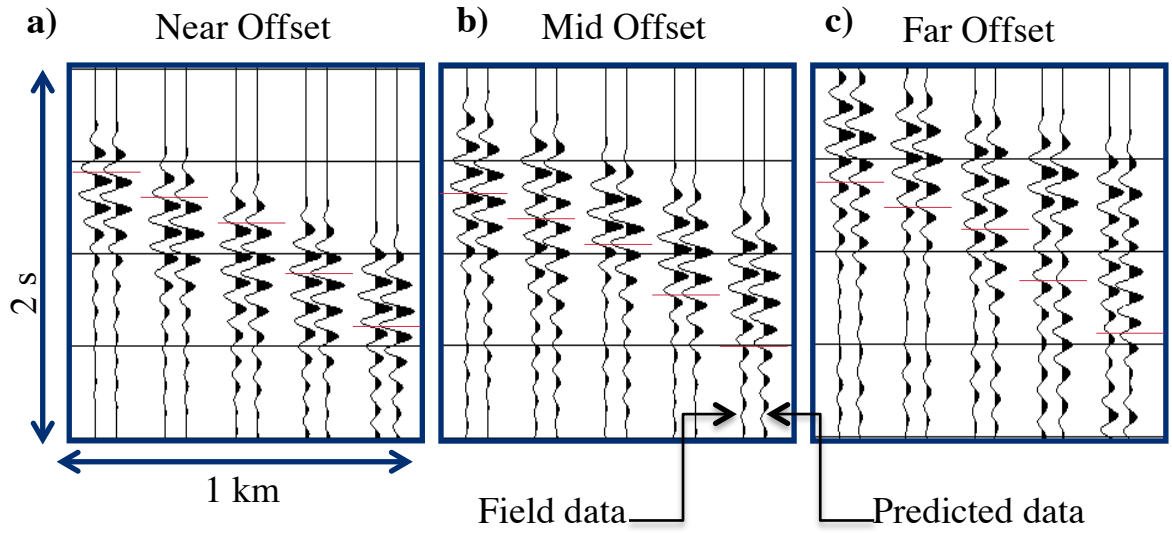


Figure 4-6: Enlarged view of Figure 4-1 at: a) near, b) mid and c) far offset locations comparing the field and predicted data time domain traces illustrating the systematic mismatch.

Phase Residuals

Phase residual plots are useful in illustrating the mismatch at every shot location. These residual phase plots for all shots at each receiver generally have greater coherency than correlation plots. The residual phase in Figure 4-7 below is the phase difference between the observed phase and predicted phase using the starting model on the left and FWI recovered model on the right. These plots were generated using a Matlab code whereby the modelled data for a single receiver and all the corresponding shots is firstly time-weighted to focus on the early arrivals. Subsequently, the phase is extracted and residual plots between the observed and modelled data are generated (Figure 4-7). When the phase skips 180 degrees (red to blue), this indicates regions of cycle-skipping – evident near bottom left edges of starting model phase residual. The phase residual plot for the FWI model is mostly pink, which means that the predicted data are mostly late for all shots at this receiver location (Figure 4-7). The predicted data is approximately 30 degrees out-of-phase as indicated in the phase residual plot, equivalent to ~12ms in the time-domain. Thus, a mismatch is apparent.

These phase residual plots are important tools in identifying cases of cycle-skipping – instances of significant mismatch between observed and predicted data – generally for the starting model and the very early iterations of FWI. For the late iterations, after FWI, the changes in phase are quite minor and sometimes not easily distinguishable. As such for

comparison purposes for later tests involving the latter iterations, the time-domain traces give a vivid comparison and these are easily understood by most in the field of geophysics.

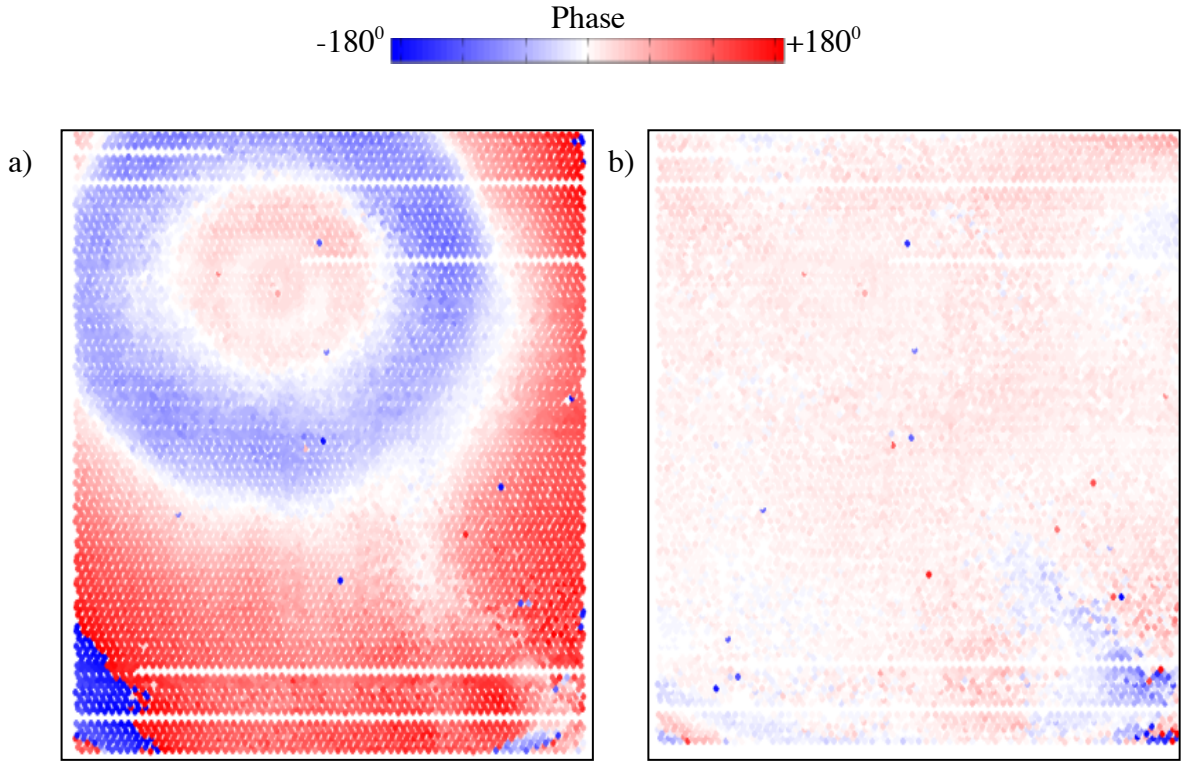


Figure 4-7: Phase residual plots for a) the starting model and b) the original FWI recovered model.

Tests to improve mismatch

In view of the unexplained mismatch, a suite of tests was conducted to verify whether the misfit can be removed by making adjustments to the source, increasing the number of iterations, perturbing the starting velocity model or changing the finite difference grid spacing.

Varying the source wavelet

The accuracy of the source wavelet is important for FWI particularly at the lowest frequencies (Lua *et al*. 2007; Warner *et al*. 2012). During our original inversion, an initial attempt to use the wavelet supplied by the acquisition contractor was made. This however leads to a poor match between the observed and predicted first arrivals at short offsets at the lowest frequencies (Warner *et al*. 2013). This is unsurprising since the simulations used to

generate these wavelets are of only short duration, are designed to produce a good match at higher frequencies only, and do not attempt to model the bubble correctly; consequently, they provide only a poor representation of the true source at the very low frequencies used to begin FWI. Consequently, the source wavelet was instead obtained from the direct arrivals recorded on short-offset ocean-bottom hydrophones acquired in deeper water depths due to the absence of the ghosts even though the dataset is shallow marine. All traces with offsets less than 25 m were selected; quality controlled thereby removing anomalous traces; and finally shifted and stacked with the start time at zero. From these, the source ghost and the first and second seafloor multiples was then removed, correctly taking into account the finite offset and the effects of divergence, and applying a low-pass Ormsby filter rolling off from 5.0 to 7.5 Hz as shown in Figure 4-8 (Warner *et al*. 2010). The ghost and sea-bottom multiples are re-generated with the forward modelling of the wavefield during FWI through the use of a free surface boundary condition. This approach provides an extremely accurate match to the field data at short offset prior to inversion.

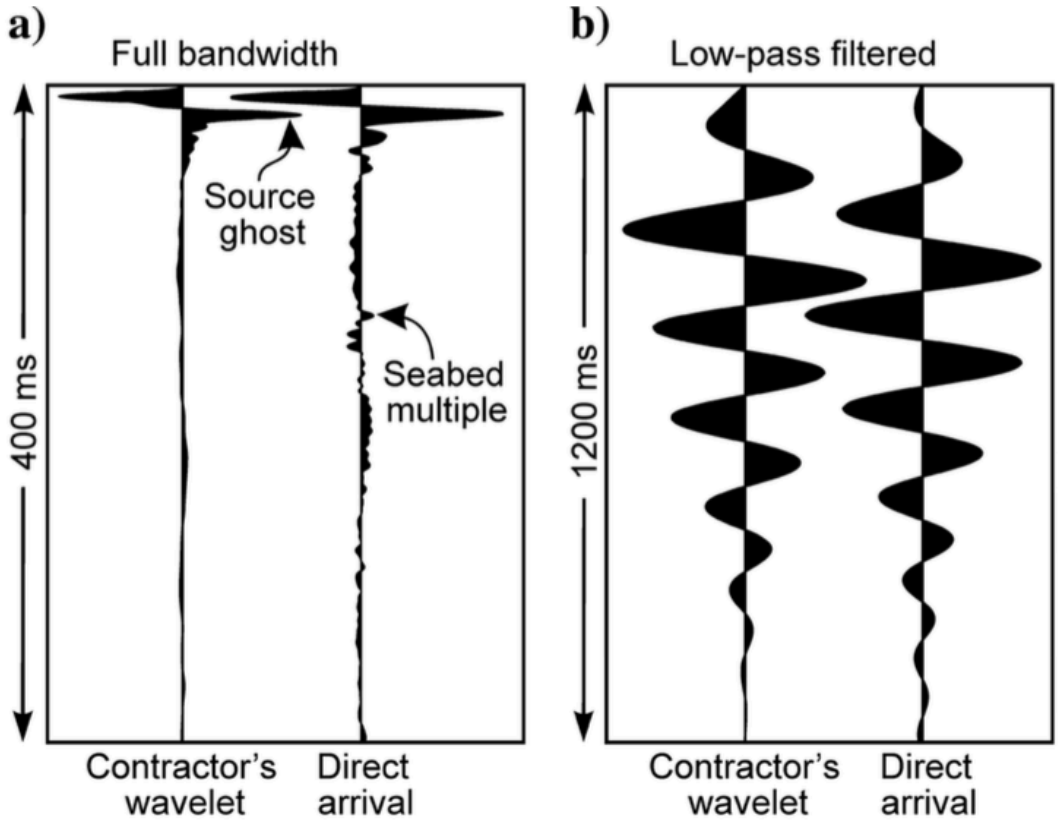


Figure 4-8: Source signatures (a) Full-bandwidth waveforms. (b) Low-pass filtered waveforms at different scale (Source: Warner *et al.* 2013)

If followed with direct source inversion in an attempt to improve the match further, minimal additional changes to the source wavelet occur, and critically such an inverted wavelet does not contain any systematic time shift that would serve to compensate the effect seeking to be explained.

Since the predicted data arrive late, a potential cause is that the source is delayed at the frequencies used for the inversion. To investigate this, the source wavelet was advanced in time and the inversion repeated. If the apparent time delay was a function of source timing errors, then this test would tend to remove, or at the very least tend to change, the apparent time delay. However the final inverted model was almost indistinguishable from that originally recovered, and critically, it was discerned that the delay in the predicted data remained (Figure 4-9). From this, and a suite of similar tests on source timing and source inversion, it was concluded that errors in the source cannot explain the mismatch – such errors may produce errors in the velocity model, but cannot prevent FWI from bringing the observed and predicted data into close temporal alignment.

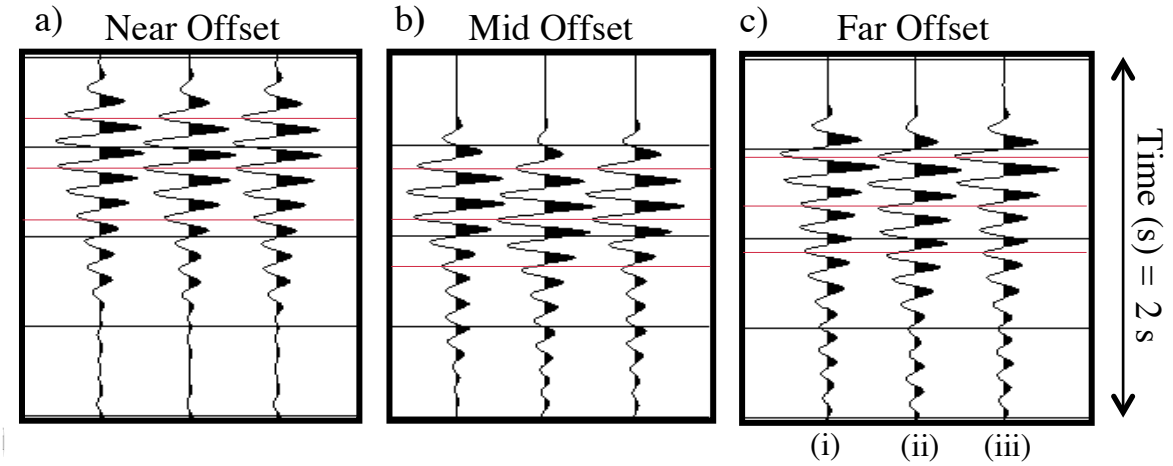


Figure 4-9: Comparison between (i) field data, (ii) predicted data obtained for the FWI-recovered model obtained when using the original source wavelet, and (iii) predicted data obtained from FWI when using a wavelet that has been advanced in time. (a) Near, (b) mid, and (c) far offsets are shown. The delay largely remains, demonstrating that incorrect source timing does not cause the mismatch.

Increasing the number of iterations

FWI is a local optimisation scheme whereby the misfit function is minimised so that the difference between the observed and predicted data gradually reduces towards zero. Thus it is possible that the inversion has not yet converged to the global minimum model, and that the travel-time mismatch might continue to reduce with continued iteration. Hence, doubling the number of iterations in each frequency band may thereby yield a final model after 216 iterations for the inversion. However, no further improvement was observed in the travel-time mismatch, and the delay remained (Figure 4-10). Also, substantially the same result is obtained with re-inversion from the final model, re-starting from low to high frequency.

Perturbing the velocity model

A poor initial starting model may result in incomplete global convergence, with the inversion converging to a local minimum. As the predicted data were systematically late, the final velocity model was perturbed, increasing the velocity model everywhere by 1%, such that the predicted data were initially systematically early in time with respect to the field data. If the observed mismatch is caused by a systematic error in the starting model, then perturbing the velocity model in this fashion and then re-running the inversion should lead to either a better final travel-time fit or a mismatch of the opposite sense – such that the predicted data would then be systematically early instead of late. However, as with all our tests, the model velocities were reduced by FWI to their original lower values, and the final predicted data were returned to their original delayed state (Figure 4-10).

This result is particularly revealing. It demonstrates that the best fitting model is indeed the one that produces data that appear to be systematically late since forcing the predicted data initially to be early, still leads to a final outcome that is late. Thus, the final FWI model recovered by both strategies results in a data match whereby convergence is complete. Whether an increase in the number of iterations or the perturbation of the model, the end results are the same in both velocity and residual – the delay in the predicted data remains.

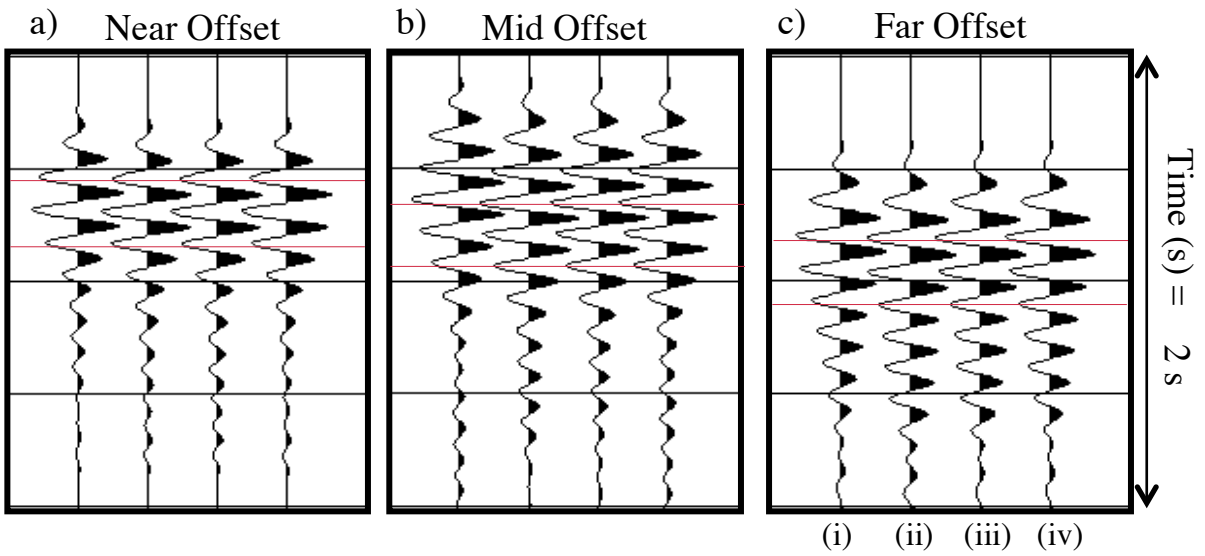


Figure 4-10: Comparison between (i) field data, predicted data obtained from the recovered FWI model (ii) after 108 iterations, (iii) after 216 iterations, and (iv) after 108 iterations, perturbation by +1% followed by a further 108 iterations. (a) Near, (b) mid, and (c) far offsets are shown. It was discerned that the delay remains in each case illustrating that the mismatch is not caused by incomplete convergence, or by a systematic bias in the starting model as convergence has perhaps reached a plateau.

Changing the finite difference grid spacing

In this study, a finite-difference scheme is used for the forward modelling that employed a 50-m mesh size. In this survey, the water depth is about 75 m. In finite-difference modelling schemes, the water bottom is not defined explicitly in the model. Rather it is defined implicitly, in this case with the velocity at 50m being that of water, and the velocity at 100m being that of the sub-seabed. Given the coarse mesh and shallow water, it is possible that the travel-time mismatch could be caused by an inaccurate representation of the sea-bottom boundary. This was investigated using a range of different mesh sizes, from 50 to 15 m, generating predicted data for each one, and comparing their accuracy. It was realised that, regardless of the mesh size, the timing of the predicted data remained unchanged – an example of this with a 20 m mesh size is shown in Figure 4-11. It was also noted, that even if a modelling scheme or representation of a sharp boundary is inaccurate, this will lead FWI to change the velocity model in order to improve the data fit. This means that the resultant velocity model recovered by the inversion could be wrong, but the resultant synthetic data would still provide a good match to the observed data – it is this match that drives FWI, and

it is this mismatch that FWI always seeks to minimise. FWI will minimise the data mismatch whether or not it is caused by the velocity model, by numerical inadequacies in the model scheme, or by inadequacies in the source wavelet. The fact that the apparent timing mismatch is robust throughout all these tests carries the message that something subtler is happening here.

Test deductions

The obvious potential simple explanations for the temporal mismatch observed are not correct. Further, analogous systematic delays in the predicted data is not observed when inverting data from synthetic velocity examples, whether or not the original data were generated with a different source or on a different mesh size. As such, the mismatch is presumed to be likely due to physical effects that are not properly accounted for when inverting field data. One possibility is that this mismatch is attributable to the shallow portion of the model, and especially to the multiple-generating properties of the seabed.

The seabed is a significant boundary because there is a large difference in acoustic impedance between water and rock, and p-wave reflectivity and transmission amplitudes are strongly affected by conversions to transmitted s-waves and by an unknown density contrast at the seabed. However, without being able to populate models of near-surface density, attenuation, anisotropy and elastic properties, the seabed reflectivity, and especially improper modelling of its variation with angle and frequency, we will not have the data required to model or to invert for these properties convincingly. Thus, the mismatch observed may indeed be caused by an inadequate representation of the shallow part of the model.

In an acoustic inversion, FWI will attempt to match the travel-times of the early arriving wavefield (a function of the water velocity and depth, and sub-seafloor velocity) and of the water-bottom multiples (a function of the water velocity, water depth and impedance contrast at the sea-bed). In an attempt to improve the match between the observed and predicted data, the possibility of using non-physical values for water density is explored, since density is the simplest parameter that can freely change to alter amplitudes without introducing kinematic errors. This use of non-physical density values thereby accounts for possible seabed amplitude-variations with offset as well as elastic and other physical effects associated with

the seabed interface, which led to the mismatch. Adopting this strategy to remove these effects from the data, can lead to a more accurate p-wave velocity model.

Possible physical effects

Elastic effects

The computationally feasible and efficient, acoustic, anisotropic FWI technique was performed on this 3D dataset. Therefore, the visco-elastic nature of the earth, which needs to be considered to extract fully quantitative models of the subsurface, was not fully accounted for with an acoustic approximation, facilitating a quicker forward modelling process. Elastic effects from this 3D shallow-water, field dataset are thus evident, with the strongest elastic effects being generated near the seabed. Superposition of the acoustic P-waves and surface, evanescent waves, which fade away rapidly with distance from a boundary, may have lead to the aforementioned (approximately 12ms) mismatch, between the field data and the FWI-modelled data. An elastic inversion to test this theory, thereby exactly attributing these physical elastic effects to the mismatch, was not undertaken. Addressing elastic effects on acoustic FWI, through elastic inversion tests, is an entire PhD subject currently being undertaken by a colleague. Nonetheless, a strategy has been developed here, to remove these possible physical effects leading to a more accurate velocity model.

Amplitude-variations with offset (AVO)

Acoustic approximations lead to incorrect modelling of the amplitudes of the seismic waves, especially with respect to amplitude variation with offset (AVO), and therefore have a direct impact on the inversion results. The acoustic approximation holds for the kinematics but not for the wave amplitudes, except for compressional waves having a normal incidence or a small incidence angle (Barnes and Charara, 2009). As such, incorrectly accounting for this physical effect, the variations in amplitude of the different seabed-related arrivals arriving at different times may have lead to the aforementioned (approximately 12ms) mismatch. Adopting a strategy involving the use of use of a non-physical water density to address this issue will now be discussed.

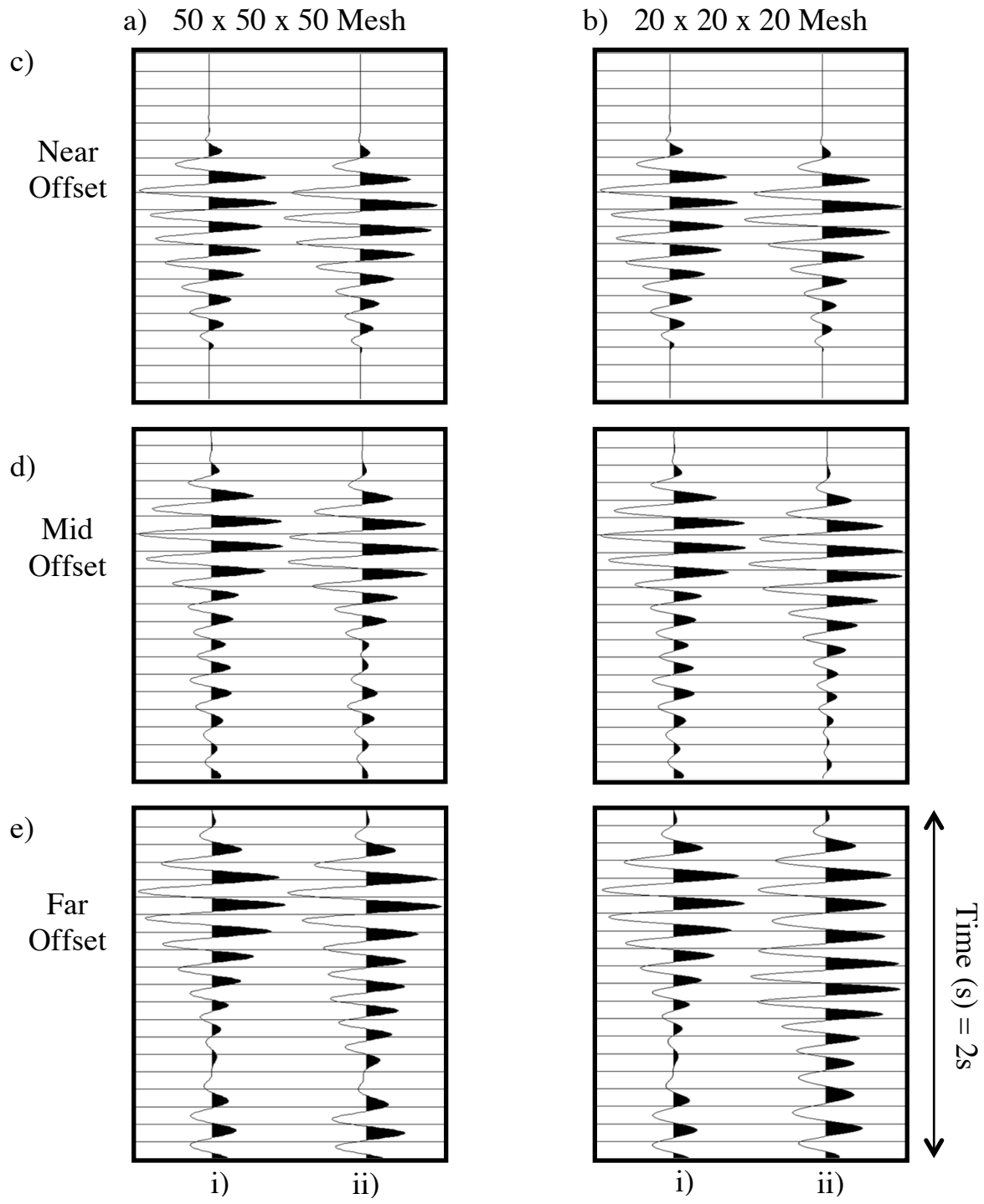


Figure 4-11: Comparison between (i) observed and (ii) predicted data for different finite difference meshes of a) 50 m, and b) 20 m, at c) near, d) mid, and e) far offset. It was discerned that the delay remains in each case illustrating that the mismatch is not caused by improper representation of key reflective/elastic horizons e.g. seabed boundary, on the finite difference mesh.

Use of non-physical water density

A heuristic investigation, to determine the effect of different water densities on the arriving wavefield is executed. Data were generated using the original, recovered FWI velocity model (after 108 iterations) but with a variety of non-physical densities in the water layer. The use of non-physical water-densities changes the apparent travel times (Figure 4-12) because the early arriving wavefield is in reality an interference pattern between refracted and sea-bottom multiple arrivals. Changing the density of the water layer alters the relative strength of the water-bottom multiples, and thus changes the positions of individual peaks and troughs within the extended wave train. This in turn changes apparent arrival times. The predicted and field data can be compared to determine which densities provide the best match. Figure 4-12 shows that, at short offsets, a better match is produced using a water density of about 500 kg m^{-3}, whilst at longer offsets, a better apparent travel-time match is obtained using a density of about 250 kg m^{-3}.

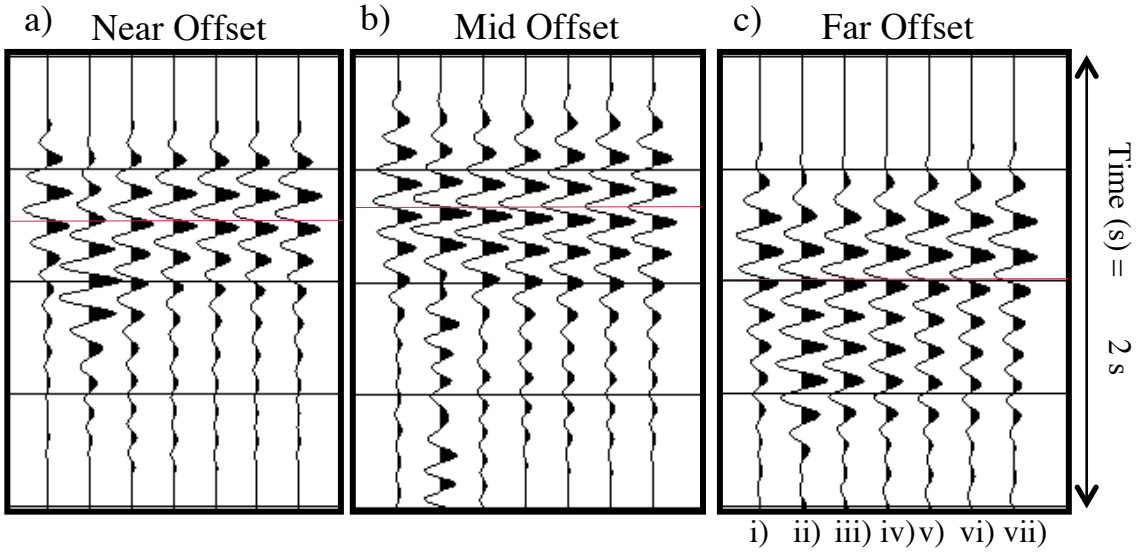


Figure 4-12: Comparison between (i) field data, (ii) predicted data obtained using the original recovered FWI model water densities of 250 kg m^{-3}, (iii) 500 kg m^{-3}, (iv) 750 kg m^{-3}, (v) 1000 kg m^{-3}, (vi) 1250 kg m^{-3}, and (vii) 1500 kg m^{-3}. (a) Near, (b) mid, and (c) far offsets are shown. These non-physical water densities change the reflectivity of the seabed and the amplitude of water-bottom multiples, thereby changing the interference pattern of different arrivals resulting in an apparent change in travel time. A better match is obtained with a density of 500 kg m^{-3} at near offset and 250 kg m^{-3} at far offsets.

A quantitative representation of this is shown in Figure 4-13. The normalised cross-correlation between the field and forward-model synthetics for different water densities show time lags ranging between 5 and 12ms (Figure 4-13 a and c). Furthermore, the relationship between density and maximum correlation lag (Figure 4-13 b and d) emphasizes that at a density of ~500 kg m^{-3} for near offsets and ~250 kg m^{-3} for far offsets, there is a near-perfect match between the two datasets corresponding to a time lag of zero. This suggests that an offset-variable model of water density should be able to remove the systematic mismatch obtained in the original inversions.

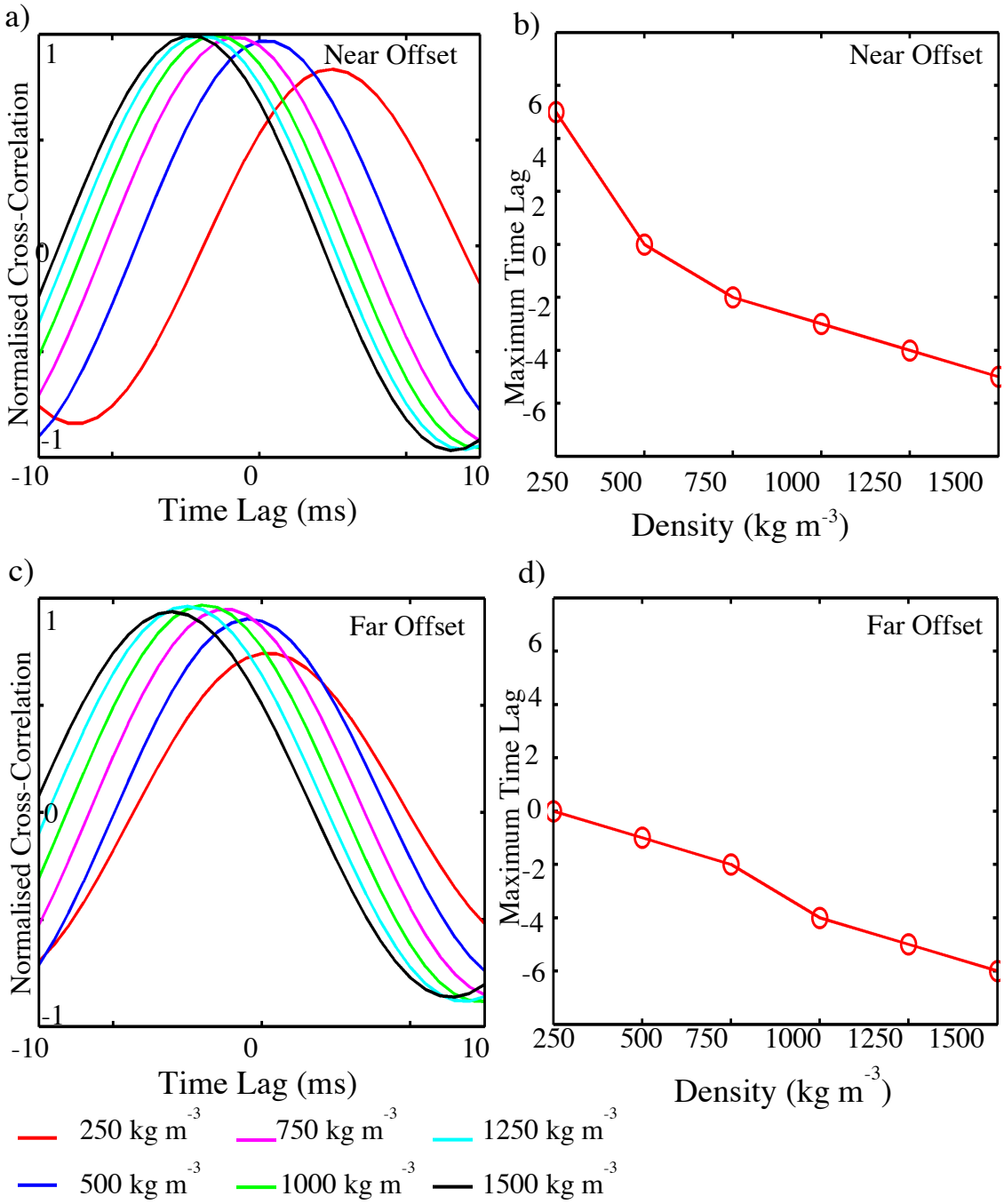


Figure 4-13: Normalized cross-correlation between the observed and predicted data and the corresponding maximum correlation time lag for different water densities at (a), (b) near and (c), (d) far offsets. Time lags range between 5 and 12ms with zero lag corresponding to a good data match. A linearly decreasing water density from b) near to d) far offset results in a time lag close to zero, implying a good match between field and predicted data.

Implementation

The inversions are computed source by source, that is, the wavefield is calculated for one source at a time. Consequently it is feasible to simulate an offset-dependent density in the water layer during the forward calculation; the water-density model for every source position is different, and this density is a function of distance from the source. The specific values for density were fixed by the non-physical density tests (Figure 4-12 and Figure 4-13); at zero offset the density was set to 500 kg m^{-3}, and this was reduced to 250 kg m^{-3} at the largest offsets. The zero-offset density is initially kept constant and then, at a specified offset, is decreased linearly until it reaches the far-offset density at a specified distance from the source. Given the consistency of the shot records across the dataset, a variation of offset-dependent water-density with shot location has not been applied here. Offset is principally being used as a proxy for incident angle at the seabed. It might be beneficial, however, to allow offset-dependent water density to vary with shot location in datasets where the near-surface is less laterally homogenous. Note that, during the inversion, each source is modelled independently of all the others so that it is straightforward to use a different density model for each shot.

This change in water density with increasing offset appears to be able to reproduce the change in amplitudes of the sea-bottom multiples for different sea-bed reflection angles that occur in the field data but that do not occur in pure acoustic modelling. When the model velocity values are above that of water velocity, the density model is populated in the normal way, following Gardner's law (Gardner *et al*. 1974), proven to be a sufficient approximation regardless of the geological environment, in many FWI applications (Borisov *et al*. 2014). Using this scheme, the inversion was run again using the original parameterisation and inversion strategies.

Results

Figure 4-14 and Figure 4-15 show horizontal and vertical slices through the a) starting velocity model, b) original velocity model recovered using FWI (from Warner *et al*. 2013), and c) the new velocity model recovered using FWI with an offset-variable density scheme. In these slices the new velocity model is sharper, has stronger negative velocity anomalies within the gas cloud, and appears to resolve better the faults leading away from the gas cloud.

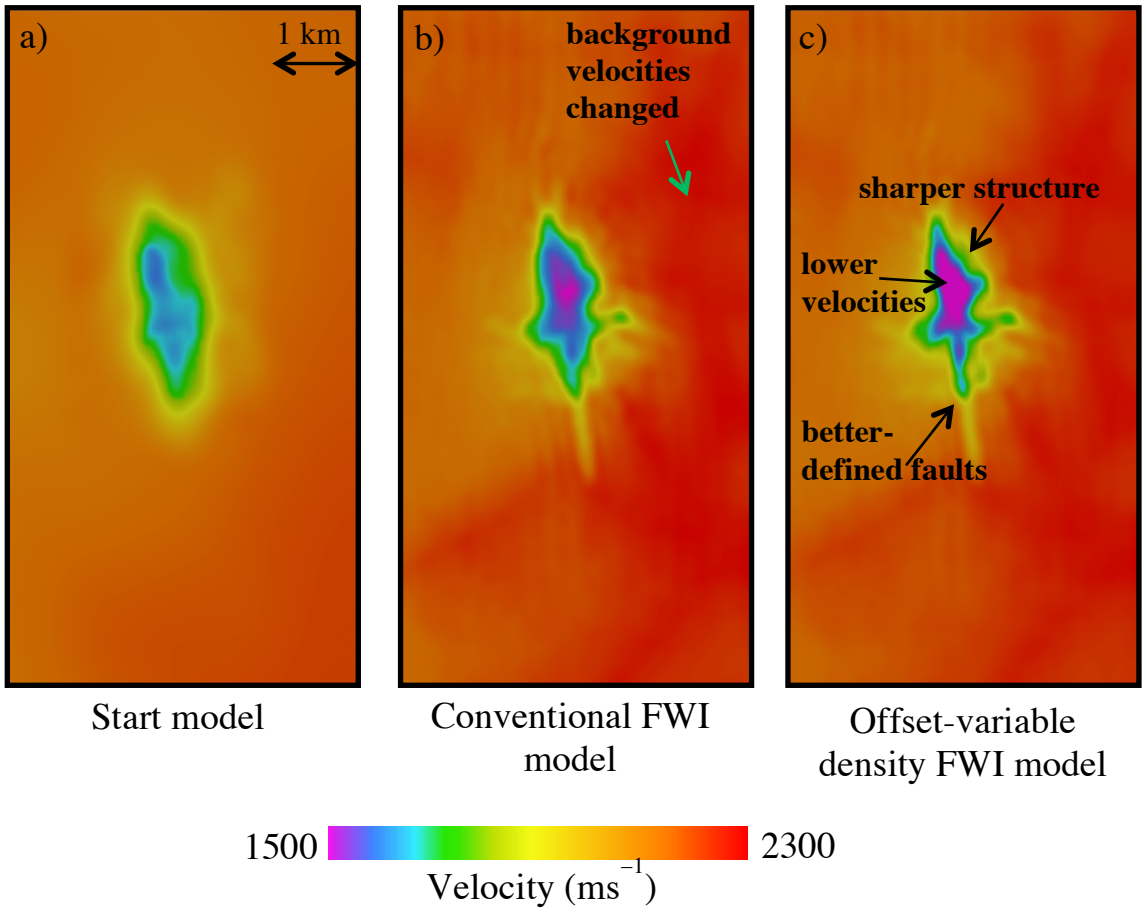


Figure 4-14: Horizontal slices at 1200 m depth through: a) the starting velocity model b) original FWI recovered model and c) FWI recovered model using an offset-variable water density. The model shown in (c) suggests improved definition of the gas-cloud and of gas-charged faults within the offset-variable model.

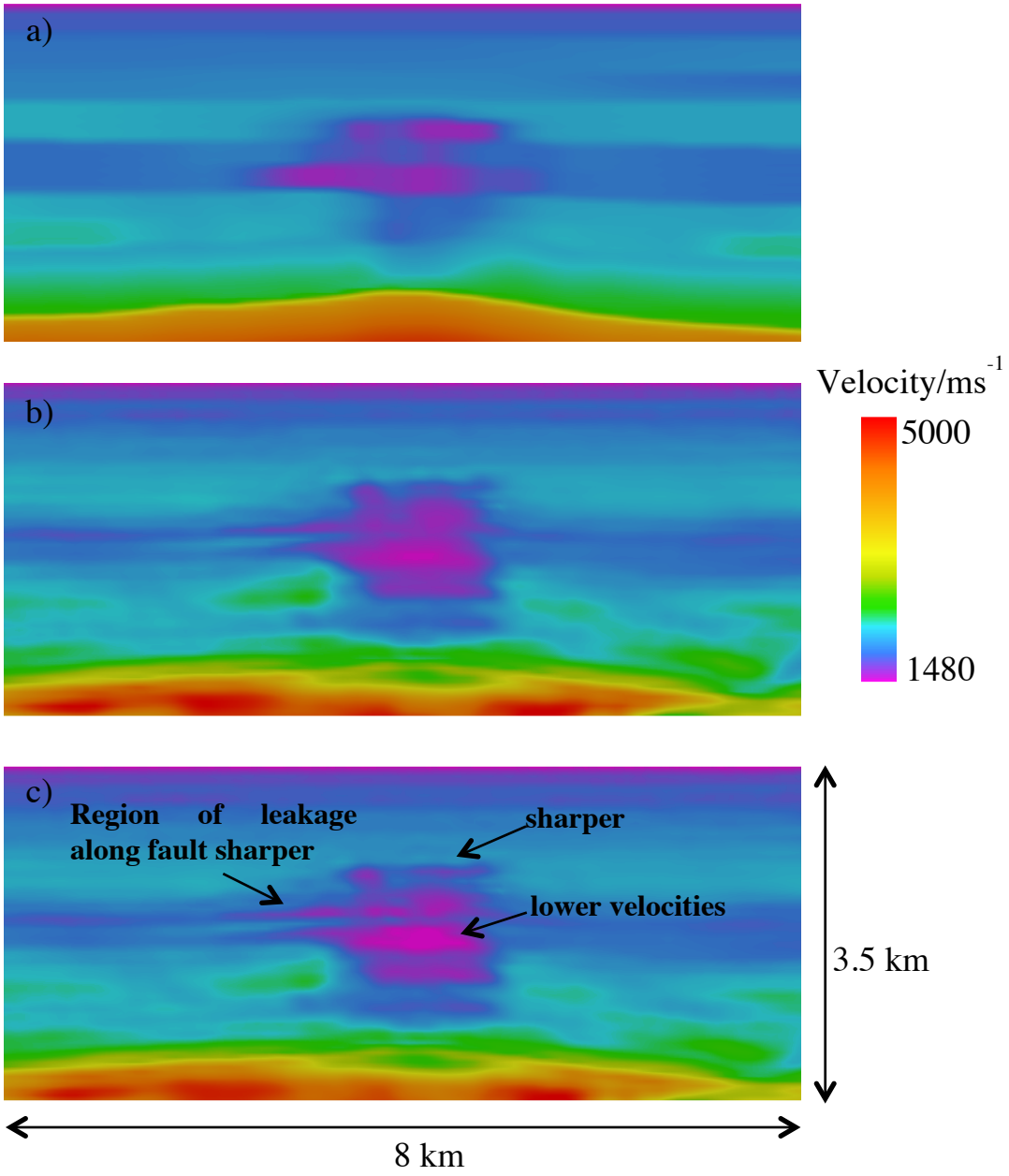


Figure 4-15: Vertical depth slices through: a) Starting model b) Conventional FWI model c) Offset-variable water-density FWI model

Well Ties

The vertical pseudo wells through the original and offset-variable FWI models as compared to the well log profile for this field confirms that the offset-variable density scheme does in fact improve the model resolution and fidelity (Figure 4-16), but this effect is small in the deeper parts of the model.

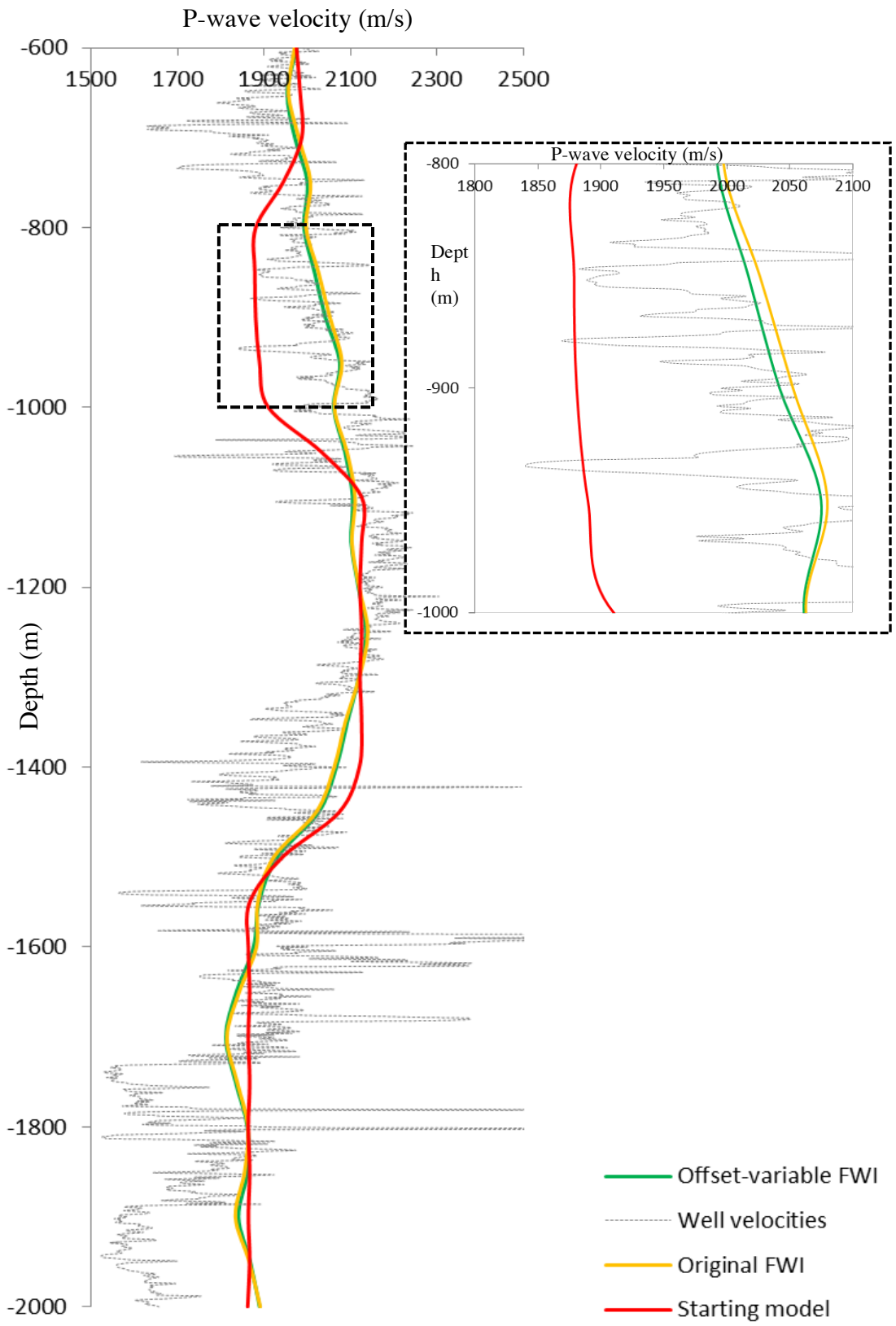


Figure 4-16: Well log comparison to vertical pseudo profiles from the starting model, original FWI recovered model and the offset-variable density FWI model

Forward Synthetics

Synthetics were generated to investigate whether the velocity model generated using the offset-variable density scheme had addressed the systematic travel-time mismatch. Figure 4-17 shows a comparison between the synthetics generated by both the original and offset-variable FWI models and the field data. The systematic mismatch evident with the synthetic obtained using original FWI is less evident in the offset-variable FWI synthetic. The wave train remains similar in amplitude and phase, and the delay is now reduced. The visible improvement in the match between the field and predicted data (Figure 4-17) is confirmed by a reduction in the objective function.

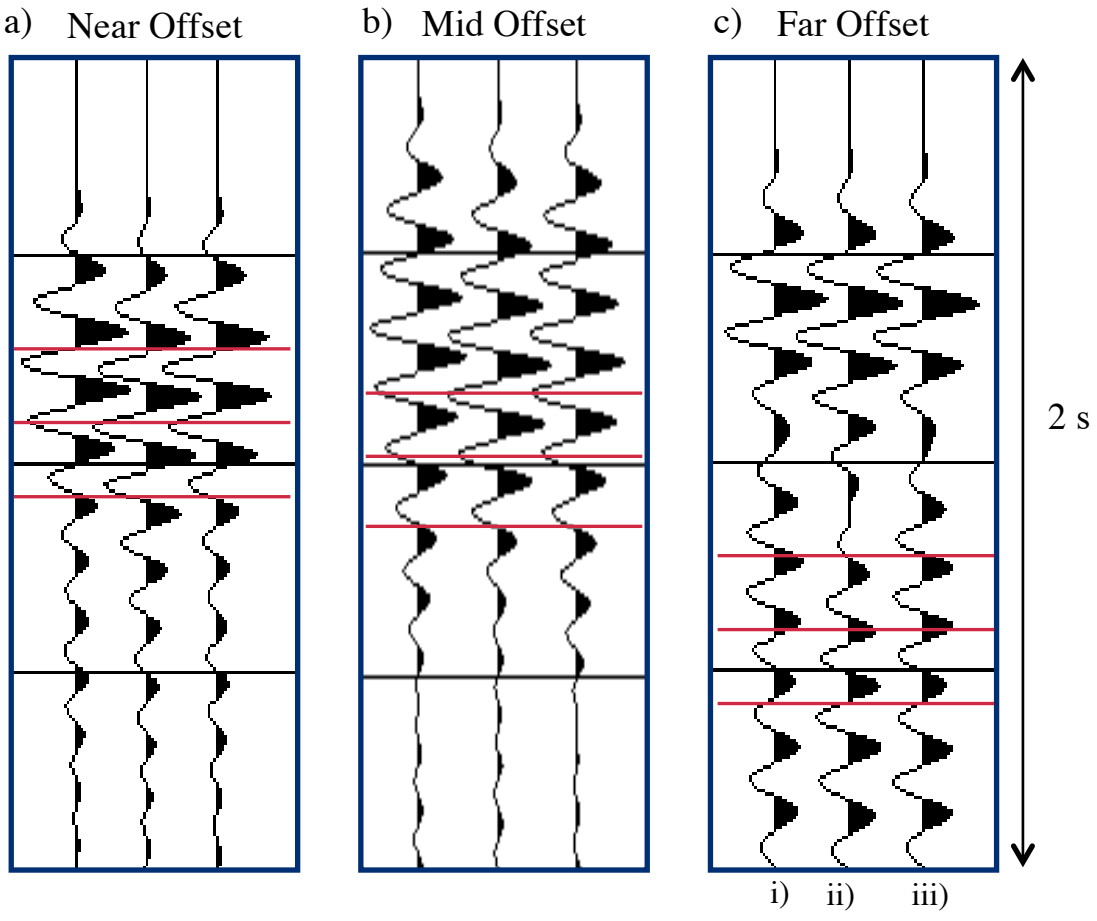


Figure 4-17: Data at (a) near, (b) mid, and (c) far offsets, for: (i) field data, (ii) synthetics generated from the conventional FWI model, (iii) synthetics generated from offset-variable density FWI model. The offset-variable density FWI model better fits the field data.

Depth Migration

To test further whether the model recovered using an offset-variable density is a better representation of subsurface velocity, the velocity model was used to migrate the reflection data using reverse time migration (RTM) (Figure 4-18). The original processing contractor (CGG) undertook this migration using the FWI models generated by this research. The input data to the migration includes: the original 3D contractor's model of anisotropy; the source wavelet used in FWI; and the FWI recovered model processed to remove edge effects that were introduced during FWI. The processing of the FWI model entailed ramping the FWI velocity model smoothly back into the starting model around the periphery of the model. This processing resulted in small qualitative differences in the migrations using the original and newly recovered FWI models. A defined density was not used in the migration and processes such as smoothing to remove a minor shallow acquisition footprint were also not undertaken. The migrations were performed on a 50-m mesh, as was the case for the FWI.

It is apparent that the reflectors in this migration show better continuity; directly above the broad anticline faults and horizons are clearer and simpler. With a delayed compactional diagenesis and the onset of hydrocarbon production at the reservoir leading to an unexpected degree of subsidence, the anticlinal structure is expected to be symmetric. Figure 4-19 shows that the rim of the anticlinal structure is subtly smoother due to the offset-variable density approach and so it can be concluded that the RTM image with this scheme yields a more geologically plausible result.

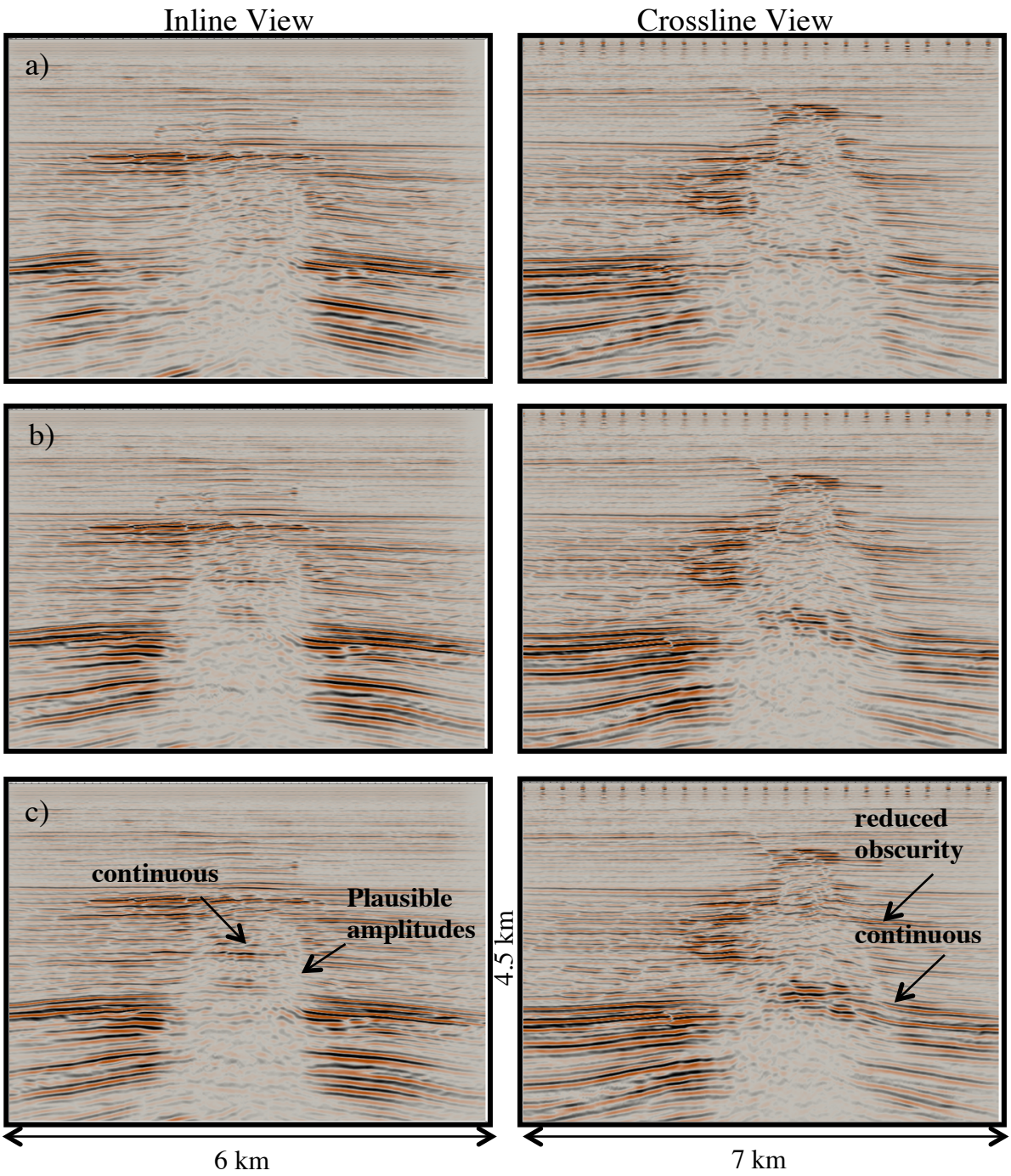


Figure 4-18: Vertical depth slices, inline on the left and crossline on the right, through the RTM images generated by CGG obtained using (a) the starting model, (b) the original FWI model, and (c) the offset-variable density FWI model. There is continuous improvement in the imaging from (a) to (b) to (c).

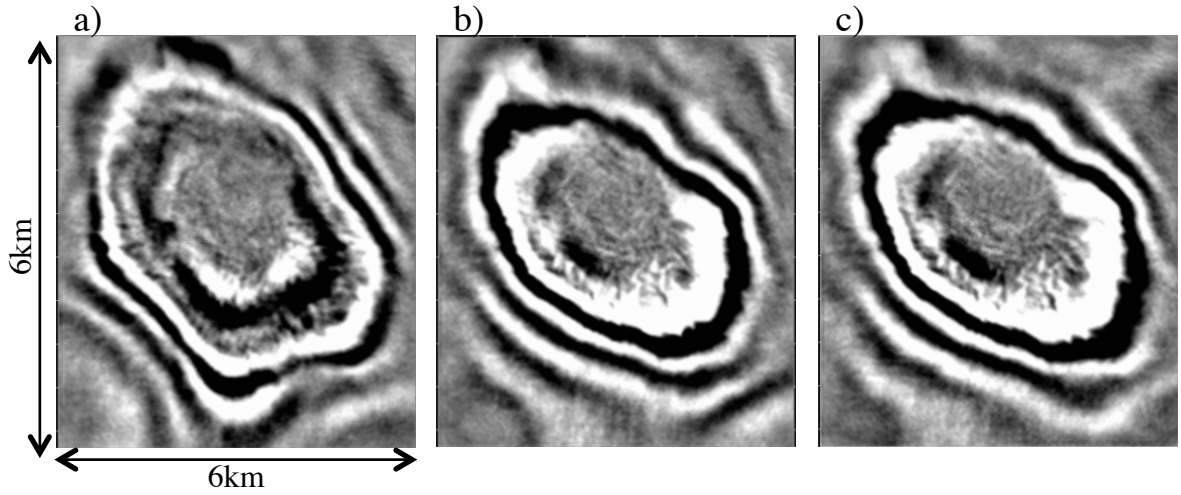


Figure 4-19: Horizontal depth Slices through the RTM images produced by CGG, illustrating an improvement with increased simplification in the structure moving from (a) starting model to (b) original FWI model to (c) offset-variable density FWI Model.

Summary

For the inversions of the shallow marine field dataset shown here, the predicted data from the original recovered FWI velocity models were delayed with respect to the field data, and the delay was more apparent at later arrival times. Here, it has been demonstrated that using an incorrect source, incomplete convergence, or the use of a poor starting velocity model did not cause the delay. The mismatch may be a common occurrence when using acoustic FWI codes, together with imprecise density and attenuation models, to invert field data that has previously gone unnoticed because the delay is quite small. The delay may be more pronounced in the dataset used here as a result of the shallow water and presence of strong water-bottom multiples. It is unclear as to the precise cause of the apparent delay, given that there are several effects that are not properly accounted for (fine-scale anisotropy, anelastic attenuation, and elasticity), and that the wavefield will not be accurately modelled if the density and/or velocity contrast at the seabed are incorrect or are incorrectly captured on a coarse mesh. In this study, seawater density values were chosen empirically, based upon the observed match between predicted and field data for selected gathers. However in principle, it would be straightforward to invert for the optimal density variation with offset during conventional acoustic FWI.

It has been established that using non-physical water densities can improve the match between the predicted and field data, and that this leads to an improvement in resolution in the recovered velocity model, with the shallow gas anomaly and associated fault structures better defined, leading to higher fidelity of the final RTM image. This suggests that inaccuracies in modelling the wavefield at the seabed, that are caused by a variety of phenomena, can be addressed and at least partially compensated through the use of a non-physical, offset-variable density in the water layer. This is a simple, efficient and effective scheme that improves the performance of acoustic FWI when applied to 3D field data.

Chapter 5 : 3D Time Domain FWI – Non-linearly migrating reflectivity into the velocity model

Overview

3D time-domain FWI technique is the subject of considerable industry activity due to its potential for:

- Resolving unprecedented velocity heterogeneity – stemming from tackling the true non-linear relation between acoustic subsurface properties and surface-acquired seismic;
- Automation – stemming from computational feedback loops replacing the role of human effort and subjectivity.

These factors combined make it technically and economically advantageous for FWI to advance towards superseding tomographic ray-based velocity model building on the long length scale end and migration on the short length scale end of subsurface characterisation. Whilst within the scope of FWI to achieve this, the fundamental limiting factor to date is sensitivity to local false minima where the computed model gets stuck away from the real global-minimum solution and further iterations of the optimisation bring no reward.

Our goal is to take two FWI-suited ocean-bottom-node datasets and without succumbing to local-minimum convergence be able to incorporate higher frequencies and a greater weight on reflected energy during the inversion to valuably push the limits of the resolution and depth penetration of the update. The end game is for reflectivity to be non-linearly migrated into the velocity model via FWI acting on raw unprocessed waveforms. This chapter will delve into:

- Illustrating the inherent waveform misalignment risk that builds with inversion frequency, and the nature of local-minimum inferior models that have been averted;
- Demonstrating the widening range of length scales, from background trends to fine-scale geological detail, being captured in a fully-data-driven no-constraints-applied manner;

- Describing the time-domain FWI platform utilized to invert the data, together with a spotlight on the features devised for enhanced convergence extracting maximal resolution with minimal artefacts.

Figure 5-1 gives an indication of the benefits of high bandwidth FWI in comparison to the tomographic vendor velocity models and corresponding migrated images. Describing the remaining gains/outstanding issues still to be addressed will conclude this chapter.

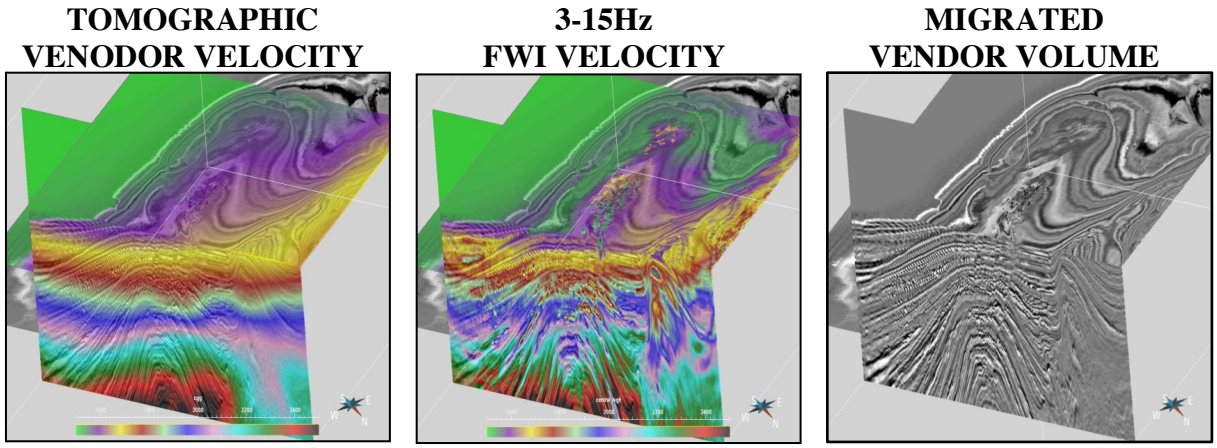


Figure 5-1: Comparison between the tomographic velocity model and the high bandwidth FWI velocity model obtained via processes described in this chapter. The independent migrated vendor volume based on the tomographic velocities is also illustrated.

Introduction

Like any seismic inversion technique, full-waveform inversion (FWI) seeks to create a subsurface characterisation model in an area of interest, from a field dataset. Figure 5-2 illustrates an example of using raw observed data to generate a high resolution, FWI recovered velocity model (Warner, 2014). FWI iteratively updates a trial starting model by matching computer-generated model-predicted data to recorded field data, until convergence is achieved. However, FWI is the one inversion technique, which goes all the way back to raw shot gathers for its mathematical formulation, modelling predicted data using the two-way wave equation. This unique feature of FWI sets it apart. It operates on the original field traces, prior to processing and migration, harnessing information from refractions, reflections, interbeds and free-surface multiples to compute the model update. It is fundamental for FWI to advance towards superseding tomographic ray-based velocity model building on the long length scale and migration on the short length scale. Whilst within the scope of FWI to achieve this, the fundamental limiting factor to date is sensitivity to local minima where the computed model gets stuck away from the real global-minimum solution, and further iterations of the optimisation bring no reward, yielding significant data misfit between observed and predicted data. In order to assess this, a closer examination of the data follows.

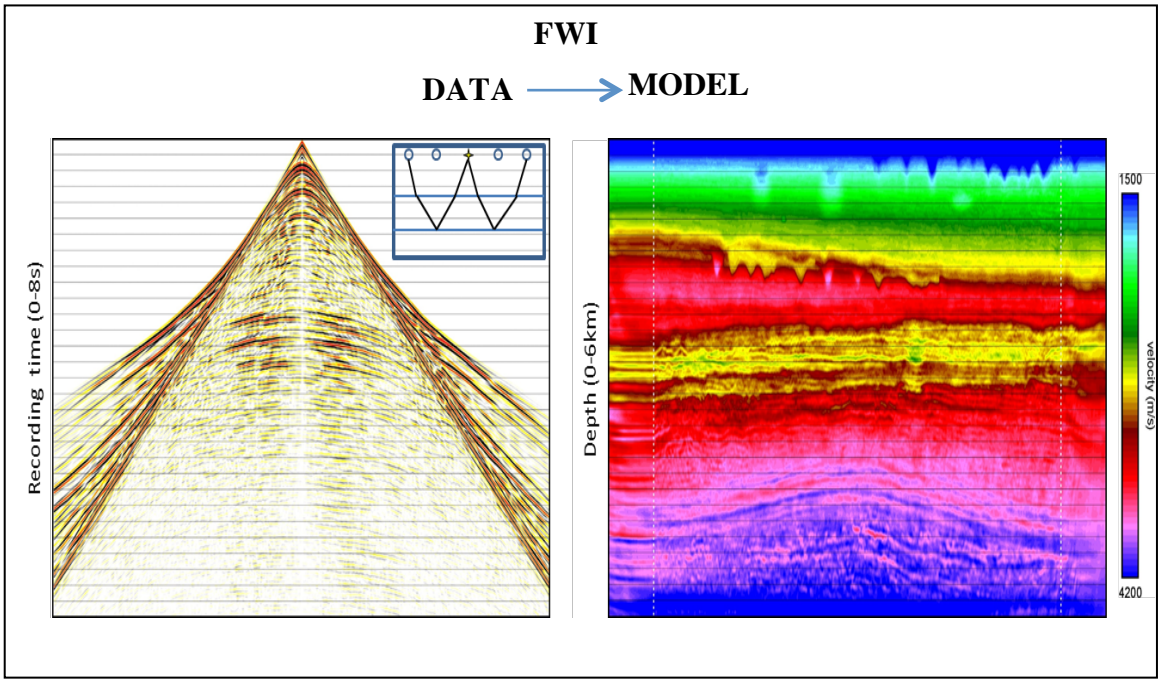


Figure 5-2: Illustration of the use of time-domain FWI to recover a high-resolution, heterogeneous velocity model (right) using raw shot gathers (left). This example is of the best result on the synthetic Chevron benchmark test (Warner, 2014).

In full-waveform inversion, it is crucial that the early-arriving wavefield for the recorded field data, at the relevant bandwidth for FWI, is within half-cycle to the computer-generated predicted data from the featureless, almost one dimensional, starting models. Figure 5-3 shows the frequency spectrums, both the low and high bandwidth cases, at which FWI is undertaken. Filtering the original field dataset to the frequencies required for FWI was the only pre-processing performed.

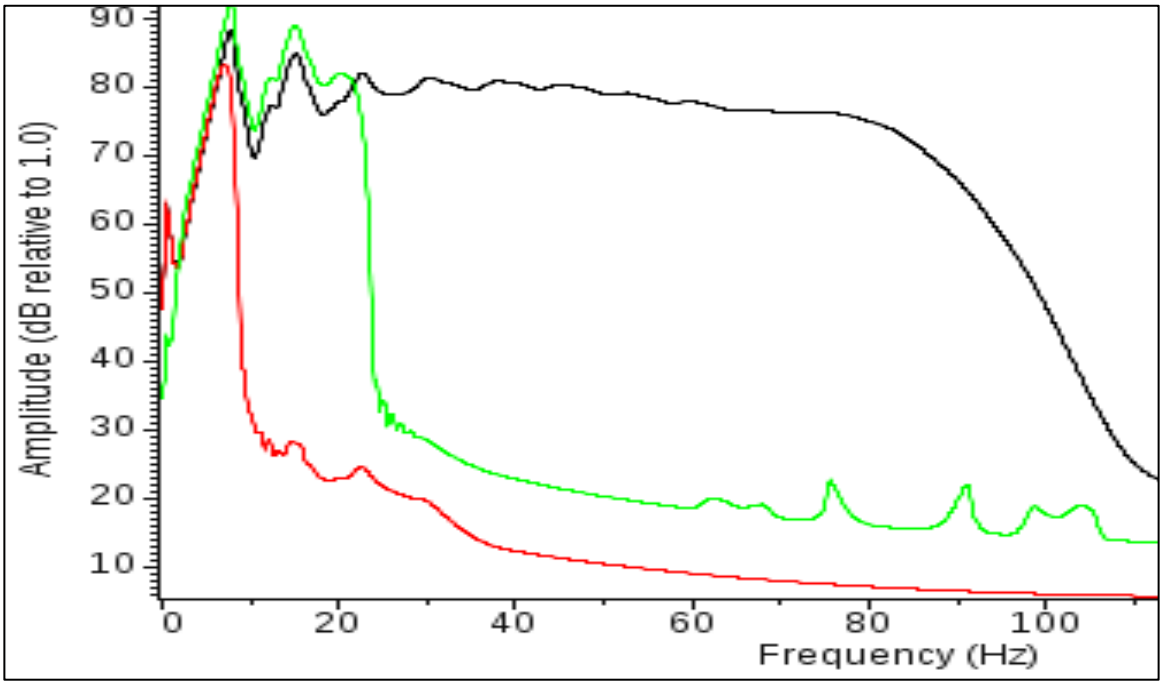


Figure 5-3: Comparison between the low (red) and the high (green) bandwidth observed data used for FWI, to the raw observed data (black) at full bandwidth.

The ultimate priority of FWI is to obtain a good match and avoid data misalignment. The observed data and source signature was thus examined at different bandwidths. An examination of the observed and modelled data (Figure 5-4) at the 0-6 Hz bandwidth is shown at the near (top) and far (bottom) offset locations. These locations are illustrated on the node patches shown in Figure 5-4. A good match between the observed and modelled data for all events – reflections, refractions, multiples – is necessary in FWI.

However, the main risk of FWI – data misalignment, also known as cycle skipping – must be kept in mind. This risk of cycle skipping increases with a move to higher frequencies. Figure

5-5 shows a comparison between the observed and modelled data at the 0 -15 Hz bandwidth. As illustrated, climbing to higher frequencies implies the presence of a tighter wavelet or signature. What is needed is an algorithm, which is stable and robust and avoids local minimum at these higher frequencies. Can higher frequencies be incorporated and a greater weight be placed on the reflections to valuably push the limits of resolution and depth penetration of the update without getting stuck in a local minimum?

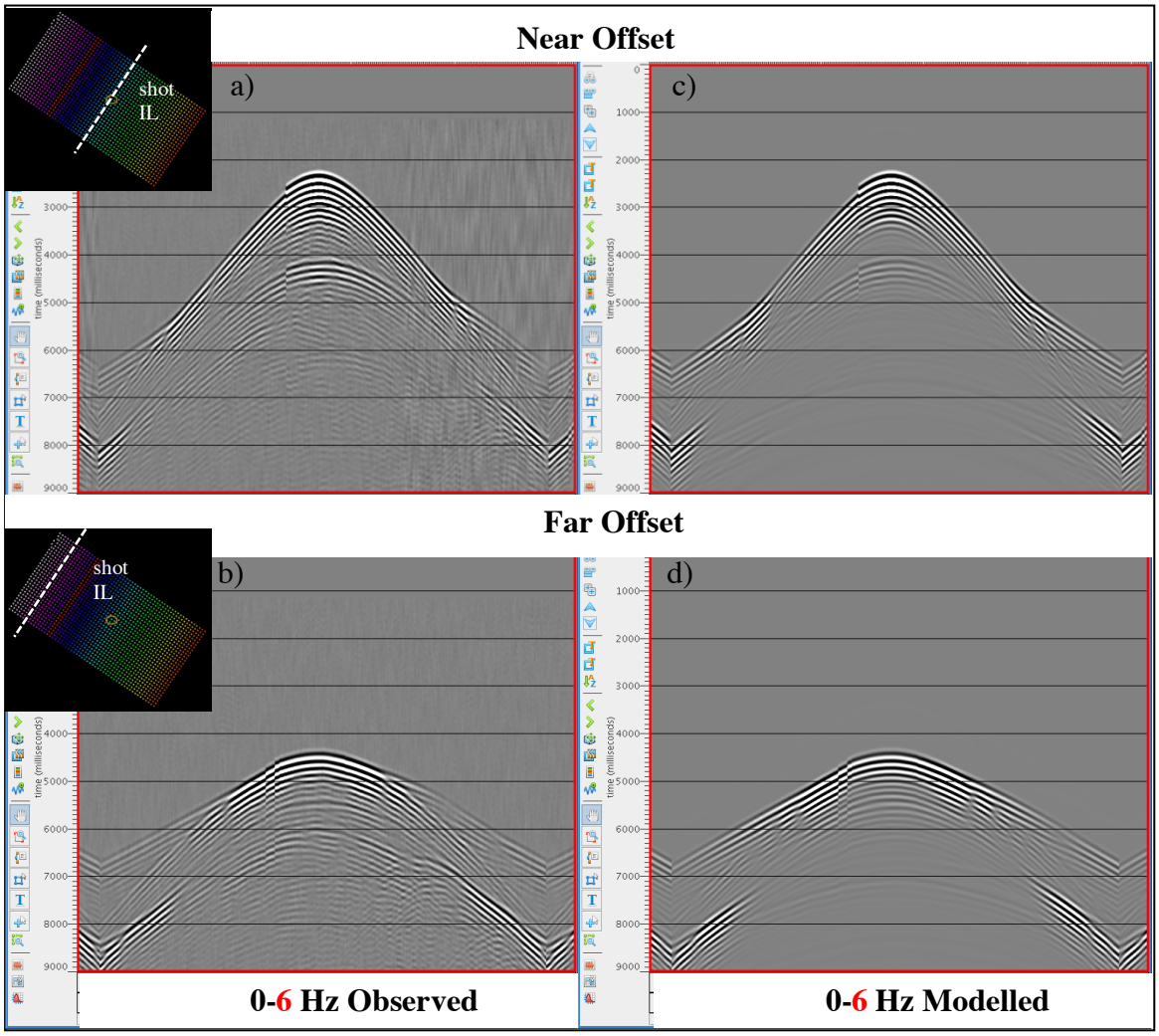


Figure 5-4: Comparison of the observed (a & b) and modelled (c & d) data at near (top), and far (bottom) offset locations for the 0 -6 Hz low frequency bandwidth

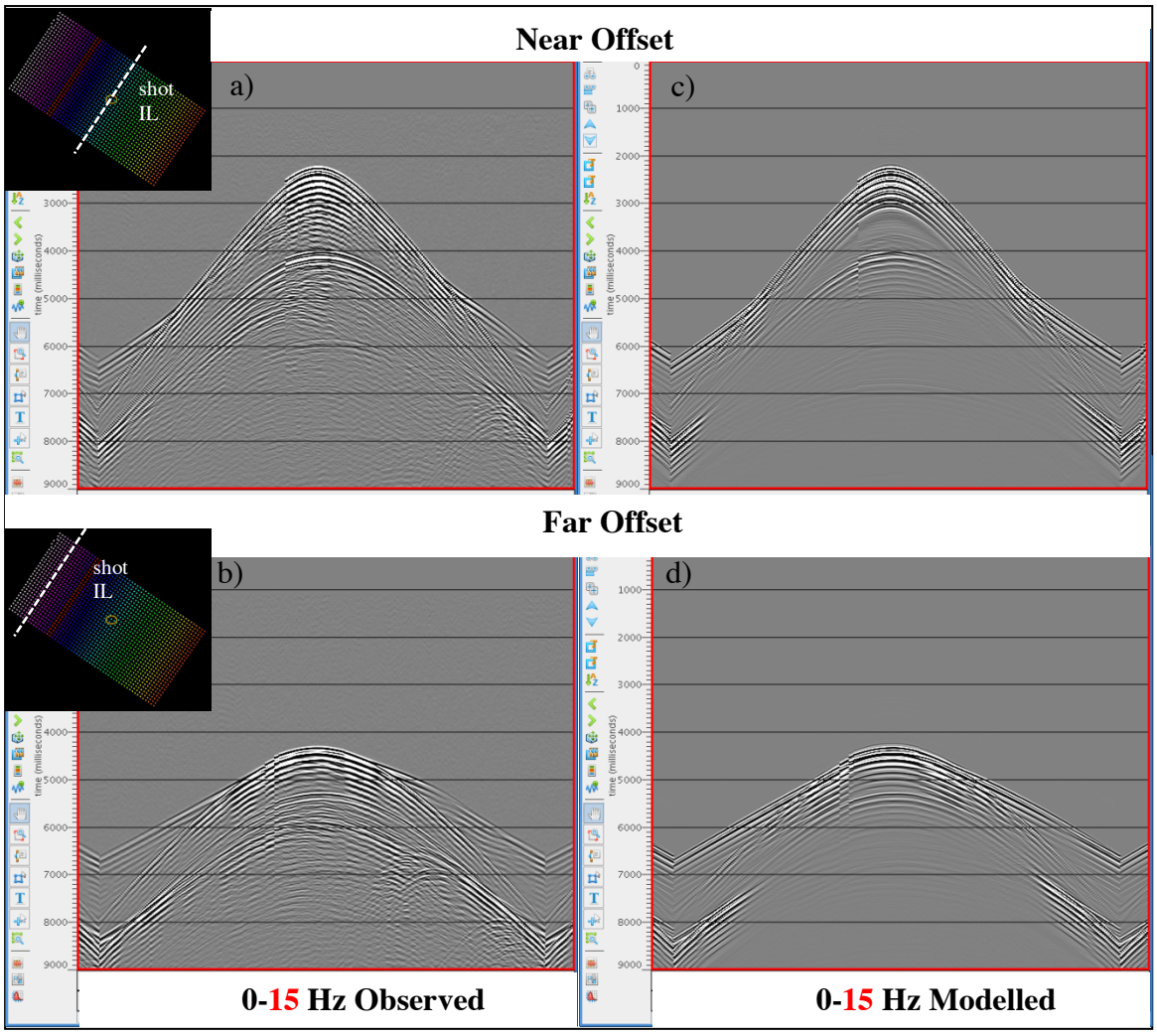


Figure 5-5: Comparison of the observed (a & b) and modelled (c & d) data at near (top), and far (bottom) offset locations for the 0 -15 Hz high frequency bandwidth

Figure 5-6 illustrates an example of full-waveform inversion when applied to two datasets at the low frequency bandwidth. Significant detail is already introduced at this low bandwidth. At these low frequencies, uplift in the velocity is evident. But the questions which remain includes,

1. Can the bandwidth be extended without being stuck in a local minimum?
2. Can the reflection energy be exploited further without being stuck in a local minimum?
3. Can the resolution of the model continue to increase?

These are the questions that have been answered by this research and a full account of this is documented here.

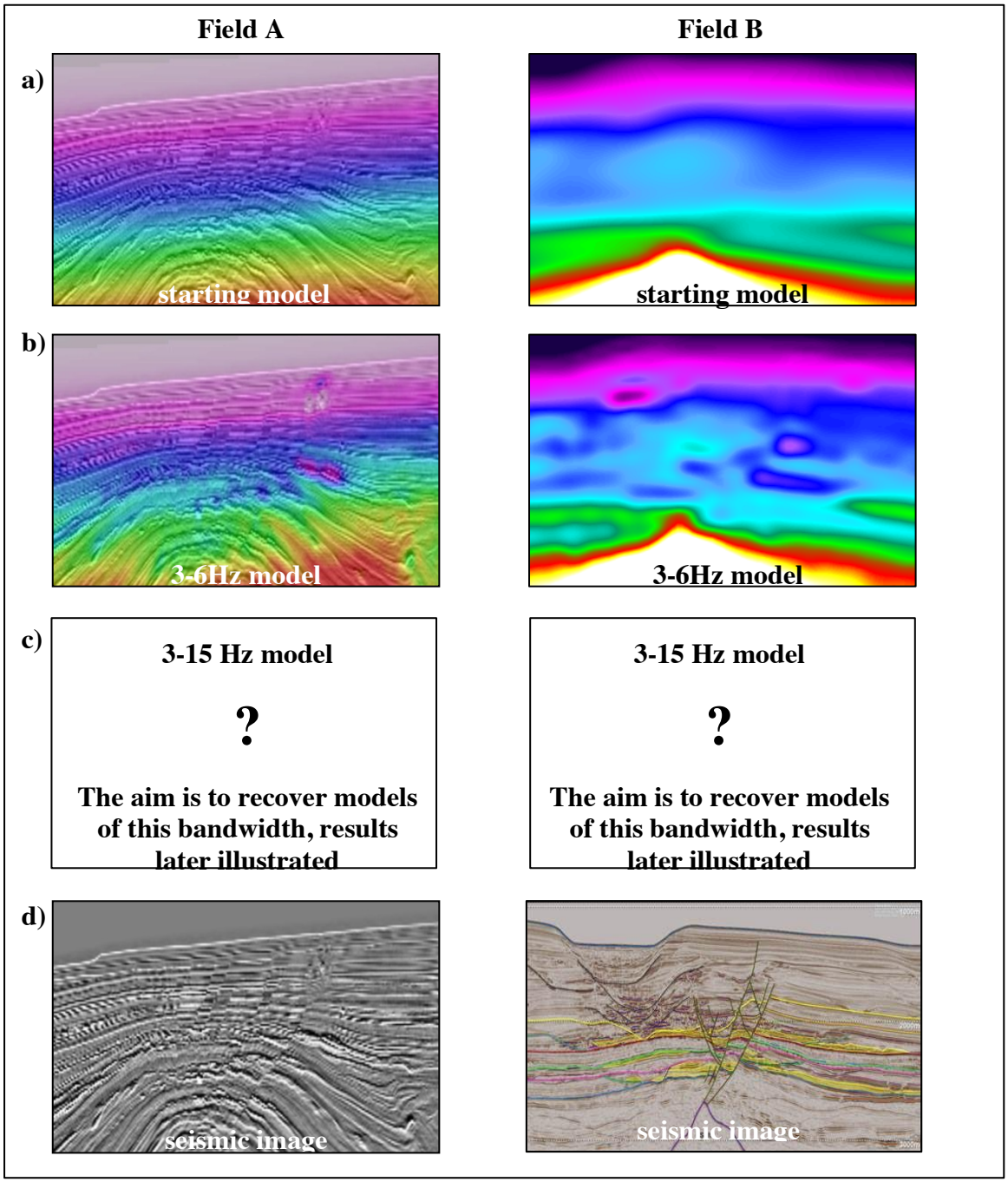


Figure 5-6: Illustration of the a) starting models obtained from Chevron b) 3-6Hz FWI recovered models c) indication of climbing to higher frequencies and d) seismic image; for Field A and Field B

FWI setup and a new workflow

This section describes one key aspect of the solution that helps in averting inferior local minimum models but instead leads to a superior result, which will be described later.

Data Match

In achieving a higher resolution model, with extended bandwidth through further exploitation of the reflection energy, a new workflow has been developed which aims to better adapt the predicted data to the observed data, before undertaking full-waveform inversion. In so doing, the observed and predicted has been more closely examined.

Figure 5-7 illustrates a line through an observed dataset with zero time at 1s, the direct arrival arriving at 2.6s and a strong water-bottom multiple evident at 4.2s. A schematic of these arrivals is shown on the top right-hand corner. A single trace is extracted, yielding a closer look at the key arrivals. The observed data trace to the far right is then compared to the predicted data (middle) - generated using the source (extracted from the observed data) to the far left. The key arrival times are also marked on the extracted traces. The early arrivals predicted are accurate in both phase (as required by FWI) and amplitude when compared to the observed data. Also, the water-bottom multiple, another significant arrival, is generated in the predicted data. The question that arises though is: can the fit of that arrival before FWI be optimised?

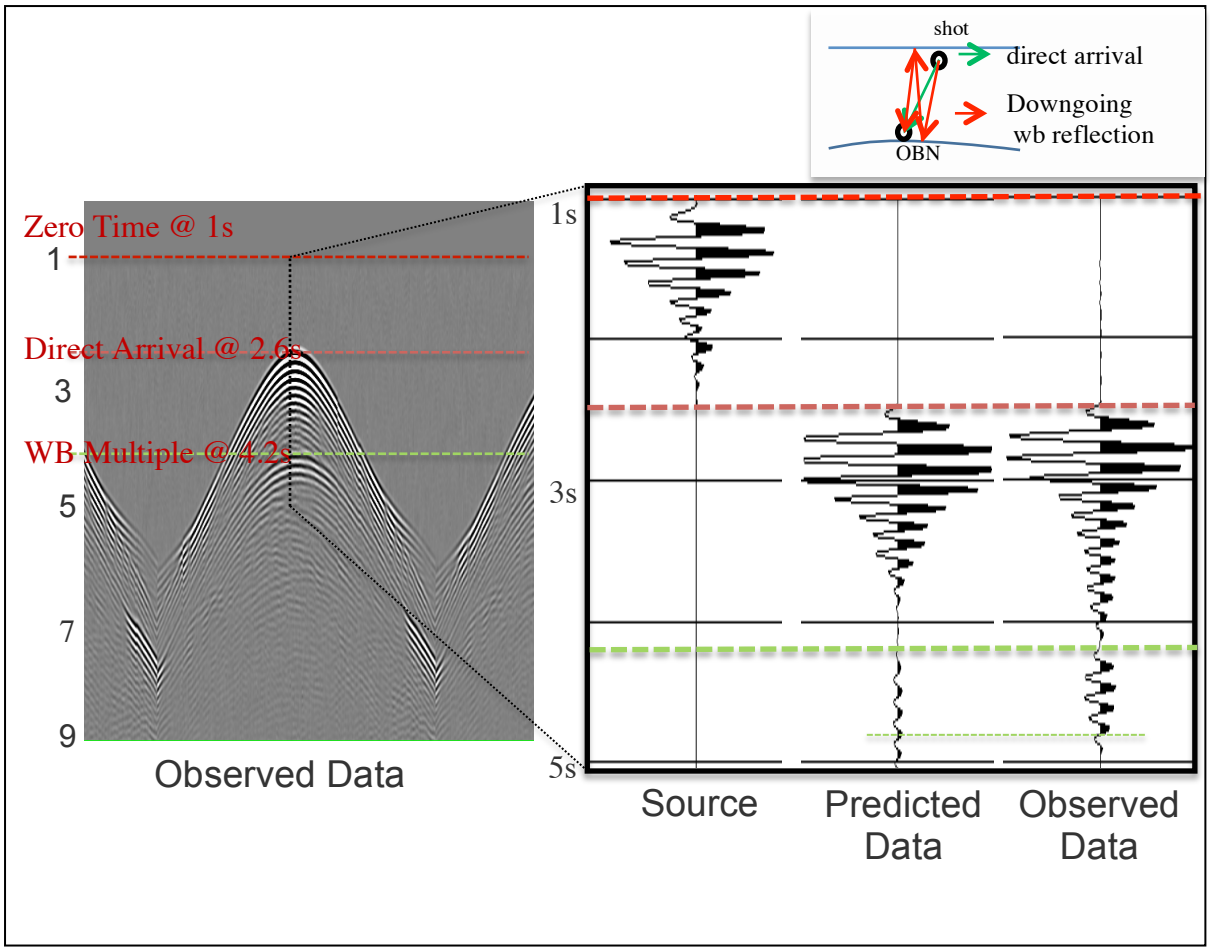


Figure 5-7: A closer look at the data, illustrating the key arrivals in the observed, and the starting model predicted data. The source signature extracted from the observed data and a schematic of these arrivals is also indicated.

Optimizing the fit of the water-bottom multiple

Two key aspects in the optimisation of the multiple events are its amplitude and phase. On the model side, the apparent travel-time mismatches of the multiple events were previously accounted for by inserting the reflectivity of the seabed into the starting model, which originally has a smooth transition across this known elastic boundary. This involves the variation of the velocity-density relationship across the seabed interface, similar to the strategy adopted for FWI of the shallow-water OBC dataset in the previous chapter. The smooth velocity transition across the seabed interface is evident in both datasets, which are in a deep-water geological environment.

Forward model tests revealed the correct reflectivity parameterisation necessary to correct time shifts of the first-order multiple arrivals between the predicted and observed data (Figure

5-8). A minimum rock velocity of 1515ms^{-1} and water velocity of 1490ms^{-1} was sufficient to correct the apparent travel-time shift. Different arrivals (primaries and multiples) are arriving at similar times, and so the interference between them results in this apparent travel time shift.

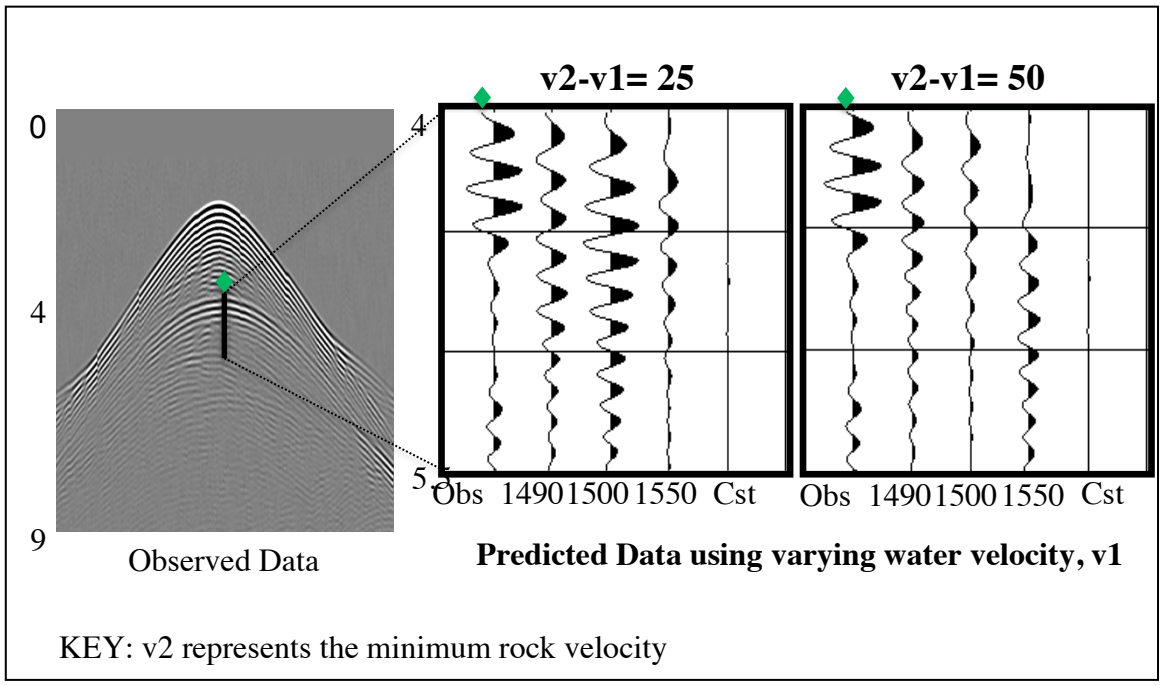


Figure 5-8: Forward model tests revealed the correct reflectivity parameterization necessary to correct time shifts of the multiple events between the predicted and observed data. A water velocity of 1490ms^{-1} and minimum rock velocity of 1515ms^{-1} was sufficient to correct apparent travel-time shift.

Here, one step further to account for amplitude differences is taken as well. On the data side, the multiple events of the predicted data replaces that of the observed data and/or the multiple events of the observed data replaces that of the predicted data, using an adaptive matching technique. In other words, the multiple events are switched. Because of issues of confidentiality, I am not permitted to explain the procedure that I used in detail in this workflow. I am however permitted to explain the high-level strategy behind the workflow. This was to use a matching algorithm, of a type more-typically used for surface related multiple elimination (SRME), to ensure that the amplitude and waveform of the first simple sea-bottom multiple in the predicted data were matched closely to the amplitude and waveform of the multiple in the field data without changing other portions of either of the

two datasets. This essentially involved a modification to equation 2-6 to incorporate a filter, F, applied to the predicted data,

$$\boldsymbol{d}'_{calc}(\mathbf{m}) = \mathrm{F}\big(\mathbf{d}_{\mathrm{calc}}(\mathbf{m})\big), \tag{5-1}$$

resulting in a modified objective function,

$$f(\mathbf{m}) = \frac{1}{2}\left|\left|\mathbf{d}_{\mathrm{obs}} - \boldsymbol{d}'_{calc}(\mathbf{m})\right|\right|^2. \tag{5-2}$$

Figure 5-9 shows the comparison between the observed data and the predicted data obtained by inserting the seabed reflectivity in the starting model thereby generating the multiple arrivals at near, mid and far offset locations. Also illustrated are the predicted data generated by both inserting the seabed reflectivity as well as conditioning the data using the adaptive matching technique at all offsets. In the later case the multiple event is well matched in both amplitude and phase.

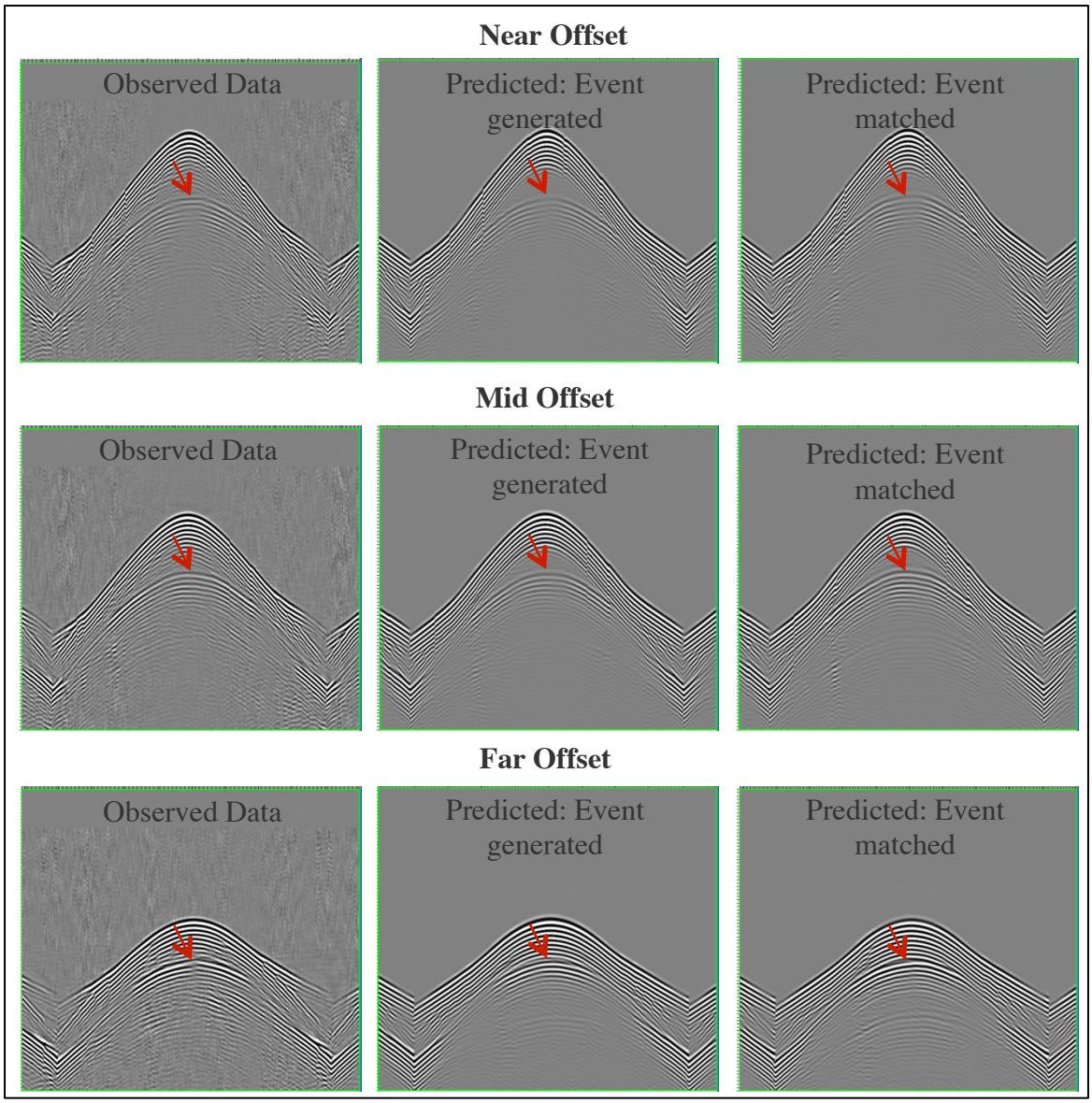


Figure 5-9: Comparison between the observed data (left), predicted data obtained by inserting seabed reflectivity into the starting model resulting in the generation of the sea-bottom multiple (middle), and predicted data obtained by both inserting the seabed reflectivity in the model as well as conditioning the data through an adaptive matching technique (right). These are shown at the near, mid and far offset locations.

Test one shot gradient direction

Using the predicted data, with the multiple matched in both amplitude and phase, a one shot inversion was performed to test the effect, with and without this new workflow. Figure 5-10 illustrates a vertical slice showing the gradient direction after one-iteration, with and without this new workflow. A prominent migration smile centered on the reciprocal shot location is significantly down-weighted in the vertical slice, with the use of the new workflow. In the horizontal direction, a depth slice showing the gradient direction after one-iteration shows the occurrence of rings around the reciprocal shot location (Figure 5-10). The migration smile appears as a ring in the horizontal direction.

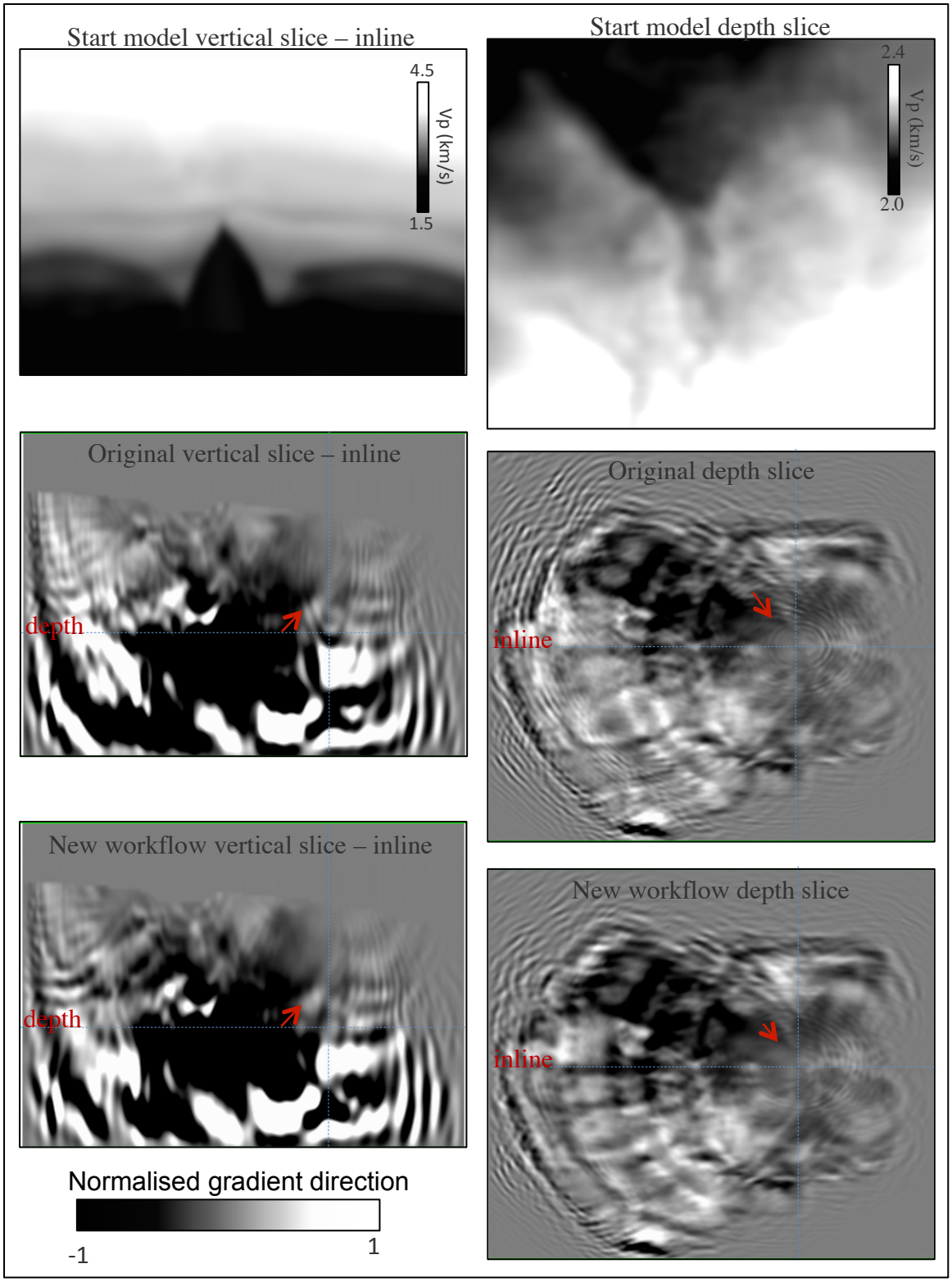


Figure 5-10: Horizontal and vertical slices through the gradient showing the effect of the new workflow on a one-shot gradient direction test

Desired verses undesired convergence

Using this new workflow as described in the previous section, its full effect is now illustrated. Figure 5-11 illustrates the observed data before performing full-waveform inversion (FWI). Refractions, reflections, and the multiple events are all indicated. Using the original predicted data without the application of the new workflow, FWI up to 15Hz is performed and the recovered model is used to generate synthetics, which are then compared to the observed data. The early arrivals are well matched to the observed data. However, reflections, late refractions and the multiple arrivals are not well matched (Figure 5-11). In some instances, the reflections are completely absent. Thus, it can be stated that the recovered model is converging to a local-minimum in this instance (Figure 5-11). On the other hand, using the predicted data with the application of the new workflow before FWI, all arrivals – reflections, refractions, multiple – in the recovered-model synthetics match well. All key events are present, with the reflection events (not present in the starting model) being built into the correct positions. In this instance, it can be stated that the recovered model is converging to the desired minimum (Figure 5-11).

Horizontal slices through the starting and FWI models at different depths are illustrated in Figure 5-12. The quality of the recovered models are masked by unwanted effects – particularly evident at the deeper depth 2– in the local-minimum case. With continued input of higher frequencies into the inversion, the solution, if stuck in a local minimum, will not produce the desired uplift in the velocity model or match in the data. In the case where the data are conditioned before FWI using the new workflow, the quality of the FWI models is enhanced, and the model resolution and fidelity are improved. This improvement is evident at both the shallow depth 1 and deeper depth 2. Thus, the frequency range can be continually increased producing desired uplift in the velocity for the desired minimum case. The algorithm is robust and efficient at higher bandwidths. An enhanced convergence, extracting maximum resolution with minimal artefacts, using the previously described workflow, has proven to be attainable.

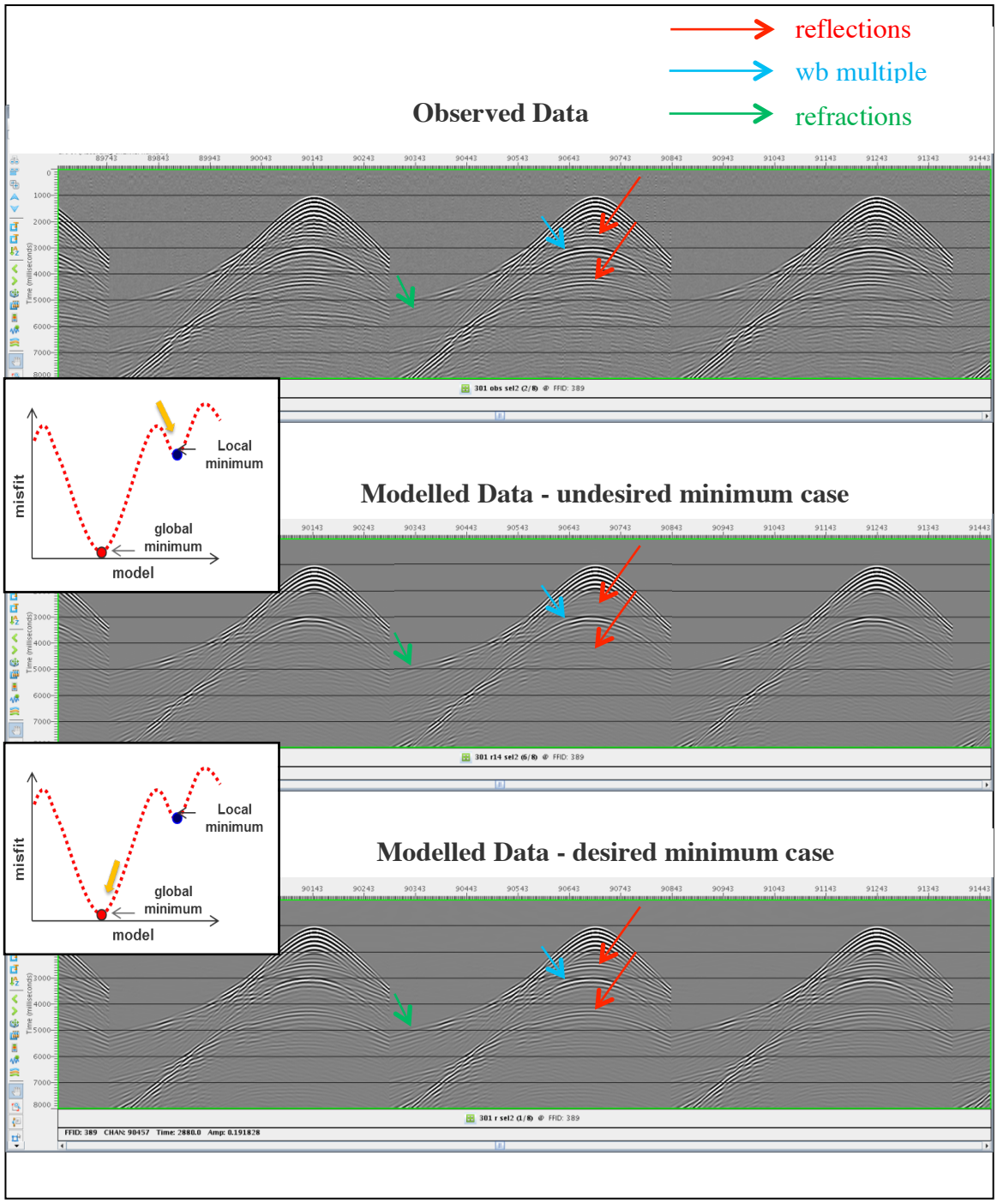


Figure 5-11: Comparison between the observed data obtained from Chevron and the recovered model synthetics generated with (desired-minimum case) and without (undesired-minimum case) the application of the new workflow before FWI

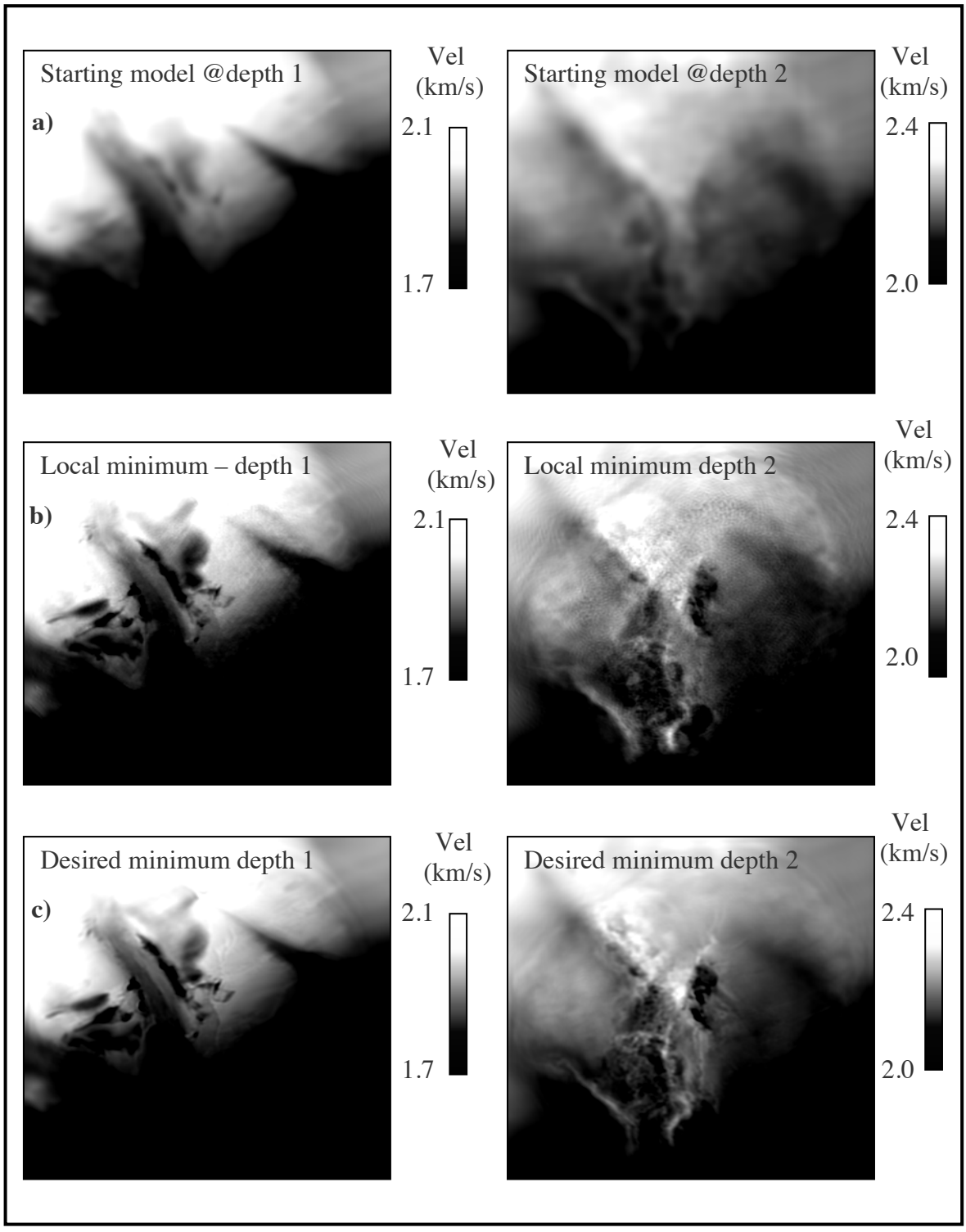


Figure 5-12: Comparison between a) starting model slices obtained from Chevron b) FWI model slices without the use of the workflow – local minimum case c) FWI model slices with the use of the workflow – desired minimum case; at the shallower depth 1 and deeper depth 2 levels.

Results and Consequences of results

The stability of the forward modelling was confirmed prior to inversion with a dispersion-free, good match of the multiples at both low and high bandwidths needed for the inversions. Table 5-1 summarises the inversion parameters used for both high and low bandwidth inversions. The bandwidth of the high frequency inversion ranged from 3Hz to 15Hz. The low frequencies, up to 6Hz, were at 0.5Hz interval and the high frequencies, up to 15Hz, were at 1Hz frequency intervals, with 8 iterations per frequency block.

Parameter Sets	Field A	Filed B
Minimum velocity (m/s)	1490	1500
Minimum rock velocity (m/s)	1535	1550
Minimum frequency (Hz)	3	3
Grid spacing (m)	50 (l); 25 (h)	50 (l); 25 (h)
Maximum frequency (Hz)	6 (l); 15-20 (h)	6 (l); 15-20 (h)
Maximum velocity (m/s)	3000	4000
Number of frequencies	7 @ 0.5Hz interval 9 @ 1Hz interval	7 @ 0.5Hz interval 9 @ 1Hz interval
Number of iterations/frequency	8	8
Free Surface	Yes	Yes
Slowness	Yes	Yes
Normalise	Yes	Yes
Amplitude	No	No
Spatial Preconditioning	Yes	Yes

Table 5-1: Summary of inversion parameters for the different inversions, where (l) represents low bandwidth and (h) represents high bandwidth. Parameter sets are defined in Chapter 2.

The filter applied to the source wavelet and observed data varied from the low frequency to the high frequency inversion. Additionally, subsampling in time and space was undertaken to allow for the use of the finite difference mesh that will allow modelling to both low and high frequency. For the low frequency inversions the 4^{th} order in space and 2^{nd} order in time kernel was used verses the 10^{th} order in space, 2^{nd} order in time kernel at higher frequency. For the high frequency inversion, the starting model was limited in depth to 3600m (for Field A) and a subset of the model within key structural trends of interest, was used to reduce the computational effort for initial tests on both datasets. The same parameterization: free surface, slowness, normalise and others, was used for both the low and high frequency inversions as outlined in Table 5-1 above. The source and receiver geometry for these ocean-

bottom-node datasets used in these inversions are illustrated in Table 5-2. The symmetry and configuration of the source gun-array for both datasets minimizes the effects of source directivity. This is well-suited to full-azimuth acquisition and long offset coverage thereby increasing the information extractable by FWI.

Node Geometry		
	Field A	**Field B**
Total # nodes	1595	776
Node Interval	390 m Rectangular	375 m Hexagonal
Node Line Spacing (nominal)	390 m	325 m
Receiver Area	~230 sq. km.	~95 sq. km.
Source Geometry		
Total # sources	~650,000	~205,500
Source Line Spacing	30 m	37.5m
Source Area	~582 sq. km.	~232 sq. km.

Table 5-2: Source and Receiver geometry for the different datasets

The results and consequences of results on Field A and B illustrate the ever-widening range of length scales from background trends to fine-scale geological detail.

Field A Results

The starting model for FWI is fairly one-dimensional with varying water depths, and a slow sea-bottom, attributable to geology. After several full iterations of FWI, structural features were introduced into the starting model.

Shallow FWI Results

Shallow depth slices, Figure 5-13 to Figure 5-16, illustrates that FWI was able to recover both the geometry and the quantitative property – velocity, down to a sub-resolution level. In other words, the resolution of the shallow structures in the velocity model was not limited by the wavelength of the seismic wavefield at 6Hz.

The shallower depth slice (Figure 5-13) shows evidence of shallow structures, of low velocity, believed to be small gas pockets of varying extents (100m to 300m). A zoomed (enlarged) version of these pockets on both the FWI recovered model and the corresponding migration overlay clearly illustrates the individually resolved pockmarks with an exact conformance to the migrated section (Figure 5-14). In looking at a deeper depth slice (250 m below the first), a known shallow gas region from previous analysis is observed and indicated by the white circle in Figure 5-15. A FWI model-seismic overlay confirms the presence of these sub-resolution pockets (Figure 5-16). Clearly evident in the update model are smooth and sharp trends (Figure 5-16) unlike conventional processing. These details are useful in geohazard analysis of the shallow overburden, and can aid well planning. The resolution of the velocity model at only 6Hz recovers structural details in the shallow overburden comparable to that evident in the high frequency seismic image.

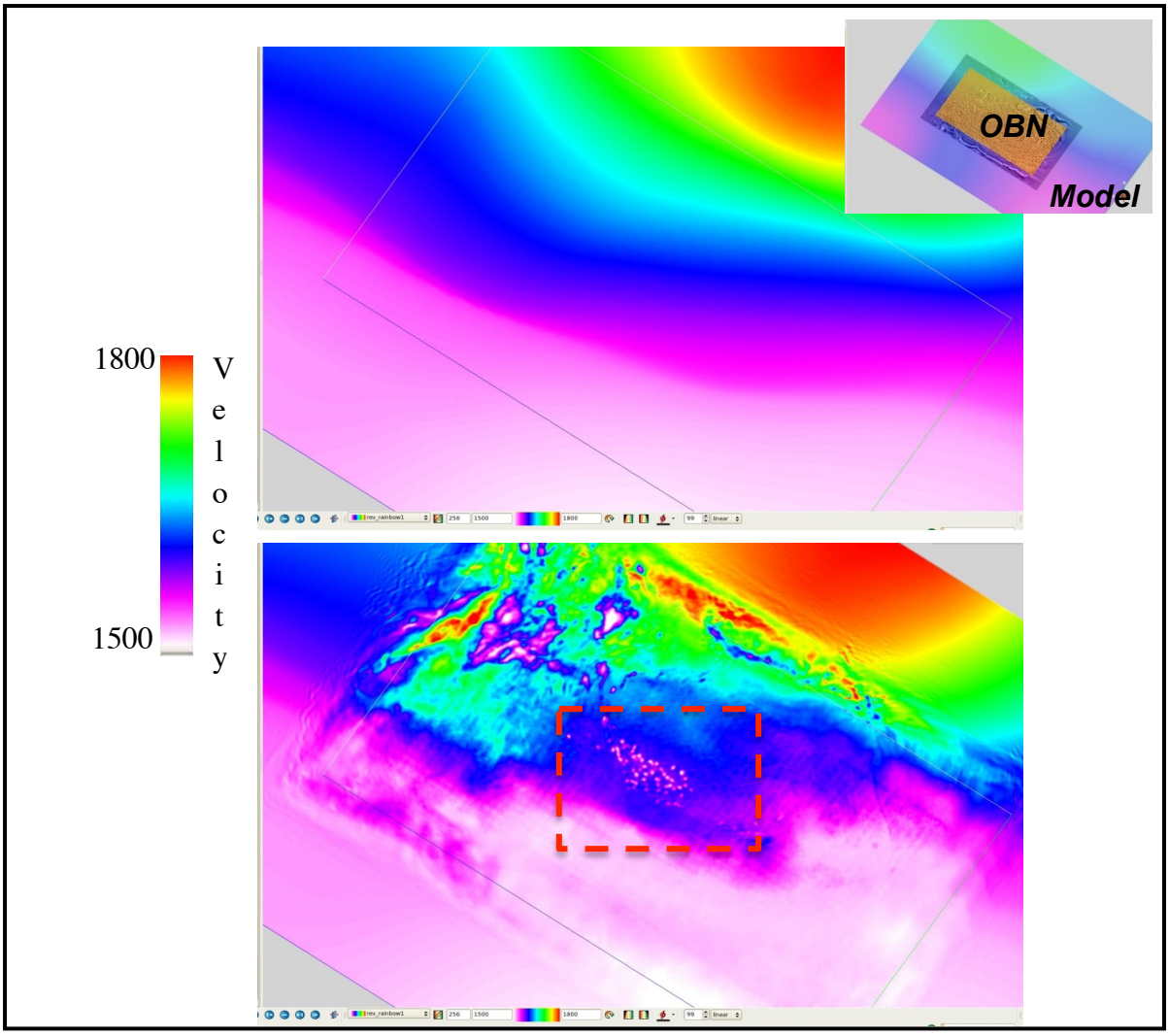


Figure 5-13: Shallower depth slice showing taken through the starting model (top) and 6 Hz recovered model (bottom). Low velocity shallow gas pockets of varying dimensions evident in the red dashed rectangle. These will be closer examined in Figure 5-14.

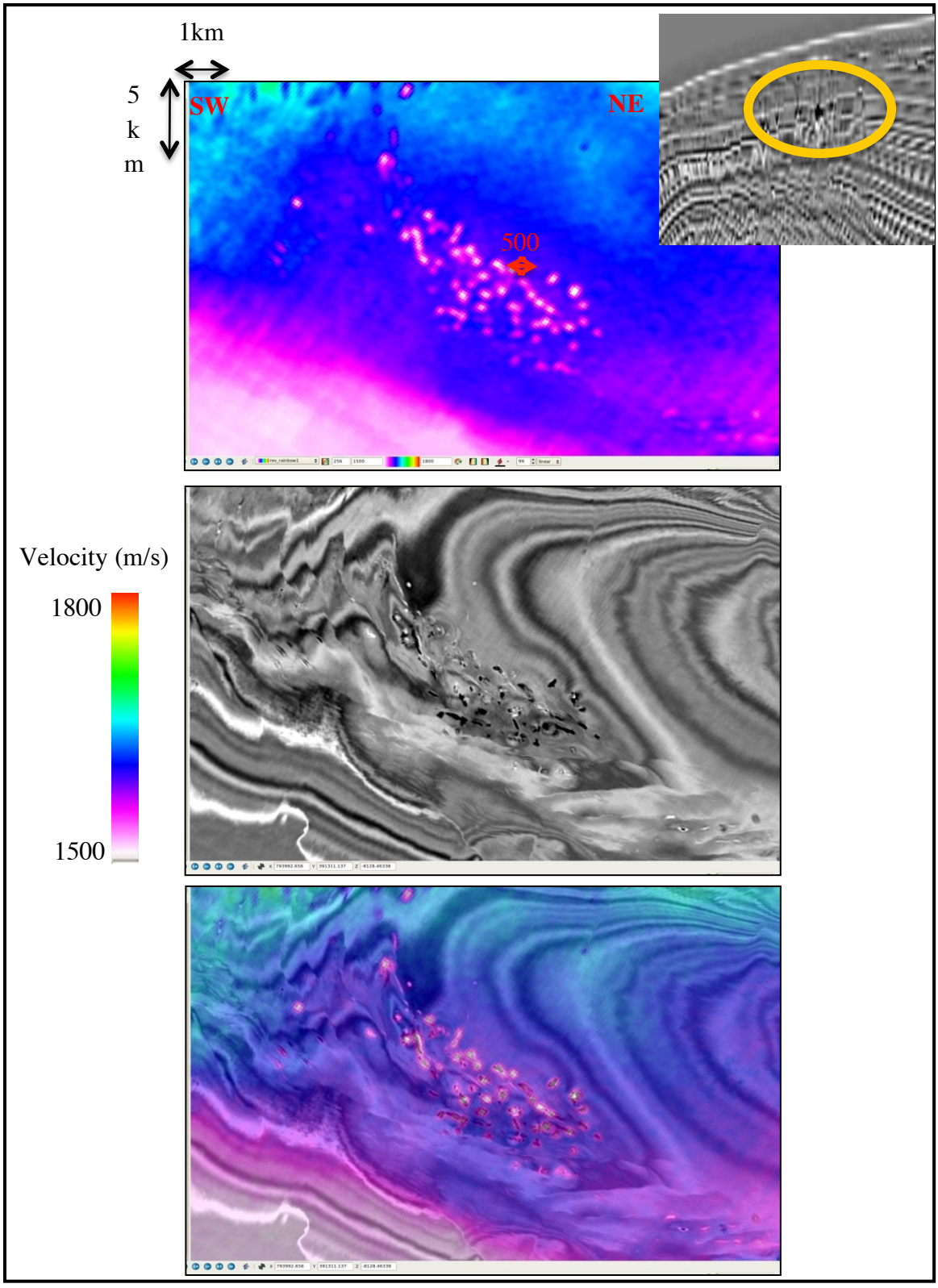


Figure 5-14: Zoomed version of the shallow gas pockets at the shallower depth (top), the corresponding seismic image (middle) and velocity-seismic overlay (bottom) showing exact conformance of the low velocity pockets of varying dimensions with the independent seismic image

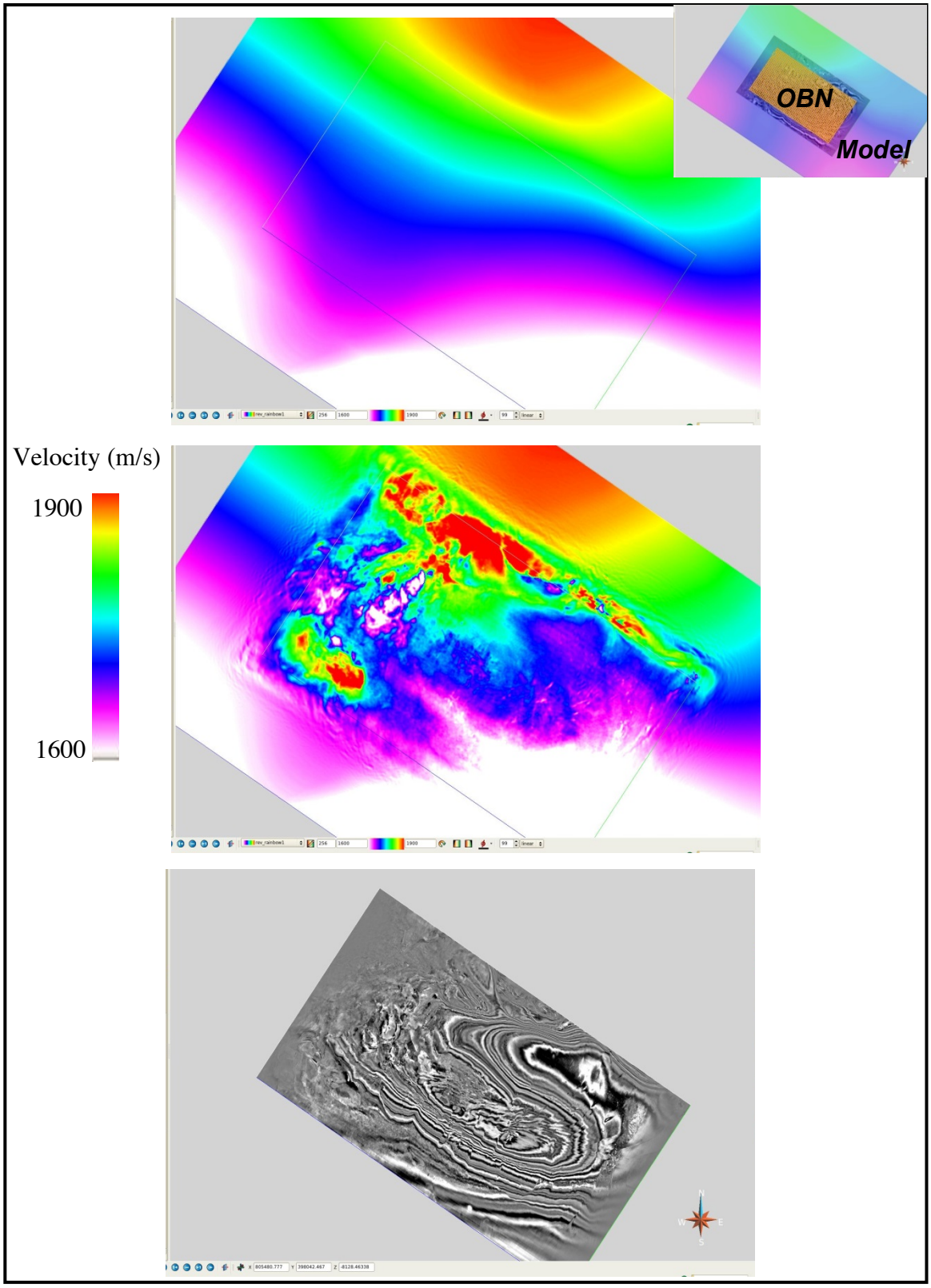


Figure 5-15: Depth slice (250 m below the shallower depth) through the starting model (top), recovered model (middle) and corresponding independent seismic image (bottom) showing varying extents of low velocity anomalies

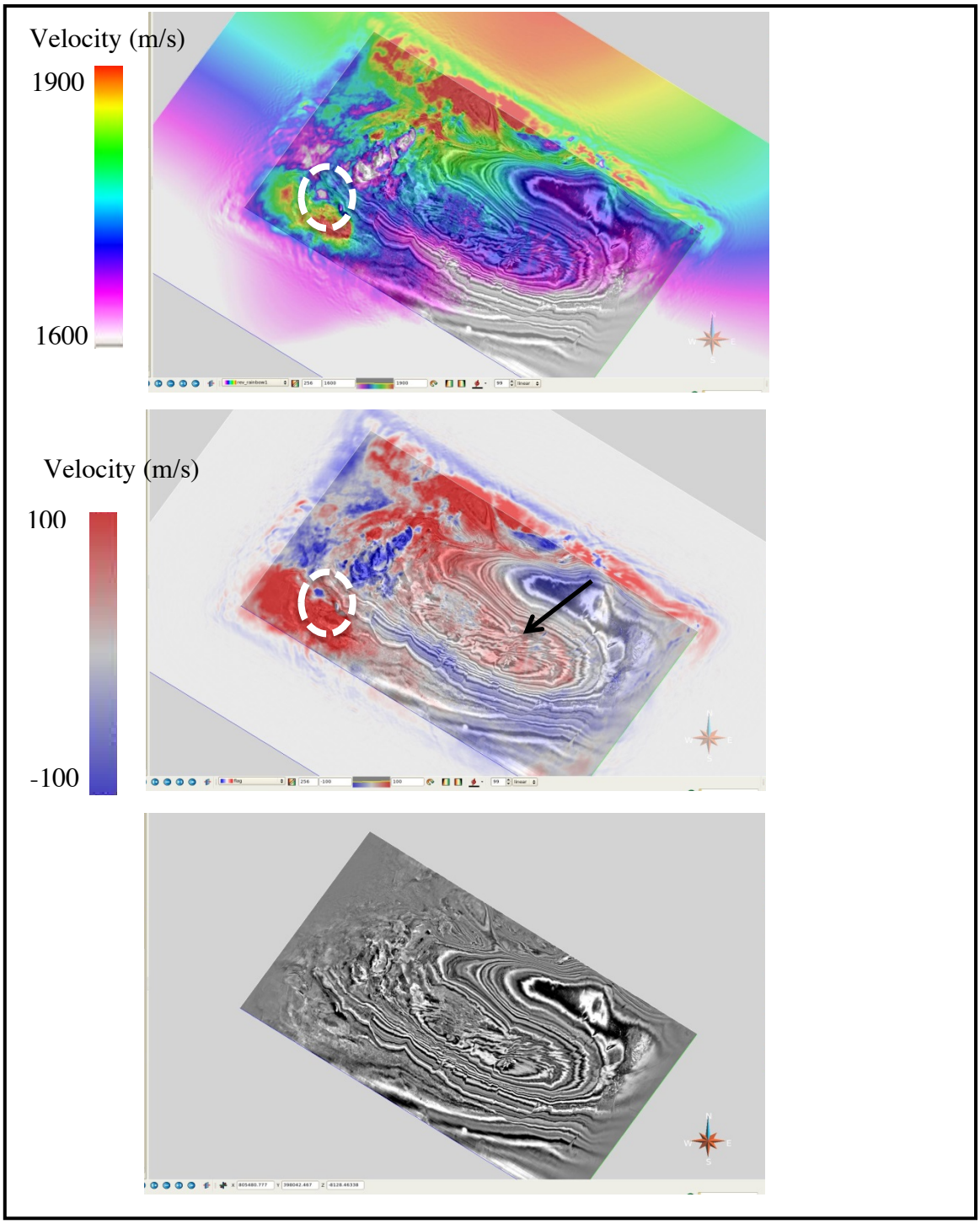


Figure 5-16: Recovered model overlay (top), update model overlay (middle) and the corresponding independent seismic image (bottom) at depth slice (250 m below the initial). The white circle indicates area of known gas anomaly not evident in independent image; the arrow indicates regions with sharp variations in velocity.

Case Study – Fault Interpretation

The high-resolution structures evident in FWI velocity models has permitted horizon and fault interpretation. Like the datasets used for FWI in this research, Beele *et al*. (2014) showcased their FWI capability on an Indonesian field dataset (the Bekapai OBC dataset) with similar characteristics - low frequencies, large offsets and wide azimuth. The former (Bekapai) dataset is shallow-water, while, Filed A dataset is in a deep-water environment. A frequency selection strategy is applied to invert the seismic data within a bandwidth ranging from 2 Hz to 10 Hz for the Bekapai OBC dataset and 3Hz to 6Hz as well as 3Hz to 15Hz for Field A OBC dataset. The high-end of this bandwidth for both datasets are significantly higher than achieved by most field dataset FWI applications with typical bandwidths of 2Hz to 7Hz (Sirgue *et al*. 2009; Warner *et al*. 2013).

With the advancement of FWI, the game-changer, remarkable results are being achieved. FWI is participating in recovering shallow gas anomalies and helps imaging the deeper targets for both datasets. Beele *et al*. (2014) succesfully demonstrated the interpretatbility of faults present in its FWI models recovered at a peak freqency of 10Hz (Figure 5-17). However, a closer examination of their results (Figure 5-17) shows that striping and ringing is evident in the velocity model. In comparison, interpretable faults are also evivent with FWI at a peak frequency of 6Hz on Field A dataset without evidence of striping and ringing (Figure 5-18). In both cases, when looking at the FWI velocity model, in a black and white scale the fault patterns appear more distinctly. Also, for this study and that of Beele *et al*. (2014), both the faults as well as the detail around the faults which correspond to saturated sand, are recovered (Figure 5-18). This comparable FWI result at different bandwidths, between the Bekapai study undertaken by Beele *et al*. (2014) and this study, demonstrates that the workflow adopted here at a lower bandwidth, supercedes the work Beele *et al*. (2014) at a higher bandwidth. Here, higher frequencies continue to provide uplift in the velocity model.

Higher frequencies (10Hz and beyond) are not necessarily synonymous with uplift in the FWI model. To achieve uplift in the model, with added details to aid fault interpretation which has not been common in velocity models in previous years, assurance of not being stuck in a local (undesired) minimum is fundamental, as demonstrated by the new workflow.

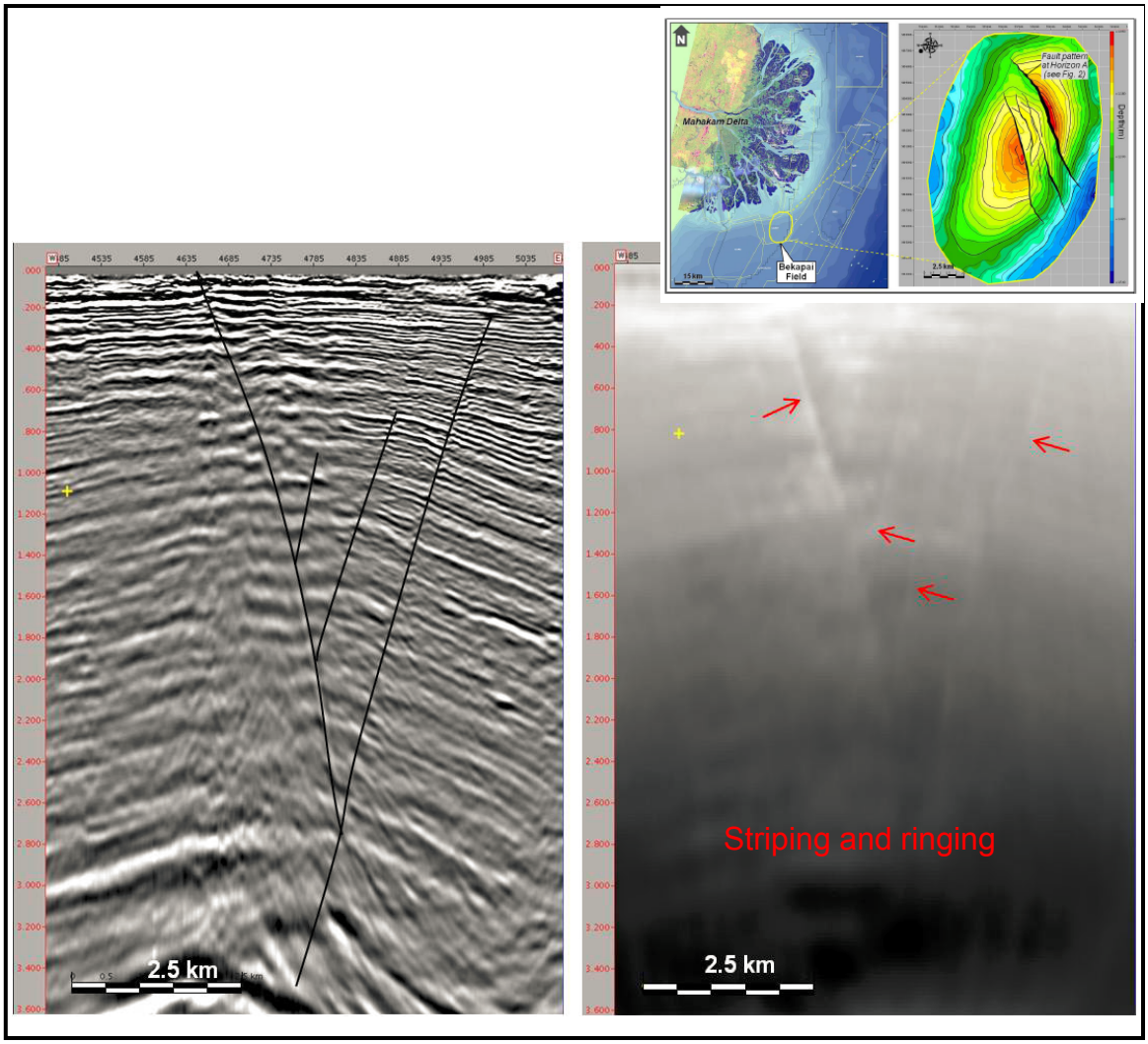


Figure 5-17: Showcase of FWI capability for the Bekapai Field Indonesia by Beele *et al.* (2014). The independent seismic image is illustrated on the left and the FWI model is illustrated on the right.

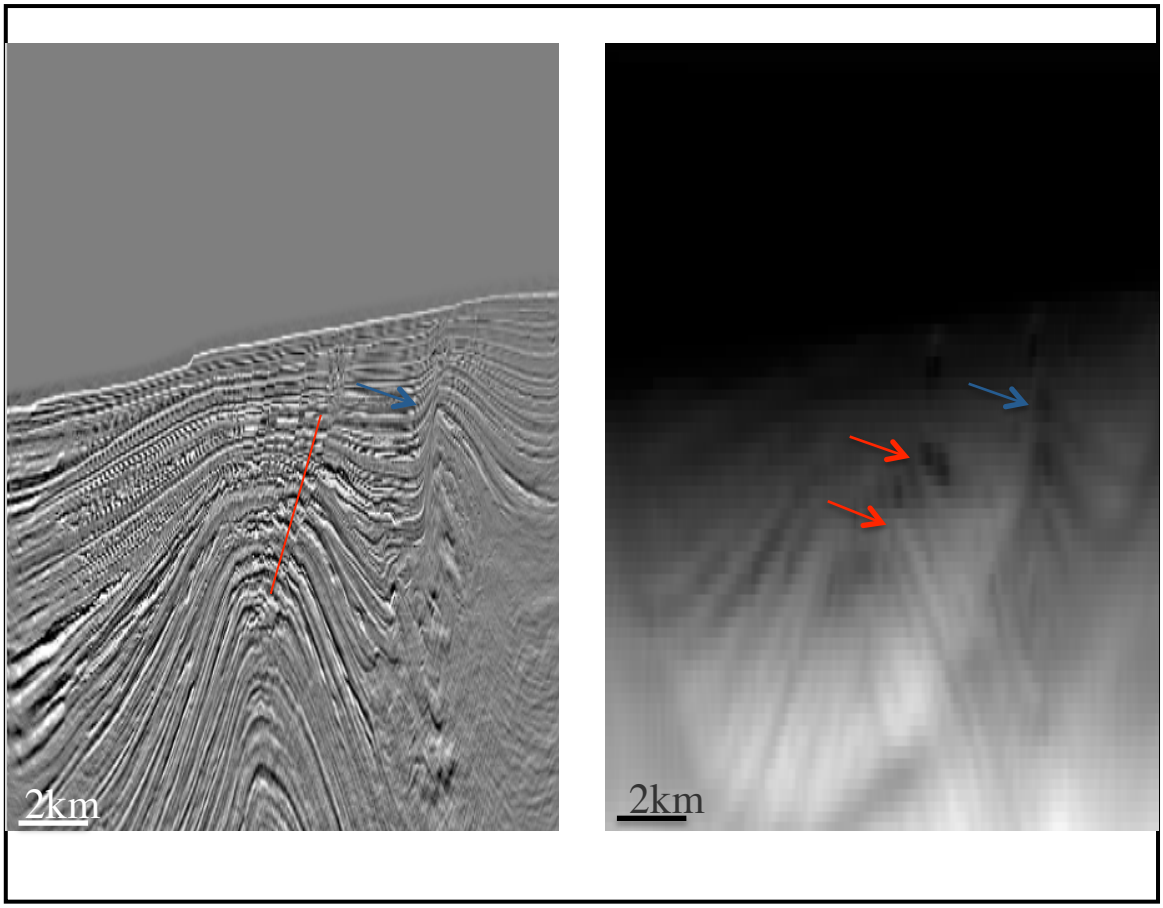


Figure 5-18: Capability at 6Hz showing the recovery of faults for Field A. The independent seismic image is illustrated on the left and the 6Hz FWI model is illustrated on the right.

In this study, at 15Hz, the effect of using the conditioned data is illustrated with a remarkable increase in the resolution of the model (Figure 5-19). The fault is clearly identified, the shale diapir structure to the right is also clearly evident. If some of the features in the FWI algorithm used are removed, the result will be stuck at the lower standard (comparable to that of Beele *et al*. (2014)) as shown in Figure 5-18. There is thus a big quality differential with this work compared to that of others, due to specific features in the FWI code (e.g spatial preconditionning of the gradient as described in Chapter 2). Moving to higher frequencies can thus lead to a continued advancement in the model.

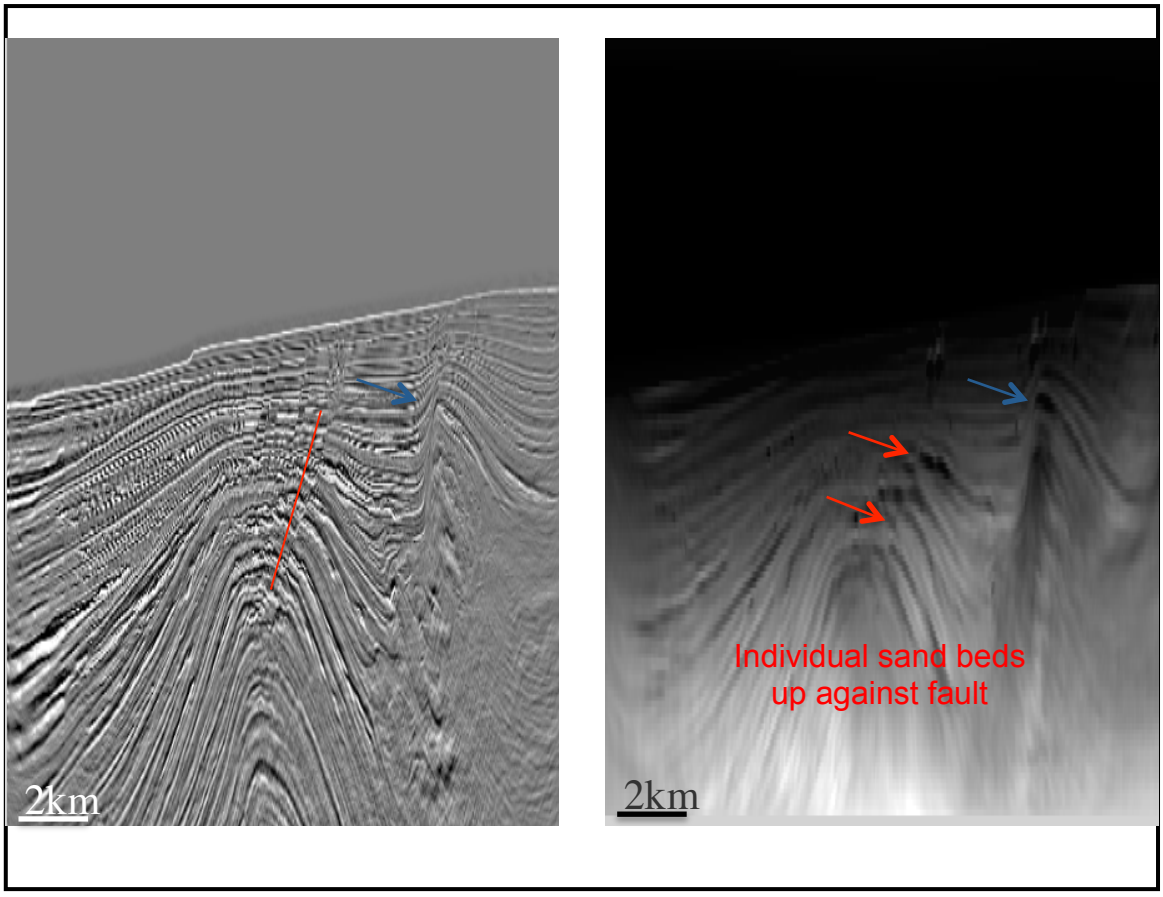


Figure 5-19: Capability at 15Hz showing the interpretability of the faults and individual bedding planes with saturated sands near the faults. This added capability involves the use of the new workflow. The independent seismic image is illustrated on the left and the 15Hz FWI model is illustrated on the right.

High Frequency results

FWI aids in the identification of the structural traps, and the reservoir intervals - pay zones. Figure 5-20 shows a vertical section through the starting model (top) and low frequency 6Hz FWI recovered model (bottom), both with and without the seismic overlay, highlighting the shallow low velocity pockets and the lateral extensive low velocity regions at the crest of the anticline, indicative of the presence of gas. The high frequency result for this same vertical section is then analysed. Figure 5-21 shows this detailed vertical section, through the 15Hz high frequency result, indicating the structural value FWI adds. The main symmetric anticline and the shallow asymmetric shale diapiric structure are also evident on this vertical section through the FWI model (Figure 5-21). Fault-related traps are also evident with saturated sands being bounded by fault.

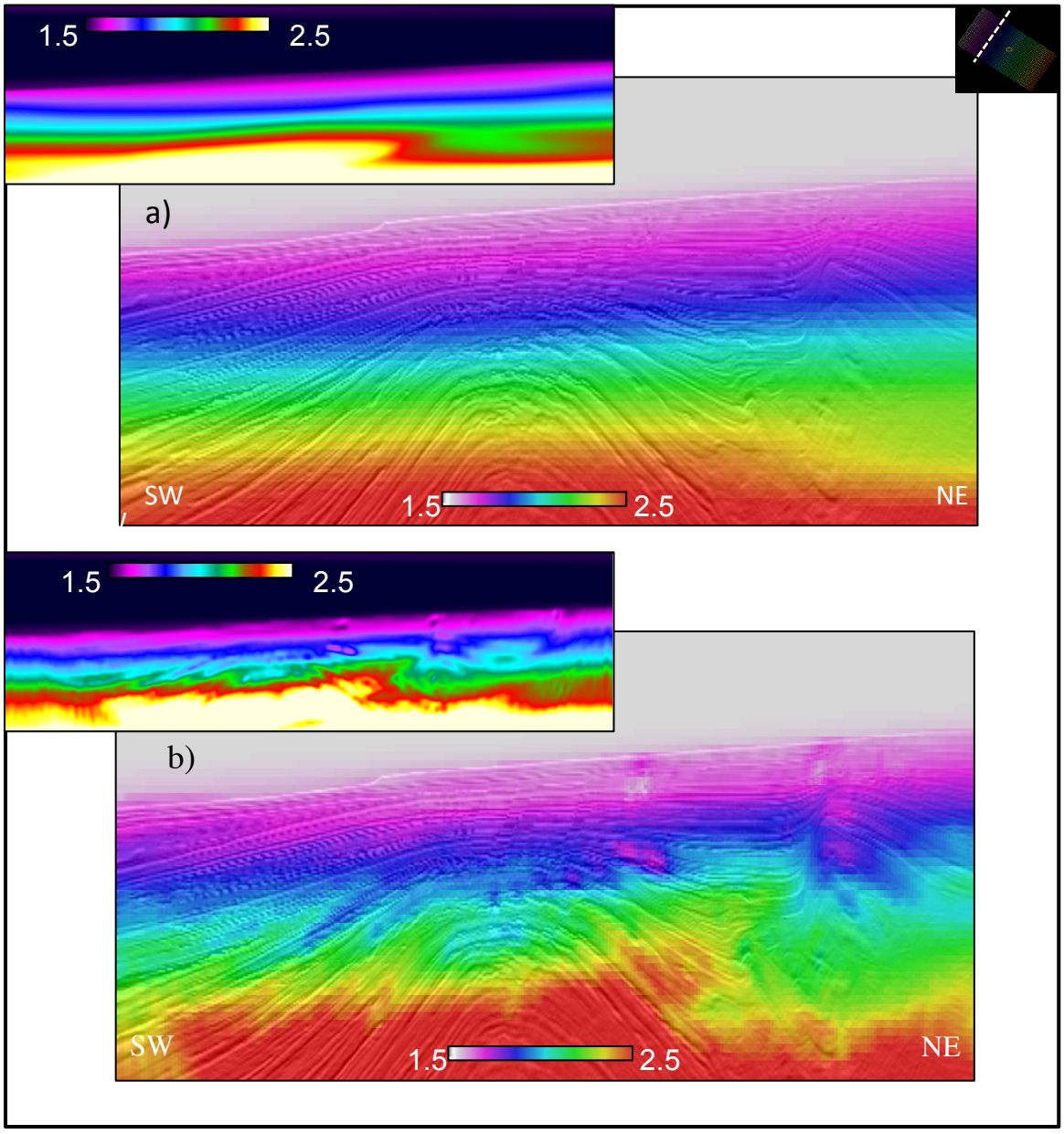


Figure 5-20: Vertical inline through starting (top) and 6Hz FWI recovered model (bottom). Shallow gas pockets are clearly visible and emergence of saturated sands bounded by a normal fault is evident.

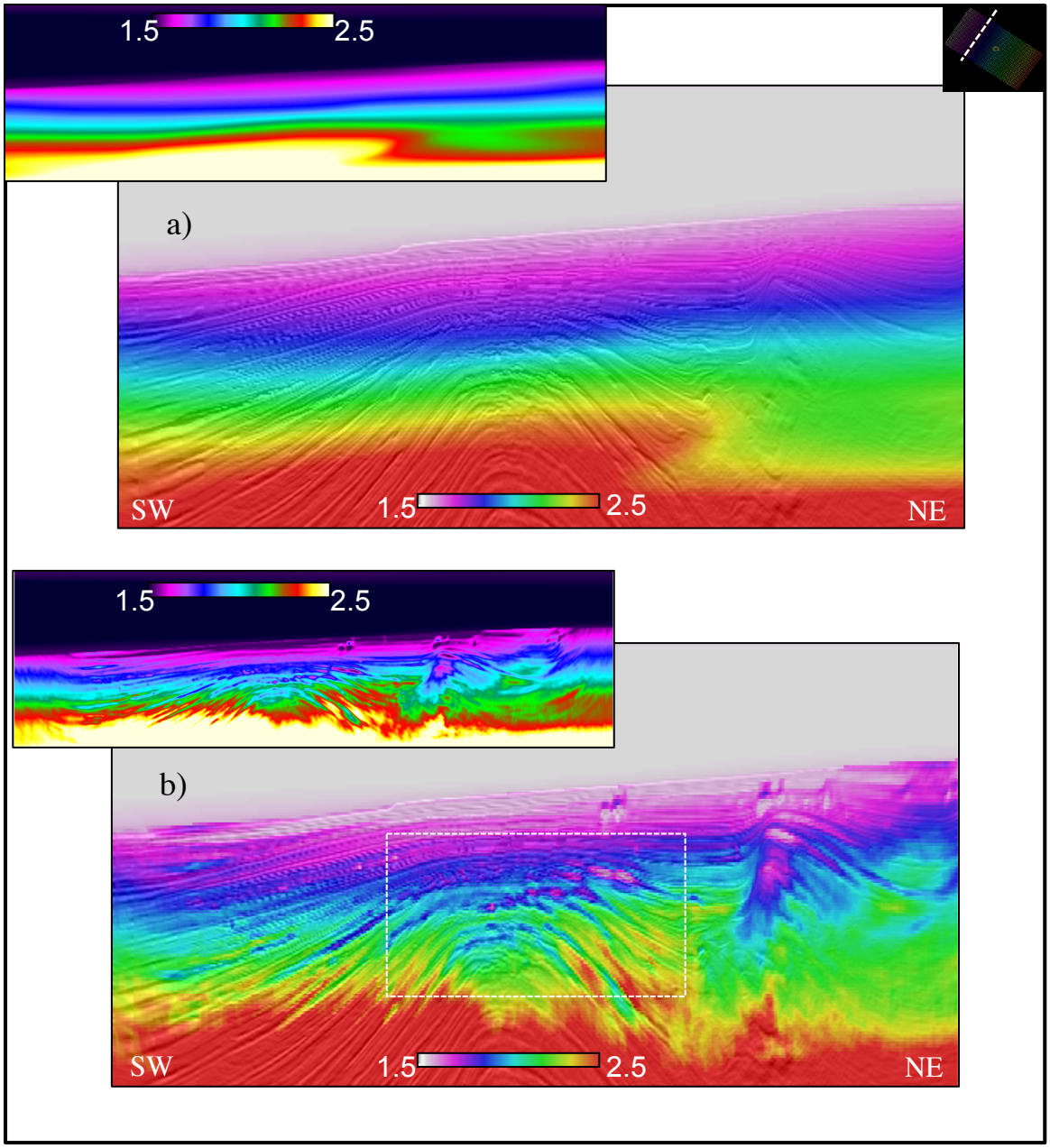


Figure 5-21: Vertical inline through the starting (top) and 15Hz FWI recovered model (bottom) overlay. Clear definition of gas pockets, saturated sands, faults and shallow diaper structure are shown. The white box indicates the enlarged region that follows in Figure 5-22.

A zoomed version across the anticlinal structure (Figure 5-22) shows clear pinchouts of saturated sands bounded by the well-defined normal fault. This is clearly visible on a) the recovered model b) the velocity model overlay and c) seismic image.

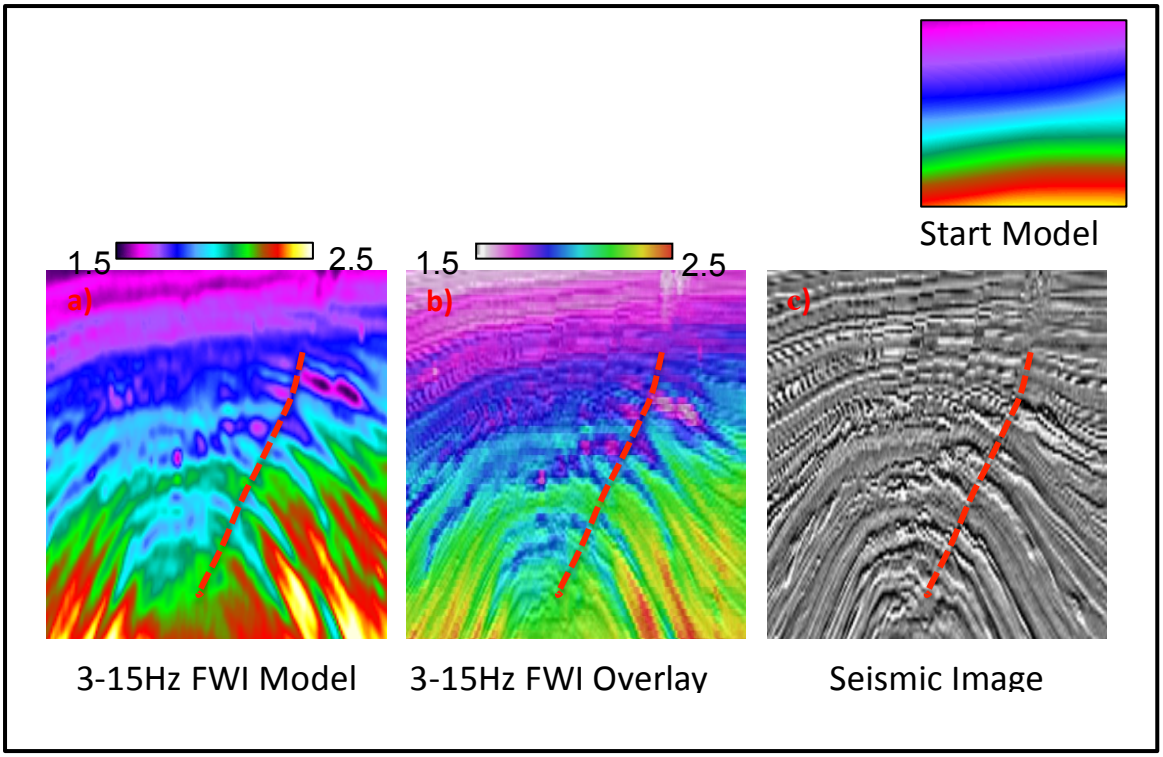


Figure 5-22: Zoomed in segment of the anticlinal structure of Figure 5-21 through the a) recovered model, b) model-seismic overlay, c) independent seismic image.

The velocities demonstrate conformance with the geology. Horizons can be carefully interpreted on this FWI recovered model, which can aid reservoir characterisation. When overlain with the seismic image, the strong correlation between both affirms the accuracy of the FWI model. However, FWI has the potential as a direct route to rock property estimation without the need to image the seismic data. Both anticlinal and fault-related structural traps, evident in the FWI models, can aid enhanced seismic interpretation. Additionally details for the velocities along the fault structures can give indication of the sealing and non-sealing nature of the faults.

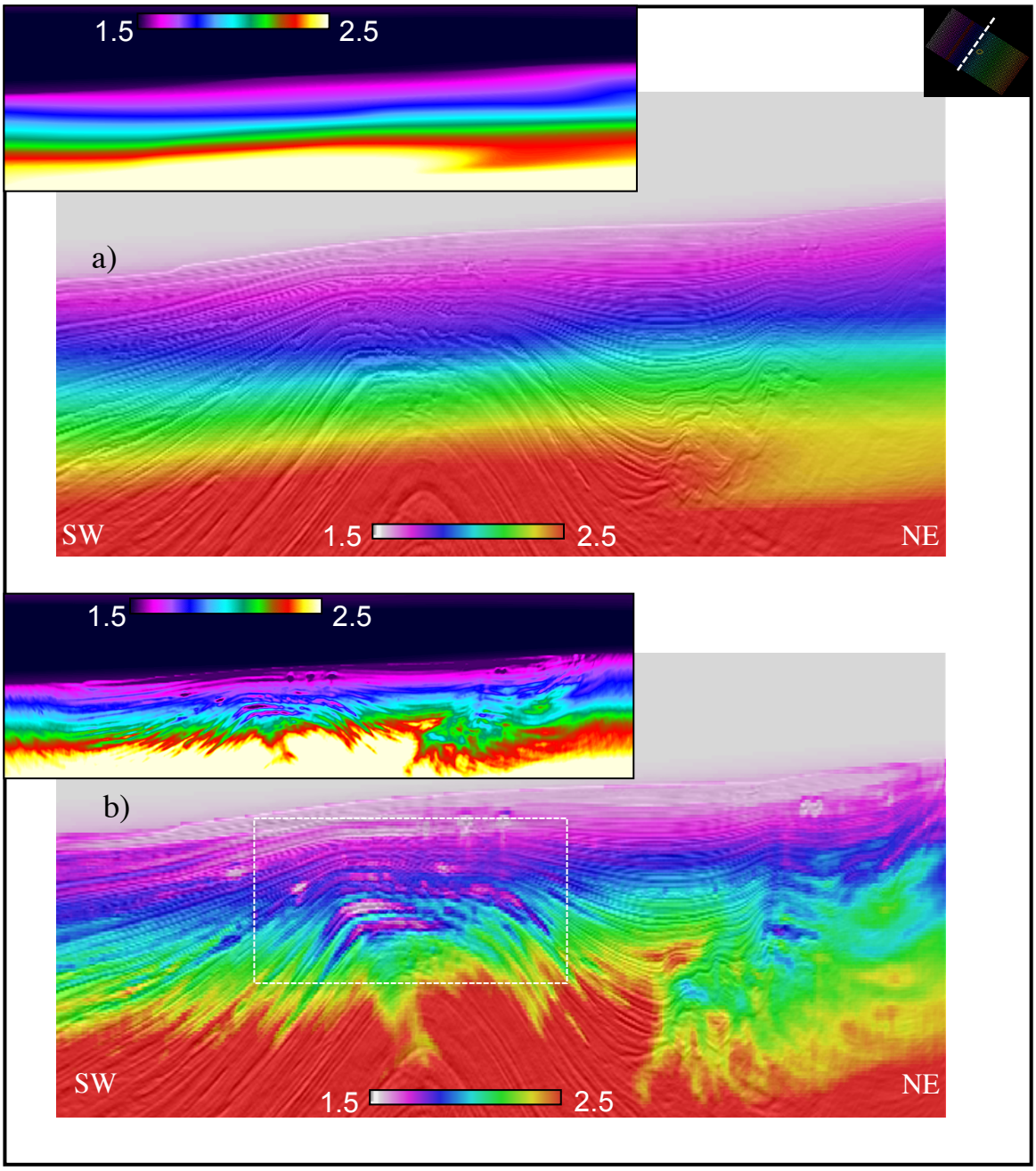


Figure 5-23: Vertical slice through a) the starting model overlay and b) 15Hz FWI model overlay. A series of normal faults are clearly discernable at the crest of the anticline. The white box highlights the zoomed region that follows in Figure 5-24.

Figure 5-23 shows another vertical section highlighting a series of faults at the crest of the anticline, evident in the FWI model and the seismic image. Figure 5-24 shows an enlarged view of the structural significance FWI adds.

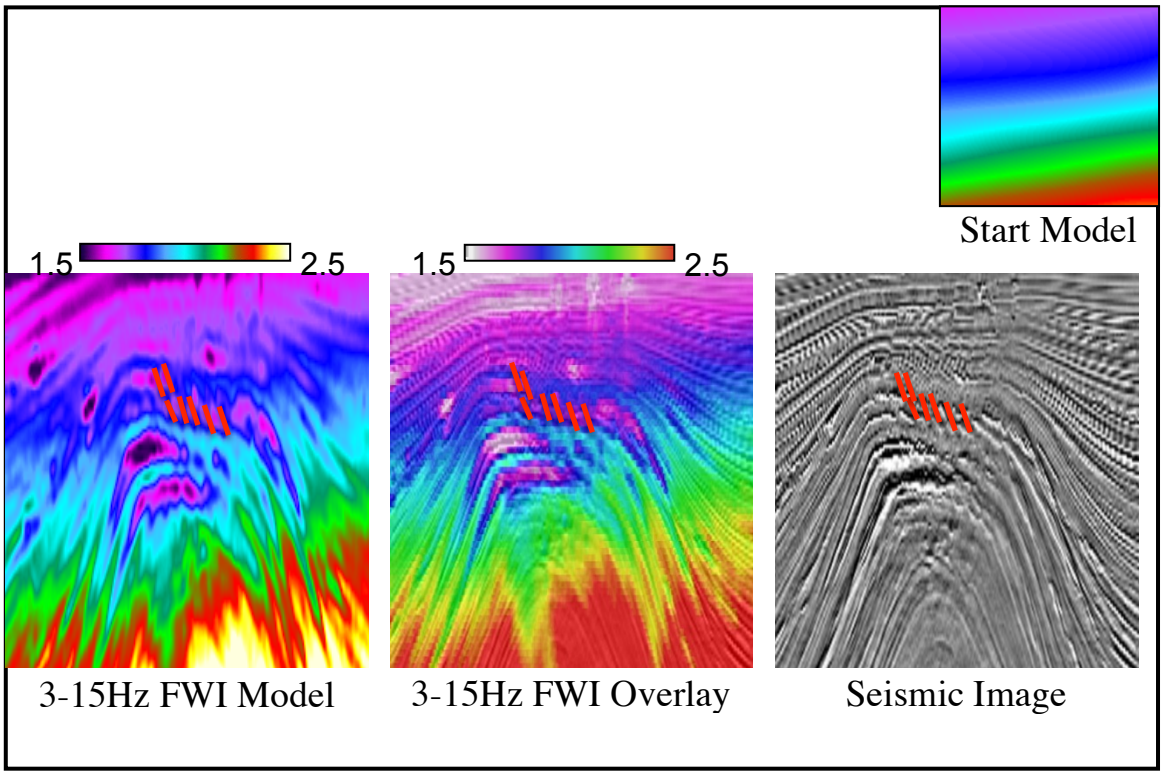


Figure 5-24: Zoomed in segment across the crest of the anticline showing the series of normal faults in the FWI model, the model-seismic overlay and the independent seismic image.

Migration

The subsurface angle gathers 1-69(2) degrees, four azimuths, were examined though inline 1890 by the Migration team within Chevron. Using the initial model, the raw migration output was generated by the Chevron migration team and is illustrated in Figure 5-25. Here the gathers obtained using the starting model for migration is not flat as is obtained with the use of the correct velocities. Using the FWI model in the generation of the gathers, the gathers are much better flattened (Figure 5-25). As a result of these improved gathers a better image of the thrust fault in the stacked image produced by the Chevron Migration team and is shown in the comparisons between the a) initial output and b) the FWI stacked output in Figure 5-26. This improvement is due to the change of the velocity models generated by this research. Added heterogeneity in the velocity model with FWI has improved the migration image. However, the question, which arises, is: Can the migration step be omitted and the FWI model used to generate a reflectivity volume?

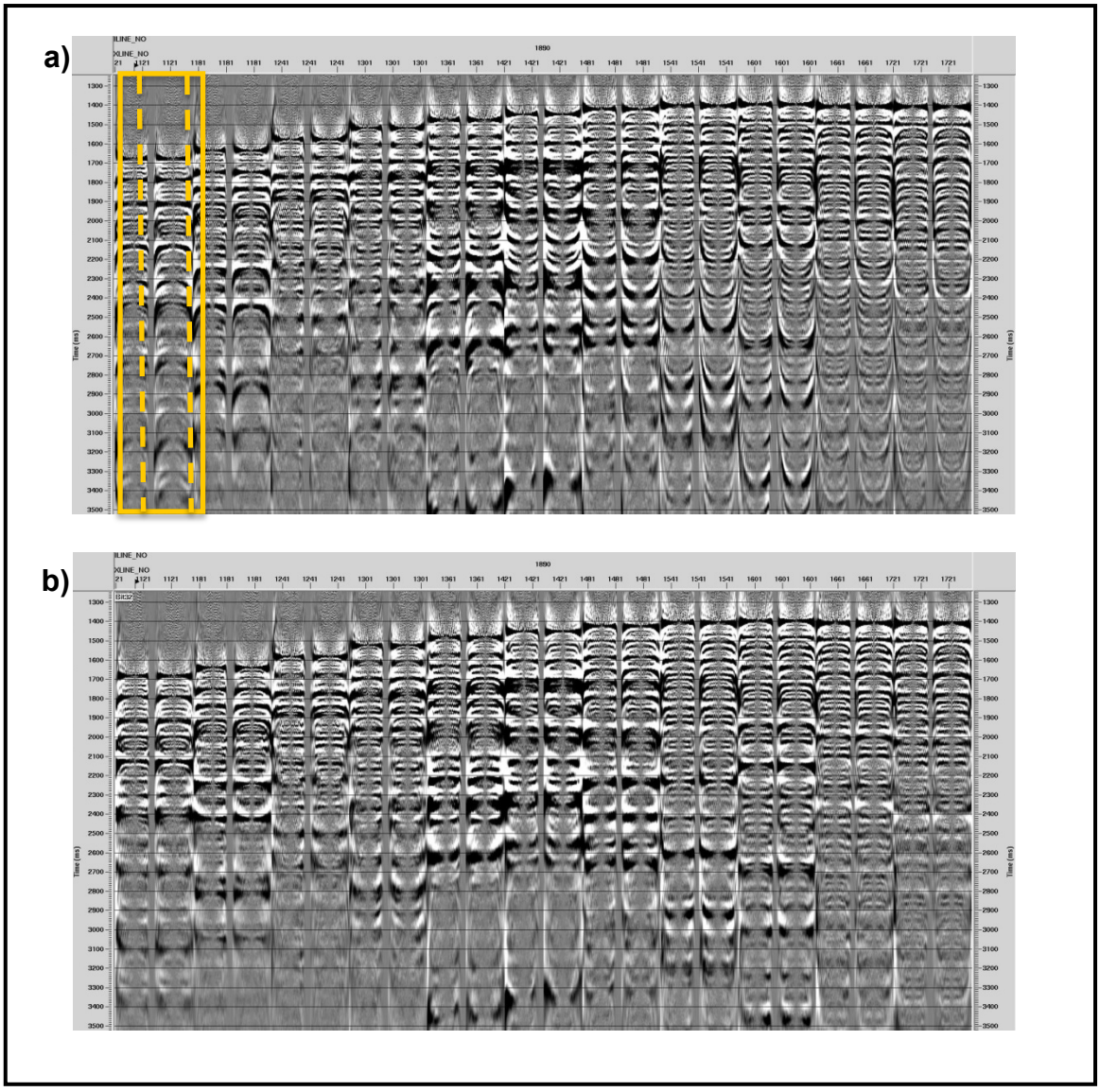


Figure 5-25: Raw migration gathers generated by the Chevron Migration team for a) initial model and b) FWI model produced from this research. Increased flatness of the gathers attributable to a better velocity model generated by FWI.

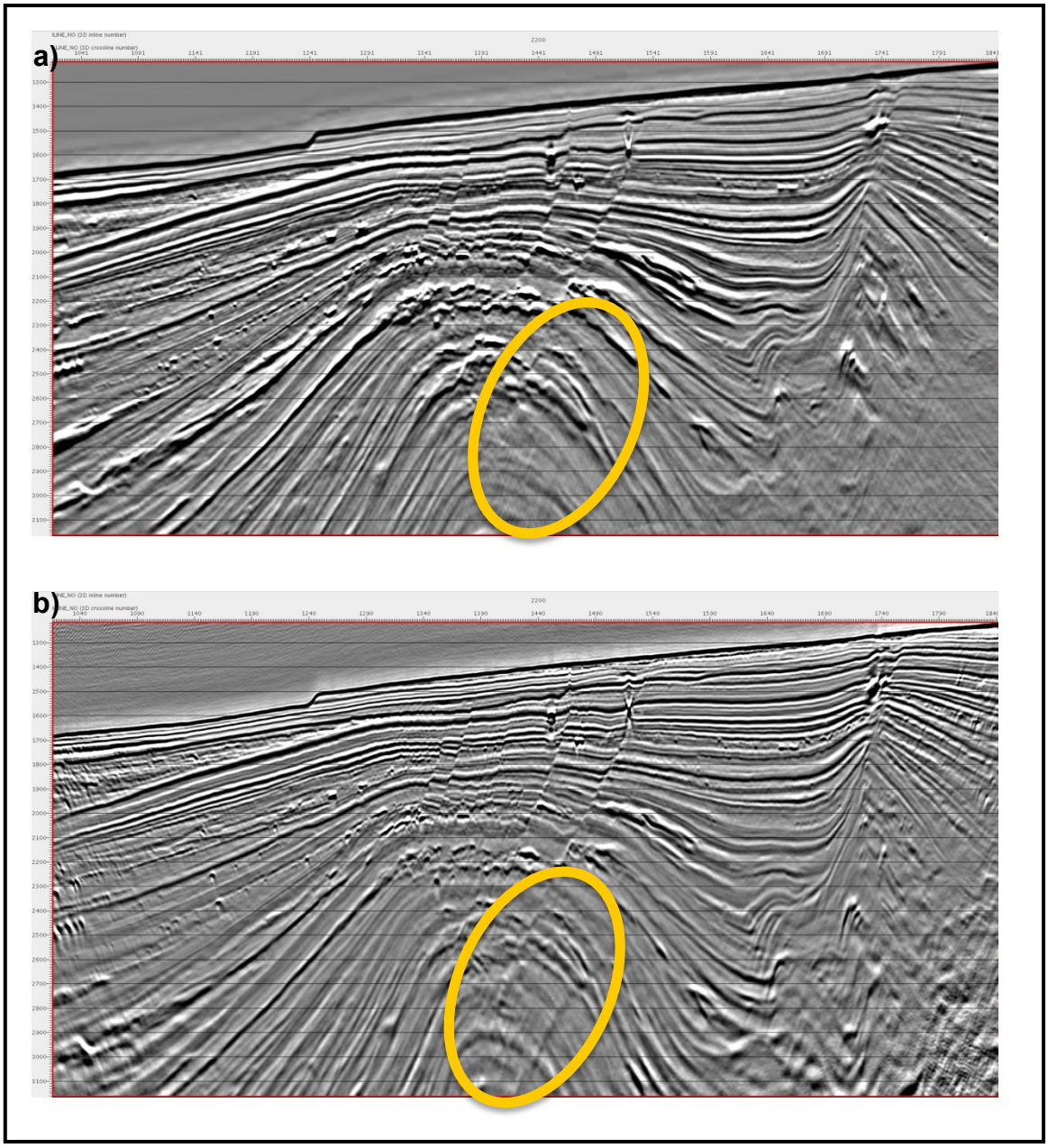


Figure 5-26: Stacked migration image generated by the Chevron Migration team generated using a) the starting model and b) FWI model produced by this research. Better definition of faults and geological interfaces.

Impact of Anisotropy

A fixed anisotropic model, that is, a vertical transverse isotropic (VTI) model, with limited lateral variations was used for the inversions. The different horizontal and vertical velocities are related by Thomsen's anisotropic parameters delta (δ) and epsilon (ε) (Warner *et al* 2013). These fixed anisotropic structures have proven sufficient for desired convergence, in

the direction of the most accurate FWI velocity model, as indicated by improved recovery, flatter common image gather and a better stacked image. Nonetheless, tests were undertaken to test the impact of a single verses a multi-parameter inversion, thereby assessing the effect of using a simple anisotropic model for FWI. When moving from single to multi-parameter inversion, the use of the full Hessian matrix becomes increasingly essential. The Hessian gives an indication of the curvature of the objective function and this will be of special importance with the introduction of more degrees of freedom – more parameters. The computational cost and efficiency however, remains unreasonable. Instead a first-order approximation to the diagonal of the Hessian – spatial preconditioning – is used. This preconditioning is computed such that every point of the diagonal is divided by the square of the incidence wavefield of the model. The pre-conditioned gradient-based update can be given by the formula,

$$\delta \mathbf{m} = -\alpha \boldsymbol{D}^{-1} \nabla_{\mathbf{m}} f. \tag{5-3}$$

Different parameterisations have varying degrees of compatibility with the pre-conditioned gradient approach. Here three different parameterisation procedures are explored. In each case delta is kept fixed at its good initial estimate because of ambiguity that arise between epsilon and delta, especially when delta doesn't change laterally. Epsilon can be defined by the following equation,

$$V_h^2 = V_v^2 (1+2\,\varepsilon), \tag{5-4}$$

where V_h is the horizontal velocity, V_v is the vertical velocity and ε is epsilon. The proposed formulation is a combination of the vertical velocity, V_v, and the horizontal velocity , V_h. Possible parameterisations included:

1. V_v and ε
2. V_v and V_h,
3. V_v+V_h and V_v-V_h – Proposed formulation

Data-misfit surfaces for a two-parameter model test were plotted as illustrated in Figure 5-27. These surfaces give a representation of how V_v, vertical axis of vertical velocity, vary with V_h, the horizontal axis of horizontal velocity. These objective function contour lines of constant travel times (data misfit surfaces) are oblique to the chosen axis of parameterisation forming narrow troughs – the basin of attraction. FWI aims to find the global minimum model that gives the smallest misfit at the centre of the basin of attraction. The diagonal of the Hessian serves to scale the gradient along the axis of parameterisation. Hence, given the orientation of the objective function, minimum valley, the axis of parameterisation is rotated by 45 degrees, thereby diagonlising the Hessian (i.e. allowing for effective scaling of the gradient). The new, orthogonal parameter axes are V_v-V_h=constant and V_v+V_h=constant; are now aligned with the objective function axes. The V_v-V_h=constant axes corresponds to the direction of maximum change of misfit. This is so because a positive perturbation in both V_v and V_h is required to keep the V_v-V_h axes constant thereby giving a maximum rate of change of misfit indicated by the objective function contours being closer together. The V_v+V_h=constant axes corresponds to the direction of minimum change of misfit. This is so because opposite signs of perturbation for V_v and V_h respectively, is required to keep the V_v+V_h axes constant thereby giving a minimum rate of change of misfit indicated by the objective function axes being further apart.

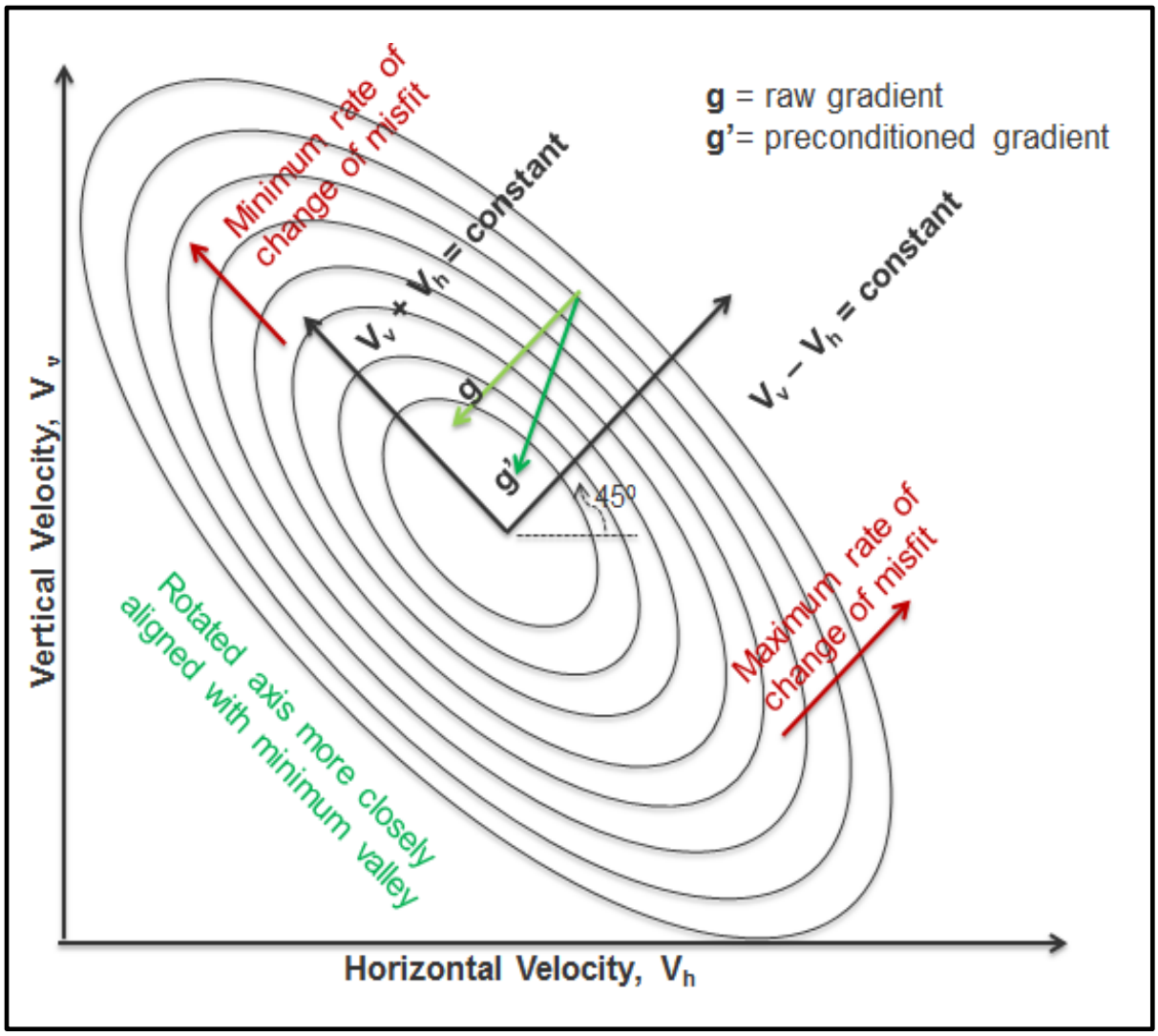


Figure 5-27: Representation of Objective Function surface in terms of horizontal and vertical velocities

Here, an example using the rotated parameter axes parameterisation to give output back to both velocity and epsilon is explored. A true P-wave velocity, V_p and true epsilon models were modelled to generate a synthetic observed dataset (Figure 5-28). The updated epsilon model is investigated with the inversion setup being illustrated in Figure 5-29. Using a zero epsilon starting model and inverting only for epsilon keeping V_p fixed at its true value, the predicted data is slow as the extra speed gained when propagating along the horizontal direction compared to the vertical (i.e. epsilon) is unaccounted for.

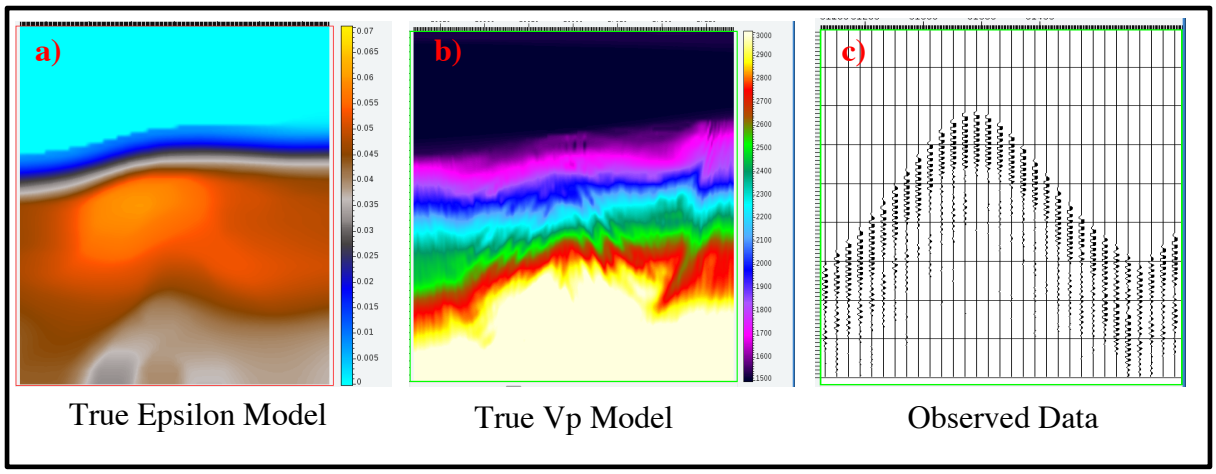


Figure 5-28: The a) true epsilon model; b) true velocity model and the c) corresponding observed dataset

The long offsets thus play a key role in an epsilon FWI model update. As such, the limits of the update are limited to the central portion of the model with update at depth and at the edges being zero, that is, the starting model remained unchanged at zero.

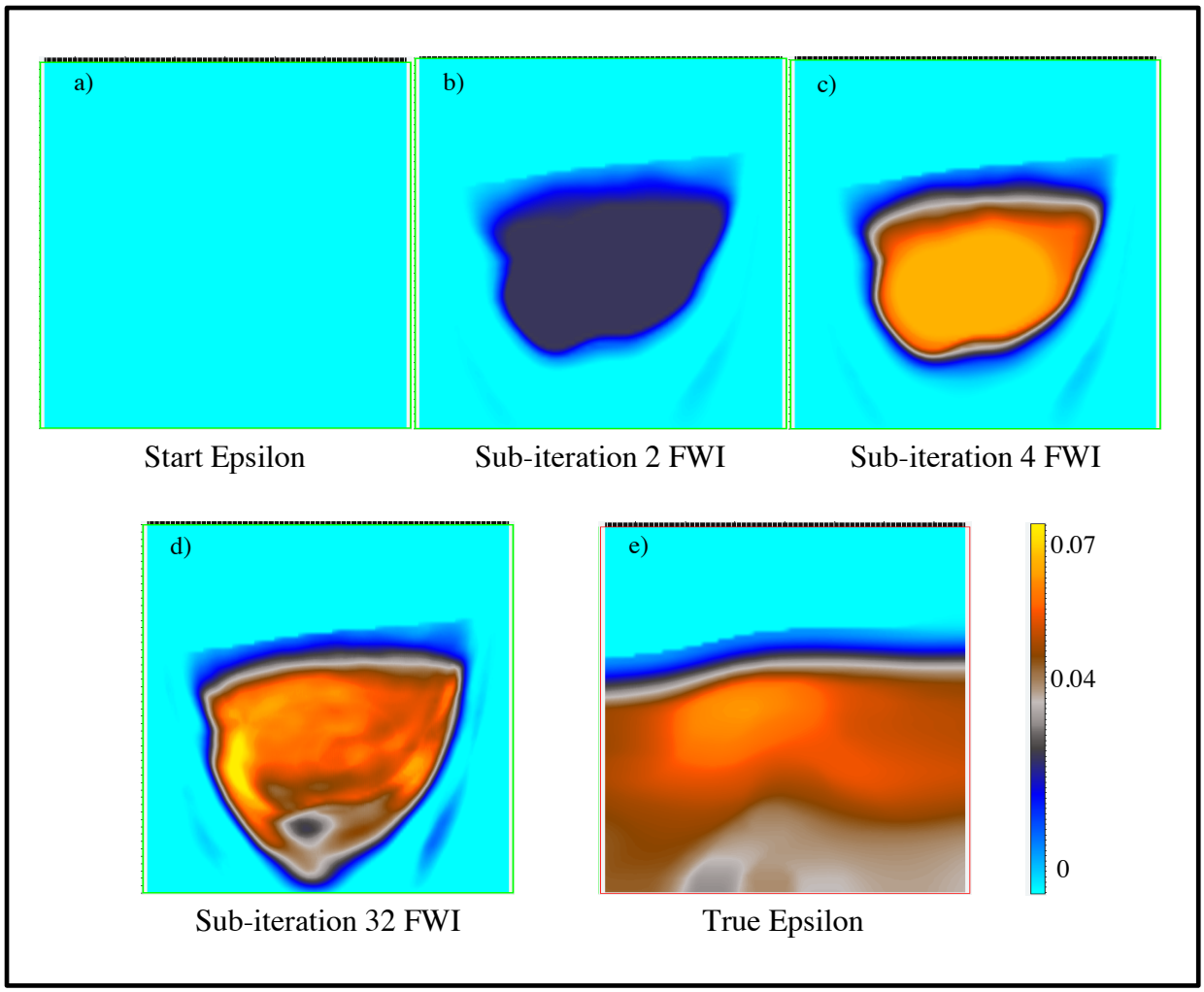


Figure 5-29: The inversion for anisotropy using a) start epsilon of zero and the FWI recovered epsilon models after b) 2 sub-iterations c) 8 sub-iterations d) 32 sub-iterations and the corresponding e) true epsilon model. The update is focused in the central portion of the model.

The updated epsilon model, after 1 iteration and 2 sub-iterations was heading in the correct direction with the delay in predicted data becoming less at the far offsets (See Figure 5-29 and Figure 5-30). After 4 sub-iterations the recovered model epsilon values were almost quantitatively correct with the mismatch in travel-time between the observed and predicted data being removed. Inverting up to 32 iterations refined the epsilon model, correcting areas of over and under-estimation and introduced epsilon variations with depth. This lead to a further improvement in the predicted data relative to the observed data – the shape of the waveform and the amplitude variations was improved (See Figure 5-30).

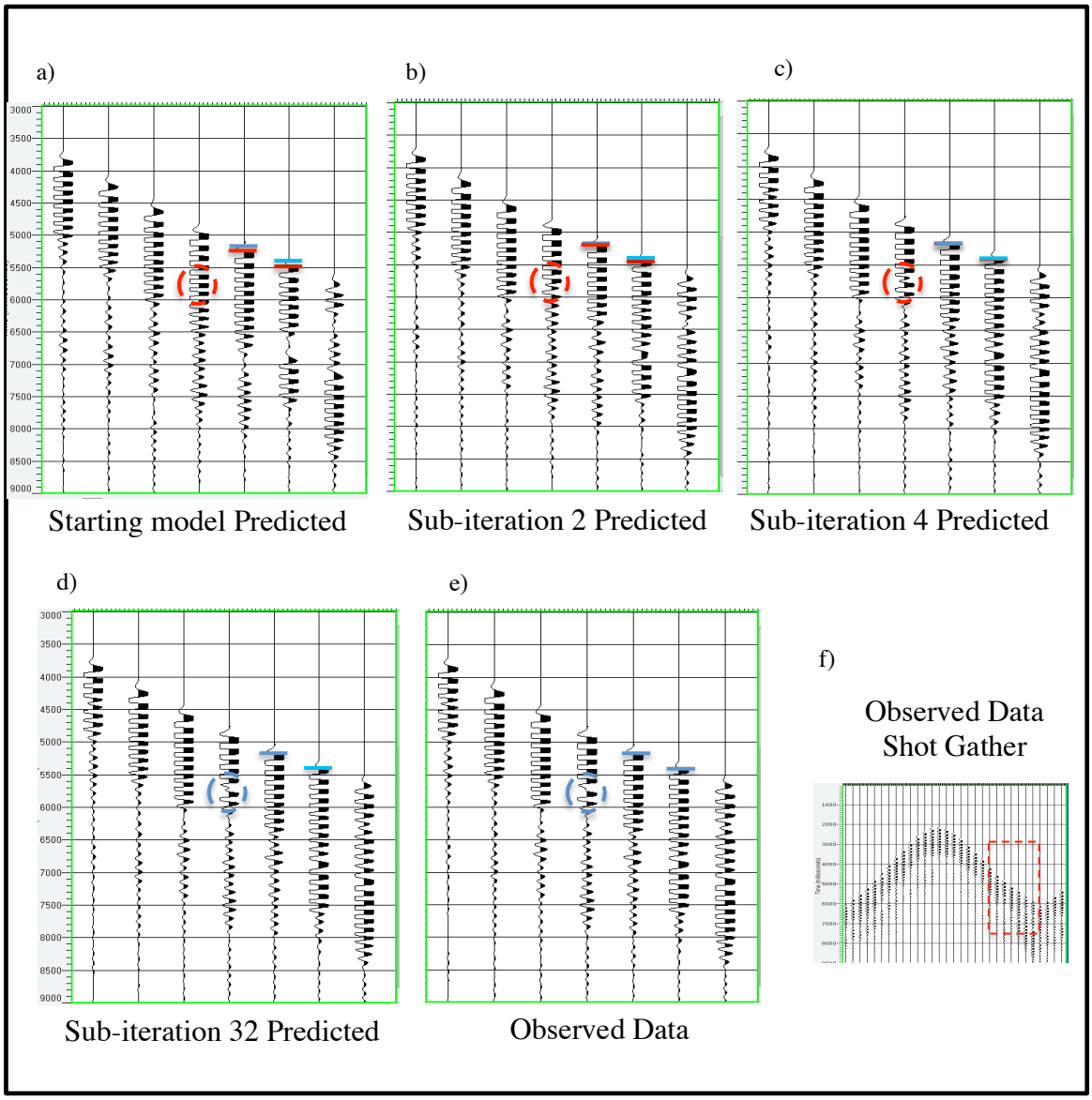


Figure 5-30: The long offset arrivals for different models: a) starting model b) sub-iteration 2 FWI model c) sub-iteration 4 FWI model d) sub-iteration 32 FWI model and the corresponding e) observed dataset extracted from the shot gather as shown in f).

Depth slices at 2050m also show more clearly the coverage of the epsilon model update as well as the quantitative accuracy with which the FWI epsilon model update is recovered (Figure 5-31).

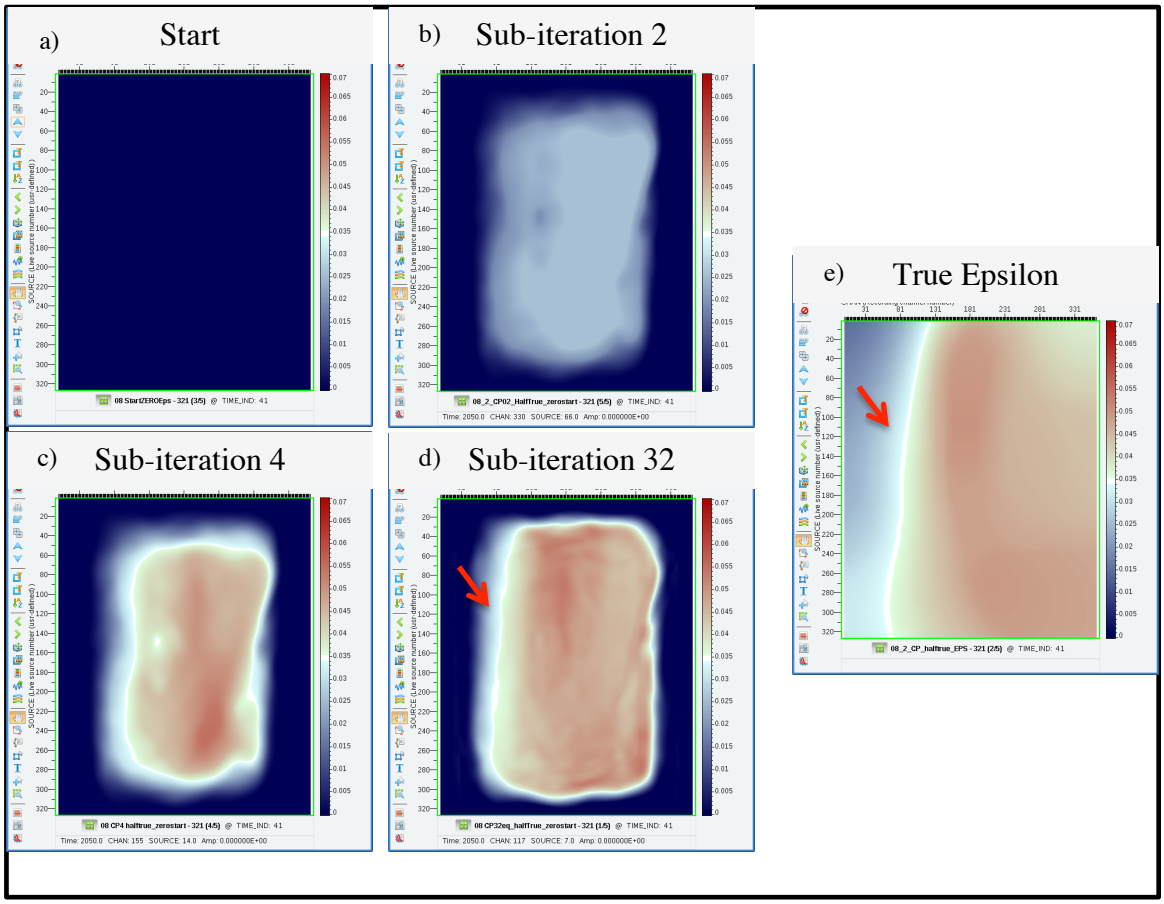


Figure 5-31: 2050m depth slices showing the recovery of specific structures in the epsilon model

The models have been updated in a rotated parameter space with results in the velocity and epsilon space. The recovery of the varying epsilon trend with depth is observed with this scheme. The quantitative values of recovered epsilon are accurate and the data fits in both the travel-time and waveform detail. With multi-parameter inversion, where multiple starting models are used to initiate FWI, particular attention is paid to the data misfit, ensuring that the starting models used are always within half-cycle of the observed data. Current multi-parameter FWI work focuses on a hybrid inversion scheme, for surface seismic data, that combines global inversion for anisotropy with local inversion for P-wave velocity (Debens *et al*. 2015). Debens *et al*. (2015) demonstrated that the global approach does not capture the intensity of the high epsilon layer, however, it captures the form and structure of the model to deeper depths. Thus, a hybrid inversion scheme for anisotropy whereby global FWI provides a desirable starting model for subsequent local FWI is the recommended route forward. Updating both the P-wave velocity and epsilon models will further enhance the subsurface characterisation of the earth aiding improved oil/gas exploration and development.

Field B Results

The starting model is a legacy model from streamer data. FWI has introduced several features, which correlate strongly with the geology for the field. FWI gives both the property and the geometry that is the velocity and the shape, of the reservoir interval as well as shallow gas pockets. Figure 5-32 shows the inline and crossline views through the starting model and the respective 6Hz FWI model. The fault blocks are discernable on the FWI model with displacement evident along listric growth faults and accompanying antithetic faults. The crossline view through the FWI model also shows the extent of the reservoir to be 5km across and 100m deep. The bottom slope channel complex is compartmentalized (Figure 5-32b) due to erosion as the above complex was deposited. The right hand side is encased by shale and this is evident on the logs as well. The reservoirs form part of a slope valley system, which can be characterized by a bypass phase, a disorganized channel phase, an organized channel phase, and an abandonment (transgressive) phase. Forced regressive high density massive turbiditic sands form the disorganized channel complexes of higher net-to-gross and low-density, turbiditic stacked lowstand channel levees form the organized channel complexes (lower net-to-gross). The internal structure of the reservoirs is a key component of the petroleum system for this field and indications of this internal structure are evident in the FWI velocity models.

The high contrast top salt boundary is also fine-tuned. Using seismic only, shows only the geometry of identified features. Low velocity zones of larger extents, once identified, can add to the geological interpretation of the prospectivity of the field as low velocity zones are highly linked to higher porosity. With this added lithological significance with FWI, and better understanding of the low velocity reservoir architecture with a good match to well logs, the injector and producer positions can be better determined thereby draining the area with fewer wells. Added information, that corroborates the geological information learnt from the well logs and other necessary tools, the gross-rock volume can be recomputed using this new FWI product and thereby pin point where injectors are relative to producers.

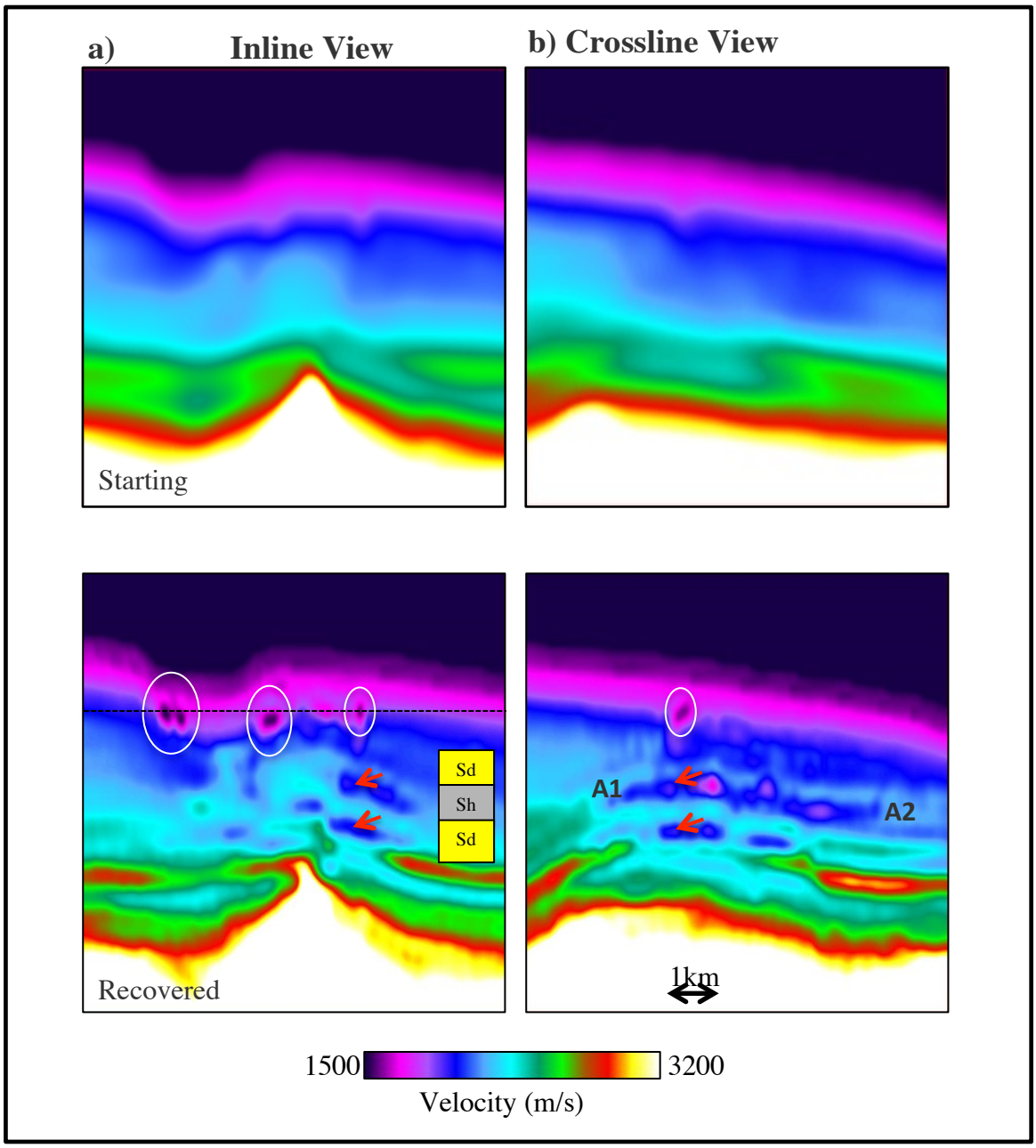


Figure 5-32: Starting model produced by Chevron (top) and high resolution FWI model - growth fault, reservoirs architecture, extent of reservoir, shallow gas pockets are all identified

A closer look at the shallow gas pockets and the fault planes are shown in Figure 5-33 and Figure 5-34 respectively. Figure 5-33 highlights a shallow depth slice through the starting and the FWI model. The geometry and extent of these pockets are evident and clearly visible. The fault planes are also evident as shown in Figure 5-34. Two faults clearly intersect at the apex forming three different fault blocks. The upper sand reservoir highlighted at this level shows four-way closure with a combination of fault-related structural closure and stratigraphic closure.

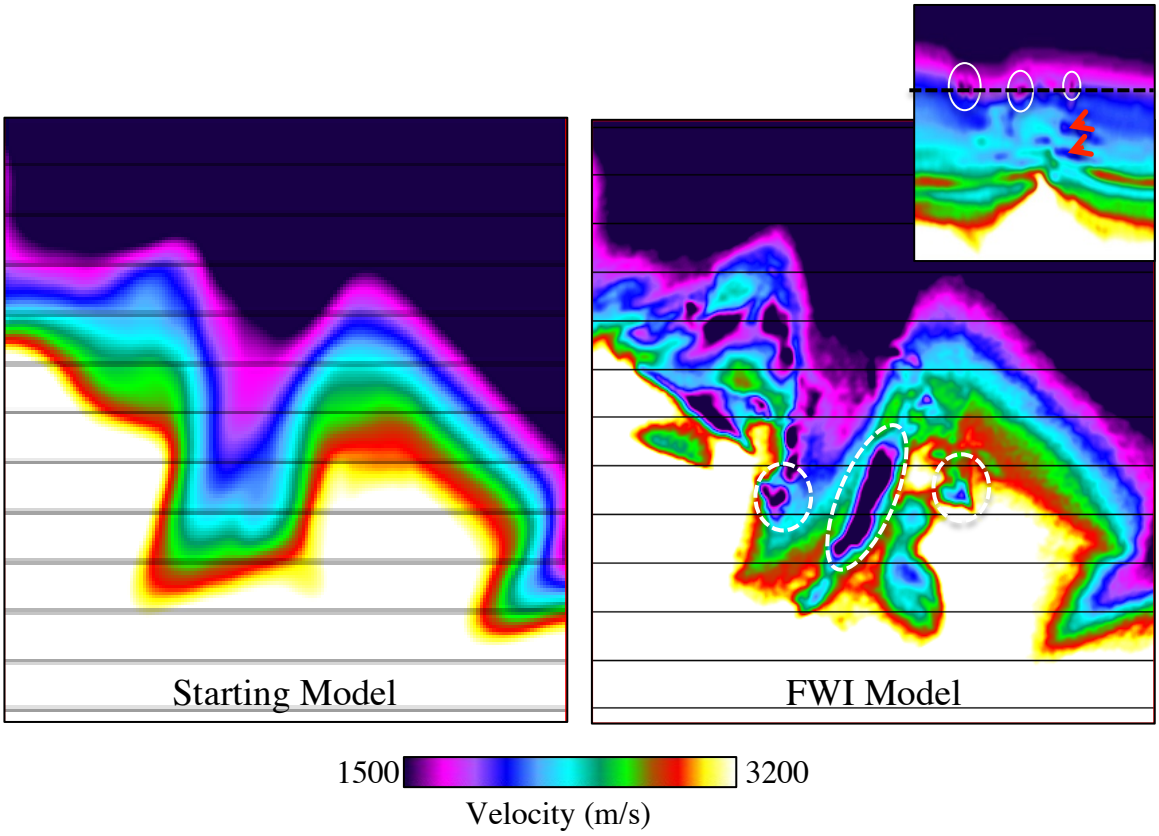


Figure 5-33: Depth slice through gas pockets at shallow depth showing its geometry and extent

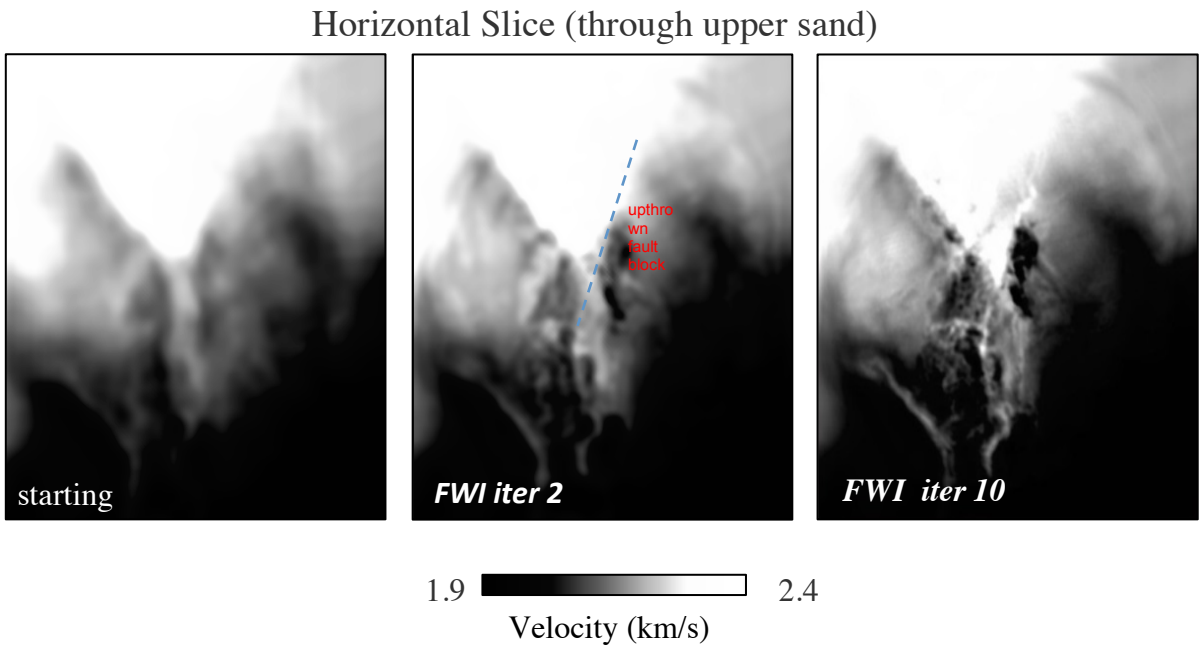


Figure 5-34: Depth slice showing the reservoir formation in the upthrown block with fault & dip closure

Reflectivity sections from FWI models

A reflectivity volume at normal incidence, analogous to the derivative of the FWI velocity model for Field A, was computed using the equation 5-5 below, where ϱ is the density and v is the velocity,

$$Refelctivity = \frac{\rho_2 v_2 - \rho_1 v_1}{\rho_2 v_{2+} \rho_1 v_1}.$$

(5-5)

The reflectivity models are generated such that an increase in acoustic impedance with depth, for example at the seabed, is indicated by a hard loop (black) and a decrease in acoustic impedance is represented by a soft (white) loop. Figure 5-35 shows a schematic of this concept.

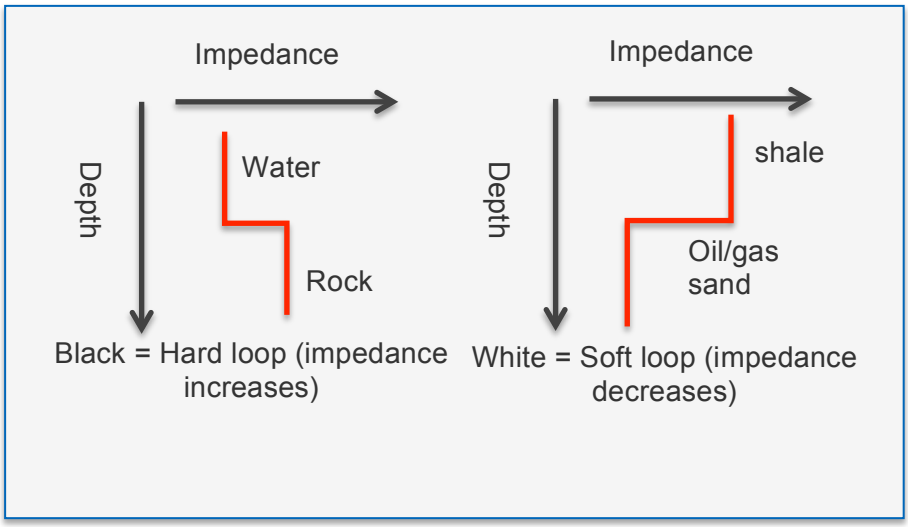


Figure 5-35: Schematic of the meaning of an impedance increase and decrease.

The velocity models were examined at different frequency bands (Figure 5-36) and the corresponding reflectivity models (Figure 5-37) were generated. As the frequency is increased from 3-10Hz band to 3-15Hz band, a clear sharpening of the reflector interfaces is observed. As the frequency band is increased further to the 3-20 Hz band, even more sharpening of the reflector interfaces is discerned. There is a slow change in the velocity (and hence the reflectivity) at the seabed interface, typical of deep-water datasets, due to the slow compaction.

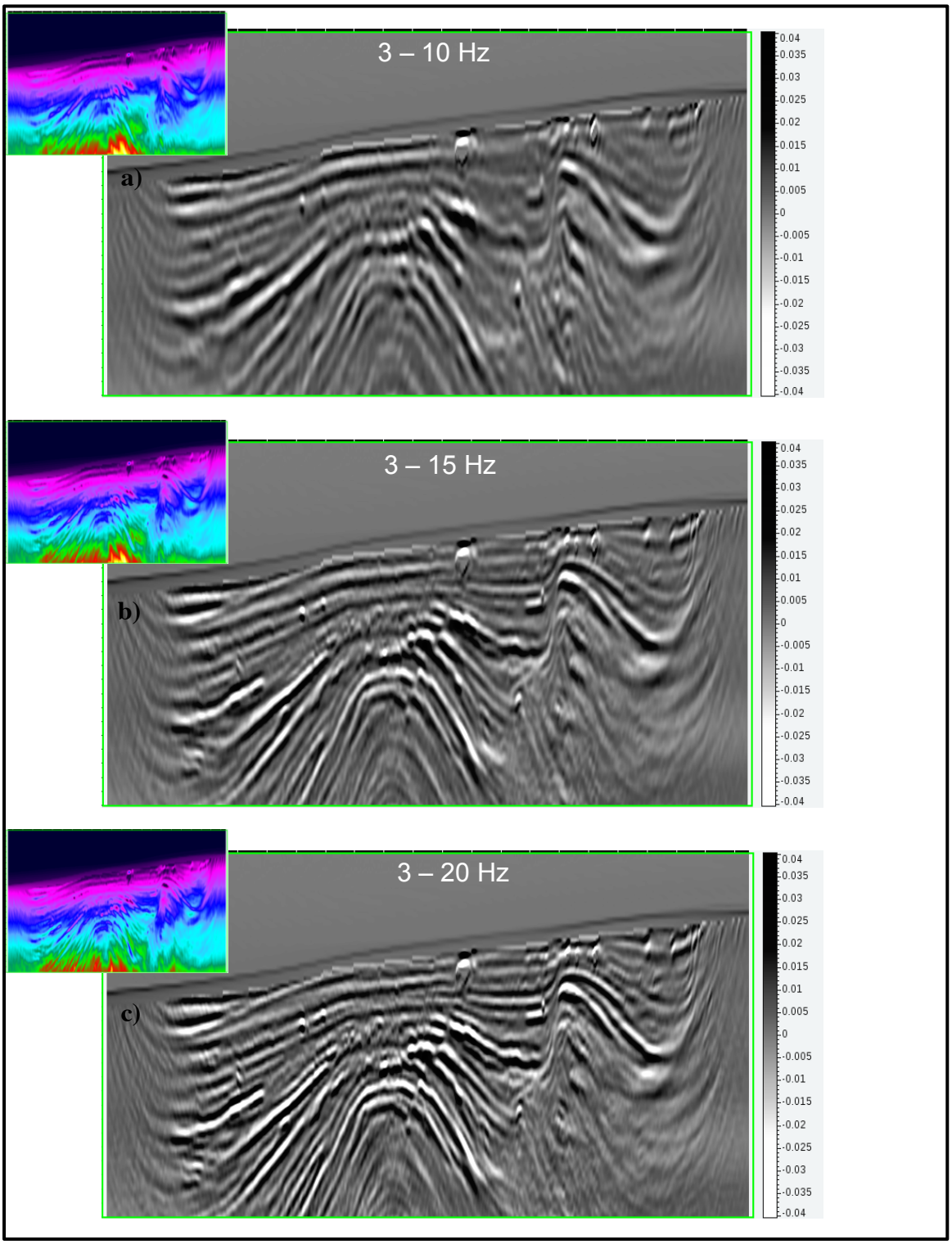


Figure 5-36: Reflectivity sections obtained directly from the FWI velocity models at a) 3-10Hz band b) 3-15Hz band c) 3-20Hz band with the corresponding FWI recovered velocity models in the insets

All the information contained in the seismic record is being mapped into the velocity model. The two fields recovered by full waveform inversion add tremendously to the direct interpretability and reservoir-aided characterisation that FWI brings to the table. Figure 5-37 summarizes the computation of these two fields and illustrates the next logical step forward – the use of a decomposed gradient where the wavefield indicated in blue represents the reflected energy and the wavefield indicated in red represents the incidence energy. With these advancements, FWI can eventually replace conventional processing and migration – all that is needed, is a full-bandwidth velocity model.

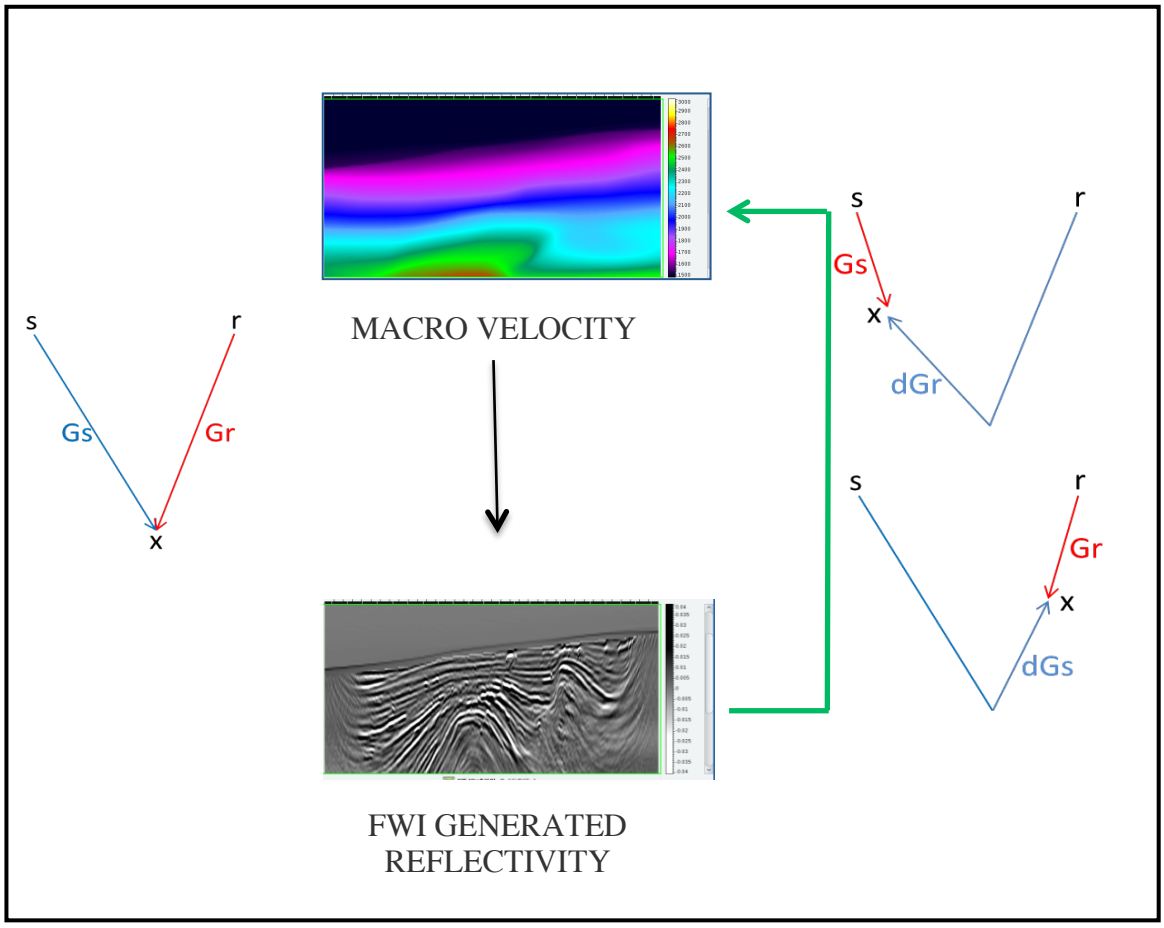


Figure 5-37: Schematic showing the 2 fields extracted from FWI – the macro-velocity and the FWI reflectivity. The gradient representation on the left is the current practice and the decomposed gradient representation on the right is the next logical step to close the loop

FWI and 4D seismics

Advancements in FWI leading to an extension to higher bandwidths and recovery at deeper depths, can also aid subsurface reservoir characterisation and improved imaging, through FWI of time-lapse data, producing remarkable results. The application of FWI to 4D seismic data whereby time-lapse velocity model changes can be directly obtained from the data is an area of continued research (Routh *et al*. 2012). This research thesis revealed that FWI to higher bandwidths can update both low and high frequency components of the velocity field and this is ideally suited for 4D problems. Two approaches that can be used in obtaining a time-lapse velocity anomaly, useful in assessing injection and production effects for different oil and gas fields are discussed in Routh *et al*. (2012). Using a model differencing approach, the base and the monitor data can be inverted starting with the same initial model and the time-lapse velocity anomaly being obtained by differencing the base and monitor FWI models. The second approach, as discussed by Routh *et al*. 2012, uses the base FWI model as the starting model for the monitor inversion with the resulting time-lapse anomaly from the monitor FWI. Routh *et al*. (2012) found that the second approach was proven to be superior to the differencing approach with fewer artefacts and a clear high-resolution time-lapse anomaly in the region of the reservoir. As such, continued advancements in FWI and 4D seismic technology can be useful for direct monitoring interpretation.

Summary

The bandwidth of FWI was successfully extended with a seamless transition from low to higher bandwidth without getting stuck in a local minimum. With this increased bandwidth, reflections were accurately inverted leading to an increase of the FWI depth penetration. The increased resolution and detail introduced by FWI with progress from low bandwidth to higher bandwidth leads to a good match to the independent seismic image. With further advancement and use of a decomposed gradient, a reflectivity image from FWI is successfully generated.

As a result there is an increased capability with FWI aiding reservoir characterisation, improving shallow hazard analysis, enhancing fault/horizon interpretation, yielding higher resolution models. This capability was demonstrated on Field A and B with a summary of the results highlighted in Figure 5-38. Taking this technology even further is the ultimate aim

thereby impacting more assets with FWI, and impacting them earlier in their life cycle – in the pre-production phase where the objective is mainly to increase discoveries and volumes. At its current stage, the production phase, FWI can reduce well counts and increase recovery rates with better reservoir characterisation and field development.

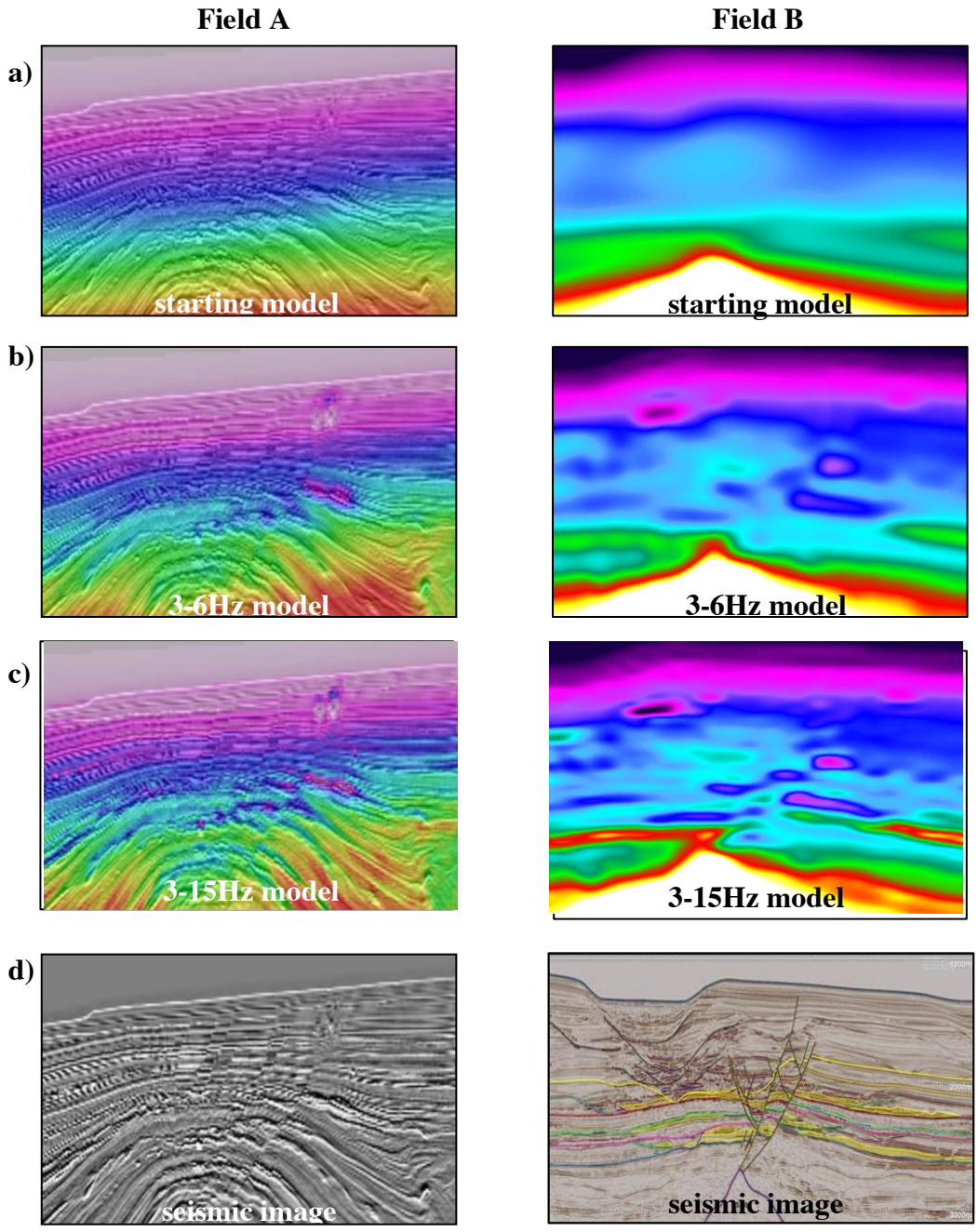


Figure 5-38: Illustration of the a) starting models b) 3-6Hz FWI recovered models c) 3-15Hz FWI models and d) independent seismic image; for Field A and B.

Chapter 6 : Conclusions

Successful practical strategies for three-dimensional, acoustic, anisotropic full-waveform inversion (FWI) were developed and implemented. Key strategies for the inversion of a simple reflection-dominated synthetic dataset were investigated to exploit the use of primarily reflection energy in the inversions. Workflows and significant strategies were also developed with the aim of increasing the model resolution and depth penetration, for the inversion of both shallow-water and deep-water ocean-bottom-node (OBN) field datasets.

Synthetic inversion tests exploiting primarily the reflection energy revealed that muting of the early-arrivals, time windowing, and layer-stripping, are all key strategies to be adopted. These strategies have been incorporated into other schemes being developed on the inversion of solely reflection targets. Development of schemes to allow for FWI on these reflection-only types of datasets is on going and very promising. This will allow for FWI of exploration-type streamer datasets, taking the technique to a more influential level in the bid-round phase of the oil and gas business.

FWI of the shallow-water OBN dataset revealed that there is a systematic mismatch between the observed and predicted data for the FWI model, with the predicted data being consistently delayed in time. The mismatch was suspected to have arisen because of inadequacies in the physics to account for unknown physical effects are used during inversion. An offset-variable water density strategy was developed and it was found to compensate efficiently and heuristically for these inaccuracies during the inversion; improving the travel-time match, increasing the model resolution, better flattening common-image gathers, thereby giving a closer fit to well logs, and an improvement in the pre-stack depth-migrated image. However, automating the density selection process will further improve the efficiency of this strategy.

FWI of two deep-water OBN datasets was undertaken using an enhanced version of the afore-mentioned density-selection process near the sea-bottom, whereby the densities generated are based on the minimum water and rock velocities specified. This leads to a better fit of the first-order water-bottom multiple. Additionally, the observed data was conditioned using an adaptive matching strategy. This adaptive-matching strategy conditions the observed data such that the early-arriving wavefield and the first-order water-bottom multiple are well matched to that of the predicted data from the starting model prior to FWI, thereby avoiding local minima and gaining further model improvements with further

iterations of optimisation. Moreover, the accuracy of the macro-model update obtained using the transmitted arrivals is enhanced. With the introduction of higher frequencies, the limits of depth penetration and model resolution of the update is valuably pushed, with greater weight being placed on the reflected energy during the inversion. The reflectivity is thus non-linearly migrated into the velocity model via FWI acting on raw unprocessed waveforms. With these advancements, FWI can eventually replace conventional processing and migration – all that is needed, is a full-bandwidth velocity model.

A full-bandwidth FWI velocity model will serve as a game-changer in different oil and gas business sectors: exploration, reservoir production and development and 4D seismic field monitoring. A bright future lies ahead; using FWI for reservoir characterisation in both the exploration and development phases as well as in 4D seismic time-lapse projects for direct reservoir monitoring and interpretation. This research serves as a stepping-stone and testimony that FWI of field datasets to aid seismic interpretation and reservoir characterisation is feasible.

The use of the reflection strategies, the offset-variable density scheme and the adaptive matching technique, all developed here, maximises the model resolution with minimal artefacts. Integrating these FWI workflows and strategies developed into the everyday tasks of oil and gas industry experts, is beneficial. Interpretable FWI velocity models obtained from the inversion of these two deep-water OBN datasets, results in an increased capability with FWI aiding reservoir characterisation, improving shallow hazard analysis, and enhancing fault/horizon interpretation. Taking this technology even further is the ultimate aim thereby impacting more assets with FWI, and impacting them earlier in their life cycle – in the pre-production phase where the objective is mainly to increase discoveries and volumes. At its current stage, the production phase, FWI can reduce well counts and increase recovery rates with better reservoir characterisation and field development.

References

Aifei, B. and Wenhui, Y. (2011) Layer-stripping full waveform inversion with damped seismic reflection data, *Journal of Earth Science,* **22,** 241-249.

Alkhalifah, T. and Plessix, R. (2014) A recipe for practical full waveform inversion in anisotropic media: An analytical parameter resolution study, *Geophysics,* **79,** R91-R101.

Baeten, G., de Maag, J., Plessix, R., Klaassen, R., Qureshi, T., Kleemeyer, M., ten Kroode, F. and Rujie, Z. (2013) The use of low frequencies in a full-waveform inversion and impedance inversion land seismic case study, *Geophysical Prospecting,* **61,** 701-711.

Barnes, C. and Charara, M. (2009) The domain of applicability of acoustic full-waveform inversion for marine seismic data, *Geophysics*, **74**, 6, WCC91-WCC103.

Beele, M., Fleury, C., Strobbia, C., Choliq, M., Bonnafe, J. and Vallon, G. (2014) Full Waveform Inversion: A Game-Changer Technology For Our Seismic Imaging Workflows. *Presented at the Proceedings of Indonesian Petroleum Association, 38th Annual Convention & Exhibition*.

Borisov, D., Stopin, A. and Plessix, R.E. (2014) Acoustic pseudo-density full waveform inversion in the presence of hard thin beds. *Presented at the 76th EAGE Conference & Exhibition, Extended Abstracts*. Amsterdam, the Netherlands.

Brossier, R., Operto, S. and Virieux, J. (2015) Velocity model building from seismic reflection data by full-waveform inversion, *Geophys.Prospect.,* **63,** 354-367.

Bunks, C., Saleck, F., Zaleski, S. and Chavent, G. (1995) Multiscale seismic waveform inversion, *Geophysics,* **60,** 1457-1473.

Debens, H. A., Warner, M. R. and Umpleby, A. (2015) Global anisotropic FWI. *Presented at the 77th EAGE Conference & Exhibition Extended Abstracts*, Madrid, Spain, Th-N104-09.

Fei, T. and Larner, K. (1995) Elimination of numerical dispersion in finite-difference modelling and migration by flux-corrected transport, *Geophysics,* **60,** 1830-1842.

Gardner, G.H.F., Gardner, L.W. and Gregory, A.R. (1974) Formation velocity and density – the diagnostic basics for stratigraphic traps, *Geophysics,* **39,** 770-780.

Gauthier, O., Virieux, J. and Tarantola, A. (1986) Two-dimensional nonlinear inversion of seismic waveforms: numerical results *Geophysics,* **51,** 1387-1403.

Granli, J.R., Arntsen, B., Sollid, A. and Hilde, E. (1999) Imaging through gas-filled sediments using marine shear-wave data, *Geophysics,* **64,** 668-677.

Graves, R.W. (1996) Simulating seismic wave propagation in 3D elastic media using staggered-grid finite differences, *Bulletin of the Seismological Society of America,* **86,** 1091.

Guasch, L. and Warner, M. (2014) Adaptive Waveform Inversion – FWI Without Cycle Skipping – Applications, *Presented at the 76th EAGE Conference and Exhibition*.

Guasch, L., Warner, M., Nangoo, T., Morgan, J., Umpleby, A., Stekl, I. and Shah, N. (2012) Elastic full-waveform inversion, *Presented at the 82nd Annual International meeting, SEG, Expanded Abstracts*.

Jones, I. (2010) *An Introduction to: Velocity Model Building,* EAGE Publication, Netherlands.

Kapoor, S., Vigh, D., Wiarda, E. and Alwon, S. (2013) Full waveform inversion around the world, *Presented at the Proceedings of the 75th EAGE Conference, Extended Abstracts*.

Kolb, P., Collino, F. and Lailly, P. (1986) Pre-stack inversion of 1-D medium, *Presented at the Proceedings of IEEE*.

Lailly, P. (1983) The seismic inverse problem as a sequence of before stack migrations: Conference on inverse scattering: theory and application. *Presented at the Society for Industrial and Applied Mathematics*. Philadelphia.

Levander, A.R. (1988) Fourth-order finite-difference PW seismograms, *Geophysics,* **53,** 1425.

Lu, R., Lazaratos, S., Wang, K., Cha, Y.H., Chikichev, I. and R. Prosser, R. (2013) High-resolution Elastic FWI for Reservoir Characterisation, *Presented at the Proceedings of the 75th Anuual EAGE Conference and Exhibition, Extended Abstract*.

Lua, K.W.H., White, R.S. and Christie, P.A.F. (2007) Low-frequency source for long-offset, sub-basalt and deep crustal penetration, *Leading Edge,* **28,** 36-39.

Mora, P. (1989) Inversion = migration + tomography, *Geophysics,* **54,** 1575.

Mora, P. (1988) Elastic wave-field inversion of reflection and transmission data, *Geophysics,* **53,** 750-759.

Morgan, J.V., Warner, M., Bell, R., Ashley, J., Barnes, D., Little, R., Roele, K. and Jones, C. (2013) Next-generation seismic experiments: wide-angle, multi-azimuth, three-dimensional, full-waveform inversion, *Geophysical Journal International,* **195,** 1657-1678.

Mulder, W.A. and Plessix, R.E. (2008) Exploring some issues in acoustic full waveform inversion, *Geophys.Prospect.,* **56,** 827-841.

Nangoo, T., Warner, M., Morgan, J., Umpleby, A., Stekl, I. and Bertrand, A. (2012) Full-waveform Seismic Inversion at Reservoir Depths, *Presented at the 74th Conference and Exhibition, EAGE, Extended Abstracts, W015*.

Plessix, R.E. and Perkins, C. (2010) Full waveform inversion of a deep-water Ocean Bottom Seismometer data set, *First Break,* **28,** 71-78.

Plessix, R., Baeten, G., Willem de Maag, J., Klaassen, M., Rujie, Z. and Zhifei, T. (2010) Application of acoustic full waveform inversion to a low-frequency large-offset land data set, *Presented at the SEG Annual Meeting*.

Plessix, R. (2006) A review of the adjoint-state method for computing the gradient of a functional with geophysical applications, *Geophysical Journal International*, **167,** 495–503.

Pratt, R.G., Shin, C. and Hicks, G.J. (1998) Gauss-Newton and full Newton methods in frequency domain seismic waveform inversion, *Geophysical Journal International,* **133,** 341-362.

Pratt, R.G. and Worthington, M.H. (1990) Inverse theory applied to multi-source cross-hole tomography. Part I: Acoustic wave-equation method, *Geophysical Prospecting,* **38,** 287-310.

Ratcliffe, A., Win, C., Vinje, V., Conroy, G., Warner, M., Umplebly, A., Stekl, I., Nangoo, T. and Bertrand, A. (2011) FWI: A North Sea OBS case study, *Presented at the A. 81st Annual International meeting, SEG, Expanded Abstracts, 2384.*

Routh, P., Palacharla, G., Chikichev, I., and Lazaratos, S. (2012) Full Wavefield Inversion of Time-Lapse Data for Improved Imaging and Reservoir Characterization. SEG Technical Program Expanded Abstracts 2012: pp. 1-6.

Shah, N. (2014) *Seismic Full Waveform Inversion for wrapped and unwrapped phase,* PhD thesis, Imperial College, London.

Shah, N., Warner, M., Washbourne, J., Guasch, L. and Umpleby, A. (2012) A Phase-unwrapped Solution for Overcoming a Poor Starting Model in Full-Wavefield Inversion, *Presented at the 74th EAGE Conference and Exhibition.*

Shin, C. (2009) Waveform inversion in the Laplace–Fourier domain, *Geophysical Journal International,* **177,** 1067.

Shipp, R. and Singh, S. (2002) Two-dimensional full wavefield inversion of wide aperture marine seismic streamer data *Geophysical Journal International,* **151,** 325-344.

Silverton, A., Warner, M., Umpleby, A., Morgan, J. and Irabor, K. (2014) Non-physical water density as a proxy to improve data fit during acoustic FWI, *Presented at the 76th Conference and Exhibition, EAGE, Extended Abstracts, We ELI1 16.*

Sirgue, L., Barkved, O.I., Dellinger, J., Etgen, J., Albertin, U. and Kommedal, J.H. (2010) Full waveform inversion: the next leap forward in imaging at Valhall, *First Break,* **28,** 65-70.

Sirgue, L., Barkved, O.I., Van Gestel, J.P., Askim, J. and Kommedal, J.H. (2009) 3D Waveform Inversion on Valhall Wide-azimuth OBC, *Presented at the 71st EAGE Conference & Exhibition.*

Sirgue, L. (2006) The Importance of Low Frequency and Large Offset in Waveform Inversion, *Presented at the EAGE 68th Conference & Exhibition.*

Sirgue, L. and Pratt, G. (2004) Efficient waveform inversion and imaging: A strategy for selecting temporal frequencies, *Geophysics,* **69,** 231-248.

Song, Z.M., Williamson, P.R. and Pratt, R.G. (1995) 2.5D Full-Wave Frequency domain crosshole modelling an inversion: Part II: Inversion method and synthetic experiments, *Geophysics,* **60,** 796-809.

Symes, W. (2012) Objective Functions for Full Waveform Inversion, *Presented at the 74th EAGE Conference and Exhibition*.

Tarantola, A. (1986) A strategy for nonlinear elastic inversion of seismic reflection data. *Geophysics,* **51,** 1893-1903.

Tarantola, A. (1984) Inversion of seismic reflection data in the acoustic approximation, *Geophysics,* **49,** 1259-1266.

Umpleby, A., Warner, M. and Stekl, I. (2010) Time vs Frequency for 3D wavefiel tomography, *Presented at the 72nd Conference and Exhibition, EAGE, Extended Abstracts, Workshop WS6*.

van Leeuwen, L., Herrmann, F. and Peters, B. (2014) A new Take on FWI - Wavefield Reconstruction Inversion, *Presented at the 77th EAGE Conference & Exhibition*.

Vigh, D., Jiao, K. and Watts, D. (2012) Elastic full-waveform inversion using 4C data acquisition, *Presented at the 82nd Annual International meeting, SEG, Expanded Abstracts*.

Vigh, D., Kapoor, J. and Li, H. (2011) Full-waverform inversion application in different geological settings, *Presented at the 81st SEG Annual Meeting and International Exhibition*.

Vigh, D., Starr, B., Kapoor, J. and Li, H. (2010) 3D Full Waveform Inversion on a Gulf of Mexico MAZ Data Set, *Presented at the 80th SEG Annual International Meeting*.

Virieux, J. and Operto, S. (2009) An overview of full-waveform inversion in exploration geophysics, *Geophysics,* **74,** WCC1-WCC26.

Wang, H., Singh, S., Jian, H. and Calandra, H. (2012) Integrated Inversion of Long and Short Wavelength Velocity Structures Using Combined Wave Equation Tomography and FWI, *Presented at the 74th EAGE Conference and Exhibition*.

Wang, Y. and Rao, Y. (2009) Reflection seismic waveform tomography, *Journal of Geophysical Research,* **114,** BO3304.

Warner, M. (2014) Adaptive Waveform Inversion. *Presented at the SEG Workshop,* Denver Colorado.

Warner, M., Ratcliffe, A., Nangoo, T., Morgan, J.V., Umpleby, A., Shah, N., Vinje, V., Stekl, I., Guasch, L., Win, C., Conroy, G. and Bertrand, A. (2013) Anisotropic full waveform inversion. *Geophysics,* **78,** R59-R80.

Warner, M., Morgan, J.V., Umpleby, A., Stekl, I. and Guasch, L. (2012) Which physics for full-wavefield inversion, *Presented at the 74th Conference and Exhibition, EAGE, Extended Abstracts, W029*.

Warner, M. (2012) Full-waveform inversion - FWI, *Presented at the Imperial College Fullwave III Consortium Meeting*. London.

Warner, M. (2011) Full-Wavefield Tomography/Full-Wavefield Inversion: a Game-Changing Technology, *Presented at the EAGE Education Days*.

Warner, M., Umpleby, A., Stekl, I. and Morgan, J. (2010) 3D full-wavefield tomography: imaging beneath heterogeneous overburden, *Presented at the 72 EAGE Conference & Exhibition*.

Warner, M., Stekl, I. and Umpleby, A. (2008) Efficient and Effective 3D Wavefield Tomography, *Presented at the 70th EAGE Conference & Exhibition*.

Warner, M., Stekl, I. and Umpleby, A. (2007) Full Wavefield Seismic Tomography – Iterative Forward Modelling in 3D, *Presented at the EAGE 69th Conference & Exhibition, 11-14 June*.

Xu, S., Wang, D., Chen, F., Zhang, Y. and Lambare, G. (2012) Full Waveform Inversion for Reflected Seismic Data, *Presented at the 74th EAGE Conference & Exhibition*.

Yao G., Warner M. and Silverton A. (2014) Reflection FWI for both Reflectivity and Background Velocity, *Presented at the 76th EAGE Annual Meeting*. Extended Abstracts.

Yao, G. and Warner, M. (2015) Bootstrapped Waveform Inversion: Long- wavelength Velocities from Pure Reflection Data. *Presented at the 77th EAGE Conference & Exhibition*.

Yoon, K., Suh, S., Cai, J. and Wang, B. (2012) Improvements in time domain FWI and its applications, *Presented at the SEG Annual Meeting Las Vegas*.

Appendices

APPENDIX I –ELASTIC

Elastic Parameterisation

A 3D version of the Marmousi model and a variable Vp/Vs ratio, illustrated in Figure I, was used to generate an elastic dataset. The model dimensions are 201 *201*60 nodes and the grid spacing is 20m. The first two nodes of the model correspond to the water layer and therefore do not get updated across iterations, their value is fixed to 1500 m/s and 0 m/s for Vp and Vs respectively.

.

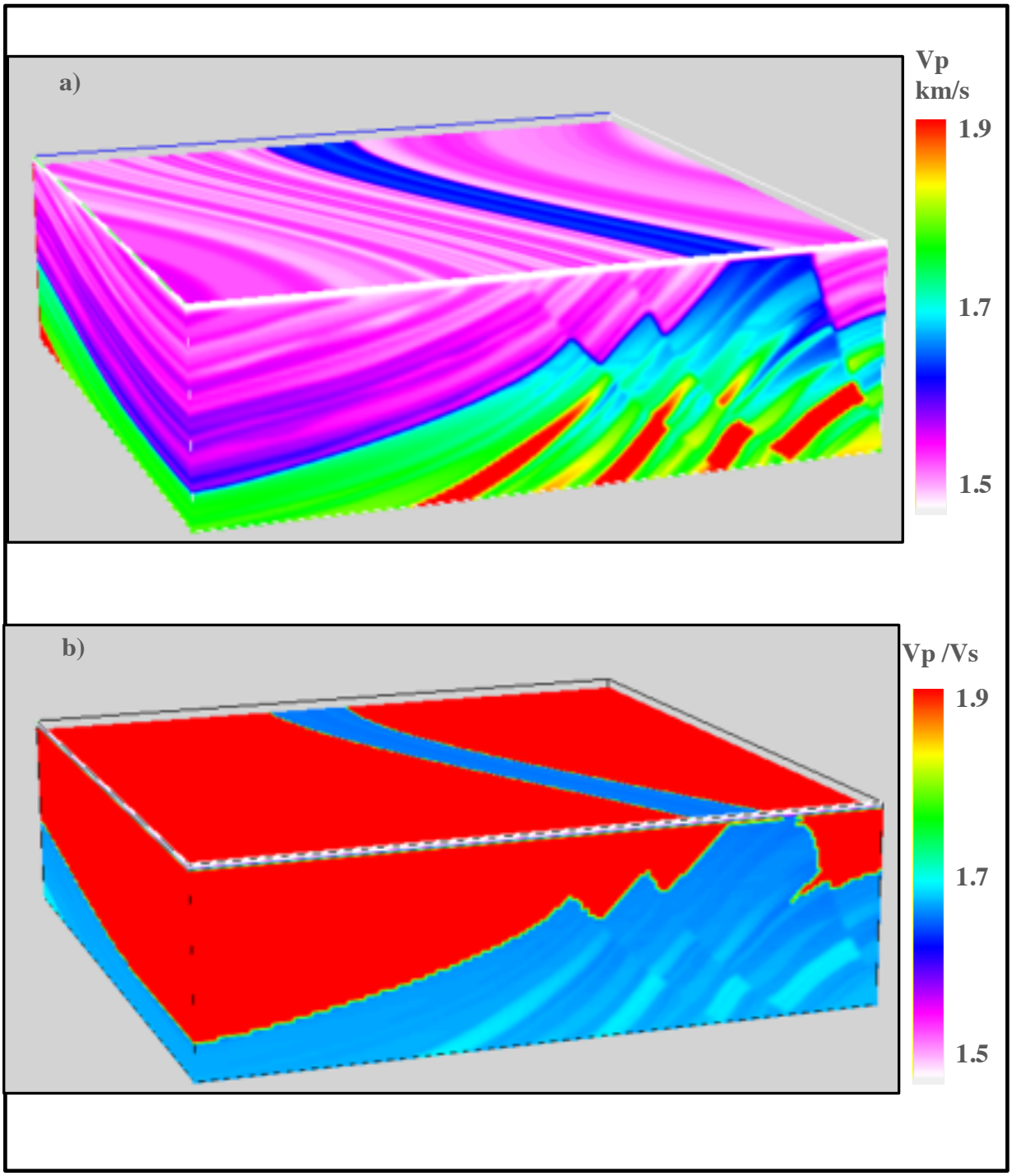


Figure I: 3D Marmousi Model b) variable Vp/Vs ratio. The models vary in all three directions.

3D shot gather corresponding to a purely acoustic case and an elastic case are shown in Figure II. The total amplitude of the gathers has been normalised and the values have been clipped to highlight the relevant events in the seismograms. The shear wave phenomena introduce in the elastic case creates a completely different distribution of events in terms of amplitude, for example, the presence of a strong elastic impedance contrast in the seabed

where the velocity of shear waves goes from zero to some value around 800m/s. Using this data and corresponding models, a series of inversions were undertaken.

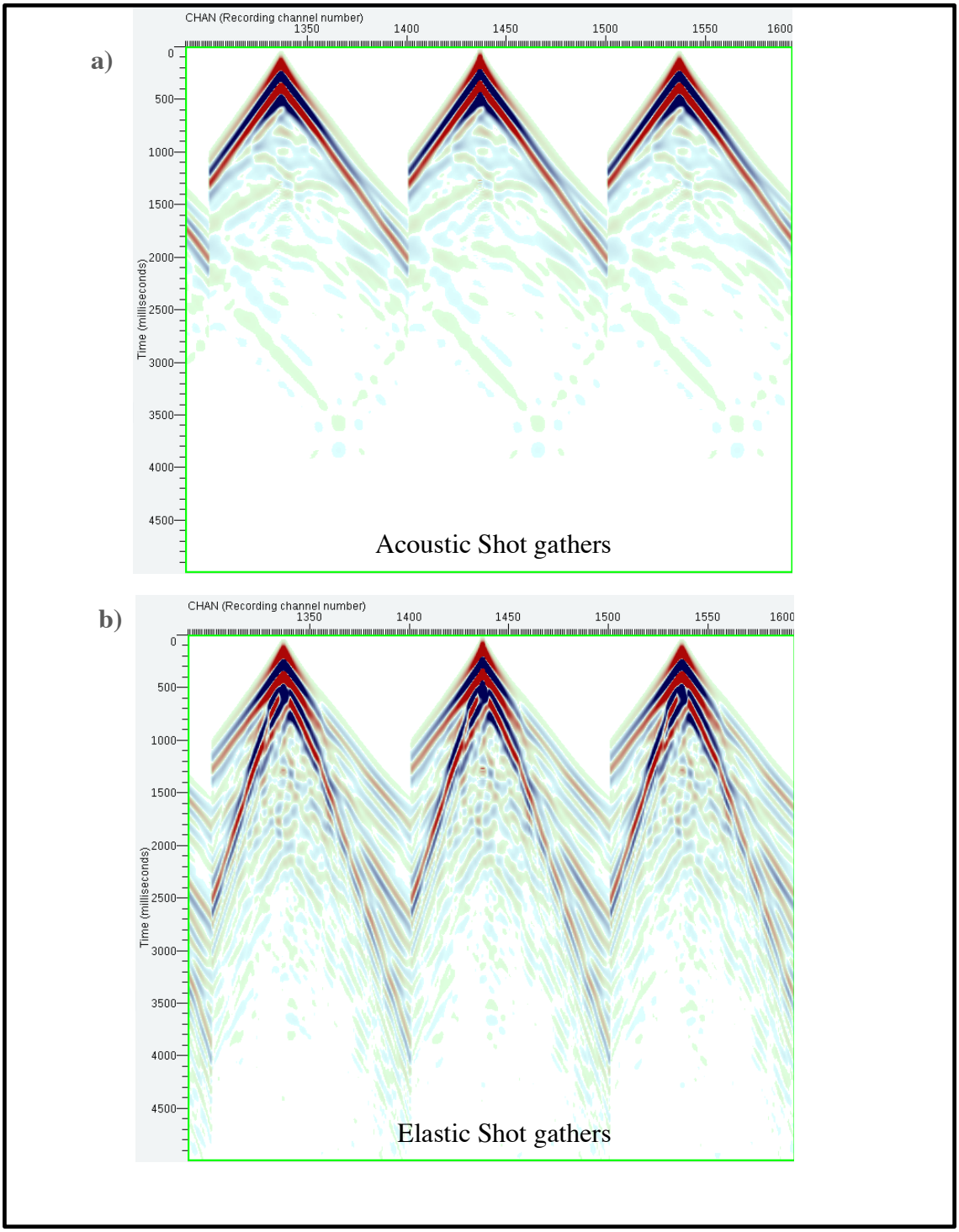


Figure II: a) Acoustic shot gathers and b) elastic shot gathers.